

**An experimental and field-based investigation  
into decimetre-scale bedforms formed by  
turbidity currents**

Isabel Sophie de Cala

Submitted in accordance with the requirements for the degree of  
Doctor of Philosophy

The University of Leeds  
School of Earth and Environment  
Institute of Applied Geoscience



The candidate confirms that the work submitted is their own, except where work which has formed part of jointly authored publications has been included. The contribution of the candidate and the other authors to this work has been explicitly indicated below. The candidate confirms that appropriate credit has been given within the thesis where reference has been made to the work of others.

The work in Chapter 3 of the thesis has appeared in publication as follows:

de Cala, I., Ohata, K., Dorrell, R., Naruse, H., Patacci, M., Amy, L., Simmons, S., McLelland, S.J., McCaffrey, W.D. (2020). Relating the Flow Processes and Bedforms of Steady-state and Waning Density Currents. *Frontiers in Earth Science, Sedimentology, Stratigraphy and Diagenesis*. 8, 409.

Author contributions:

IC Primary author, lead the research, interpreted the data and created the figures. IC and KO carried out the experiments and the experimental design and set up was done by IC, KO, RD, HN, SS, and SM. IC, KO, RD, HN, and WM designed the focus of the research. The MATLAB code to control the pump speed was written by SS. Feedback on the manuscript and edits were provided by all the authors.

Submitted: 17th February 2020

Accepted: 28<sup>th</sup> August 2020

This copy has been supplied on the understanding that it is copyright material and that no quotation from the thesis may be published without proper acknowledgement.

The right of Isabel de Cala to be identified as Author of this work has been asserted by Isabel de Cala in accordance with the Copyright, Designs and Patents Act 1988.

## Acknowledgments

None of this work would have been possible without the Turbidites Research Group and my supervisors Bill McCaffrey, Lawrence Amy, Rob Dorrell and Marco Patacci. I would like to give my sincerest thanks for all their support and guidance throughout my PhD and for giving me the opportunity to be involved in such varied and interesting research. For their financial support towards this project, the sponsors of the TRG must also be thanked (Aker, BP, BP, ConocoPhillips, CNOOC, Equinor, Eni, Hess, Murphy, OMV, Oxy and Shell), as well as the Leeds Anniversary Research Scholarship.

The research presented in Chapter 3, which has since been published, was carried out by a team which included, Koji Ohata, Robert Dorrell, Hajime Naruse, Marco Patacci, Lawrence Amy, Steve Simmons, Stuart McLelland and William McCaffrey. My own contributions, fully and explicitly indicated in the thesis, have been to lead the research, writing of the manuscript, interpretation of the data and creation of the figures. Isabel de Cala and Koji Ohata carried out the experiments, the experimental design and set up was done by Isabel, Koji Ohata, Robert Dorrell, Hajime Naruse, Steve Simmons and Stuart McLelland. Isabel de Cala, Koji Ohata, Robert Dorrell, Hajime Naruse, and William McCaffrey designed the focus of the research. The MATLAB code to control the pump speed was written by Steve Simmons. I would also like to thank the Editors and Reviewers who have helped to refine the research presented in Chapter 3; Anne Bernhardt, Christopher Stevenson, Florian Pohl and anonymous.

For their expert help setting up and facilitating my experimental research I would like to thank Gareth Keevil and Helena Brown from the University of Leeds. And from the University of Hull, Brendan Murphy, Stuart McLelland, Steve Simmons, Lee Wilson and the research students at the University of Hull.

For her geological and wild boar fighting expertise in the field, and her continued friendship over the years, I would like to give special thanks to Sophie Cullis.

Finally, to my family, thank you for your constant love and support, I love you. And to Jake, who has been with me every step of the way, and whose support on this journey has meant so much to me, I dedicate this milestone in my life to you.

## Abstract

Decimetre-scale cross-stratification is relatively rare in turbidites, yet it has been identified in both ancient and modern systems. However, the type of bedform associated with cross-stratification development and the processes involved in its formation remain poorly understood. Similarly, variations in the styles of decimetre-scale cross-stratification occurrence, the sedimentary character of individual turbidite beds and their evolution downstream remain poorly constrained. Consequently, the extent to which the occurrence of decimetre-scale cross stratification may be used as a diagnostic tool to interpret the likely downstream evolution of a system remains uncertain.

Three work elements are presented within this thesis. The first describes a series of laboratory experiments that investigate the controls on bedform development under both steady and waning saline density currents. Decimetre-scale bedforms developed within and scaled with a lower denser layer of the current below the height of the velocity maximum, whose dynamics dictated the bedform type. Dunes were distinguished from ripples, downstream migrating antidunes and upstream migrating antidunes on the basis of their out-of-phase relationship with the upper surface of the lower layer of the current. The associated flow regimes were calculated using the bulk Froude number based on the less stratified lower layer of the flow. Using this approach, the new experimental data refine the subcritical bedform phase spaces and antidune phase-spaces of the bedform phase diagram for density currents.

The second work element describes a series of experiments that test how beds of non-uniform, bimodally distributed sediment impact bedform development and kinematics, with application to both open channel flows and turbidity currents. Bedform phase diagrams that characterise sediment using the median grain-size, are found to inaccurately predict bedform development from non-uniform sediment beds made up of different grain-size distributions. The new data further refine bedform phase diagrams and improve understanding of the stabilising effect on the substrate of the fine grain-size fraction in sediment mixtures.

The final work element characterizes the occurrence of decimeter-scale cross-stratification within the turbidites of the Peira Cava outlier, of the Tertiary Foreland Basin of SE France. Within the Peira Cava system a greater level of variability is observed in the cross-stratified bed types than has hitherto been recognised. This facies is interpreted as being formed by dunes, which are confined to the proximal regions. Bed correlations indicate that dunes are not associated with 'significant bypass' of sediment to distal locations, as predicted by some existing facies tract models.

## Table of contents

<b>Acknowledgments</b> .....	<b>iv</b>
<b>Abstract</b> .....	<b>v</b>
<b>Table of contents</b> .....	<b>vi</b>
<b>List of tables</b> .....	<b>xi</b>
<b>List of figures</b> .....	<b>xii</b>
<b>Abbreviations and symbols</b> .....	<b>xxii</b>
<b>Chapter 1. Introduction</b> .....	<b>1</b>
1.1 Thesis background and rationale .....	1
1.2 Thesis aims and objectives .....	2
1.3 Thesis outline .....	3
<b>Chapter 2. Literature Review</b> .....	<b>5</b>
2.1 Turbidity currents .....	5
2.2 Introduction to sediment transport .....	9
2.2.1 Thresholds of sediment transport.....	9
2.2.2 Non-uniform and cohesive sediment .....	11
2.3 Bedform generation .....	13
2.4 Bedform classifications and phase diagrams .....	14
2.4.1 Defining dunes versus ripples .....	15
2.4.2 Types of antidunes and the processes relating to their migration direction .....	17
2.4.3 Bedform phase diagrams .....	19
2.5 Turbidity current bedforms.....	20
2.5.1 ‘Megaripples’ in turbidites .....	21
2.5.2 Turbidity current sediment waves .....	23
<b>Chapter 3. Relating the flow processes and bedforms of steady-state and waning density currents</b> .....	<b>25</b>
3.1 Abstract.....	25
3.2 Introduction .....	26
3.2.1 Bedform classifications and phase diagrams.....	27
3.3 Methodology.....	29
3.3.1 Experimental set up and methods .....	29
3.3.2 Experimental parameters.....	32
3.4 Data Processing.....	35
3.4.1 Analysis of bedform dimensions .....	35
3.4.2 Drag Coefficient .....	36

3.5 Results .....	36
3.5.1 Current density .....	36
3.5.2 Flow velocity .....	39
3.5.3 Bedforms .....	40
3.5.3.1 Subcritical bedforms .....	42
3.5.3.2 Supercritical bedforms.....	45
3.6 Discussion .....	46
3.6.1 Bedform development under steady flows .....	46
3.6.2 Bedform development under waning flows: Maintenance of flow conditions in the lower layer of the density current .....	48
3.6.3 Influence of pre-existing bed state .....	49
3.6.4 Phase diagram analysis of new data .....	51
3.6.4.1 Phase diagram for steady open channel flow .....	51
3.6.4.2 Phase diagram for steady density currents.....	52
3.7 Conclusions.....	54
<b>Chapter 4. Bedform development and morphodynamics of beds of varying bimodal grain-size distributions .....</b>	<b>56</b>
4.1 Introduction.....	56
4.2 Methodology .....	57
4.2.1 Experimental set up.....	57
4.3 Experimental parameters and data processing .....	59
4.3.1 Froude number .....	60
4.3.2 Shear velocity .....	61
4.3.3 Drag coefficient .....	62
4.3.4 Calculation of sediment parameters.....	62
4.3.5 Analysis of bedform dimensions.....	63
4.3.6 Bedform migration rate .....	63
4.3.7 Analysis of core sediment samples .....	64
4.4 Results .....	64
4.4.1 Shields Parameter and sediment mobility .....	64
4.4.2 Observed bedform types .....	65
4.4.3 Bedform evolution.....	68
4.4.3.1 Experiment 1: Coarse-grained, unimodal grain-size distribution.....	68
4.4.3.2 Experiment 2: Fine-grained, unimodal grain-size distribution .....	72
4.4.3.3 Experiment 3: Narrow bimodal grain-size distribution .....	72
4.4.3.4 Experiment 4: Wide bimodal grain-size distribution.....	75

## VIII

4.4.3.5 Bedform Equilibrium .....	77
4.4.4 Bed grain-size variation .....	78
4.5 Discussion .....	80
4.5.1 Bedform equilibrium .....	80
4.5.2 Observed bedforms versus bedform stability fields .....	81
4.5.3 Hiding factor .....	84
4.5.4 Existing models that explain bed stability in non-uniform sediment .....	85
4.5.5 Development of fine laminations - grain sorting in bimodal sediment mixtures .....	86
4.5.6 Fine sediment laminations and increased bed stability .....	88
4.5.6.1 Reduced hydraulic conductivity .....	88
4.5.6.2 Armouring of the bed by fine lamination networks .....	90
4.5.6.3 Winnowing of the fine-grained fraction .....	90
4.5.7 Bedform Diminishment .....	91
4.5.8 Bedform morphological variability .....	92
4.6 Conclusions .....	93
<b>Chapter 5. Cross-stratified turbidite beds in the Grès de Peïra Cava, SE France .....</b>	<b>95</b>
5.1 Introduction .....	95
5.2 Geological setting .....	96
5.2.1 Plate tectonic framework of the southern Alpine Foreland Basin .....	96
5.2.2 Depositional setting - the Alpine Foreland Basin morphology and topography .....	97
5.2.3 Correlation framework - Peïra Cava basin stratigraphy .....	98
5.2.4 Basin architecture and depositional facies of Peïra Cava .....	101
5.2.5 Cross-stratified units of the Peïra Cava basin: previous facies descriptions and models .....	105
5.3 Collection of field data .....	108
5.3.1 Field site locations and stratigraphic setting .....	108
5.3.2 Sedimentary logging .....	111
5.3.3 Bedform geometric analysis .....	113
5.3.4 Palaeocurrent measurements .....	113
5.4 Results .....	114
5.4.1 Stratigraphic correlations .....	114
5.4.2 Comparison of the different bedforms found in the Peïra Cava basin fill .....	118
5.4.3 Types of Cross-stratified beds and facies associations .....	120
5.4.4 Downstream evolution of cross-stratified beds .....	133
5.4.5 Cross-stratification geometry .....	136
5.4.6 Mud intervals .....	138

5.4.7 Paleoflow .....	138
5.4.8 Cross-stratification grain-size .....	139
5.5 Discussion .....	140
5.5.1 Defining the type of bedform associated with cross-stratification in Peira Cava .....	140
5.5.1.1 Palaeoflow .....	140
5.5.1.2 Megaripple terminology .....	141
5.5.1.3 Ripples .....	141
5.5.1.4 Decimetre-scale cross-stratification. ....	142
5.5.2 Depositional mechanisms and current conditions relating to cross-stratified beds ..	146
5.5.3 How well do existing facies tract models describe the spatial occurrence of cross-stratified units in the Peira Cava basin? .....	150
5.5.3.1 Model description summaries .....	151
5.5.3.2 Proximal – distal correlations of cross-stratified beds in the Peira Cava basin ...	152
5.5.4 Depositional sequences .....	155
5.5.4.1 Single or multiple events .....	155
5.5.4.2 Coarse sand cross-stratified intervals overlain by thin muds.....	156
5.5.4.3 Interpretations of temporal and spatial variation in current capacity and competency .....	159
5.6 Conclusions.....	161
<b>Chapter 6. Further discussion .....</b>	<b>164</b>
6.1 The impact of grain-size distribution on dune development in Peira Cava .....	164
6.2 Vertical flow structure and estimation of flow depth from bedform dimensions .....	169
6.3 Equilibrium in dune formation.....	172
6.4 Areas for future research.....	173
<b>7. Conclusions.....</b>	<b>175</b>
<b>References.....</b>	<b>178</b>



**List of tables**

**Table 2.1.** Ripples, dunes and megaripples dimensions as defined by Dalrymple *et al.* (1978) and van Rijn (1989).....22

**Table 3.1.** Experimental parameters and characteristics of the plastic sediment that was used for the channel substrate in each experiment. Densimetric Froude number (*Frd*) calculation shown in Equation 1.....31

**Table 4.1.** Experimental Parameters. The experiments were run either with a unimodal sediment size distribution in the substrate (Experiments 1 and 2), or with a bimodal distribution, formed by mixing different end-member sediment types (Experiments 3 and 4).....60

**Table 4.2.** Critical parameters for median grain-size for all grains.....64

**Table 4.3.** Critical parameters for bimodal sediment fractions (*Di*).....65

**Table 4.4.** Hiding factor: Critical parameters for bimodal sediment fractions (*Di*).....85

**Table 5.1.** A summary of each site name, its location denoted by coordinates, the thickness of the stratigraphic interval studied and an approximation of each site’s position within the basin.....110

**Table 5.2.** Classification scheme of sediment grain-size (represented by the median grain-size), applied to the Peira Cava turbidites, based on the Wentworth scale.....112

**Table 5.3.** Summary of cross-stratification geometry.....136

**Table 6.1.** Table 6.1. Estimations of the depth of the flow in which the Peira Cava dunes formed based on the scaling relationship defined in Eq. 6.1, and on the possible ranges of total current thickness associated with each dune height based on the lower layer of the flow equalling between 15 – 50 % of the entire flow thickness.....1

## List of figures

- Figure 2.1. (A)** Schematic representation of the Bouma sequence with descriptions of facies  $T_a$  –  $T_e$  (Bouma 1962). **(B)** Schematic representation of the Lowe sequence (Lowe 1982). **(C)** A hypothetical representation of the spatial distribution of sediment by medium-grained turbidity currents. (Bouma 1962). **(D)** A hypothetical representation of the spatial distribution of sediment (From Sumner *et al.*, 2012) deposited by coarse-grained turbidity currents.....8
- Figure 2.2.** Hjulstrom’s diagram showing the critical velocity required to move sediment of a given grain-size (From Cheel, 2005).....10
- Figure 2.3.** Shields plot (modified after Church 2006) defines the threshold of traction movement, highlighting the widely regarded upper and lower limits of sediment motion. The Y-axis plots the Shields parameter ( $\theta$ ) and the x-axis plots the Particle Reynolds Number ( $Re_*$ ). The approximate boundaries define modes of sediment transport (after Dade and Friend 1998).....11
- Figure 2.4.** Schematic representation of an armour layer where the surface sediment is coarser than the subsurface sediment.....12
- Figure 2.5.** A schematic representation of the hairpin vortices that are produced from the turbulent boundary layer, which initiate sediment transport and the formation of bed defects. (After Best, 1992).....14
- Figure 2.6.** Conceptual diagram representing the interaction of a flow over 2D ripples and dunes. Figures **A-C** also describe the development of dunes from ripples: **(B.i)** dune generation due to bedform growth by ripple coalescence (modified after Schinder and Robert, 2005). **(B.ii)** Dune generation by the formation of a larger than average ripple (rogue ripple) (modified after Bennet and Best, 2016).....16
- Figure 2.7.** A log-log plot of bedform height and wavelength of 1491 flow transverse subaqueous bedforms (Flemming 1988), from Ashley (1990). The green circle identifies ripples and the red circle identifies dunes.....17
- Figure 2.8. (A)** Sediment transport and deposition over an upstream migrating antidune, as described by Kennedy (1963). Water depth variation over **(B)** upstream migrating

- antidunes, **(C)** downstream migrating antidunes and **(D)** stationary antidunes (modified after Nuñez and Vide, 2011).....19
- Figure 2.9.** Examples of dimensionless bedform phase diagrams for open channel flow. **(A)** Southard and Boguchwal (1990), showing mean flow velocity against flow depth for grain-sizes between 0.4 and 0.5 mm. **(B)** Southard & Boguchwal (1990), showing mean grain-size against the mean flow velocity for flow depths between 0.25 and 0.4 m. **(C)** van den Berg and Van Gelder's (2009) adaptation of van Rijn's (1984) dimensionless phase diagram. **(D)** Fedele's *et al.* (2016) new bedform phase diagram for density currents.....20
- Figure 2.10.** Logarithmic plot of wavelength versus wave height for global bedform examples associated with turbidity currents. Three groups are identified, (i) small-scale sediment waves with mixed relief, (ii) large scale sediment waves with mixed relief and (iii) large scale scours. From Symons *et al.* (2016).....24
- Figure 3.1.** Experimental set up.....30
- Figure 3.2.** Experiments 1 - 5 **(A - E)**, interpolated velocity profiles based on shear velocity calculations for the lower layer of each density current. For steady flow experiments, shear velocity was time-averaged over the whole run. For unsteady flows, shear velocity was time-averaged over 5-minute intervals.....34
- Figure 3.3.** Schematic diagram of asymmetric bedforms. The red points depict the locations of the x, y coordinates, which were recorded on each bedform.....36
- Figure 3.4.** Vertical concentration profiles averaged over 2 - 3 minutes. The black dashed line denotes the height of the interface between upper and lower denser layer, and the red crosses attribute this point to specific profiles, depicting the constant height of the interface throughout the run. Experiments 2 and 4 are waning currents, the red triangles mark the change in height of the upper surface of the current with the ambient fluid over time. They depict the gradual reduction in height as the flow is slowed. Plot **(F)** shows average density profiles for each run based on available data in **(A - E)**. Experiments 1 - 5 correspond to plots **(A - E)**, respectively.....38
- Figure 3.5.** Contour plots of the downstream velocity component throughout Experiments 1 (supercritical steady flow) **(A)** and 2 (supercritical waning flow) **(B)**. The dashed red lines identify the height of the upper surface of the lower denser layer of the density current. The black dots indicate the height of the substrate beneath the vectrino. **(C)** Contour

plot of the downstream velocity component throughout Experiment 4 (subcritical waning flow), recorded within the bottom dense layer of the flow. Velocity measured between 0 - 18 minutes and 33 - 43 minutes was recorded by vectrino 1 which was positioned higher above the bed. Velocity measured between 18 – 44 minutes was recorded by vectrino 2, positioned lower in the flow. The red dots indicate the height of the substrate beneath vectrino 1 and the black crosses indicate the height of the substrate beneath vectrino 2.....40

**Figure 3.6. (A)** Ratio between bedform wavelength and the height of the lower layer of the current. **(C)** Bedform development timeline for Experiments 1 - 5 (DSMA, Downstream migrating antidunes. LWA, Long wavelength antidunes) and **(B)** the associated drag coefficient change.....41

**Figure 3.7.** Bedform dimensions (data from all experiments).....42

**Figure 3.8.** Bedform current interaction. Two layers can be recognised in the density current: the lower denser layer of the density current is dyed red/pink, the upper surface of the lower denser layer is indicated by a yellow dotted line. The current interface with ambient water is indicated by a solid yellow line. Direction of flow is indicated by an arrow in each photograph. **(A)** There is no interaction between ripples and the lower layer upper surface (Experiment 3). **(B)** Dunes formed towards the end of Experiment 5. The dunes are out-of-phase with the upper surface of the lower layer. From photo (A) it is hard to determine the height of the upper surface of the current. **(C)** is taken from another flume angle at the same time as photo (A), in which the upper surface of the current can be distinguished.....43

**Figure 3.9.** Average height and wavelength of bedforms measured every 30 seconds in a 2-metre-wide window located 4 - 6 m from the upstream end of channel. **(A)** Bedform wavelength. **(B)** Bedform height. Steady flow experiments depicted by dashed lines. Waning flow experiments depicted by solid lines.....44

**Figure 3.10.** Superimposed dunes upon the relict remains of a long wavelength antidune (Experiment 2). The dotted line depicts the upper surface of the lower denser layer. The solid line depicts the approximate height of the current interface with the ambient fluid (based on Figure 3.4b). Flow is from right to left (arrow). The superimposed dunes interact with this upper surface in an out-of-phase manner. Mixing between the lower

and upper layers of the flow can be observed; the upper layer has become light pink.....45

**Figure 3.11. (A)** Experiment 1. Example of the in-phase, downstream migrating antidunes formed under steady flow conditions. The yellow dotted line defines the upper surface of the lower denser layer of the current. **(B)** Experiment 2. Example of a long wavelength antidune. It is in-phase with the upper surface of the lower denser layer of the current (dyed pink). **(C)** Partial reworking of the long wavelength antidune. Flow is from right to left in all photos (arrows).....47

**Figure 3.12.** Conceptual phase diagram with a third axis for time, depicting how a bed under steady conditions might evolve (based on Experiment 5), compared to bedforms under a waning current (based on Experiment 2).....51

**Figure 3.13.** Bedforms developed during the present experiments are plotted onto bedform phase diagrams for open-channel and density driven flows. **(A)** van den Berg and Van Gelder’s (2009) dimensionless phase diagram. **(B)** A modified version of Fedele’s *et al.* (2016) new bedform phase diagram for density currents: Particle parameters ( $D_*$ ) were calculated and re-plotted against  $Fr_d$ . The red markers signify bedforms and associated  $Fr_d$  numbers calculated for the lower layer of the current. Grey markers signify the same bedforms and associated  $Fr_d$  numbers calculated for the entire current.....54

**Figure 4.1.** Experimental set up.....58

**Figure 4.2.** Grain-size distribution at the start of each experiment. Measurement of particle size distribution was carried out using a Malvern 2000e particle sizer.....58

**Figure 4.3.** The blue curve follows the standard logarithmic profile away from the bed based on the logarithmic law of the wall. The curve of circles is a measured velocity profile. The data excluded from shear velocity calculations are identified by the open circle datapoints. The final estimation for shear velocity was taken as the value corresponding to the line of best fit with the highest value of the coefficient of determination to the log-law.....61

**Figure 4.4.** de Cala *et al.* (2020): Schematic diagram of asymmetric bedforms of different dimensions, indicating the points where each x, y coordinate was taken.....63

- Figure 4.5. (A)** Example of a dune interacting with the flow. This can be observed as there is high concentration of suspended sediment eroded off the bedform crest and stoss side, which is incorporated into the wake region that extends from the bedform crest. Shear layers are approximately defined in relation to the wake region. Mixing between the shear layer and wake region can be seen best towards the top of the wake region. **(B)** A view from above the flume looking down onto the flow's surface. An example of a 'boil' is visible due to high concentration of suspended sediment within the wake region. 'Boils' are the result of the wake region reaching the surface as strong turbulent 'ejection events' rise through the flow.....66
- Figure 4.6.** Examples of **(A)** dune bedforms formed in Experiments 1 and 3, and **(B)** ripples formed in Experiments 2 and 4.....67
- Figure 4.7.** Bedform dimensions recorded throughout Experiments **(A)** 1, **(B)** 2, **(C)** 3 and **(D)** 4. Experiments 1 and 3 formed the largest bedforms with wavelengths greater than 50 cm.....68
- Figure 4.8.** Moving average of **(A)** bedform height **(B)** wavelength and **(C)** steepness, including 2-standard deviations from the mean and the moving average of bedform migration rate (orange). The absence of data in Experiment 1 is due to a camera malfunction between 17 – 22 hours where no bedform dimensional data could be collected.....70
- Figure 4.9.** Stages of bedform change throughout Experiment 1.....72
- Figure 4.10.** Experiment 3. Examples of fine bottomsets – one beneath a migrating bedform and the other deposited and buried deeper within the substrate as a fine lamination. The cross-stratified intervals are bound by the bottomsets top and bottom.....73
- Figure 4.11.** Experiment 3. **(A – H)** depict the process of bedform diminishment caused by its interaction with a previously preserved fine bottomset within the substrate. White lines depict the fine sediment laminations.....74
- Figure 4.12.** Examples of sediment starved ripples formed in Experiment 4. In the upper region of the bed there is a laterally extensive and intricate network of fine sediment laminations.....75
- Figure 4.13.** Experiment 4. **(A – E)** depict the process of bedform diminishment caused by its interaction with a previously preserved fine bottomset within the substrate. White lines depict the fine sediment laminations.....76

- Figure 4.14.** Percent of bedforms that increase in size.....78
- Figure 4.15.** The percentage of fine sediment (0 – 300  $\mu\text{m}$ ) content found at different levels of the bed for Experiments 1 – 4. This data is extracted from the grain-size distributions calculated for bed core samples taken from different points across the flume, which were then averaged across equivalent bed levels.....79
- Figure 4.16.** Bedforms developed during the present experiments are plotted onto van den Berg and Van Gelder’s (2009) dimensionless bedform phase diagram.....83
- Figure 4.17.** Experiment 3. Photograph depicting characteristic mechanisms of sediment deposition over the lee slope. Grain fall of fine sediment from suspension forms fine toset deposits, grain flow forms cross-strata that deposit ontop of the tosets and preserve them.....87
- Figure 4.18.** Schematic representations of the ability of water to enter and move through the bed in a wide grain-size distribution. **(A)** Some water is able enter and flow through the bed (signified by black arrows) when the fine and coarse grain-size fractions are poorly distributed. **(B)** Representative of the bed in Experiment 4, the grey-coloured grains represent the fine sediment lamination which formed within the top 5 cm of the bed in Experiment 4. The diagram shows how the flow’s ability to pass through a single fine lamination is reduced (signified by red arrows) due to the impermeability of the fine lamination. As a result, much of the flow is prevented from penetrating to deeper levels of the bed. **(C)** Also representative of Experiment 4, this diagram depicts a wider section of the anastomosing fine-grained lamination network that further obstructs the flow’s capacity to move through the bed as the fine-grained lamination network extends through poorly sorted parts of the bed in multiple directions and at different angles....89
- Figure 4.19.** For clarity, a series of photographs were converted into a schematic diagram of a bedform interacting with a fine sediment lamination. The red dotted line highlights the steeper migratory path of the bedform as dictated by the immobile fine laminations. The yellow dashed line depicts the inferred migratory path of the bedform had it not encountered the fine sediment laminations and was able to continue scouring at the same rate and depth into the bed. **(A)** The bedform is unable to mobilize and erode the sediment making up the fine laminations. **(B – C)** The steepness of the bedform is reduced as its angle of climb steepens as it migrates over the fine lamination. Flow is from right to left.....92

- Figure 5.1. (A)** Chronostratigraphic diagram for the Palaeogene Provençal Basin that shows three lithostratigraphic units collectively known as the 'Nummulitic Trilogy' or the Priabonian Trilogy' (Modified by Boussac, 1912, from Cunha *et al.* (2017)). **(B)** Paleogeography of the main Annot Sandstone sub-basins (from Joseph and Lomas, 2004, modified by Cunha *et al.* (2017)) **(C)** Geological map of the structural elements of the main Grès d'Annot sub-basins, including the Peira Cava system (from Du Fornel *et al.* (2004), modified by Cunha *et al.* (2017)).....97
- Figure 5.2: (A)** Map of the Peira Cava basin. **(B)** geological map of the Grès de Peira Cava stratigraphic sequence via a schematic structural cross-section (modified from Ravenne *et al.*, 1987).....99
- Figure 5.3.** Bed to bed correlations established by Amy (2000) across the Peira Cava outlier, in a 420 m stratigraphic interval, exposed over a 10 by 6 km area (also see Amy *et al.*, 2007).....100
- Figure 5.4. (A)** Mutti's (1992) turbidite depositional sequence scheme **(B)** Idealized 'Bouma' sequence (Bouma, 1962) from Sumner *et al.* (2012). **(C)** Diagram showing an idealized turbidite depositional sequence after Lowe (1982), containing, tractional structures (R1); inversely graded gravel (R2); normally graded gravel (R3); coarse sand also with tractional structures (S1); coarse sand containing thin horizontal layers (S2); structureless coarse sand that may be graded (S3); sand containing tractional structures ( $T_{bc}$ ) interlaminated silt and mud ( $T_d$ ); and structureless mud ( $T_e$ ), from Sumner *et al.* (2012).....103
- Figure 5.5.** Cunha *et al.* (2017): six bed types identified in the Peira Cava outlier.....104
- Figure 5.6. (A)** Mutti (1992) facies tract model. **(B)** Kneller and McCaffrey (2003) Down-dip profiles of the proximal region of deposits. **(C)** paleogeographic scheme and facies tracts of the turbidite deposits of the Annot Sandstone in the Peira Cava sub-basin (from Cunha *et al.* (2017)). The letters A, B and C indicate the facies tracts in the proximal area, along the steep western margin and in distal area respectively. **(D)** from Tinterri *et al.* (2017): Far left – location of bedforms within the Priabonian-Rupelian, Ranzano Sandstone, formed by a deflected flow towards the NW. Middle - Depiction of the progressive formation of tractive structures related to the shear stress produced by the bypassing upper turbulent flows. Far right – Asymmetrical cross current facies tract and related processes of turbidite deposits containing cross-stratified beds. Paleocurrents

are directed towards the page. <b>(E)</b> Downstream evolution of cross-stratified beds in the Marnoso-Arenacea Formation, Italy, Tinterri and Tagliaferri (2015).....	107
<b>Figure 5.7.</b> Diagram shows the stratigraphic interval and locations of correlative sections 1 – 5 within the stratigraphic context of Amy’s (2000) correlation of the wider system along a SW – NE transect. Figure modified from Amy (2000).....	109
<b>Figure 5.8.</b> Map of all site locations.....	111
<b>Figure 5.9.</b> Examples of cross-stratification planes exposed in 3-dimensions.....	114
<b>Figure 5.10.</b> Bed-to-bed correlations over 8 km through the Peira Cava Basin. Correlations highlighted in orange correlate cross-stratified beds. Blue correlations indicate the presence of hemiplegic sediment that was often coloured yellow, white or blue.....	116
<b>Figure 5.11.</b> Correlations of cross-stratified beds.....	117
<b>Figure 5.12.</b> Ripple and cross-stratification height.....	119
<b>Figure 5.13.</b> Heights vs wavelengths of both Ripples and cross-stratified intervals.....	119
<b>Figure 5.14.</b> Bed Type 1.....	121
<b>Figure 5.15.</b> Bed Type 2.....	122
<b>Figure 5.16.</b> Bed Type 3.....	123
<b>Figure 5.17.</b> Bed Type 3.....	124
<b>Figure 5.18.</b> Bed Type 4.....	125
<b>Figure 5.19.</b> Bed Type 5.....	126
<b>Figure 5.20.</b> Bed Type 6.....	127
<b>Figure 5.21.</b> Bed Type 7.....	128
<b>Figure 5.22.</b> Bed Type 7.....	129
<b>Figure 5.23.</b> Bed Type 8.....	129
<b>Figure 5.24.</b> Bed Type 9.....	130
<b>Figure 5.25.</b> Bed Type 9.....	131
<b>Figure 5.26.</b> Bed Type 10.....	132

<b>Figure 5.27.</b> Bed Types 1-10.....	133
<b>Figure 5.28.</b> Detailed logs of correlative beds that were found to contain either cross-stratification or have a bed top that thins and thickens. The bed colours relate to the bed type.....	135
<b>Figure 5.29.</b> Palaeoflow measured for the present research (top left), Amy (2000) and Cunha <i>et al.</i> (2017).....	139
<b>Figure 5.30.</b> From Cartigny <i>et al.</i> (2014). Examples of antidune sedimentary deposits.....	143
<b>Figure 5.31.</b> Examples of downstream migrating antidunes. <b>(A)</b> Cartigny <i>et al.</i> (2011) <b>(B)</b> Fedele <i>et al.</i> (2016) <b>(C)</b> Núñez-González and Martín-Vide (2011) <b>(D)</b> de Cala <i>et al.</i> (2020), also in Chapter 3.....	145
<b>Figure 5.32.</b> Bed types are grouped by the processes that are interpreted to be involved in their formation.....	147
<b>Figure 5.33.</b> Arnott and Al-Mufti (2017), cross-stratification development as a result of scour infill and not tractional bedform migration.....	150
<b>Figure 5.34.</b> Schematic diagram of the downstream evolution of cross-stratified beds in the Peira Cava basin, based on the present research compared to the downstream evolution models proposed by Kneller and McCaffrey (2003) and Cunha <i>et al.</i> (2017).....	154
<b>Figure 5.35.</b> Schematic representation of the depositional evolution of proximally amalgamated cross-stratified beds, which downstream deposit as distinctly separate flow events separated by a mud interval.....	156
<b>Figure 5.36.</b> Schematic representation of a cross-stratified bed that is followed by a mud interval, followed by Tc - Te of the Bouma sequence.....	158
<b>Figure 5.37.</b> Idealized turbidite deposits. The coarsest sediment is deposited first (orange), then finer sand (yellow) deposits into a slightly different part of the basin, the horizontal lines depict an area that does not experience fine sand deposition. In this location, coarse sand may be followed directly by fine silts and muds which are deposited last (grey)..	159
<b>Figure 6.1.</b> An example a fine-grained bottomset lamination that has formed a laterally extending and fine-grained lamination through the bed.....	165

- Figure 6.2.** Photos of complex deposits of widely distributed cross-stratified beds in Peira Cava that contain multiple sets of cross-stratification separated by fine-grained laminations.....166
- Figure 6.3.** A comparison between the deposits of (A) experimental bedforms (c.f. Chapter 4) and (B) field-based cross-stratified beds found in the Peira Cava basin (Bed 523). Both have formed from bimodally distributed sediment.....167
- Figure 6.4.** A schematic 3-dimensional bedform phase diagram that represents a flow through time and space in the Peira Cava basin.....169

## Abbreviations and symbols

DMA	Downstream migrating antidunes
LWA	Long wavelength antidunes
TES	Total Environment Simulator, University of Hull
SD	Standard deviation
km	kilometres
SE	South East
SW	South West
N	North
S	South
E	East
W	West
NE	North East
NW	North West
NNE	North, North East
SSW	South, South West
F0 – 10	Facies 0 – 10
VFL	Very fine lower sand
VFU	Very fine upper sand
FL	Fine lower sand
ML	Medium lower sand
MU	Medium upper sand
CL	Coarse lower sand
CU	Coarse upper sand
VCL	Very coarse lower sand
VCU	Very Coarse upper sand
G	Gravel
m	Metres
cm	Centimetres
mm	Millimetres
Hz	Hertz

L	Litres
°	Degrees
μm	Micrometres
secs	Seconds
%	Percent
<i>H</i>	Flow depth
<i>U</i>	Depth averaged Flow velocity
<i>u</i>	Current velocity
Fr	Froude number
<i>Fr<sub>d</sub></i>	Densimetric Froude number
<i>u*</i>	Shear velocity
<i>u*<sub>cr</sub></i>	Critical shear velocity
<i>d<sub>50</sub></i>	Median grain-size
<i>Re*</i>	Particle Reynolds number
<i>g</i>	Acceleration due to gravity
<i>K</i>	von Kármán constant (0.41)
<i>z</i>	height above the bed
<i>z<sub>0</sub></i>	height above the bed where flow velocity is zero
<i>r<sup>2</sup></i>	coefficient of determination
<i>C<sub>d</sub></i>	Drag coefficient
<i>θ</i>	Shields parameter
<i>θ<sub>cr</sub></i>	Critical Shields number
<i>θ'</i>	Grain mobility parameter
<i>τ</i>	Dimensional shear stress
<i>τ<sub>c</sub></i>	Critical shear stress
<i>ρ</i>	Density of the fluid
<i>ρ<sub>a</sub></i>	Ambient water density
<i>ρ<sub>s</sub></i>	Density of sediment
N	Newtons
<i>D*</i>	Dimensionless grain-size/ Particle parameter
<i>ν</i>	Kinematic viscosity of water
<i>L</i>	Bedform wavelength
<i>h</i>	Bedform height

$AR$	Bedform aspect ratio
$C'$	Chézy coefficient
$i$	Grain-size fraction
$D_i$	Median grain-size of the size fraction $i$
$D_m$	Mean grain-size of all the grains in the sediment mixture
$Re^*$	Particle Reynolds Number

# Chapter 1. Introduction

## 1.1 Thesis background and rationale

Cross-stratification is a common structure in many depositional environments. Despite being nominally stable across a range of grain-sizes and flow conditions, decimetre-scale cross-stratification is relatively rare in turbidites (Walker, 1965; Walton, 1967; Allen, 1970; Lowe, 1988; Arnott, 2012). When it does occur, it creates a distinct facies within the turbidite sequence that has been identified in ancient and modern turbidite systems, in outcrop and as part of subsurface hydrocarbon reservoirs and cores (Stevenson *et al.*, 2015; Cunha *et al.*, 2017). However, the bedform type associated with the cross-stratification, and therefore the processes associated with its development, the variations in its styles of occurrence (i.e. the sedimentary character of individual beds and their evolution downstream), and the extent to which it may be relied upon to interpret the downstream facies tract character, remain poorly understood.

The shear imparted upon a substrate by a turbidity current may be comparable to that exerted under open channel flow conditions (Kneller *et al.*, 1999; Dorrell *et al.*, 2019). Therefore, the substantial body of research into bedform development under open channel flow conditions (for example, Shields, 1936; Allen, 1962; 1963; 1984; Baas, 1994; 1999; Best, 1996; Best *et al.*, 2001; Leeder, 2012; Perillo *et al.*, 2014, amongst others) may be applied to bedform development beneath turbidity currents. For example, research into thresholds of sediment transport and modes of sediment transport established for open channel flow conditions are widely applied to turbidity currents (Bouma, 1962; Lowe, 1982; Parker *et al.*, 1987; Mutti, 1992; Sequeiros *et al.*, 2010; Fedele *et al.*, 2016, amongst others). However, while there has been much research into sediment transport for non-uniform sediment, further work is needed to improve understanding of how bedform development and bedform kinematics are impacted by non-uniform sediments characterised by different grain-size distributions. Results from this research may then be applied to deep sea turbidity currents and open channel flows.

Due to the limited amount of experimental research that specifically investigates bedform development under density currents (Koller *et al.*, 2017; Fedele *et al.*, 2016), open channel flow research underpins the entire study of bedform development in turbidity currents. Therefore, it is important to know the extent to which this research is applicable to turbidity currents, and how bedform formative mechanisms may be different. For example, predicting bedform development

by turbidity currents principally relies upon bedform phase diagrams constructed for open channel flows, but recent research has shown that open channel flow phase diagrams incorrectly predict bedform development beneath density currents (e.g. Koller *et al.*, 2017; Fedele *et al.*, 2016).

This thesis reports on three complementary areas of research that involve experimental and field-based research. This research entails an investigation into bedform development and maintenance under steady and waning saline density currents, bedform development from non-uniform sediment beds characterised by different grain-size distributions, and the characterisation of decimetre-scale cross-stratification preserved in outcrop.

## **1.2 Thesis aims and objectives**

The thesis aims to answer the following questions:

1. How do different types of bedforms, formed by saline density currents, evolve under steady and waning flows?
2. How well do existing bedform phase diagrams for open channel flows predict bedform development under density currents?
3. How does the fine fraction of non-uniform sediment mixtures of wide and narrow grain-size distributions impact bedform development, dimensions and kinematics?
4. What are the different styles of decimetre-scale cross-stratification in the Peira Cava basin?
5. Can specific bedform types be associated with the development of decimetre-scale cross-stratification in the Peira Cava basin?
6. How well do existing facies tract models describe the spatial occurrence of decimetre-scale cross-stratified units?
7. What does decimetre-scale cross-stratification tell us about the flow conditions of the currents that deposited them?

The objectives of this research are as follows:

1. To run a first series of experiments (using a newly designed experimental set up in the Total Environmental Simulator at the University of Hull), to analyse bedform development under steady and waning saline density currents.

2. To run a second series of experiments in open channel flow conditions to analyse how fine sediment fractions in non-uniform substrates, made of different grain-size distributions, impact bedform development, and to apply the results to bedform development by turbidity currents.
3. To carry out field research in the Peïra Cava basin, SE France, to document the different styles of cross-stratification occurrence and to correlate decimetre-scale cross-stratified beds from proximal to distal parts of the system.

### 1.3 Thesis outline

**Chapter 2** reviews the key literature to provide an introduction to turbidity currents and an introduction to sediment transport. Particular attention is given to the processes that lead to bedform development, how different types of bedforms are classified, and how bedform phase diagrams are used to predict bedform development in different sedimentary environments. In addition, the different types of bedforms that are associated with turbidity currents are reviewed, along with an appraisal of the usefulness of the term ‘megaripple’ to describe decimetre-scale cross-stratification found in turbidites.

A new experimental set-up was designed and built in the Total Environmental Simulator at the University of Hull. **Chapter 3** reports a series of experiments that investigate the controls on bedform development under both steady and waning saline density currents, and under different flow regimes. The ability of bedform phase diagrams for open channel flows to accurately predict bedform development under density currents is also discussed. (This work has been accepted for publication within *Frontiers in Earth Science, Sedimentology, Stratigraphy and Diagenesis*, under the title ‘Relating the Flow Processes and Bedforms of Steady-State and Waning Density Currents’).

**Chapter 4** reports on a series of experiments investigating how beds of non-uniform and bimodally distributed sediment mixtures impact bedform development and bedform dynamics. Specifically, this chapter describes how the fine fraction of non-uniform sediment mixtures of wide and narrow grain-size distributions impact bedform development, dimensions and kinematics. Chapter 4 also investigates how accurately bedform phase diagrams that characterise the substrate sediment using the median grain-size predict bedform development from beds made of sediment with a wide grain-size distribution.

Field-based research examining decimetre-scale cross-stratification within turbidites was carried out in the Peira Cava basin, SE France. **Chapter 5** reports on the different styles of cross-stratification occurrence and correlates individual cross-stratified beds from proximal to distal ends of the system. An interpretation of the type of bedform associated with the cross-stratification is made, and the applicability of existing models that describe the evolution of cross-stratified beds through different systems are compared to the findings of the present research.

**Chapter 6** includes a discussion which extends those that have been presented in the individual data chapters and proposes suggestions for future work, which include potential methodological improvements and ideas for further application of the research.

Finally, in accordance with the aims stated in Section 1.2, **Chapter 7** summarises the research presented in the thesis.

## Chapter 2. Literature Review

This literature review provides a succinct overview of the themes discussed within this thesis, including an introduction to sediment transport and bedform development, bedform classification, and an introduction to turbidity currents and turbidity current bedforms. Chapters 3 – 4 further review the literature specific to the research presented in the chapter.

### 2.1 Turbidity currents

The ocean floor sedimentary systems are the largest on Earth, acting as a sink for sediment transported from continent to coastal zones (Milliman & Meade 1983; Mutti *et al.*, 2009; Bouma *et al.*, 2012). Clastic sediments are transported by turbidity currents and other gravity-driven flows into the deep-seas, which gradually build up to form deep-sea fans, which are the most extensive accumulations of sediment on Earth (Talling *et al.*, 2012a&b; 2013). Turbidity currents and their deposits (turbidites) are the subject of wide study as they can form reservoirs that host large oil and gas reserves (Pettingill 2004; Nielsen *et al.*, 2007); active turbidity currents also pose a risk to important seafloor infrastructure, such as communication cables and pipelines (Bruschi *et al.*, 2006; Carter *et al.*, 2014; Sumner & Paull, 2014; Talling *et al.*, 2015; Clare *et al.*, 2016; 2017).

Due to their powerful nature and speed, turbidity currents have commonly destroyed the analytical equipment set up to measure them (Azpiroz-Zabala *et al.*, 2017; Paull *et al.*, 2018; Sequeiros *et al.*, 2019). As a result, compared to other sedimentary settings – for example, fluvial systems – there are relatively few studies that have collected data directly from active turbidity currents (Talling *et al.*, 2015). However, more recently, advances in technology have allowed turbidity currents to be measured directly using mainly acoustic Doppler current profilers to measure current velocity and sediment concentration, for example, Xu *et al.* (2004; 2010), Clare *et al.* (2015), Hughes Clarke (2016), Dorrell *et al.* (2019), Paull *et al.* (2018), Wang *et al.* (2020) and Simmons *et al.* (2020). Nevertheless, to date, the study of turbidity currents has relied heavily upon sea floor surveys (Normark *et al.*, 1980), experimental research (Parker *et al.*, 1987; Alexander *et al.*, 2008; Spinewine *et al.*, 2009; Sequeiros *et al.*, 2010; Cartigny *et al.*, 2011; 2014; Fedele *et al.*, 2016; Koller *et al.*, 2017; 2019), and geological studies based on cores and outcropping turbidites preserved in the rock record. A large number of geological studies has been carried out, but the key pieces of work that directly relate to the research presented in this thesis

include: Bouma (1962), Lowe (1982), Mutti (1992), Amy (2000) Kneller and McCaffrey (2003), and Cunha *et al.* (2017).

Turbidity currents are particle-laden, gravity-driven flows that occur underwater – they flow downslope due to the density difference between the current and the ambient water (Lowe, 1982; Kneller *et al.*, 1999; Mulder & Alexander, 2001). The dominant sediment transport mechanism is the suspension of particles by turbulence (Mulder and Cochonat, 1996; Kneller and Buckee, 2000; Meiburg and Kneller, 2010). Turbidity currents exchange particles with the substrate via deposition and erosion of particles; they exchange fluid principally with the ambient water through which the turbidity current flows (Parsons and Garcia, 1998; Ouillon *et al.*, 2019). If the slope along which the current flows is steep enough, the forward momentum of the flow is able to generate sufficient turbulence to maintain the suspension of particles or to entrain more sediment from the underlying bed into suspension. This type of current is known as an autosuspending current (Bagnold, 1962; Pantin, 1979). Non-autosuspending currents deposit particles from the flow, and gradually slow (Bouma, 1962; Lowe, 1982).

Turbidity currents may be initiated by the transformation of a mass of sediment failed from submarine slopes, often triggered by earthquakes (Heezen and Ewing, 1952; Normark & Piper, 1991; Parsons *et al.*, 2007; Talling *et al.*, 2013; 2015). Alternatively, they may initiate as hyperpycnal flows that most commonly form as a fluvial sediment suspension enters a body of water of lower density via a river, often during flood events (Mulder *et al.*, 2003; Talling, 2012b), which may be associated with glacial melts. In addition, shelfal nepheloid sediment circulation (McCave, 1986; Wilson and Roberts, 1995), bottom layer flows, or the suspension of mud on continental shelves by storm events (Traykovski *et al.*, 2000; Wright *et al.*, 2001) may be associated with turbidity current initiation. The duration of a turbidity current varies greatly, ranging from minutes to hours (Xu, 2010; Xu *et al.* 2014; Hughes Clarke, 2016; Paull *et al.*, 2018), to weeks (Cooper *et al.*, 2013; 2016; Azpiroz-Zabala *et al.* 2017; Simmons *et al.* 2020).

Turbidity currents may exhibit a range of different sediment concentrations, which were simply divided into high-density or low-density turbidity currents by Lowe (1982). Because turbidity currents display grain-size stratification through the height of the flow, i.e. a vertical gradient in current concentration (Kneller, 1995; Kneller and Buckee, 2000), theoretical and experimental research describes turbidity currents as two-layered flows. They are characterised by a dense basal layer (the inner region, or lower shear layer) which interacts with the sea floor (Middleton, 1967; Postma *et al.*, 1988; Garcia and Parker, 1993; Kneller and Buckee, 2000; Mulder and Alexander, 2001; Postma *et al.*, 2009; Sequeiros *et al.*, 2010; Postma and Cartigny, 2014;

Fedele *et al.*, 2016; Cartigny and Postma, 2017; Luchi *et al.*, 2018). The basal layer is overlain by a less dense, more homogeneous and thicker layer (the outer region, or upper shear layer), which mixes with the ambient fluid. Two-layered flows have also been directly measured from real-world turbidity and density currents, by Xu *et al.* (2004), Clare *et al.* (2015), Hughes Clarke (2016), Dorrell *et al.* (2019), Paull *et al.* (2018), Wang *et al.* (2020), and Simmons *et al.* (2020). The inner and outer regions of turbidity currents are separated by the horizontal velocity maximum (Hughes Clarke, 2016; Dorrell *et al.*, 2019; Wang *et al.*, 2020; Simmons *et al.*, 2020) However, the relative thickness of the two layers varies with the seafloor roughness, the critically of the current (Sequeiros *et al.* 2010; Dorrell *et al.*, 2019) and the total current thickness (Simmons *et al.*, 2020).

Deposition from turbidity currents is affected by the distribution of grain-sizes through the flow, sediment concentration, flow velocity non-uniformity (i.e. spatial differences in flow velocity), and flow unsteadiness (i.e. changes in flow velocity over time) (Kneller and Buckee, 2000; Kneller and McCaffrey 2003). Kneller and McCaffrey (2003) describe how these variables determine the capacity and competency of a current and subsequently whether deposition from a current is capacity-driven or competency-driven. Competency-driven deposition takes place when the shear velocity of the current falls below the threshold to keep the coarsest sediment fraction in the flow in suspension (Kuenen and Sengupta, 1970; Kneller and McCaffrey, 2003). Capacity-driven deposition takes place when there is insufficient turbulent kinetic energy to maintain the entire suspended mass of sediment within the current (Kuenen and Sengupta, 1970; Hiscott, 1944a&b; Middleton, 1993).

Two seminal models describe the vertical depositional sequences and spatial distribution of sediment associated with low density (Bouma, 1962) and high density (Lowe, 1982) turbidity currents. Bouma (1962) defined a depositional sequence of five divisions ( $T_a - T_e$ ) which contain specific sedimentary characteristics; the original Bouma sequence was based on the turbidites of the Peira Cava basin, SE France. Figure 2.1a schematically represents the Bouma sequence with descriptions of facies  $T_a - T_e$ . Figure 2.1c is a hypothetical representation of the spatial distribution of sediment by “medium-grained turbidity currents” (Bouma, 1962). The Bouma sequence records sedimentation from a progressively waning current (Leeder, 2012). The  $T_a$  interval may be weakly graded or massive, and is related to rapid deposition whilst there are high sediment concentrations within the base of the flow which can prevent the differential deposition of differently sized grains under traction. The  $T_b$  interval is characterised by planar laminated sands, deposited at low enough rates to allow traction, and is followed by the  $T_c$  interval containing ripple cross-laminations, then the  $T_d$  interval of laminated silts and mud. Capping the whole sequence is the  $T_e$  mud interval.

Coarse-grained high-density turbidity currents are described by Lowe (1982) who proposed an extension to the Bouma Sequence. The Lowe sequence describes the deposits of flows that contain a wide range of grain-sizes (cobbles to mud) that are distributed through the flow to form a current in which the basal part of the flow is hyper-concentrated and the upper part of the flow is more dilute. The sequence relates to deposition taking place in phases as specific grain-size populations can no-longer be supported by the flow as the flow decelerates. Figures 2.1b and 2.1d schematically represent the Lowe Sequence and the downflow spatial distribution of deposits. The  $R_1$  interval is formed by initial tractional sedimentation of cobbles and gravels, which may develop bedforms. The  $R_2$  interval follows, characterised by inversely graded gravel, related to the development and instantaneous freezing of traction carpet. The  $R_3$  is a normally graded interval formed by grains settling out from suspension.

The same sequence of processes associated with the deposition of the  $R_1 - 3$  intervals (suspension sedimentation followed by traction, frictional freezing of traction carpets and suspension sedimentations without traction), is responsible for the deposition of the finer gravels and sands which characterise the  $S_{1-3}$  intervals. The  $S_3$  facies is equivalent to the Bouma  $T_a$  division (Figures 2.1a and 2.1b).

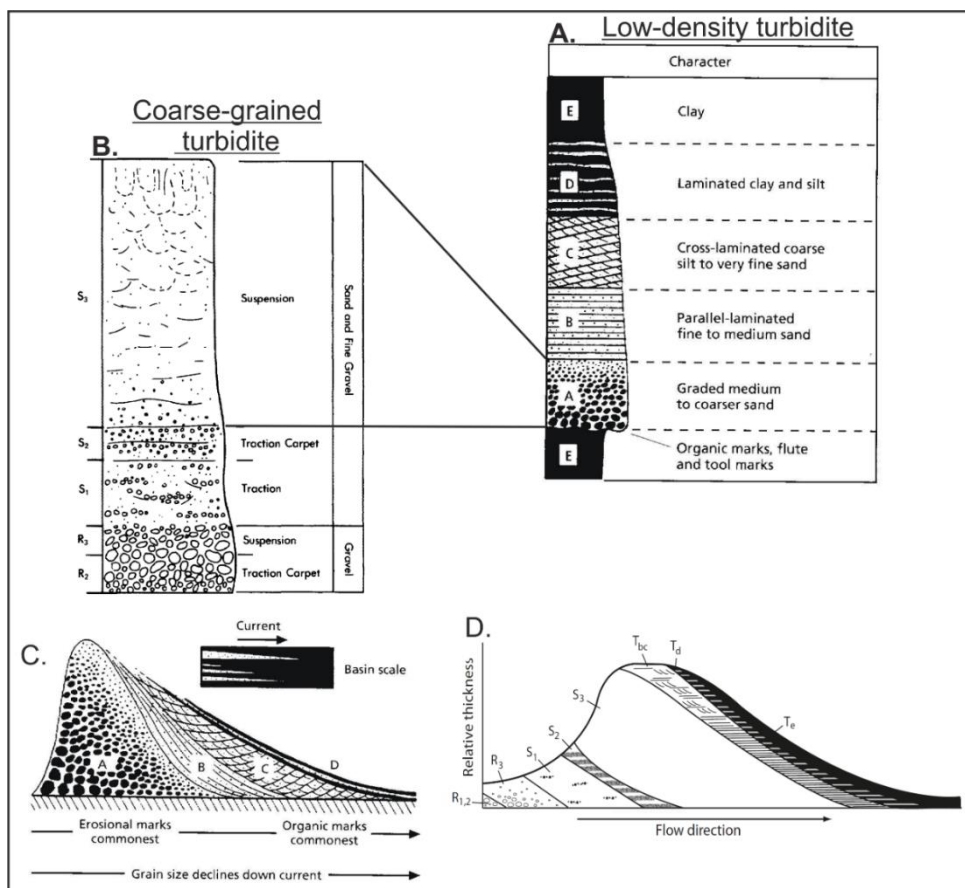


**Figure 2.1.** (A) Schematic representation of the Bouma sequence with descriptions of facies  $T_a - T_e$  (Bouma 1962). (B) Schematic representation of the Lowe sequence (Lowe 1982). (C) A hypothetical representation of the spatial distribution of sediment by medium-grained turbidity currents. (Bouma 1962). (D) A hypothetical representation of the spatial distribution of sediment (From Sumner et al., 2012) deposited by coarse-grained turbidity currents.

## 2.2 Introduction to sediment transport

Knowledge of the basic concepts of sediment transport is needed to understand bedform development. Here a review of the related literature describing sediment transport for uniform and non-uniform sediment beds and bedform development associated with open channel flow is provided; as noted above, these concepts can be applied to turbidity current sedimentary processes.

### 2.2.1 Thresholds of sediment transport

For sediment transport to take place, the fluid velocity must be sufficiently high for the shear stress ( $\tau$ ) exerted upon the bed to meet the critical shear stress ( $\tau_c$ ) for incipient motion of sediment – i.e. the shear forces must overcome the restrictive forces of inertia and friction that resist particle movement. The shear stress at which particle motion takes place is known as the critical shear stress (van Rijn, 1993; van Rijn, 1984). This simple criterion for particle movement may be written as:  $\tau = \tau_c$

The Hjulstrom diagram (Figure 2.2) aims to quantify the critical flow velocity needed for particle motion for different sized sediments (Hjulstrom, 1939). It shows that greater flow velocities are required to initiate sediment transport of larger grains, and that if the flow velocity falls below the critical threshold for sediment transport, deposition will take place as the flow is not competent to sustain sediment transport. A fundamental drawback of the Hjulstrom diagram is that it does not consider flow depth, sediment density or grain shape.

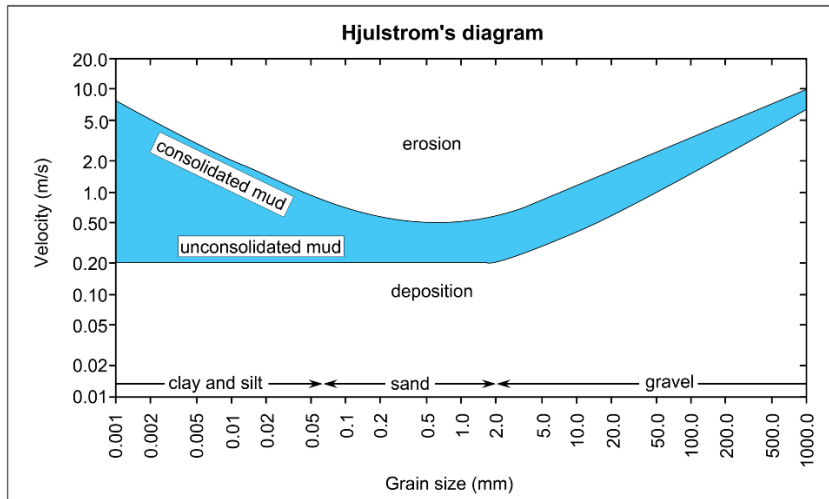


**Figure 2.2.** Hjulstrom's diagram showing the critical velocity required to move sediment of a given grain-size (From Cheel, 2005).

The Shields parameter ( $\theta$ ) (Shields, 1936) makes improved predictions relating to sediment transport for unimodal sediment by considering the influence of particle size and density. This approach considers the ratio of the shear forces exerted upon the bed by the flow to the submerged weight of the particle that resists movement:  $\theta = \frac{\tau}{(\rho_s - \rho)g d_{50}}$ , where  $\tau$  is the dimensional shear stress,  $\rho_s$  is the density of sediment,  $\rho$  is the density of the fluid,  $g$  is acceleration due to gravity, and  $d_{50}$  is the median grain-size of sediment. The curves on the Shields diagram (Figure 2.3) plots the critical shear stress (or the critical Shields number) based on experimental data, as a function of particle Reynolds number:  $Re_* = \tau d/v$ , where  $v$  is the kinematic viscosity of water. It shows that for Particle Reynolds numbers less than 10, the critical shear stress increases with reducing grain-size. This is because the finest grains are submerged within the laminar sub-layer (also called the viscous sub-layer). The laminar sub-layer is a layer of the flow that experiences non-turbulent flow: it forms between a surface and an overlying turbulent layer above (Carling, 1992; Leeder, 2012). Within this region the grains are not exposed to shear stress imparted by turbulence higher up in the flow. Soulsby (1997) and Soulsby and Whitehouse (1997) used the Shields experimental data to derive an algebraic expression that relates the critical Shields number to the dimensionless grain-size in order to calculate the threshold of sediment motion (see Chapter 4, Section 4.3.3 for the equation and associated information).

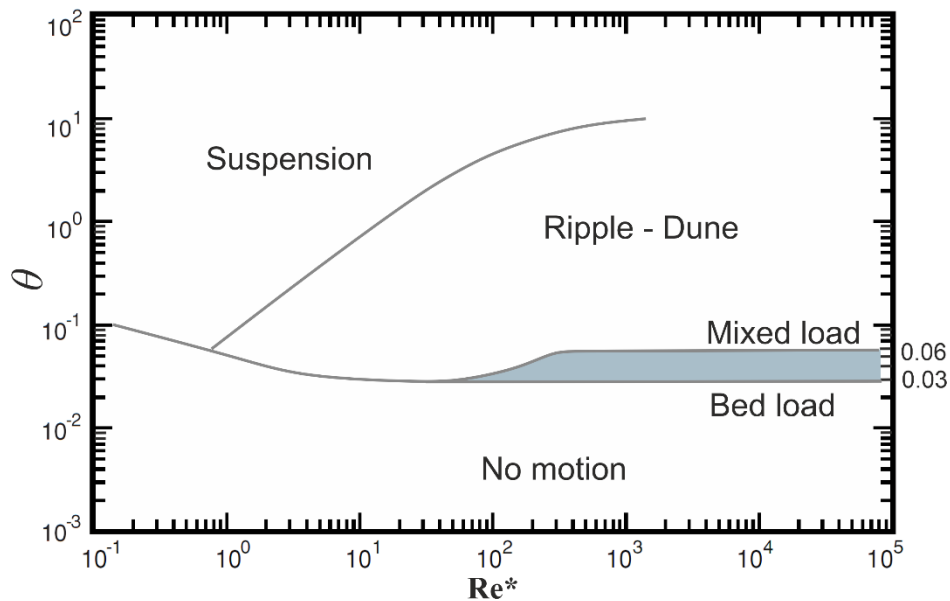


**Figure 2.3.** Shields plot (modified after Church 2006) defines the threshold of traction movement, highlighting the widely regarded upper and lower limits of sediment motion. The Y-axis plots the Shields parameter ( $\theta$ ) and the x-axis plots the Particle Reynolds Number ( $Re_*$ ). The approximate boundaries define modes of sediment transport (after Dade and Friend 1998).

### 2.2.2 Non-uniform and cohesive sediment

Although the Shields parameter based on the mean grain-size is widely used in engineering and sedimentology, its use is limited as it does not consider substrates made up of non-uniform sediment. Non-uniform, or poorly sorted, sediment is the focus of the research presented in Chapter 4. In mixed sediment beds, the threshold of motion changes due to the relationship between a grain and the surrounding grains of different sizes. For example, substrates of mixed sediment sizes might influence particle mobility due to the degree to which a grain is exposed to the flow (Fenton and Abbot, 1997). Coarse grains are more easily entrained as they protrude from the bed and are more exposed to the flow, and sheltering of finer grain fractions means they are less likely to be transported. To account for the hiding and exposure effects of non-uniform sediment, some authors (Einstein, 1950; Egiazaroff, 1965; Ashida and Michiue, 1973; Wilberg and Smith, 1987; Wilcock, 1993; McCarron *et al.*, 2019) have developed sediment transport models for gravel and sand sediment mixtures that account for the 'hiding factor'.

Granular segregation and bed armouring by coarse sediment also protects finer sediment from being eroded, thus increasing the critical shear stress required for sediment transport (Einstein, 1950; Wilcock, 1993; Blom, 2008; McCarron *et al.*, 2019). Armour layers may form as flows impart enough shear stress to only transport finer sediment, or via the removal of fine sediment from the bed (known as winnowing). The removal of fines from the upper portion of the bed leads to the formation of the well-documented armour layer (for example, Wilcock and McArdeell, 1997; Lanzoni and Tubino, 1999; Blom *et al.*, 2003; Almedeij and Diplas, 2005; Blom, 2008; Vendetti *et al.*, 2017) which stabilises the bed because the sediment transport criterion for the substrate is greater than the bed shear stress (Figure 2.4).

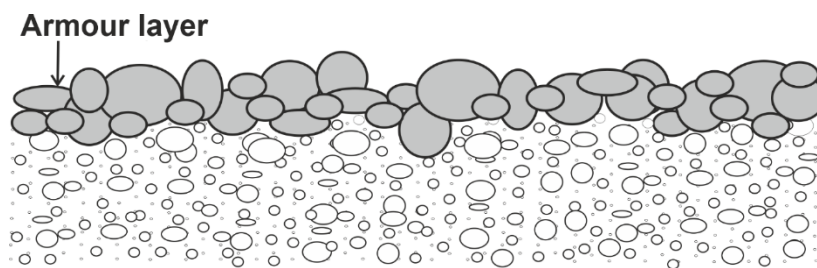


**Figure 2.4.** Schematic representation of an armour layer where the surface sediment is coarser than the subsurface sediment.

Less is known about the impact of fine sediment in non-uniform sediment mixtures. However, research by van Ledden *et al.* (2004), Bartzke *et al.* (2013) and Staudt *et al.* (2017) has shown how fine sediment can increase bed stability. van Ledden *et al.* (2004) and Bartzke *et al.* (2013) describe how non-cohesive silt particles surround coarser grains in a non-uniform sediment mixture so that the intergranular contact between the coarser grains is reduced or eliminated, thus increasing the angle of repose and the amount of shear stress needed to initiate sediment transport. Bartzke *et al.* (2013) and Staudt *et al.* (2017) also explain how fine sediment in a non-uniform substrate can stabilise the bed by reducing its hydraulic conductivity, by infilling the pore space between the coarser grains and reducing the inflow of water into and through the bed. Their research is closely linked to the discussion presented in Chapter 3, where their work is reviewed and discussed in detail.

The threshold of sediment transport may also be altered due to sediment cohesivity, where adhesive and cohesive forces act between grains (Mitchener and Torfs, 1996; Bass and Best, 2008). Cohesive sediments exist in every sedimentary environment on Earth, including fluvial, estuarine, coastal and deep-sea settings. As such, more recent research into the physically cohesive properties of muds, clays and the biologically cohesive properties of extracellular polymeric substances within the bed and the flow, has found that cohesion increases the erosion threshold and alters bedform development, dimensions and kinematics (Mitchener and Torfs,

1996 ; Lichtman *et al.*, 2018; Schindler *et al.*, 2015; Grabwoski *et al.*, 2011). However, sediment cohesion is not considered further in relation to the research presented in this thesis.

## 2.3 Bedform generation

Having established the parameters for sediment transport, a review of the research into bedform generation is presented. Two schools of thought describe how bedforms form from a flat and mobile substrate: linear stability theory and the turbulent flow motion model. Duran Vinent *et al.* (2019) clarify that a flat sand bed is the limit of vanishing bedform height. Linear stability theory explains that instabilities arise within the fluid-sediment flow system due to perturbations such as a sediment hump, seed waves or wavelets on the bed (Kennedy, 1969; Engelund and Fredsoe, 1982; Colman and Nikora, 2009; Colman *et al.*, 2011), which are then amplified due to the positive feedback between the bed and the flow as they interact (McLean, 1990). Duran Vinent *et al.* (2019) explain that as the flow interacts with a bed perturbation, the flow streamlines converge along the upstream side of the perturbation and increases flow velocity and increased sediment erosion at the crestal region and deposition downstream of the perturbation (Richards *et al.*, 1980; McLean, 1990).

The turbulent flow motion model provides a contrasting explanation for the origin of the bed perturbations to linear stability theory. Studies by Matthes (1947), Jackson (1976), Allen (1984) and Leeder (1983) propose that macro-turbulence such as Kolks events (slowly rotating 'hairpin' or 'horse shoe' vortices that tilt upwards originating near the bed at the fluid sediment boundary) are important aspects of sediment transport and bedform formation. Figure 2.5 shows that the interaction between hairpin vortices of turbulence and a mobile bed initiates sediment transport, which leads to the formation of transverse bed defects, initiating flow separation and reattachment processes (Best, 1992; Leeder 2012).

Yalin (1977) and Jackson (1976) explain that bedform generation is also the product of large-scale turbulent motions directed towards the bed (known as 'sweep events'). Sweep events can penetrate the viscous sub-layer and impact the bed initiating sediment transport. Best (1992; 1995) further explains how multiple sweep events that impact the bed, will eventually form a bed defect. Bed defects formed either by hairpin vortices or sweep events may reach a threshold height sufficient to initiate flow separation, generating the downstream propagation of bedforms now controlled by flow separation (Williams and Kemp, 1971).

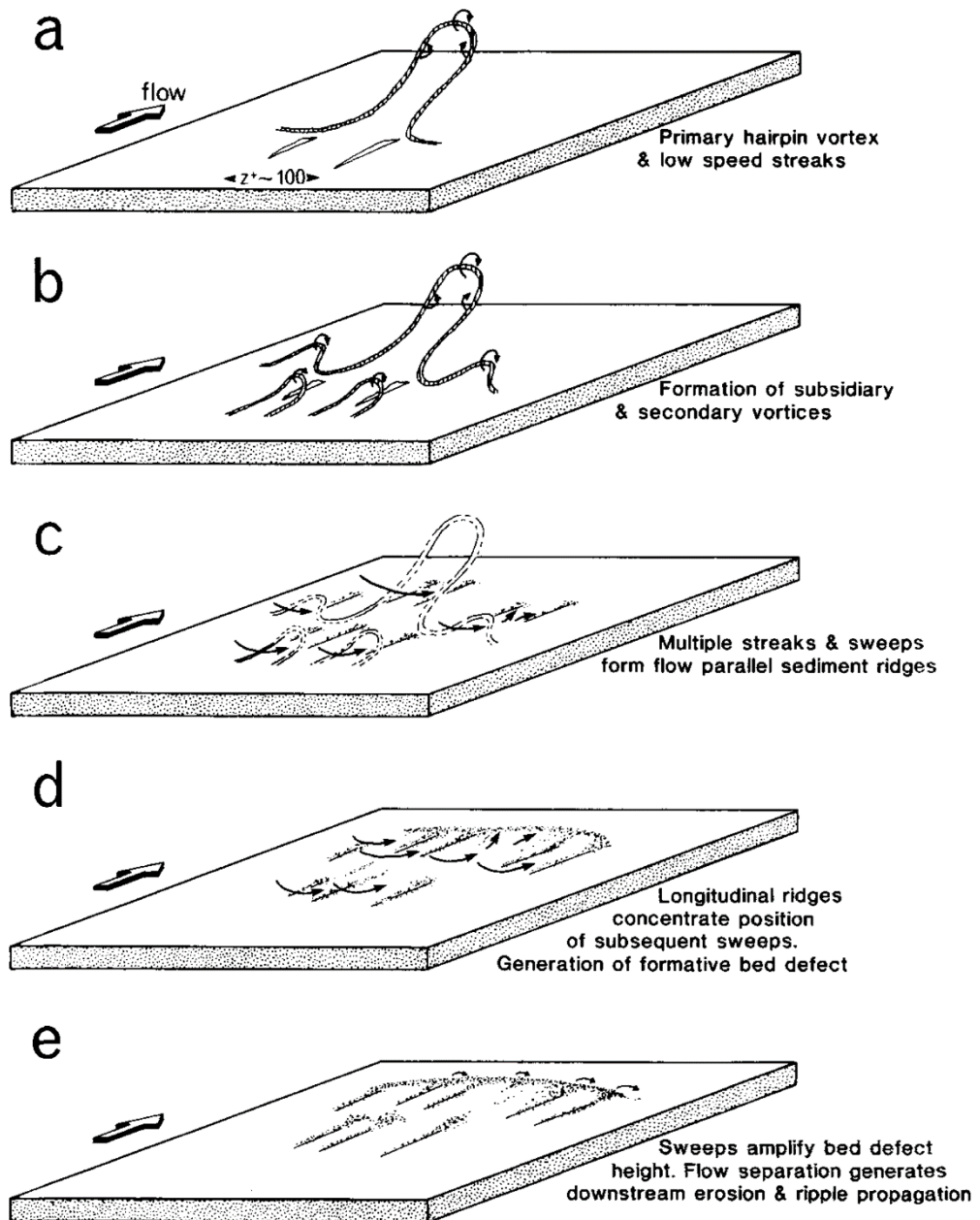


**Figure 2.5.** A schematic representation of the hairpin vortices that are produced from the turbulent boundary layer, which initiate sediment transport and the formation of bed defects. (After Best, 1992).

## 2.4 Bedform classifications and phase diagrams

Research into the origin of sedimentary bedforms, their development and their morphodynamics has mainly been carried out for open channel flows and for oscillatory flow regimes (Shields, 1936; Bagnold, 1946; Allen, 1962; 1963; 1984; Baas, 1994; 1999; Best, 1996; Best

*et al.*, 2001; Dumas *et al.*, 2005; Leeder, 2012; Perillo *et al.*, 2014, amongst many others). This body of work remains the most comprehensive area of research that studies the complex interactions between a mobile substrate and a flow (for example, Kennedy, 1969; Yalin, 1977; Engelund and Fredsoe, 1982; Ashley, 1990; Bennet and Best, 1995; 1996; Colman and Nikora, 2009; Colman *et al.*, 2011, to name just a few). Since this body of work underpins the study of bedforms in any sedimentary setting, this research will be referred to throughout this study into the formation of decimetre-scale bedforms by turbidity currents.

Bedform classification has been the subject of much research which has defined various methods to distinguish between different bedform types. A well-established classification defines bedforms based on the criticality of the flow regime that generated them (Harms and Fahnstosk, 1965). Subcritical bedforms, also known as lower-regime forms, include lower-stage plane bed, ripples and dunes. Supercritical bedforms, also known as upper-regime forms, include upper stage plane bed, antidunes and cyclic steps (Harms and Fahnstosk, 1965; Ashley, 1990; Knighton, 1998; Sun and Parker, 2005; Cartigny *et al.*, 2011).

#### ***2.4.1 Defining dunes versus ripples***

Dunes and ripples are geometrically similar. Two approaches are commonly applied to distinguish them. Firstly, dunes and ripples may be distinguished by the amount of turbulence imparted through the water column as the flow interacts with the bedforms (Bridge and Best, 1988; Bennet and Best, 1995; 1996; Duran Vincent *et al.*, 2019). Alternatively, they may be defined based on bedform dimensions (Guy *et al.*, 1961; Raudkivi, 2006; Ashley, 1990; Colombini and Stocchino, 2011). These approaches are described below.

It is widely recognised that dunes and ripples differ hydrodynamically (Richards, 1980; Bass 1994; Bennet and Best, 1995). As dunes and ripples interact with a current, both experience flow separation at the crest (Figure 2.6). As dunes are relatively large, flow separation at the crest is greater, as is the associated turbulent wake region and shear layer which generate from the crest and extend downstream (Venditti, 2013). As a result, compared to ripples, dunes generate larger-scale turbulence that arises at the shear layer generated by Kelvin Helmholtz instabilities (Baas, 1994; Bennett & Best, 1996; Schindler and Robert, 2005; Leeder, 2012; Venditti, 2013). The turbulent structures upwell through the flow depth ('ejection events') and may interact with the flow surface (known as 'boils'), (Yalin, 1992; Bennet and Best, 1995; 1996; Best, 1993; 2005; Fernandez *et al.*, 2006). Ripples have a small separation zone and shear layer that are restricted to the near bed region (30 – 40 % of the water column) and therefore do not interact with the current's surface (Baas, 1994; Bennett & Best, 1996; Schindler and Robert, 2005; Leeder, 2012;

Venditti, 2013) – see Figure 2.6. This means that dunes scale with flow depth as dunes may achieve heights of the order of the depth of their formative flows (Ashley, 1990); ripples exist independently of flow depth, but do scale with grain-size (Jackson, 1976; Yalin, 1977; Schindler and Robert, 2005).

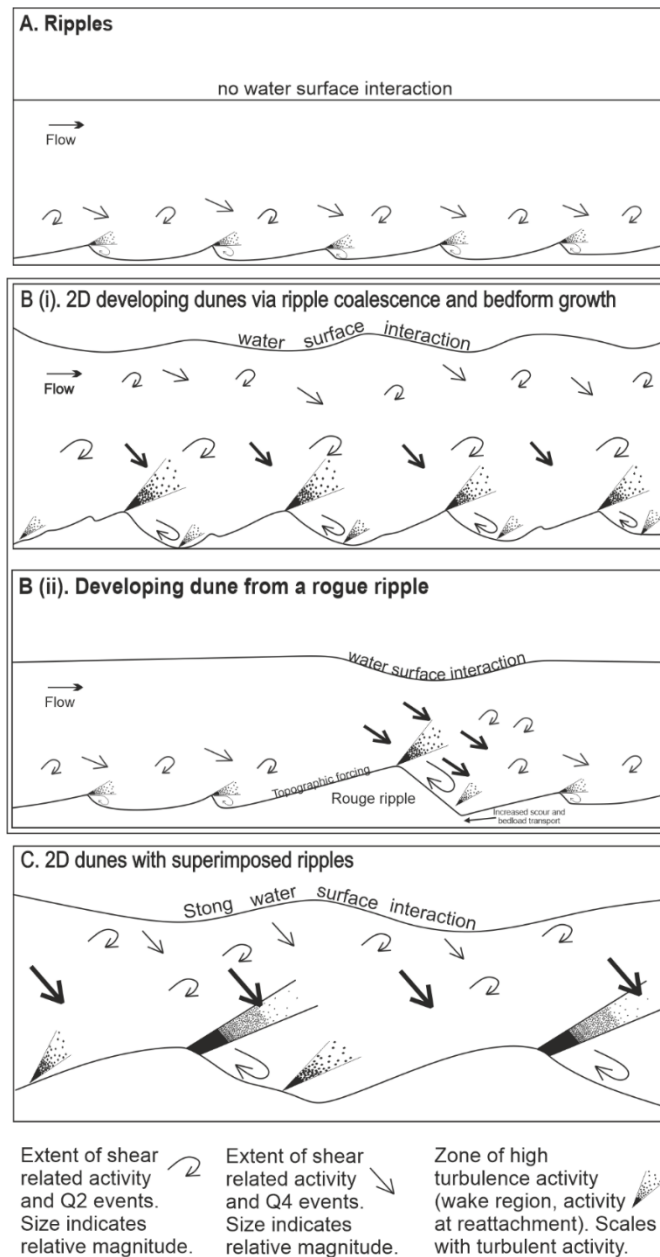


**Figure 2.6.** Conceptual diagram representing the interaction of a flow over 2D ripples and dunes. Figures A-C also describe the development of dunes from ripples: **(B.i)** dune generation due to bedform growth by ripple coalescence (modified after Schindler and Robert, 2005). **(B.ii)** Dune generation by the formation of a larger than average ripple (rogue ripple) (modified after Bennet and Best, 2016).

Dunes and ripples may also be defined according to their dimensions (Guy *et al.*, 1961; Colombini and Stocchino, 2011; Raudkivi, 2006; Ashley, 1990; Bartholdy *et al.*, 2015). Distinctions are based on bedform dimensions such as wavelength and height. Ashley (1990) suggests that dune bedform dimensional data – for open channel flow – exist as a single genetic population, separate from smaller ripple forms (Figure 2.7). Ashley (1990) interprets this dimensional distinction to be the result of different hydrodynamic processes that operated in association with the formation of ripples and dunes (Bennet and Best, 1995; 1996; Bridge and Best, 1988; Ashley, 1990).

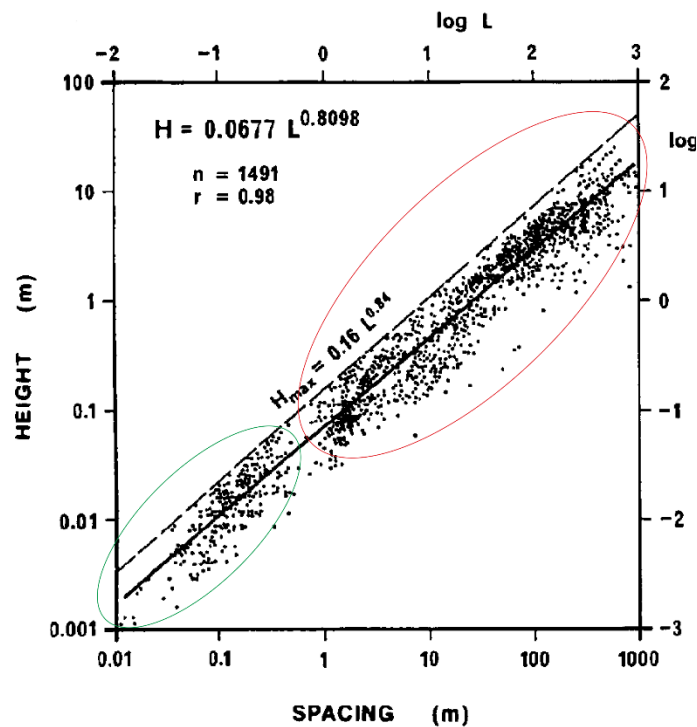


**Figure 2.7.** A log-log plot of bedform height and wavelength of 1491 flow transverse subaqueous bedforms (Flemming 1988), from Ashley (1990). The green circle identifies ripples and the red circle identifies dunes.

#### 2.4.2 Types of antidunes and the processes relating to their migration direction

Antidune development occurs under supercritical flow (Kennedy 1963; Cheel, 1990; Recking *et al.*, 2009). Supercritical bedforms develop as the mobile substrate takes on the shape and amplitude of the surface waves that propagate at the current's free surface (McLean, 1990; Fourrière *et al.*, 2010). As a result, supercritical bedforms are in-phase with the current interface, and unlike subcritical bedforms, their formation is free-surface dependent (Cartigny *et al.*, 2014).

Cheel (1990) used the umbrella term 'in-phase waves' to describe a train of bed waves that are in-phase with the current's free-surface. Cheel (1990) considered that in-phase waves are divisible into three different types of antidune bedforms that vary with different hydraulic

conditions and have different sedimentological structures. These three bedform types are: i) upstream migrating antidunes that are in-phase waves that migrate upstream when the surface wave breaks periodically; ii) standing antidunes that are in-phase waves that do not migrate either upstream or downstream; and, iii) downstream migrating antidunes (DMA) that are in-phase waves that migrate downstream (Kennedy, 1963). Compared to the extensive research carried out on upstream migrating antidunes and standing antidunes, relatively little attention has been given to the study of downstream migrating antidunes. This means that the understanding of the processes, and specifically the flow conditions, associated with their development and their resulting depositional sedimentary character is limited.

To help define the hydrodynamic and sedimentological character of DMAs this review compares upstream migrating antidunes with DMAs. It will also discuss the usefulness of previous research in identifying the DMA in the geological record and highlight the gaps in the research that might cause problems when interpreting cross-stratification. Early analysis of in-phase wave migration by Kennedy (1963) relates migration to the gradient of mean flow velocity over the bedform. For upstream migrating antidunes, the near bed flow velocity decreases from the trough to the crest, then it increases from the crest to the following bedform trough. Kennedy (1963) explains that this causes sediment to be eroded from the lee side of one antidune and then transported and deposited on the stoss side of the downstream bedform causing the bedform to migrate upstream (Figure 2.8a). Conversely, Kennedy (1963) observed that antidunes migrate downstream as the near-bed flow velocity increases from the trough to the crest and then decelerates from the crest to the trough, causing sediment to be eroded from the stoss side and transported to and deposited on the lee side of the same bedform. More recent work by Núñez-González and Martín-Vide (2011) builds on Kennedy's (1963) analysis of antidune migration. Based on the continuity and Bernoulli equations which are applied between the crest and troughs of symmetrical bedforms (a common character of antidune geometry), Núñez-González and Martín-Vide (2011) form of a theory for antidune migration. Their results successfully describe an antidune migration regime that compares well with experimental examples of in-phase waves. Núñez-González and Martín-Vide (2011) demonstrate that the ratio between the water depth over the crest compared to the trough is integral to understanding antidune migration. Figure 2.8b shows that when the flow is supercritical, the water depth is greater over the crest than over the trough ( $H_1 > H_2$ ), and the bedform migrates upstream. When the flow regime is supercritical, but the Froude number is near one, then the water depth is greater over the trough than over the crest ( $H_1 < H_2$ ), and the bedform migrates downstream (Figure 2.8c). When the water depth over

the crest and the trough is equal ( $H_1=H_2$ ), a condition associated with a supercritical flow regime in which the Froude number is closer to unity, the bedform remains stationary (Figure 2.8d).

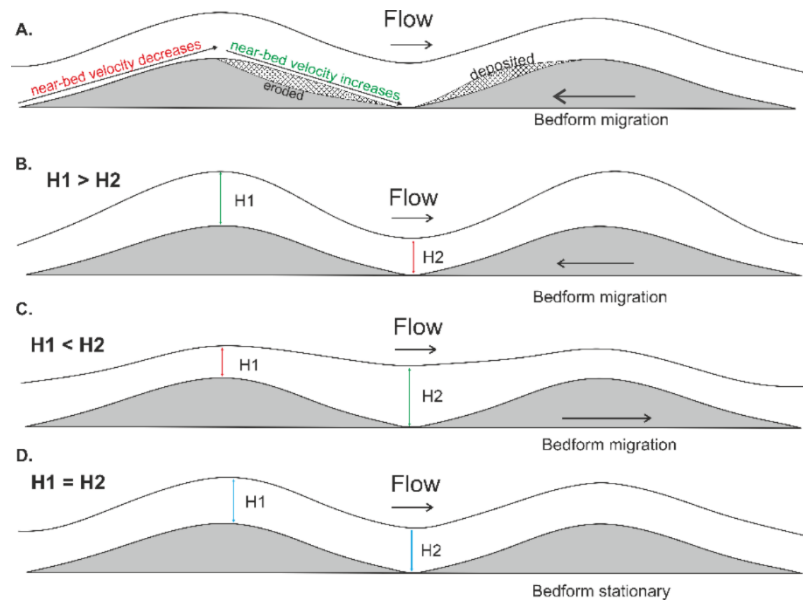


**Figure 2.8.** (A) Sediment transport and deposition over an upstream migrating antidune, as described by Kennedy (1963). Water depth variation over (B) upstream migrating antidunes, (C) downstream migrating antidunes and (D) stationary antidunes (modified after Nuñez and Vide, 2011).

### 2.4.3 Bedform phase diagrams

Observational, experimental and theoretical modelling, principally under open-channel conditions, have refined our understanding of the hydrodynamic and sedimentological conditions associated with different types of bedforms (Baas *et al.*, 2015). Early bedform phase diagrams by Allen (1968; 1984) used dimensional parameters, including flow depth, sediment size and depth-averaged flow velocity or shear stress. More recent phase diagrams use non-dimensional parameters to define the bedform phase boundaries (van Rijn 1990; 1993; Southard and Boguchwal, 1990; van den Berg and Van Gelder, 1993; 2009) – see Figures 2.9a – c. These are widely used to predict the type of bedform that will develop under specific sets of boundary conditions. Based on experiments, Fedele *et al.* (2016) developed a new stability diagram for bedforms formed under density currents (Figure 2.9d) but concluded that further refinement of the bedform stability fields was needed. They argued that collection of more hydrodynamic and sedimentological data under experimentally controlled conditions was required to advance understanding of bedform development under density currents.

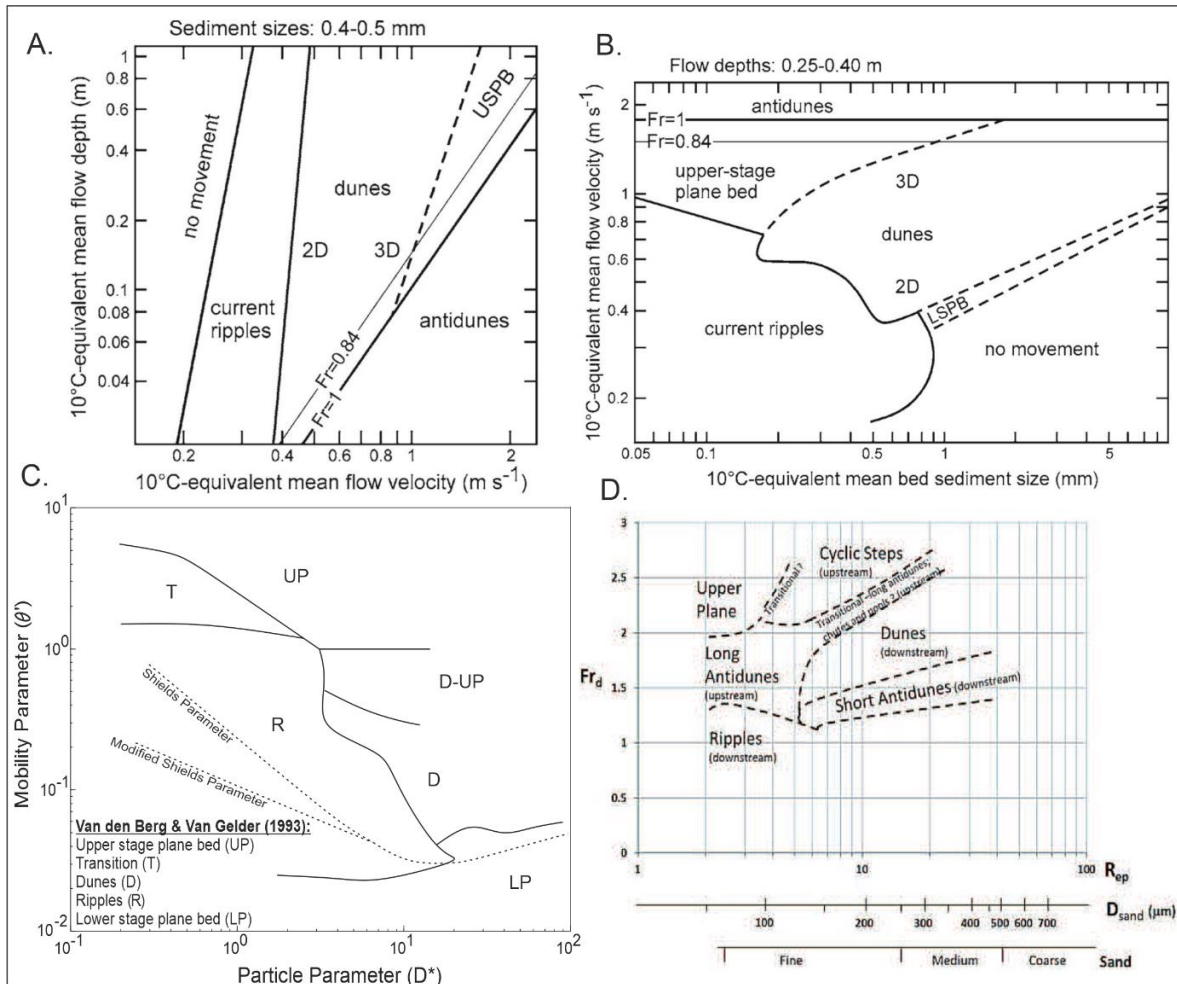


**Figure 2.9.** Examples of dimensionless bedform phase diagrams for open channel flow. **(A)** Southard and Boguchwal (1990), showing mean flow velocity against flow depth for grain-sizes between 0.4 and 0.5 mm. **(B)** Southard & Boguchwal (1990), showing mean grain-size against the mean flow velocity for flow depths between 0.25 and 0.4 m. **(C)** van den Berg and Van Gelder's (2009) adaptation of van Rijn's (1984) dimensionless phase diagram. **(D)** Fedele's et al. (2016) new bedform phase diagram for density currents.

## 2.5 Turbidity current bedforms

Ripples are a common type of bedform found in turbidites. Ripples are defined as small-scale, flow transverse ridges (Allen, 1968; Baas, 1978; 1993; 1994; 1999; Ashley, 1990). As previously established, they are included in the classic Bouma sequence within the  $T_c$  facies, they usually form from fine-grained sands, and they are the product of deposition from low-density turbidity currents (Bouma, 1962; Lowe 1982; Mutti, 1992).

Decimetre-scale cross-stratification in turbidites is a notably rare sedimentary structure (Walker, 1965; Walton, 1967; Allen, 1970; Lowe, 1988; Arnott, 2012). However, decimetre-scale cross-stratification has been found in a number of turbidite systems, including the Peira Cava Formation, SE France (Bouma, 1962; Mutti, 1992; Amy, 2000; Amy *et al.*, 2000; 2007; Kneller and McCaffrey, 2003; Cunha *et al.*, 2017); the Ainsa turbidite system, Spain (Mutti, 1992; Bakke *et al.*, 2008); the Hecho Group, Spain (Mutti, 1992); the Whitehouse Formation, Scotland (Hubert, 1966a); the Taconic Sequence, New York and Vermont, USA (Keith & Friedman, 1977); the Marnoso Arenacea Formation, Italy (Ricci Lucchi & Valmori, 1980; Muzzi Magalhaes and Tinterri, 2010; Tinterri and Muzzi Magalhaes, 2011; Sumner *et al.*, 2012); the Ocoee Supergroup, United States (Lowe, 1982); the Cloridorme Formation, Canada (Pickering & Hiscott, 1985); the Priabonian-Rupelian, Ranzano Sandstone, northern Apennines, Italy (Tinterri *et al.*, 2017); the East Carpathian Flysch Belt, Romania (Sylvester & Lowe, 2004); Higuier-Getaria Formation, Errentzun Zabal, Spain (Hodgson and Wild, 2007); the Karoo Basin, South Africa (Hodgson, 2009); the Moroccan Turbidite System, in the Agadir Canyon and basin (Hubbard *et al.*, 2014); the Reitano Flysch system, Sicily (Mutti, 1992); and the Magallanes Basin of southern Chile (Macauley and Hubbard, 2013). An example of decimetre-scale cross-stratification found in core is from offshore New Jersey (IODP Expedition 313) (Miller *et al.*, 2013). These deposits are thought to form via tractional processes under a waning density current and are commonly associated with coarse-grained sands (Mutti, 1992).

The association of decimetre-scale cross-stratification with a specific type of bedform is not very well defined. Two frequently occurring associations are with dunes and ‘megaripples’. While the term ‘megaripple’ is undefined in relation to turbidity currents (see section below), decimetre-scale cross-stratification is most commonly associated with subcritical flow regimes: Hubert (1966b); Allen (1970), Lowe (1988), Amy (2000), Amy *et al.* (2000; 2007), Kneller and McCaffrey (2003), Talling *et al.* (2007; 2012a&b), Hodgson (2009), Sumner *et al.*, (2012), Arnott (2012), and Amy *et al.* (2016) all refer to decimetre-scale cross-stratification as being formed by (subcritical) dunes. However, other researchers have also attributed the formation of turbidite decimetre-scale cross-stratification to supercritical (Tinterri and Tagliaferri, 2015; Tinterri *et al.*, 2017; Postma *et al.*, 2021), or near critical flow regimes that extend beyond the channel lobe transition zone (Hamilton *et al.*, 2017).

### **2.5.1 ‘Megaripples’ in turbidites**

The term ‘megaripple’ is commonly used to define bedforms within coastal and shallow marine settings, where oscillatory and combined flow regimes prevail. Bedform classifications in

coastal and shallow marine settings are often based on the classification schemes of Dalrymple *et al.* (1978), van Rijn (1989) and Ashley (1990). Table 2.1 depicts different types of bedforms (ripples, dunes and megaripples) and their distinguishing dimensions according to Dalrymple *et al.* (1978) and van Rijn (1989). By these criteria, megaripples are the intermediate bedform between ripples and dunes based on their size, and presumably they are the intermediate form on a bedform phase diagram, although megaripples are not typically included in phase diagrams.

**Table 2.1.** *Ripples, dunes and megaripples dimensions as defined by Dalrymple et al. (1978) and van Rijn (1989).*

	<b>Ripples</b>	<b>Megaripples</b>	<b>Dunes</b>
<b>Height (m)</b>	< 0.06	0.06 - 2	2 – 15
<b>Wavelength (m)</b>	<0.6	0.6 - 20	20 - 1000

Idler *et al.* (2004) discuss megaripple formation and offer an explanation as to how they differ from dunes. They argue that megaripples form due to the action of surface waves in shallow coastal waters, which can lead to an apparent bed roughness of 1 – 10 times larger than the actual bed roughness (depending on the depth of the surface waves). However, dune bedforms dimensions are also widely reported to encompass those defined for megaripples; dunes have also been shown to form as a continuum of dimensions that incorporate the dimensions defined for megaripples (Ashley, 1990). Ashley (1990) further explains that the continuous nature of the dune dimension range indicates that they are all formed by the same processes, whereas ripples, as previously outlined, are known to form under different formative processes and plot as a discrete data population (Figure 2.7).

Decimetre-scale cross-stratification associated with megaripples within turbidites is described by Mutti (1992), Mutti *et al.*, (2003), Hodgson and Wild (2007), Muzzi Magalhaes and Tinterri (2010), Tinterri and Muzzi Magalhaes (2011), Tinterri *et al.*, (2017), and Cunha *et al.* (2017). This definition appears to distinguish such cross-stratification from that associated with other types of bedforms – i.e. ripples, dunes or downstream migrating antidunes – that are commonly interpreted to form decimetre-scale cross-stratification. This approach suggests that there is something inherently different in the formation and possibly in the resultant appearance of the cross-stratification compared to the development and characteristics of these ripples and dunes. However, the research cited above does not provide an accompanying definition of the term ‘megaripple’ in relation to other types of bedforms. As a result, there is uncertainty as to what the significance of the presence of megaripples in turbidite beds is when making

interpretations of palaeoflow and current conditions associated with their development. That said, Muzzi Magalhaes and Tinterri (2010) and Tinterri and Muzzi Magalhaes (2011) do associate megaripples with the restricted case in which combined flows are caused by turbidity current reflection. It is possible that these authors consider that cross-stratification formed in association with bi-directional flows might resemble bedform formation in coastal settings. If so, the term ‘megaripple’ may be more appropriate, but this is not explained and remains unclear.

An aim of the present research is to define the type of bedform that is associated with decimetre-scale cross-stratification in turbidites in order to improve interpretation of the paleoflow conditions associated with their development. However, due to the uncertainty surrounding how they may be explicitly distinguished from dunes and ripples based on their dimensions, or based on their formative processes, the present research does not use the term ‘megaripple’ in relation to turbidity currents.

### **2.5.2 Turbidity current sediment waves**

Sediment waves are defined by Wynn and Stow (2002, p.8) as:

“a large-scale (generally tens of metres to a few kilometres in wavelength and several metres high), undulating, depositional bedform that are generated beneath a current flowing at, or close to, the seafloor”.

Sediment waves that are formed by turbidity currents develop via the interaction of the current with a mobile substrate by processes of sediment erosion, transportation and deposition (Hand, 1974; Flood and Shor, 1988; Piper and Savoye, 1993; Garcia and Parker, 1993; Wynn *et al.*, 2000a; 2000b; 2000c; 2000d; Postma *et al.*, 2009; Sequeiros *et al.*, 2010; Postma and Cartigny, 2014). Symons *et al.* (2016) compile a global dataset of examples of sediment waves, which resolves ‘large-scale’ and ‘small-scale’ sediment waves formed by turbidity currents (Figure 2.10). Small-scale bedforms have wavelengths ranging from approximately 20 – 300 m (shown in blue in Figure 2.10). Large-scale bedforms wavelengths range from 300 – 7200 m (shown in green in Figure 2.10). Turbidity current formed sediment waves of these sizes are widely documented using seismic reflection imagery and sea floor scanning techniques such as bathymetric profiling.

Turbidity current sediment waves form in a range of settings, including on channel levees (Normark *et al.*, 1980; Carter *et al.*, 1990; McCave & Carter, 1997; Nakajima *et al.*, 1998; Piper *et al.*, 1999; Kane *et al.*, 2010), within turbidity current channels (Morris *et al.*, 1998; Wynn *et al.*, 2000b; Wynn *et al.*, 2002a; 2002b), at the channel-lobe transition zone (Hofstra *et al.*, 2018; Brooks *et al.*, 2018; 2019), and on submarine fans (Normark *et al.*, 1980; Howe, 1996). A range of

bedform types are associated with both large and small-scale sediment waves, including cyclic steps (Kubo and Nakajima, 2002; Fildani *et al.*, 2006; Kostic and Parker, 2006; Spinewine *et al.*, 2009; Kostic, 2011; Cartigny *et al.*, 2011; Shao *et al.*, 2020; Slooman and Cartigny, 2020), antidunes (Normark *et al.*, 1980; Kubo and Nakajima, 2002; Lee *et al.*, 2002; Kostic *et al.*, 2014) and dunes (Nakajima and Satoh, 2001; Xu *et al.*, 2008).

The bedforms that Symons *et al.* (2016) describe as small-scale might be considered relatively large compared to the size of ripple cross-stratification and of decimetre-scale cross-stratification commonly found in turbidite cores and in outcrop. Critically, sediment waves appear to be built up by sequences of many flows and may be considered to be of a higher hierarchical order in terms of sedimentary architecture than the decimetre-scale cross-stratification developed beneath individual flows. The present research focuses on the formation of decimetre-scale cross-stratification and, therefore, does not further consider turbidity current sediment waves.

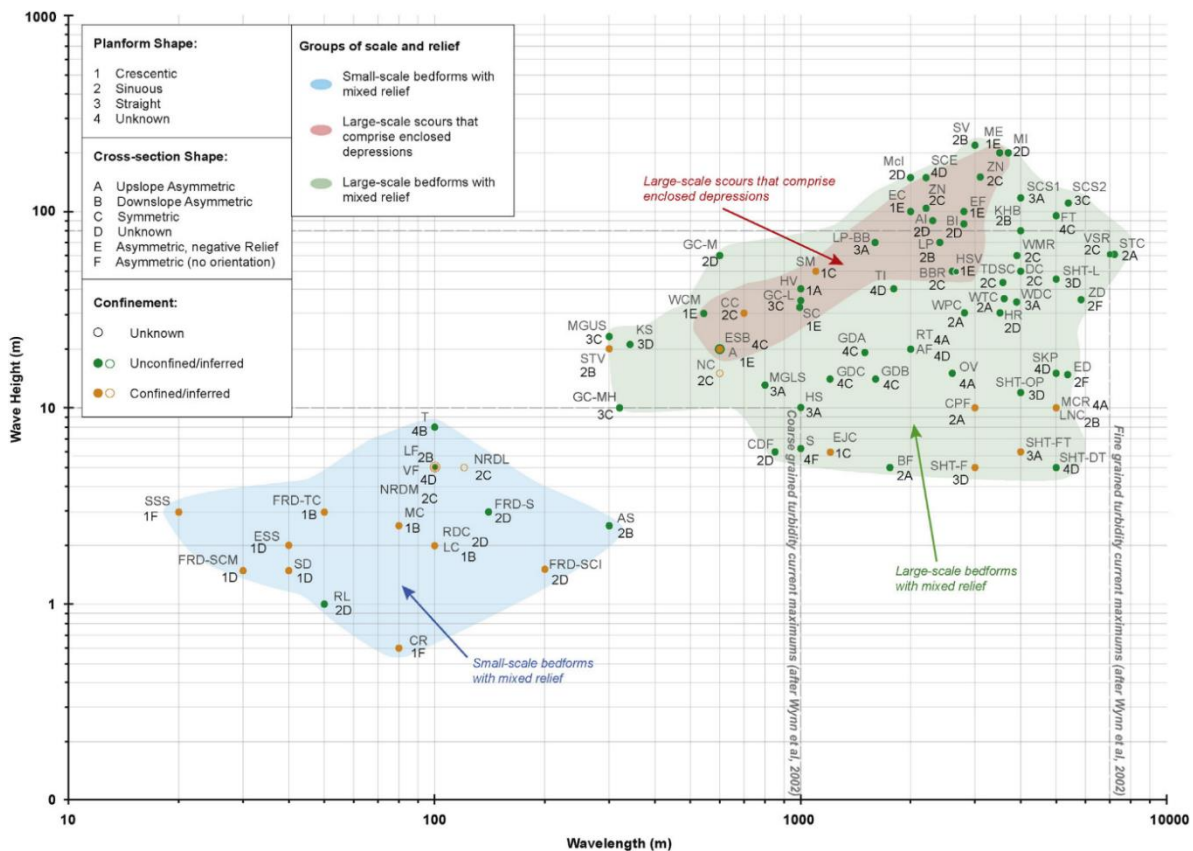


**Figure 2.10.** Logarithmic plot of wavelength versus wave height for global bedform examples associated with turbidity currents. Three groups are identified, (i) small-scale sediment waves with mixed relief, (ii) large scale sediment waves with mixed relief and (iii) large scale scours. From Symons *et al.* (2016).

## **Chapter 3. Relating the flow processes and bedforms of steady-state and waning density currents**

### **3.1 Abstract**

The interaction between turbidity currents and mobile substrates can lead to the development of different types of bedforms. Although much research has been conducted on bedform development beneath open channel flows, research into bedform development beneath waning gravity currents is relatively rare. Analysis of density current-related bedform development has therefore relied upon open channel flow phase diagrams. We report on an experimental study designed to assess the development of bedforms under steady and waning saline density currents. The experimental density currents developed stepped density profiles in which a higher-density basal zone was separated from the ambient fluid by a zone of intermediate density; any bedforms that developed were contained within the bottom layer of the current. Under different conditions ripples, dunes, downstream migrating antidunes and long wavelength antidunes were observed to form and could be distinguished based on their interactions and phase relationships with the upper surface of the lower denser layer of the current. Due to limited mixing between the upper and lower layer of the current and maintenance of current momentum, currents set with slowing discharge flow rates maintained a steady flow velocity in the lower layer of the flow. As a result, sustained bedform formative conditions were achieved within this lower layer, while waning current conditions effected the rest of the flow. Under waning currents, it was seen how pre-existing bed states can determine the subsequent evolution of bedforms. This illustrates the limitations of existing phase diagrams as they do not account for trajectory or rate of passage of flows through different bedform phase spaces. In order to establish a reliable quantitative association between the flow regime and the type of bedform development, it is critical to adopt an appropriate Froude number calculation method for stratified flow. The updated density current phase diagram indicates supercritical flow can be achieved at lower flow velocities than for open channel flows due to the effects of reduced gravity. Bedform depositional structures found in outcrop and on the modern sea floor provide data that helps to interpret the hydrodynamic and sedimentological character of the current that formed them. Therefore, understanding the processes involved in bedform development beneath density currents will enable more accurate estimation of the properties of flows.

## 3.2 Introduction

Turbidity currents are a type of buoyancy-driven flow whose density excess arises via turbulent suspension of sediment (Middleton, 1993; Kneller and Buckee, 2000). They are one of the principal means of redistributing sediment, nutrients and pollutants in the world's oceans (Masson *et al.*, 2006; Galy *et al.*, 2007; Covault, 2011; Dorrell *et al.*, 2014; Azpiroz-Zabala *et al.*, 2017; Pohl *et al.*, 2020) and pose a significant risk to offshore infrastructure (Bruschi *et al.*, 2006; Carter *et al.*, 2014; Clare *et al.*, 2016). The deposits (turbidites) are accumulations of multiple flows and collectively form the largest sedimentary landforms on the Earth's surface (Kneller, 2013). The interaction between turbidity currents and their substrate may result in the generation of various types of bedforms via processes of sediment erosion, transportation and deposition (Hand, 1974; Garcia and Parker, 1993; Wynn *et al.*, 2000a; 2000b; 2000c; Postma *et al.*, 2009; Sequeiros *et al.*, 2010; Postma and Cartigny, 2014). Collection of data directly from active turbidity currents is challenging; due to their magnitude and speed they are known to have destroyed the analytical equipment deployed to measure them (Azpiroz-Zabala *et al.*, 2017; Paull *et al.*, 2018 and references therein). However, via sea floor surveys (Normark *et al.*, 1980; Hughes Clarke, 2016; Hage *et al.*, 2018; Paull *et al.*, 2018), experimental work (Parker *et al.*, 1987; Alexander *et al.*, 2008; Spinewine *et al.*, 2009; Sequeiros *et al.*, 2010; Cartigny *et al.*, 2011; 2014; Fedele *et al.*, 2016; Koller *et al.*, 2017; 2019) and, more commonly, by studies of bedforms preserved in outcrop (e.g., Bouma, 1962; Hubert, 1966a; Keith & Friedman, 1977; Lucchi & Valmori, 1980; Lowe, 1982; Mutti, 1992; Kneller and McCaffrey, 2003; Sylvester & Lowe, 2004; Bakke *et al.*, 2008; Sumner *et al.*, 2012; Arnott, 2012) research into bedform development by turbidity currents has taken place. Yet, interpretation of depositional bedforms structures found in turbidites often relies upon research done for bedforms in open channel flows. Fedele *et al.* (2016), Koller *et al.* (2017; 2019) and Sequeiros *et al.* (2010) have shown that open channel flow bedform phase diagrams incorrectly predict bedform development and morphodynamics beneath density currents. This shortcoming has been attributed to hydrodynamic differences between density currents and fluvial flows (Fedele *et al.*, 2016; Koller *et al.* 2017; 2019; Sequeiros *et al.*, 2010), illustrating a need for further research to determine what controls bedform formation beneath turbidity currents, in comparison to other environments. Much of our understanding of the hydrodynamic and sedimentological character of turbidity currents is derived from analysis of preserved depositional structures found in turbidites. Therefore, more accurate interpretation of the turbidity current can be achieved via improved understanding of the sedimentological processes responsible for certain depositional products.

Although previous research has mainly focused on the flow dynamics of steady density currents, real-world turbidity currents are commonly characterised by the passage of high velocity heads, followed by progressive waning of mean velocity during passage of the body and tail of the current over periods of hours to days (Kneller and Branney, 1995; Kneller and McCaffrey, 2003; Azpiroz-Zabala *et al.*, 2017). To understand the development of bedforms in the prototype environment, it is therefore critical to understand how bedforms evolve both in steady and waning flow fields. This study presents results from original experiments that examine bedform development under both steady and waning saline density currents. A discussion is presented on the hydrodynamic and sedimentary processes involved in the generation of ripples, dunes and antidunes, as well as the complexities of bedform response to altering bedform phase space conditions under waning currents.

### ***3.2.1 Bedform classifications and phase diagrams***

Research into the origin of sedimentary bedforms, their development and their morphodynamics has mainly been carried out for open channel flows (Shields, 1936; Allen, 1962; 1963; 1984; Leeder, 2012). This body of work remains the most comprehensive area of research that studies the complex feedback and interactions that take place between a mobile substrate and a flow (Kennedy, 1969; Yalin, 1977; Engelund and Fredsøe, 1982; Ashley, 1990; Bennet and Best, 1995; 1996; Colman and Nikora, 2011, among others). Since this body of work underpins the study of bedforms in any sedimentary setting, this research will be referred to throughout this investigation. A review of key aspects relating to this study is therefore presented.

Bedform classification has been the subject of much research which has defined various methods to distinguish between different bedform types. A well-established classification defines bedforms based on the flow regime that generated them (Harms and Fahnestok, 1965). Subcritical bedforms are defined as lower-regime forms: these are lower-stage plane bed, ripples and dunes. Supercritical bedforms are defined as upper-regime forms: these include upper stage plane bed, antidunes and cyclic steps (Harms and Fahnestok, 1965; Ashley, 1990; Knighton, 1998; Sun and Parker, 2005; Cartigny *et al.*, 2011).

When comparing dunes and ripples, which are geometrically similar, two approaches recur in the literature: dunes and ripples may be distinguished by associated flow characteristics and bedform interaction with the flow (Bridge and Best, 1988; Bennet and Best, 1995; 1996); alternatively, they may be defined according to their dimensions (Guy *et al.*, 1961; Raudkivi, 2006; Ashley, 1990; Colombini and Stocchino, 2011).

It is widely recognised that dunes and ripples differ hydrodynamically (Richards, 1980; Bass 1994; Bennet and Best, 1995). As dunes and ripples interact with a current, both experience flow separation at the crest. As dunes are relatively larger, flow separation at the crest is greater, as is the associated turbulent wake region and shear layer which generate from the crest and extend downstream (Venditti, 2013). As a result, compared to ripples, dunes generate larger-scale turbulence that arises at the shear layer generated by Kelvin Helmholtz instabilities (Baas, 1994; Bennett & Best, 1996; Schindler and Robert, 2005; Leeder, 2012; Venditti, 2013). The turbulent structures upwell through the entire flow depth ('ejection events') and can interact with the flow surface (known as 'boils') (Yalin, 1992; Bennet and Best, 1995; 1996; Best, 1993; 2005; Fernandez *et al.*, 2006). Ripples have a small separation zone and shear layer that are restricted to the near bed region (30 – 40 % of the water column) and therefore do not interact with the current's surface (Baas, 1994; Bennett & Best, 1996; Schindler and Robert, 2005; Leeder, 2012; Venditti, 2013). This means that dunes scale with flow depth, while ripples exist independently of flow depth (Jackson, 1976; Yalin, 1977; Schindler and Robert, 2005).

Dunes and ripples may also be defined according to their dimensions (Guy *et al.*, 1961; Colombini and Stocchino, 2011; Raudkivi, 2006; Ashley, 1990; Bartholdy *et al.*, 2015). Distinctions are based on bedform dimensions such as wavelength and height: Ashley (1990) suggests that dune bedform dimensional data – for open channel flow – exists as a single genetic population, separate from smaller ripple forms. While there remains debate in the literature on the best method to distinguish between ripples and dunes (Jerolmack and Mohrig, 2005; Bartholdy *et al.*, 2015), in this study the primary method used to distinguish them was to observe the presence of a phase relationship between dune bedforms and the upper surface of the lower layer of the current (as described by Fedele *et al.* 2016); for ripples, no such relationship exists (cf. Fedele *et al.*, 2016). In addition to studying phase relationships, in this study bedform dimensional data was also collected which was expected to resolve larger dune dimensions compared to ripples.

The type of phase relationship was also observed to differentiate dunes and supercritical bedforms. Under supercritical flow conditions, supercritical bedforms develop as the mobile substrate takes on the shape and amplitude of the surface waves that propagate at the current's free surface (McLean, 1990; Fourrière *et al.*, 2010). As a result, supercritical bedforms are in-phase with the current interface. Antidune development occurs under supercritical flow (Recking *et al.*, 2009). They are free-surface dependent (Cartigny *et al.*, 2014) and may migrate upstream, downstream or remain stationary (Kennedy, 1963). Subcritical bedforms are distinguishable from supercritical bedforms as they have an out-of-phase relationship.

Fedele *et al.* (2016) and Koller *et al.* (2017; 2019) investigated the development of bedforms beneath density currents. They chose to differentiate dune and ripple bedforms on the basis of flow characteristics, specifically shear stress. They note that a lower denser layer develops within their experimental saline gravity currents and describe an out-of-phase relationship between dunes and the upper surface of this layer.

Observational, experimental and theoretical modelling, principally under open-channel conditions, have refined understanding of the hydrodynamic and sedimentological conditions associated with bedform generation and growth, leading to the development of bedform stability diagrams (van Rijn 1984; Southard and Boguchwal, 1990; van den Berg and van Gelder, 2009; Raudkivi, 1976). These are widely used to predict the type of bedform that will develop under specific sets of boundary conditions. Based on their experiments, Fedele *et al.* (2016) developed a new stability diagram for bedforms formed under density currents but noted that further refinement of the bedform stability fields was needed. They noted that collection of more hydrodynamic and sedimentological data under experimentally controlled conditions was required to advance understanding of bedform development under density currents.

### **3.3 Methodology**

#### ***3.3.1 Experimental set up and methods***

Experiments were conducted at the Total Environment Simulator (TES) at the University of Hull (see Figure 3.1 for setup). The TES is a 14 m long, 6 m wide and 2 m deep tank with two 3 m deep sump tanks situated at either end that hold 21 m<sup>3</sup> of water. A density-current channel was placed inside the larger tank. Made of transparent Perspex, and supported by Rexroth beams, it was 10 m long, 0.15 m wide and 0.60 m high. The interior channel was fully submerged when the large tank was filled to a depth of 1 m. The sump tanks enabled experiments to be run for 45 minutes without any back-water effects.

The flat base of the interior channel was set at 3 ° for Experiments 1 and 2, then was lowered to 0.7 ° for Experiments 3, 4 and 5 (Table 3.1). A mobile substrate comprising plastic sediment particles of median size 427 µm and specific gravity 1.50 was laid to a thickness of 15 cm inside the interior channel; the upper surface was smoothed before the start of each experiment. For each experiment, salt was mixed and dissolved into 4000 L of water to reach 6 %

salt concentration ( $1060 \text{ kg m}^{-3}$ ). An excess density of 6 %, above fresh water ambient ( $1000 \text{ kg m}^{-3}$ ), is equivalent to a suspended sediment load of 3.75 % v/v (of density  $2600 \text{ kg m}^{-3}$ ).

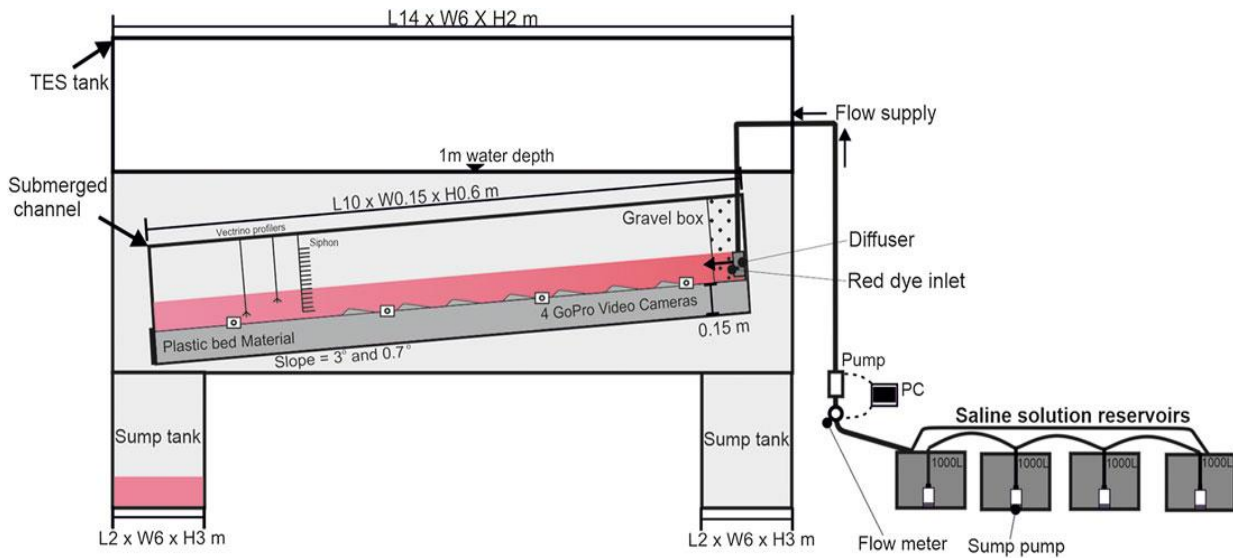


**Figure 3.1.** Experimental set up.

The saline solution was held in four 1000 L reservoirs each equipped with a sump pump enabling the circulation of the saline solution within the reservoir to ensure the total dissolution of the salt and to prevent the mixture becoming stratified. In this set-up, the sump pumps were also used to mix between the separate reservoirs. Each reservoir was sampled for both temperature and density every 10 minutes for 1 hour prior to each experiment, to check that the saline solution had reached and maintained a density of  $1060 \text{ kg m}^{-3}$ . During the experiments a larger pump extracted saline solution from one primary reservoir; the other three were connected to the primary reservoir via the sump pumps, inputting saline solution to maintain a steady hydraulic head throughout the experiment. Once extracted by the larger pump, the saline solution was introduced into the upstream inlet of the submerged interior channel. At the inlet, the flow passed through a diffuser (with concentric tubes and discharge holes) and a 40 cm long and 15 cm wide gravel box to remove the momentum inherited from the pipe flow and to distribute the flow evenly across the width of the flume as a purely gravity driven current. On exiting the gravel box, the saline density current flowed over the substrate. For runs with unsteady flow conditions, a flow meter (MAG5100W electromagnetic) and linked computer programme designed in MATLAB controlled the pump speed to ensure that the flow discharge reduced gradually and smoothly over the course of the experiment.

Immediately downstream of the gravel box, a sediment feeder was positioned to deposit more sediment onto the bed, replenishing the substrate as partial scouring took place at the point where the current exited the gravel box. To visualise the current, red pond dye was introduced to

the channel at the current outlet via a tube connected to a peristaltic pump. Inputting the dye directly into the channel, rather than mixing it inside the reservoirs, allowed more control over the height at which dye was introduced to the density current. Having periods of colourless flow also enabled better visualisation of any bedforms formed.

The measurement equipment included two Nortek vectrino profilers (with sampling frequencies of 100 Hz) to record the downstream, cross-stream and vertical velocity components of the flow. The vectrino probes were orientated and aligned with the downstream (x), cross-stream (y), and vertical (z) directions of the flume, then fixed in place so the three-dimensional components of the flow (x, y, z) were recorded accurately. The vectrinos were positioned at 8 m and 7 m from the upstream end of the channel to ensure their presence did not impact bedform development in the middle of the channel. A siphon array connected to a Watson Marlow multichannel peristaltic pump was placed into the flume, in front of the vectrinos, at specific times to collect fluid samples. The array sat 4 cm up from the bed and siphoned over 45 cm up through the saline density current and the ambient fluid. The siphon tubes were 3 mm in diameter. Samples consisting of twenty-four measurement points were taken every 7 minutes over 2-minute intervals. After each collection, the siphon array was removed from the channel while the peristaltic pump remained on. Twenty-four peristaltic pipes, each 7 m long, connected each siphon channel to the sample collection pots outside of the TES. It took 5 minutes for the collected sample to pass through the piping. This offset timing meant that first samples were collected 5 minutes after the experiment had started, whilst the last samples were collected in pots 5 minutes after the experiment had ended. Velocity data collected during siphoning was discarded. Siphon sample density and temperature measurements were collected using a handheld Anton Paar density meter (Model: DMA 35 Basic). These results were recorded within 45 minutes of their collection to ensure no significant temperature change or evaporation took place that might have affected the density reading.

To collect bedform development data, four underwater GoPro cameras were positioned inside the large tank facing different sections of the interior submerged channel, fixed at bed level height. Each GoPro had a field of view of 2.5 m.

**Table 3.1.** *Experimental parameters and characteristics of the plastic sediment that was used for the channel substrate in each experiment. Densimetric Froude number ( $F_{rd}$ ) calculation shown in Equation 3.1.*

<b>Current saline</b>	1060
---------------------------	------

<b>density (kg m<sup>3</sup>)</b>					
<b>Slope (degrees)</b>	3		0.7		
<b>Experiment</b>	1	2	3	4	5
<b>Flow state</b>	Steady flow	Unsteady slowing flow	Steady flow	Unsteady slowing flow	Steady flow
<b>Flow rate (start) (L/s)</b>	1.5	2	1.5	2	3
<b>Flow rate (end) (L/s)</b>	1.5	1	1.5	1	3
<b>Experiment run time (mins)</b>	45	45	40	45	25
<b>Densimetric Froude number (Frd)</b>	2.6	2.8 (Start) 1.2 (End)	0.7	0.8 (Start) 0.8 (End)	0.87
<b>Criticality</b>	Supercritical	Supercritical	Subcritical	Subcritical	Subcritical
<b>Substrate sediment density (kg m<sup>3</sup>)</b>	1500				
<b>Substrate grain-size distribution (μm)</b>	$d_{50}$ 286	$d_{50}$ 327	$d_{50}$ 427	$d_{50}$ 563	$d_{50}$ 649

### 3.3.2 Experimental parameters

Five experiments were carried out. Both the density of the saline current and the sediment size used for the channel substrate remained constant. The discharge flow rate and slope were varied. Table 3.1 shows the experimental parameters for each run and details the properties of the plastic sediment that was used for the sediment bed of the flume. This material was chosen as it is coarse enough for the development of a range of bedform types and has a low enough density to enable sediment transport.

The finite amount of saline solution stored in the four reservoirs meant that Experiments 1 – 4, which were carried out with a discharge between 1 – 2 L/s, had a run time of approximately 40 – 45 minutes. At times the pipe that extracted the saline solution from the reservoirs was positioned within a deeper hollow of the irregular base of the reservoir. This resulted in minor variations in total experimental run time between experiments. Experiment 5 was carried out under faster discharge flow rates (3 L/s) and as such the experimental run time was shorter at 25 minutes.

The Froude number ( $Fr$ ) is commonly used to predict the type of bedforms that are likely to develop in association with a particular flow regime. By determining the celerity of a surface wave in relation to the velocity of the current, flows can be recognised as being either subcritical ( $Fr < 1$ ), supercritical ( $Fr > 1$ ) or critical ( $Fr = 1$ ) (Baines, 1998). Under subcritical conditions, surface waves can move both upstream and downstream as celerity is slower than the flowrate. In supercritical flow, surface waves can only move downstream as celerity is faster than the flow rate. This has proven an effective measure to estimate the criticality of un-stratified open channel flows, in which depth averaged measures of current velocity and density may be used to accurately represent the current. However, Baines (1998), Thorpe (2010), Thorpe and Li (2014), Waltham (2004), Huang *et al.* (2009) and Dorrell *et al.* (2014; 2016) all recognise that for stratified flows such as turbidity currents, the use of Froude numbers based on depth averaged values can be problematic. This is because the non-uniformity of a current's density profile influences wave celerity (Baines, 1998; Thorpe, 2010; Thorpe and Li, 2014; Waltham, 2004; Dorrell *et al.*, 2014; 2016). It follows that different parts of the flow might have different effective Froude numbers (Dorrell *et al.*, 2016).

Nevertheless, the densimetric Froude number ( $Fr_d$ ; Equation 3.1) (Fedele *et al.*, 2016; Koller *et al.*, 2017; 2019) is commonly used to characterise density currents which, although it takes into account reduced gravity, is still calculated on a depth averaged basis. For the present experiments, critical conditions are nominally assumed to be achieved at  $Fr_d = 1$ .  $Fr_d$  was calculated for the lower denser layer of the flow within which all bedform development took place. The surface of the lower denser layer corresponds closely with the height of the velocity maximum, the interface of the lower denser layer with the upper less dense layer of the current is identifiable in density profiles and in photographs and videos taken throughout the experiments as it was dyed pink for current visualisation. The lower layer of the current is the least stratified part of the flow for which bulk Froude number calculations will be most accurate.

$$Fr_d = \frac{U}{\sqrt{\frac{\rho - \rho_a}{\rho_a} gH}}, \quad (\text{Eq. 3.1})$$

Where  $U$  is the average velocity of the lower layer of the density current ( $\text{ms}^{-1}$ ),  $\rho$  is the current density,  $\rho_a$  is the ambient water density (considered as  $998.2 \text{ kg m}^{-3}$ ),  $g$  is gravity ( $9.8 \text{ ms}^{-2}$ ) and  $H$  is the mean height of the lower layer of the density current (m), measured every 5 – 6 minutes and averaged over the course of the run. Measurements of the flow velocity profile in this study did not cover the entire range of the lower layer of the current. Therefore, to obtain the layer-averaged flow velocity, the velocity profile was interpolated and extrapolated using the shear velocity (Equation 3.2, below) and the height of the lower layer of the flow recorded throughout each experiment (assuming that the velocity profile in the lower layer obeys the logarithmic law of the wall). Then, the velocity profile was integrated to calculate the average velocity of the lower layer of the density current. Table 3.1 outlines the time-averaged Froude numbers associated with each experiment. Experiments carried out upon the steeper  $3^\circ$  slope were supercritical and experiments carried out upon the shallower  $0.7^\circ$  slope experienced subcritical flow, according to bulk  $Fr_d$  definitions calculated for the lower part of the flow. Figure 3.2 shows the interpolated velocity profiles based on shear velocity calculations for the lower layer of each density current. For steady flow experiments, shear velocity was time-averaged over the whole run. For unsteady flows, shear velocity was time-averaged over 5-minute intervals.

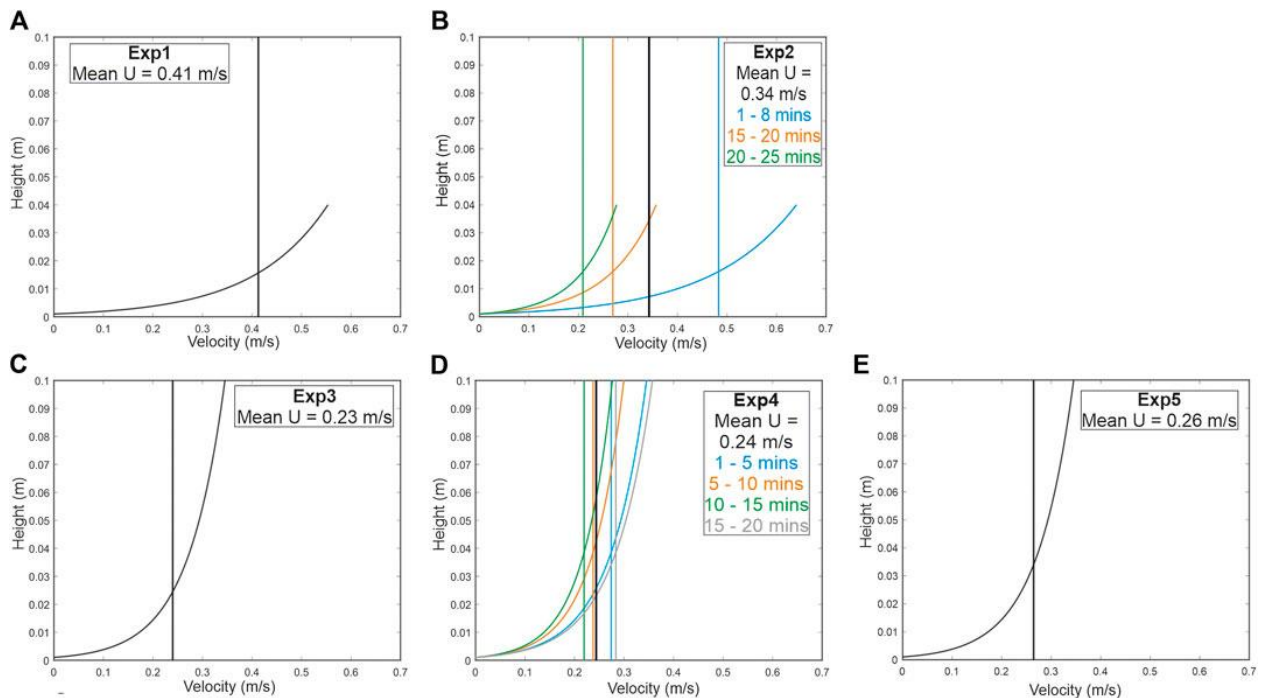


**Figure 3.2.** Experiments 1 - 5 (A - E), interpolated velocity profiles based on shear velocity calculations for the lower layer of each density current. For steady flow experiments, shear velocity

was time-averaged over the whole run. For unsteady flows, shear velocity was time-averaged over 5-minute intervals.

### 3.4 Data Processing

The velocity data was filtered (2SD from a moving mean) to remove any noise and outliers from the dataset. This velocity data was then used to calculate the near bed shear velocity ( $u^*$ ; Equation 3.2), assuming the flow followed a standard logarithmic profile away from both the near-bed boundary layer and internal velocity maximum (Petrie and Diplas, 2015). The velocity profile was fitted over 0.01 – 0.02 m away from the bed in order to avoid both the near-bed viscous sublayer and the velocity maximum where the profile may deviate from the logarithmic form

$$u = \frac{u^*}{K} \log\left(\frac{z}{z_0}\right). \quad (\text{Eq. 3.2})$$

The shear velocity is given by the gradient of the velocity profile, where  $u$  is the velocity of the density current ( $\text{ms}^{-1}$ ),  $K$  is the von Kármán constant (taken as 0.41),  $z$  is the height above the bed and  $z_0$  is the height above the bed where flow velocity is zero. As previously stated, shear velocity calculations are used in the estimation of the average velocity of the lower layer of the density currents. Shear velocity calculations were also done in association with dunes and ripples to help distinguish between them (Fedele *et al.* (2016) use shear stress to distinguish ripples and dunes). For ripples, shear velocity was calculated and averaged over the course of Experiment 3 during which ripples were the stable bedform. Shear velocity measurements associated with dunes were recorded over a shorter period during the last 5 minutes of Experiments 4 and 5 as dunes developed.

#### 3.4.1 Analysis of bedform dimensions

Videos were taken throughout each experiment to capture bedform dynamics. Images were edited to remove the barrel lens distortion effect. Image processing software (Image J) was used to obtain five  $x$  and  $y$  coordinates for each bedform: the upstream and downstream bedform troughs, and the crest and mid points of the stoss and lee slopes (Figure 3.3). Bedform wavelength was calculated by taking the upstream trough from the downstream trough ( $x_5 - x_1 = \text{wavelength}$ ). Bedform height was recorded by taking the downstream trough from the crest ( $y_3 - y_1 = \text{height}$ ).

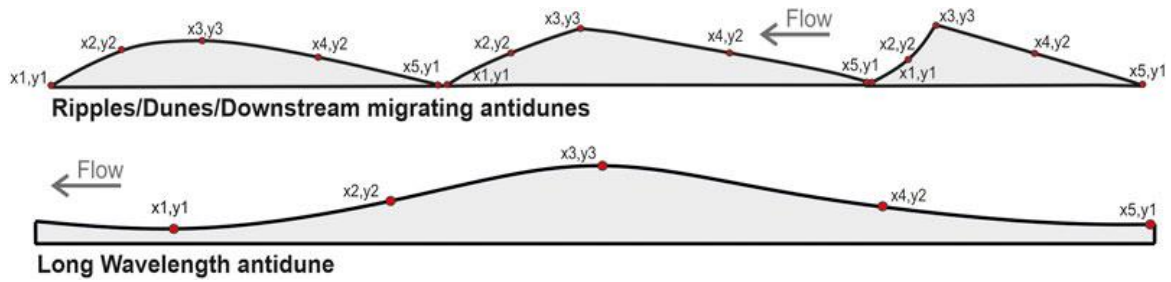


**Figure 3.3.** Schematic diagram of asymmetric bedforms. The red points depict the locations of the  $x, y$  coordinates, which were recorded on each bedform.

### 3.4.2 Drag Coefficient

The drag coefficient ( $Cd$ ) associated with different types of bedform development was estimated (Equation 3.3) for the duration of each experiment.

$$Cd u^2 = u^{*2}, \quad (\text{Eq. 3.3})$$

$u$  is the bulk flow velocity for the lower layer of the flow as used by Dorrell *et al.* (2016). The total drag corresponds to the bed interface only (as the shear at the velocity maximum is zero); the entrainment drag for the upper layer of the current is not included as all bedform development took place within the lower denser layer of the flow.

## 3.5 Results

### 3.5.1 Current density

Figures 3.4a – e show the density profiles measured for each experiment. Figure 3.4f compares the average density profiles for each experiment. Concentration measurements were not retrieved from the lower 4 cm of the density current, due to the practicalities of suspending the siphon over the channel. It is assumed that densities close to  $1060 \text{ kg m}^{-3}$  were reached in this region, as the flow close to the bed experiences virtually no flow dilution due to upper boundary entrainment.

The experiments resolved a lower layer in the flow, situated just below the velocity maximum that is denser than the upper layer of the current. Whilst a saline flow is used in the experiments that experiences no inherent stratification from sedimentation, the less dense upper layer is driven by the entrainment of ambient water. To better understand the structure of the current, the bottom layer was dyed red during each run to enable visualisation of flow interaction with the bed. Figures 3.4a – f record the lower denser layer of the flow – the dashed lines on the density profiles depict the position of its upper surface. Experiments carried out on the steeper

3 ° slope have thinner bottom denser layers, with the surface of the denser layer situated 3 – 5 cm above the bed. On the shallower 0.7 ° slope, the bottom denser layer is thicker, with the surface situated 10 – 15 cm above the bed. Slope therefore appears to be the most significant control on bottom layer thickness, via the development of an associated flow regime; thinner flows are associated with supercritical fast flowing conditions and thicker flows with subcritical, lower flow velocities. Very little mixing appears to take place across the interface between the dense lower layer and the mixing region above. This is evident in Figure 3.4 where the density profiles show an abrupt transition from the bottom denser layer into the mixing region. This transition is most abrupt for supercritical flows.

Figure 3.4 also shows how density profiles change with time during runs with steady discharge flow rates (Experiments 1, 3 and 5) compared to runs with waning discharge flow rates (Experiments 2 and 4). The steady runs are characterised by relatively constant density values throughout the experiment, whereas in unsteady runs concentrations higher up in the flow progressively decrease as discharge flow rates reduce. Figures 3.4b and 3.4d show a reduction in height of the boundary between the density current and the ambient water over time (identified by red triangle markers). However, despite a reduction in the overall height of the density current, it is notable that the slowing discharge flow rate was not associated with any change in the thickness of the denser bottom layer, which remained relatively constant. This observation will be explored further within the discussion section.

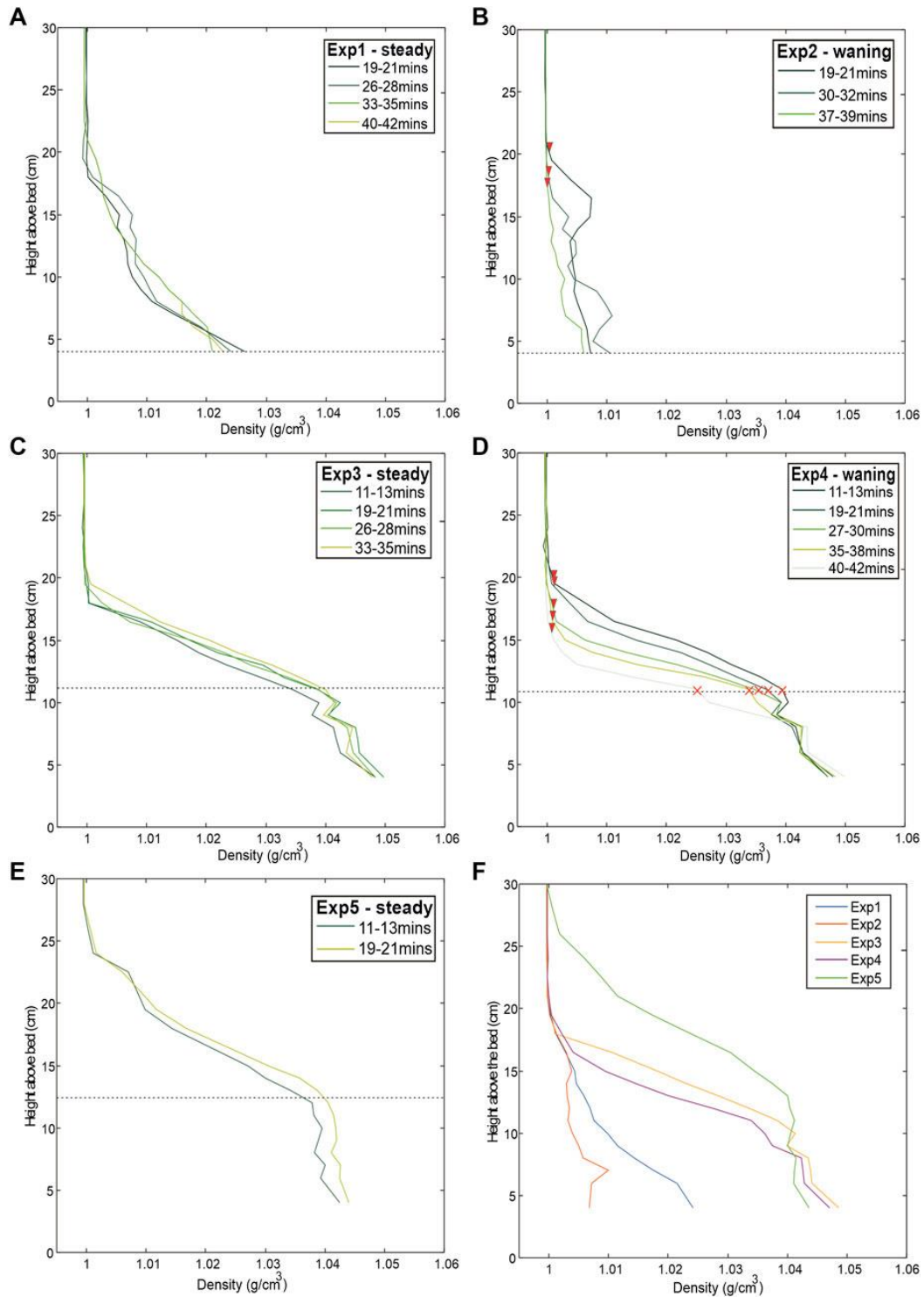


**Figure 3.4.** Vertical concentration profiles averaged over 2 - 3 minutes. The black dashed line denotes the height of the interface between upper and lower denser layer, and the red crosses attribute this point to specific profiles, depicting the constant height of the interface throughout the run. Experiments 2 and 4 are waning currents, the red triangles mark the change in height of the upper surface of the current with the ambient fluid over time. They depict the gradual reduction in height as the flow is slowed. Plot (F) shows average density profiles for each run based on available data in (A - E). Experiments 1 - 5 correspond to plots (A - E), respectively.

### **3.5.2 Flow velocity**

Figures 3.5a and 3.5b presents the velocity data recorded throughout Experiments 1 and 2. (For Experiments 3 – 5, the velocity data did not record the velocity maximum, which was situated just above the measurement window). Figure 3.5 also plots the top of the bed and the height of the upper surface of the lower denser layer of the current, which under supercritical flow was in-phase with the bed. The height of the surface of this lower denser layer is determined using the density profiles (Figure 3.4), photographs and videos taken throughout the experiments, all of which record the bottom denser layer. In both Figures 3.5a and 3.5b, the height of the velocity maximum either aligns with, or closely corresponds to, the height of the upper surface of the lower denser layer of the current. In Figure 3.5a, between 15 – 24 minutes the velocity maximum slightly decreases due to the vectorino being temporarily situated in a bedform trough where the flow is slowed. Figure 3.5b also shows an overall decrease in the velocity maximum between the start of the run (0 – 7 minutes) compared to near the end of the run. This is attributed to increased frictional drag as bedforms have become established upon the bed, whereas between 0 – 7 minutes (at the point where velocity data was being collected) bedform development had not started.

Figure 3.5c depicts how velocity changed throughout Experiment 4. Unlike Experiments 1 and 2, the velocity maximum was not recorded. However, Figure 3.5c shows that despite the discharge flow rate slowing over the course of the run, the velocity within the bottom layer of the current appears to maintain a relatively steady velocity throughout the run, while the upper layer of the flow wanes (Figure 3.4d).

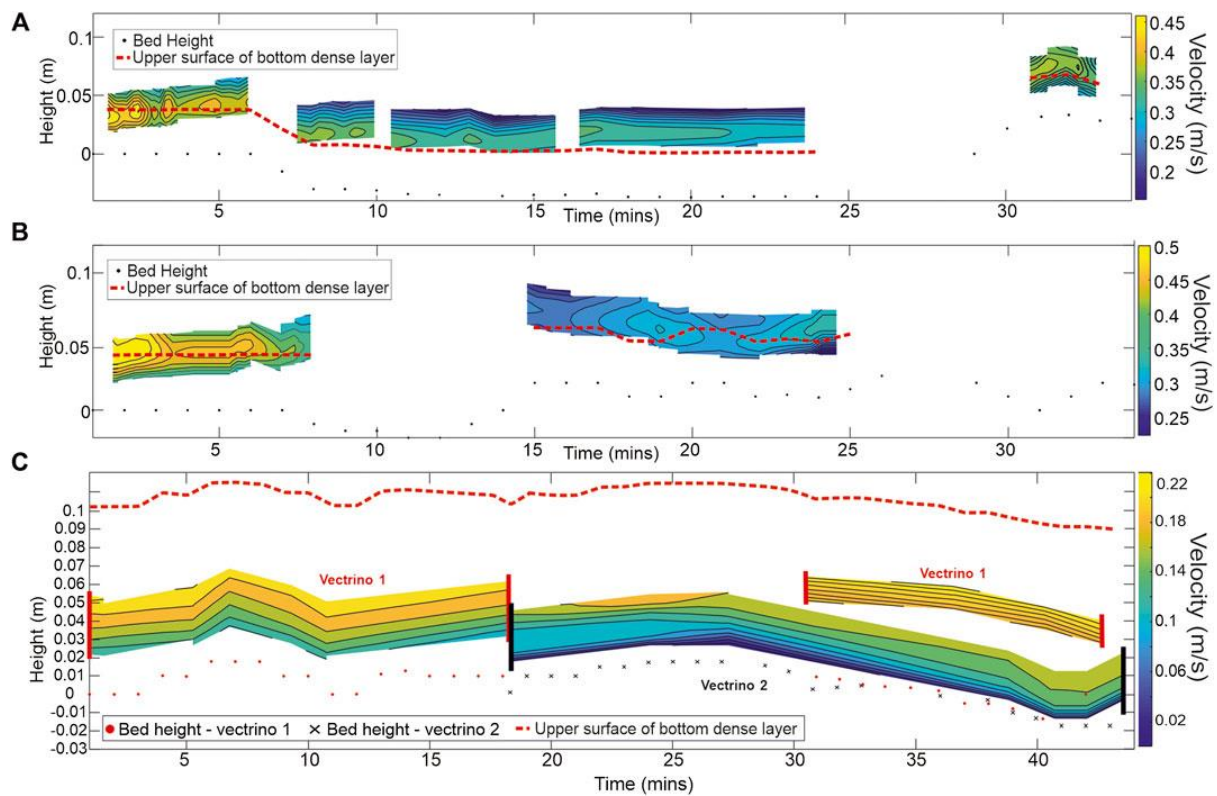


**Figure 3.5.** Contour plots of the downstream velocity component throughout Experiments 1 (supercritical steady flow) (A) and 2 (supercritical waning flow) (B). The dashed red lines identify the height of the upper surface of the lower denser layer of the density current. The black dots indicate the height of the substrate beneath the vectrino. (C) Contour plot of the downstream velocity component throughout Experiment 4 (subcritical waning flow), recorded within the bottom dense layer of the flow. Velocity measured between 0 - 18 minutes and 33 - 43 minutes was recorded by vectrino 1 which was positioned higher above the bed. Velocity measured between 18 – 44 minutes was recorded by vectrino 2, positioned lower in the flow. The red dots indicate the height of the substrate beneath vectrino 1 and the black crosses indicate the height of the substrate beneath vectrino 2.

### 3.5.3 Bedforms

Most of the substrate material was carried as bedload and some of the sediment was observed to be transported as suspended load. A variety of bedforms developed during the experiments, including ripples, dunes, downstream migrating antidunes and long wavelength antidunes. Figure 3.6 shows a timeline of bedform development for each experiment, the associated drag coefficient change and the ratio between bedform wavelength and height of the lower layer of the current.

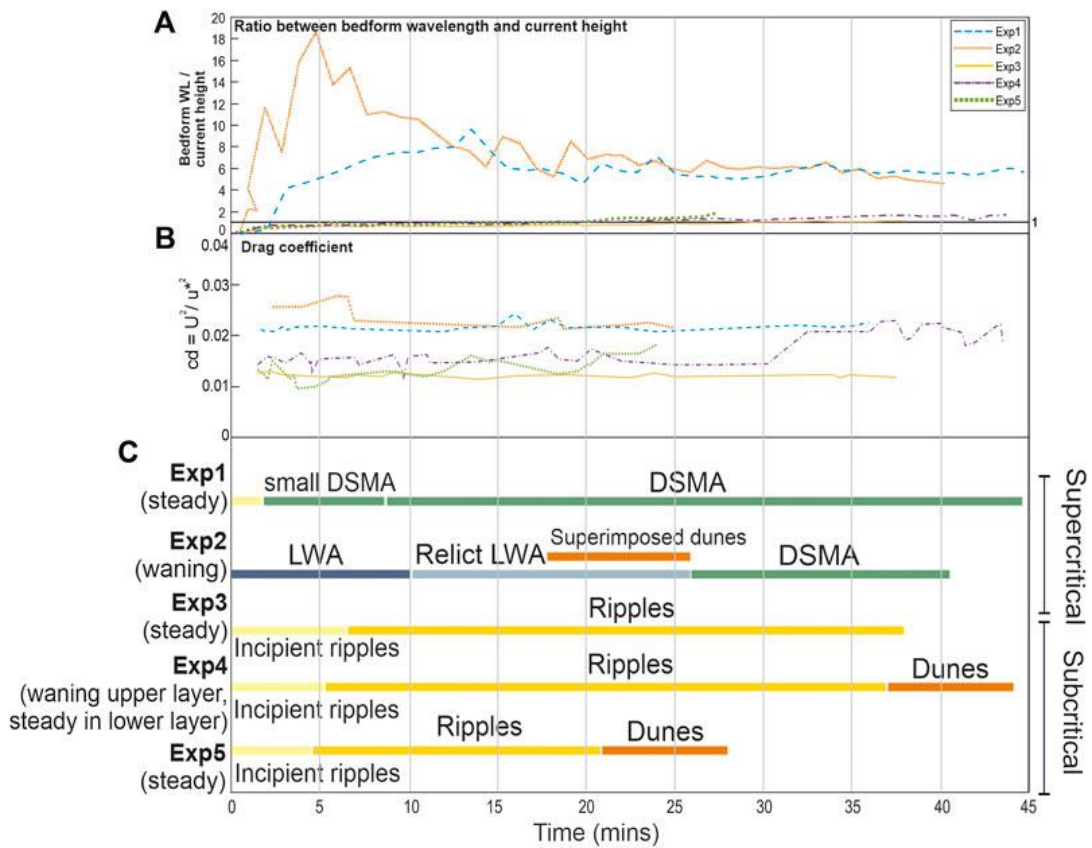


**Figure 3.6.** (A) Ratio between bedform wavelength and the height of the lower layer of the current. (C) Bedform development timeline for Experiments 1 - 5 (DSMA, Downstream migrating antidunes. LWA, Long wavelength antidunes) and (B) the associated drag coefficient change.

As noted previously, bedforms were classified according to the phase relationship of bedforms with the current interface. Bedforms developed within a lower denser layer within the current, and as such bedform phase relationship was determined with respect to the upper surface of the lower dense layer of currents (not the top of the current). To support the results of the phase-relationship method, bedform dimensional data was collected to further help distinguish ripples from dunes. Bedform dimensional data are shown in Figure 3.7.

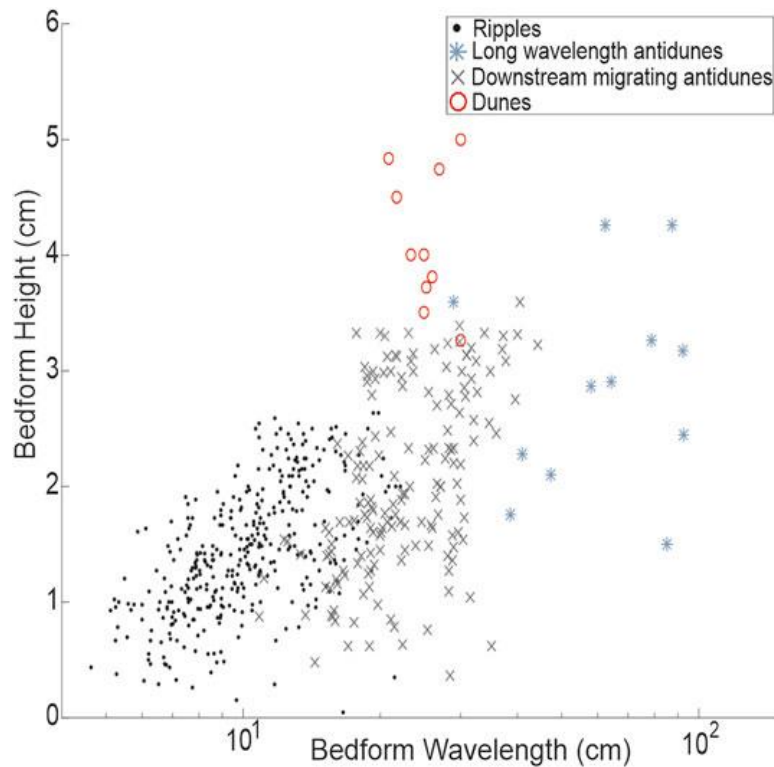


**Figure 3.7.** Bedform dimensions (data from all experiments).

### 3.5.3.1 Subcritical bedforms

Ripples formed at the start of each run, except for Experiment 2 where long wavelength antidunes formed immediately due to fast supercritical conditions. Usually, ripple development preceded the development of larger bedforms. Bedforms developed as small incipient ripples with wave heights and lengths <1 cm, gradually increasing in size to reach maximum heights and lengths of 3.5 cm and 21 cm, respectively (Figure 3.7). Ripples were asymmetric and on reaching heights of 2 – 3 cm, small separation zones with recirculation cells downstream of the bedform crest could be observed (cf. Baas, 1994). Figures 3.8a and 3.8c shows a photo of a typical ripple having no effect on the upper surface of the lower denser layer of the current. Both the low drag coefficient calculated throughout Experiment 3 and the ratio between bedform wavelength and height of the lower layer of the current that remains mainly below 1 (Figure 3.6), show that ripples formed in Experiment 3 impart the least drag on the flow.

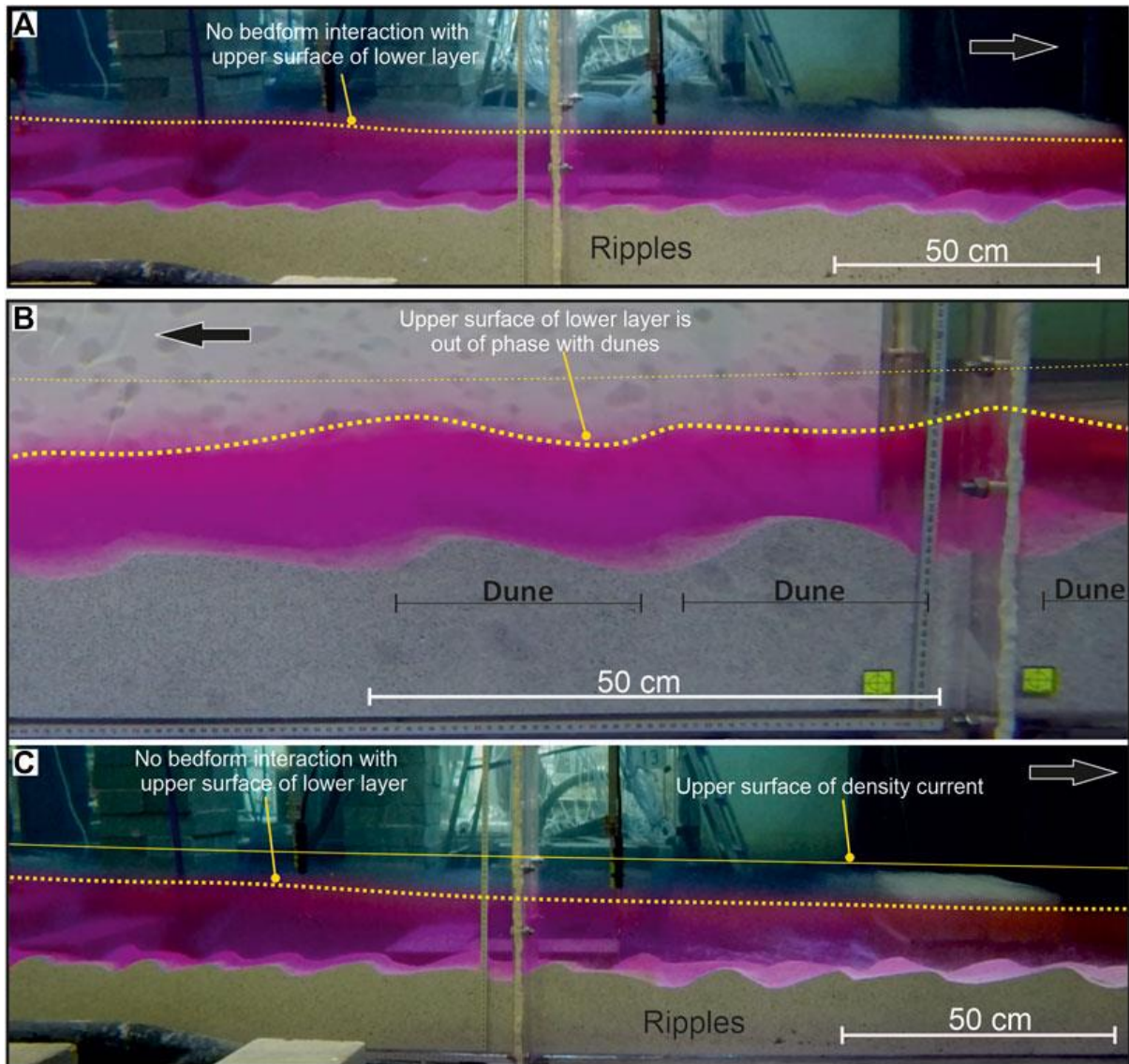


**Figure 3.8.** Bedform current interaction. Two layers can be recognised in the density current: the lower denser layer of the density current is dyed red/pink, the upper surface of the lower denser layer is indicated by a yellow dotted line. The current interface with ambient water is indicated by a solid yellow line. Direction of flow is indicated by an arrow in each photograph. **(A)** There is no interaction between ripples and the lower layer upper surface (Experiment 3). **(B)** Dunes formed towards the end of Experiment 5. The dunes are out-of-phase with the upper surface of the lower layer. From photo (A) it is hard to determine the height of the upper surface of the current. **(C)** is taken from another flume angle at the same time as photo (A), in which the upper surface of the current can be distinguished.

Dunes formed on the shallower  $0.7^\circ$  slope under subcritical flow regimes in both Experiments 4 and 5. Under steady state flow in Experiment 5; dunes developed gradually over 25 minutes (Figure 3.9). Over the course of the run, ripples evolved into dunes via steady ripple growth and by two or more ripples merging to form larger dunes. Although dunes were

established towards the end of Experiment 5, it was not possible to observe their continued development due to limitations on the duration of the experiment.

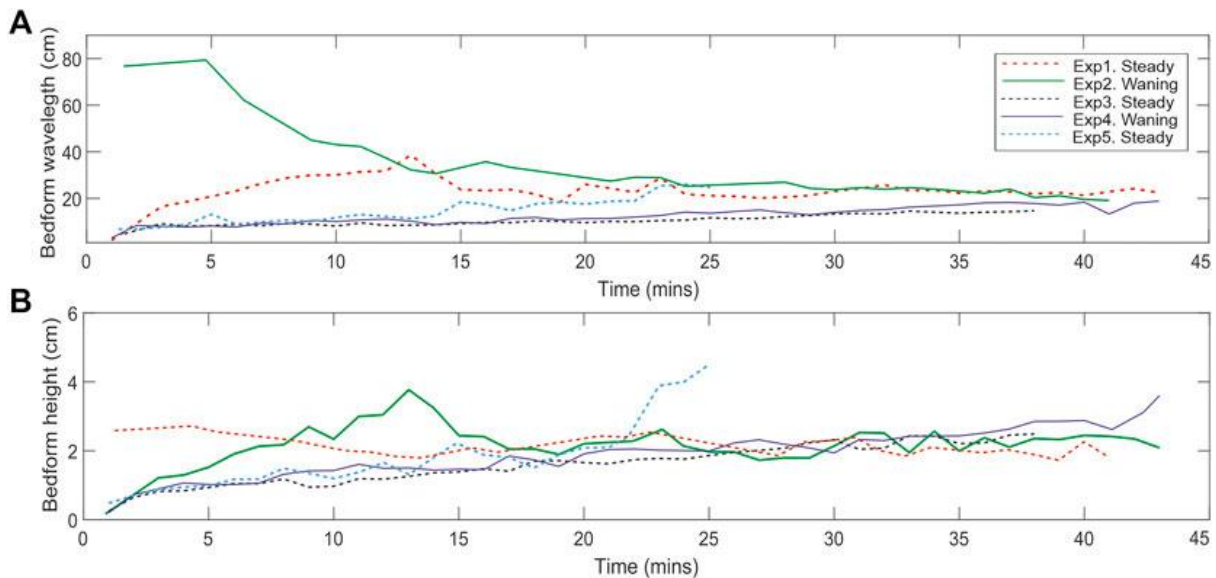


**Figure 3.9.** Average height and wavelength of bedforms measured every 30 seconds in a 2-metre-wide window located 4 - 6 m from the upstream end of channel. **(A)** Bedform wavelength. **(B)** Bedform height. Steady flow experiments depicted by dashed lines. Waning flow experiments depicted by solid lines.

Unlike the ripples in Figure 3.8a, Figure 3.8b shows the out-of-phase interaction of dune bedforms with the upper surface of the lower denser layer. Figure 3.6 shows that during Experiments 4 and 5, the ratio between bedform wavelength and the height of the lower layer of the current increases just above 1 with the onset of dune development at 30 – 32 minutes (Experiment 4) and 22 minutes (Experiment 5). Figure 3.6 also shows a simultaneous slight increase in drag with the onset of dune formation. This is evidence that dunes are beginning to obstruct the flow.

The calculated shear velocity values associated with dunes ( $0.043 - 0.05 \text{ ms}^{-1}$ ) were larger compared to ripples ( $0.03 - 0.037 \text{ ms}^{-1}$ ). Greater shear velocities lead to increased sediment transport associated with dunes compared to ripples. Therefore, it was observed that dune bedforms experienced stronger zones of flow separation from the bedform crest transporting more sediment downstream onto the following bedform. Figure 3.7 also shows that ripples and dunes have separate dimensional fields. Although the differences between these two fields is small, when this approach is considered in support of the bedform phase-relationship method, it can be concluded that there is a strong case both to identify and to distinguish the ripples and dunes developed in these experiments

Experiment 4 entailed a slowing discharge flow rate over a shallow  $0.7^\circ$  slope where subcritical conditions prevailed. It was expected that as the discharge flow rate slowed the bedforms would reduce in size. However, the bedforms in Experiment 4 gradually increased in size and grew steadily (Figure 3.9), forming an out-of-phase dune bedforms toward the end of the run despite the slowing current.

Interestingly, dunes also formed on the steeper  $3^\circ$  slope under supercritical conditions (Experiment 2, waning current), in this case superimposed upon the long wavelength antidunes that formed at the start of the experiment when the discharge flow rate was fastest. An example is shown in Figure 3.10, where the superimposed dunes are out-of-phase with the upper surface of the lower layer of the current, as highlighted by the dotted line.

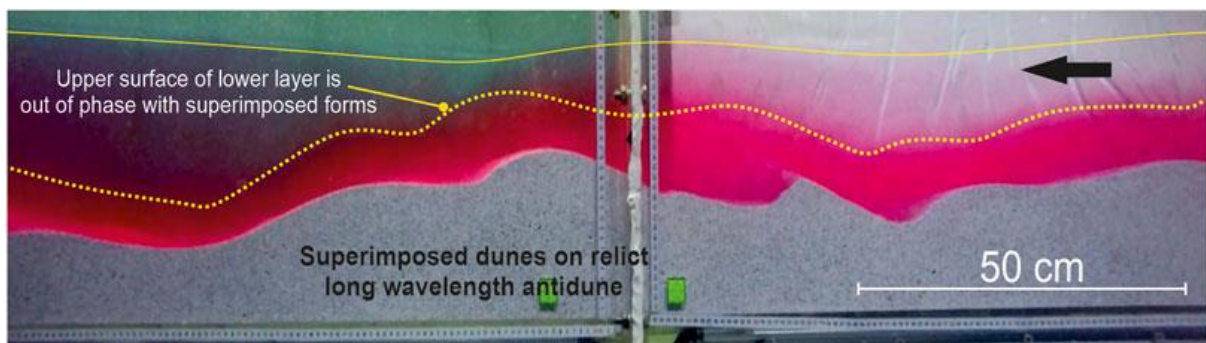


**Figure 3.10.** Superimposed dunes upon the relict remains of a long wavelength antidune (Experiment 2). The dotted line depicts the upper surface of the lower denser layer. The solid line depicts the approximate height of the current interface with the ambient fluid (based on Figure 3.4b). Flow is from right to left (arrow). The superimposed dunes interact with this upper surface in an out-of-phase manner. Mixing between the lower and upper layers of the flow can be observed; the upper layer has become light pink.

### 3.5.3.2 Supercritical bedforms

Under supercritical conditions, long wavelength antidunes and downstream migrating antidunes formed. Downstream migrating antidunes were formed only on the steeper  $3^\circ$  slopes in both Experiments 1 and 2 where supercritical flow prevailed. Downstream migrating antidunes are characterised by their clear in-phase relationship with the upper surface of the denser lower interval within the density current (Figure 3.11a). They were observed to form initially as small (1 – 2 cm high and 15 – 25 cm wavelength) symmetrical forms that migrated slowly downstream. As the bed reached equilibrium they developed into larger and sometimes asymmetric downstream migrating forms, reaching maximum heights of 3.5 cm and maximum wavelengths of 42 cm (Figure 3.7). They always remained in-phase with the lower denser interval surface. Under the steady flow conditions of Experiment 1, downstream migrating antidunes appeared to be the stable bedform.

In Experiment 2, under a slowing current, long wavelength antidunes formed at the start of the run when flow was faster, transitioning to downstream migrating antidunes as the flow decelerated.

Long wavelength antidunes formed only on the steeper 3 ° slope, under supercritical conditions, during Experiment 2. Under these fast-flowing conditions, higher shear velocities (c. 0.07 ms<sup>-1</sup>) and resulting high sediment transport rates, long wavelength antidunes were established rapidly across the bed. They reached wavelengths of up to 100 cm, heights of 7 cm and were in-phase with the upper surface of the lower layer of the current, as shown in Figure 3.11b. They had symmetrical sinuous morphologies, rounded crests and migrated very slowly upstream or were stationary. At the start of the run the long wavelength antidunes dominated the bed. As the discharge flow rate was slowed it encouraged the development of smaller downstream migrating antidunes that partially reworked the long wavelength antidune bedforms (Figure 3.11c).

Figure 3.6 shows that in both Experiments 1 and 2 the ratio between bedform wavelength and height of the lower layer of the flow have a ratio much larger than 1. As such the current will just follow a variably sloped bed rather than bedforms impeding the flow.

## **3.6 Discussion**

### ***3.6.1 Bedform development under steady flows***

Under steady flows, bedform development was gradual regardless of the current's criticality. This development or lag stage is interpreted as the bed gradually establishing equilibrium with the current (Sequeiros *et al.*, 2010). In Experiment 5, dune bedforms formed towards the end of the run. This took place via the gradual growth and coalescence of ripples that saw the gradual reduction in the number of smaller forms upon the bed (cf. Raudkivi and Witte, 1990). As previously stated, the length of Experiment 5 was shorter due to the faster discharge flow rate. However, it can be speculated that, had the run been longer, dunes would have established themselves across the entire bed, becoming the prevalent stable bedform. Eventually, bedforms became large enough to alter the hydrodynamic relationship between the bed and current due to increased turbulence associated with the onset of dune bedform development.

Under the steady supercritical flow conditions of Experiment 1, downstream migrating antidunes formed (as in Fedele *et al.* (2016)). Due to the faster velocities and higher degrees of turbulence associated with supercritical conditions, they developed and became established upon

the bed (within the first 5 minutes of the run) as the equilibrium bedform (Figure 3.6). These bedforms have been defined as downstream migrating antidunes, rather than dunes or washed-out dunes, because they are determined to have formed under different formative processes compared to dune bedforms formed under subcritical flows. Subcritical dunes form independently of the flow interface and will grow gradually, or via the coalescence of smaller ripple forms, until they become large enough to impart a greater level of turbulence throughout the flow (compared to ripples). If the flow is sufficiently shallow (as in these experiments), the dunes can force the upper surface of the lower denser layer of the flow into an out-of-phase relationship. By way of contrast, supercritical bedform development is entirely dependent on the flow interface: the bed establishes its form and behaviour due to the interaction of the surface waves that propagate at the flow interface under supercritical conditions with the bed (McLean, 1990; Fourrière *et al.*, 2010). The bed is influenced and shaped by the action of the surface waves upon the mobile substrate so that it is transformed to their shape. As a result, the resulting (antidune) bedforms are in-phase with the flow interface. The clear in-phase relationship of downstream migrating antidunes with the interface of the lower denser layer of the current can be seen in Figure 3.11a. Bedform dimensions in Experiment 1 remained relatively constant in both height and wavelength throughout the run (Figure 3.9).

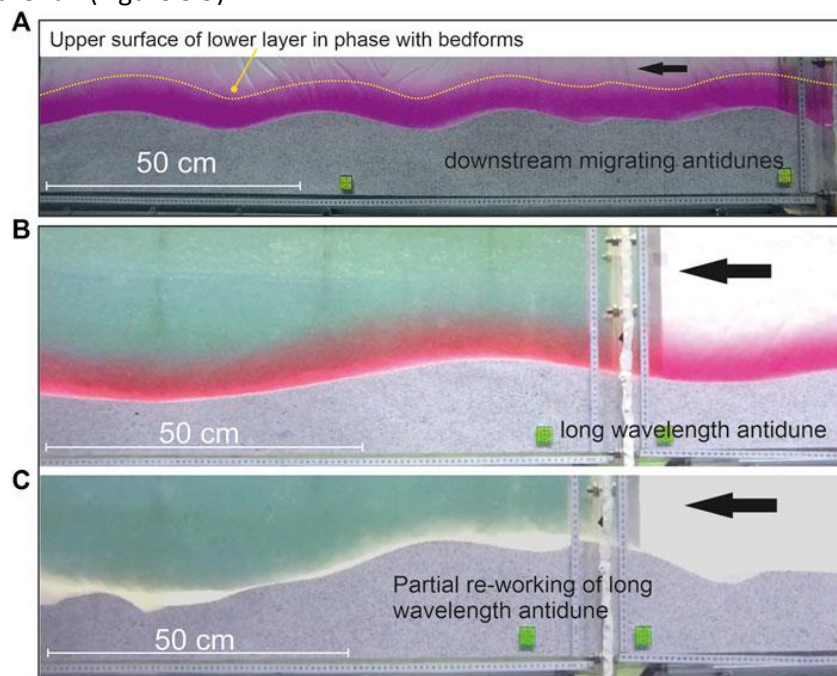


**Figure 3.11.** (A) Experiment 1. Example of the in-phase, downstream migrating antidunes formed under steady flow conditions. The yellow dotted line defines the upper surface of the lower denser layer of the current. (B) Experiment 2. Example of a long wavelength antidune. It is in-phase with the upper surface of the lower denser layer of the current (dyed pink). (C) Partial reworking of the long wavelength antidune. Flow is from right to left in all photos (arrows).

### ***3.6.2 Bedform development under waning flows: Maintenance of flow conditions in the lower layer of the density current***

Dunes formed during Experiment 4 in a similar manner to Experiment 5. Early-formed ripples gradually increased in height and wavelength by coalescence to finally form dunes toward the end of the experiment. An explanation is required to account for how bedform dimensions may have increased despite forming beneath a current set up to have a waning discharge flow rate. This may be because the waning of the flow is not sufficient to prevent the growth of bedform dimensions that occurs as the bed progressively establishes equilibrium with the flow (albeit in this case with a presumed equilibrium state that is itself progressively changing). Alternatively, data suggests that unlike the upper layer of the flow, the lower dense layer does not wane. This mechanism is discussed below.

Investigations into saline density current stratification have been carried out by Dorrell *et al.* (2019), who studied saline underflows in the Black Sea, and by Sequeiros *et al.* (2010) under experimental conditions. As is the case in the present experiments and in Fedele *et al.* (2016), the development of a dense basal layer is described, evident in vertical density profiles. An upward transition to less dense flow at or near the height of maximum flow velocity is also observed. Dorrell *et al.* (2019) attribute the development of a two-layered flow to the current's interaction with bedforms. Bedforms increase the turbulence through the water column. The resulting increased vertical fluid motion causes the development of boundary-induced internal gravity waves that create unstable flow conditions, resulting in the formation of an eddy transport barrier at the height of the velocity maximum that prohibits mixing between the upper and lower layers of the current. Dorrell *et al.* (2019) further explain that as a result, the current concentration and momentum are maintained within the lower layer. In the experiments described here, a similar density profile was developed during Experiment 4 (Figure 3.4d). It is notable that the density profile of the basal layer remained a constant thickness throughout the experiment (highlighted by red crosses, Figure 3.4d); the reduction in discharge flow rate appears to have been principally experienced in the upper region of the current as Figure 3.4d shows a progressive thinning of the upper layer of the flow as the current slowed. Figure 3.5c shows that velocity measured in the bottom denser layer of the flow does not respond to Experiment 4's reducing input flow rate. This maintenance of flow velocity in the lower layer of the current may have enabled and sustained dune formative conditions. Both Winterwerp *et al.* (1992) and Paull *et al.* (2018) explain that bedform development and dimensions may be controlled by properties of a near-bed dense layer within the density current. Although it is not observed within the timeframe of the present experiments, it is suggested that as the upper layer continues to wane it will completely diminish.

It is hypothesised that breaking of internal gravity waves at the interface between the upper and lower layers of the flow results in momentum absorption at the interface. This causes the interface to act as an energy sink that eventually causes the collapse of the upper layer of the flow.

While it is acknowledged that there are limitations in representing and scaling the stratification of natural sediment-laden density currents using experimental saline density currents, there are few other techniques to simulate bedform development in low density flows. The two-layered flow described here and by Dorrell *et al.* (2019) is thought applicable to sediment-laden density flows as the same formative mechanisms apply. Due to the effects of internal gravity waves within the current and anti-diffuse mixing within the lower layer, the stratification within the lower layer of a sediment laden density current is reduced. It is therefore suggested by Dorrell *et al.* (2019) that saline density flows might be a good proxy for low density turbidity currents. Further, Cartigny and Postma (2017) investigate how sediment concentration in the dense basal layer of turbidity currents might alter bedform development. Their phase diagrams depict the potential for subcritical bedform development in the form of ripples and dunes forming under low density turbidity currents. However, they also explain that high density currents will suppress turbulence in the lower region of the flow, preventing subcritical bedform development (Paull *et al.*, 2018), which is reliant on turbulent flow for their formation. Therefore, the results presented here may only relate to low density turbidity currents. Further, it is recognised that Luchi *et al.* (2018) have also postulated two-layer sediment gravity flows. However, these have only been established for statistically steady flows, which are unlikely to be realised in the real world due to the effects of bedform and current interaction, spatial changes and channel geometry, etc.

### ***3.6.3 Influence of pre-existing bed state***

Under supercritical waning flow conditions long wavelength antidunes were initially formed (Experiment 2; Figure 3.11b). As the discharge flow rate was reduced current conditions no longer supported their formation and the long wavelength antidunes began to be reworked and modified (Figure 3.11c). However, their large forms were not entirely reworked, leaving relict long wavelength antidunes as a dominant feature upon the bed. These relict forms created obstructions to the flow contributing to the continuously slowing current by locally producing increased vertical flow movement and turbulent stresses. This led to an increase in mixing between the upper layer and lower layer of the flow. This is evident in Figure 3.10 where the red dye used to colour the lower layer of the flow can be seen to have mixed with the more dilute upper layer of the flow. It is inferred that the combination of increased turbulence and reduced

current velocity associated with the presence of the relict bed forms meant that locally the flow met dune forming conditions allowing dunes to form, superimposed upon the relict antidunes.

In Experiment 2, partially reworked relict bedforms influenced local flow conditions so that subcritical dune forms were able to develop within a supercritical regime. Therefore, the presence of previously established bedforms should be considered when predicting the types of new bedforms that might develop under certain flow regimes. It follows that the relationship between bedform evolution and flow characteristics may be dependent on the flow history and is therefore non-unique (Osborne and Vincent, 1993; Austin *et al.*, 2007; Huntley and Coco, 2008; 2009; Martin and Jerolmack, 2013). For example, Coleman (1969), Allen (1973), Baas (1994) and Kostaschuk and Villard (1996) describe a delay in how bedforms respond to changes in flow conditions, resulting in bedform hierarchies that adjust differently depending on their size. Alternatively, change in flow conditions might occur faster than bedforms can adjust (Paarlberg *et al.*, 2010). Due to the variety of ways a bed might respond to pre-existing conditions, and the fact most experimental and modelling work focuses on bedform development starting from an initially flat bed (Huntley and Coco, 2009; Martin and Jerolmack, 2013), documentation of the nature of this dependence is incomplete. The present experiments resolve another way in which pre-existing bed morphology (relict long wavelength antidunes) can influence subsequent bedform development under density currents, as dune formative conditions were met when current conditions were locally altered in association with the relict forms.

The trajectory and rate of passage of individual flows through different bedform phase spaces are not considered in either open channel flow bedform phase diagrams, like that of van den Berg and Van Gelder (2009), or the new bedform phase diagram for density currents of Fedele *et al.* (2016). It is clear there are ramifications for the reliability of bedform phase diagrams to make accurate predictions of bedform development; the speed and direction at which currents pass through different bedform phase spaces should be considered.

Under dis-equilibrium conditions during a gradually waning flow, there are many ways in which a bed could conceivably evolve under a waning current. In the single example presented in Experiment 2, bedform evolution is influenced by the inability of the waning current to fully rework the initial large antidune bedforms which, as previously described, led to the development of subcritical dunes under prevailing supercritical conditions.

Figure 3.12 depicts a simple conceptual representation of a phase diagram that considers time as well as flow conditions and grain-size. While Experiment 2 by itself does not provide total understanding of bedform evolution under waning currents, it does highlight the added

complexities involved in bedform prediction under waning flows. Further research is needed not only into how bedforms evolve under waning currents, but also into how the rate of current waning impacts bedform development.

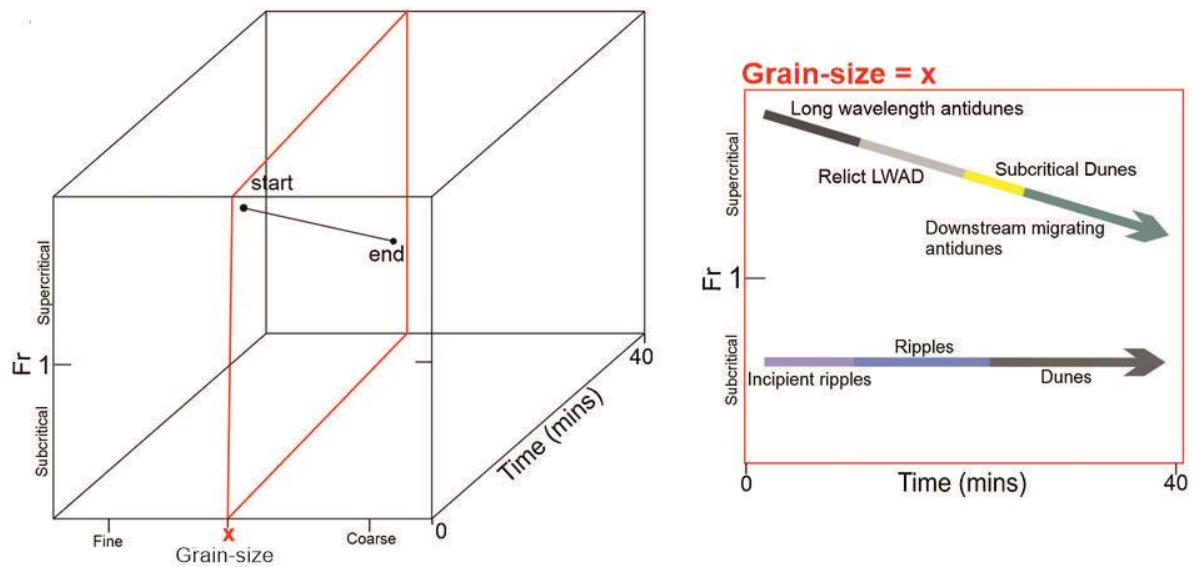


**Figure 3.12.** Conceptual phase diagram with a third axis for time, depicting how a bed under steady conditions might evolve (based on Experiment 5), compared to bedforms under a waning current (based on Experiment 2).

### 3.6.4 Phase diagram analysis of new data

Bedforms that developed under steady flows, plus long wavelength antidunes (which formed at the start of Experiment 2 as the stable bedform) are plotted onto and compared with existing phase diagrams including van den Berg and Van Gelders’ (2009) phase diagram for open channel flow and the newly developed bedform phase diagram for density currents of Fedele *et al.* (2016).

#### 3.6.4.1 Phase diagram for steady open channel flow

Results from the present experiments are plotted onto van den Berg and Van Gelder’s (2009) adaptation of van Rijn’s (1984) dimensionless phase diagram (Figure 3.13a) which plots the Particle Parameter ( $D^*$ ; Equation 3.4 (Bonafille, 1963) against the mobility parameter ( $\theta'$ ; Equation 3.5 (van Rijn, 1984)). van Rijn’s (1984) phase diagram, or variations of it, are widely used to gauge bedform regime boundaries; further, the use of these dimensionless variables allows comparison between experimental data collected under different experimental parameters.

$$D^* = D_{50} \left[ \frac{(\rho_s - 1) g d_{50}}{v^2} \right]^{1/3}, \quad (\text{Eq. 3.4})$$

Where  $\nu$  is the kinematic viscosity ( $\text{m s}^{-2}$ ).

$$\theta' = \frac{\rho U^2}{(\rho_s - \rho)(C')^2 d_{50}}, \quad (\text{Eq. 3.5})$$

Where,  $\theta'$  is the grain mobility parameter,  $\rho_s$  is the density of the bed sediment ( $1500 \text{ kg m}^{-3}$ ),  $C'$  is the Chézy coefficient and  $d_{50}$  is the mean grain-size (m).

Figure 3.13a shows that the van den Berg and Van Gelder's (2009) phase diagram is only partially accurate in predicting the bedforms made by the experimental density currents. While the subcritical bedforms (ripples and dunes) do develop close to, or in the same defined stability fields, the supercritical bedforms (downstream migrating antidunes and long wavelength antidunes) developed beneath supercritical density flows fall where the phase diagram predicts transitional bedforms between dunes and upper stage plane bed should occur. Also, the new data shows that both supercritical and subcritical bedforms exist within much tighter regions on the open channel phase diagram compared to the phase spaces relating to open channel flow bedforms.

Similarly, when plotted on the bedform phase diagram for density currents proposed by Fedele *et al.* (2016) the new data shows that the subcritical ripple bedforms plot in close proximity to supercritical bedforms, whereas in open channel flows subcritical bedforms are significantly separated from supercritical bedforms. Both results from the present experiments and that of Fedele *et al.* (2016) indicate that supercritical conditions in density currents are achieved at much slower velocities compared to open channel flows. This is due to the effects of reduced gravity (Fedele *et al.*, 2016). The apparent narrowness of the density current subcritical bedform stability field could in part explain the rarity of dune cross-stratification in turbidites.

#### 3.6.4.2 Phase diagram for steady density currents

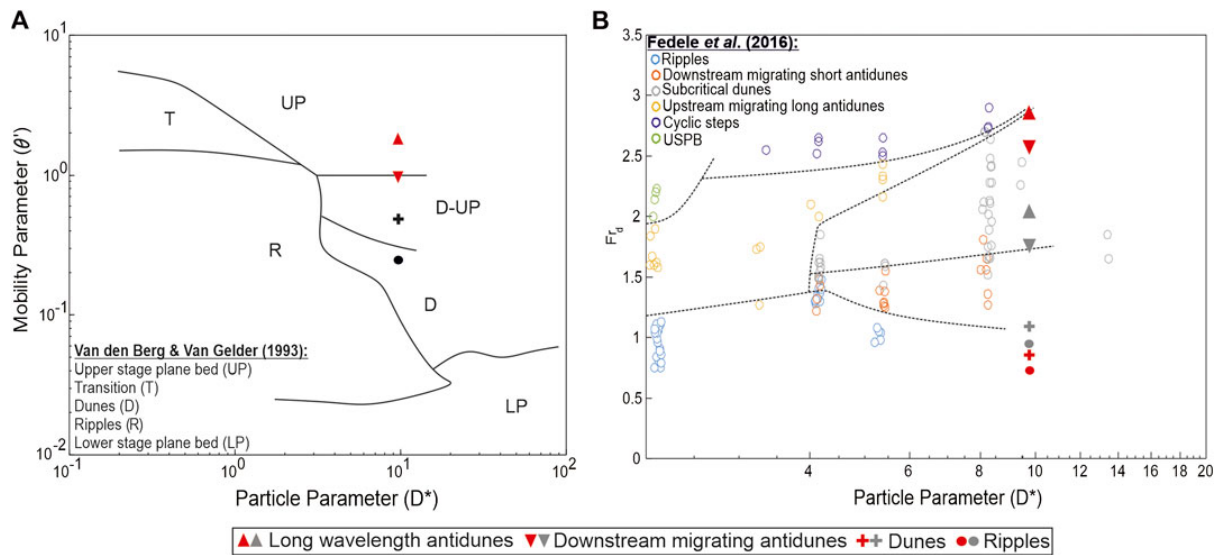
Fedele *et al.* (2016) produced a new bedform phase diagram for bedforms formed by density currents. Figure 3.13b compares the data collected in this study to a modified version of Fedele's *et al.* (2016) phase diagram, for which the Particle Parameter has been calculated (Equation 3.4). Points in red plot  $Fr_d$  numbers associated with different types of bedforms calculated for the lower layer of the flow. However, in order to better compare the present experimental data with Fedele *et al.* (2016) who calculated  $Fr_d$  for the entire current, the grey points in Figure 3.13b plot the same bedforms with estimated  $Fr_d$  numbers based on the entire height of the current.

Figure 3.13b shows that  $Fr_d$  numbers based on the entire height of the current plot associated subcritical and supercritical bedform phase spaces in much closer proximity, compared

to  $Fr_d$  numbers based on the height of the lower layer of the current (red markers). Fedele *et al.* (2016) plot dune bedforms as supercritical when  $Fr_d$  is calculated for the entire height of the current. This is a notable aspect of Fedele's *et al.* (2016) bedform phase diagram as ripples and dunes extend into supercritical region of the phase diagram. Ripples and dunes are generally considered to be subcritical forms that are not stable under supercritical conditions as the flowrates are far too fast (Harms and Fahnestok, 1965; Ashley, 1990; Sun and Parker, 2005; Colombini and Stocchino, 2011; Tilston *et al.*, 2015). However, Fedele *et al.* (2016) explain that their experimental density currents achieved supercritical conditions at much lower flow velocities compared to open channel flows and the resulting lower shear stresses and sediment transport rates enabled ripple and dune development under supercritical conditions. Yet, as outlined previously, calculating bulk Froude numbers in stratified flows is known to be problematic (Baines, 1998; Thorpe, 2010; Thorpe and Li, 2014; Waltham, 2004; Huang *et al.*, 2009; Dorrell *et al.*, 2014; 2016) as there is potential for a range of critical Froude numbers to be associated with different heights of the stratified flow (Dorrell *et al.*, 2016; Cartigny *et al.*, 2013). This suggests that making distinctions between the boundaries that separate different flow regimes using the bulk Froude number may be an inaccurate approach. Assignment of bedforms to a particular flow regime, especially if it lies near the boundary between two different regimes (as in Fedele *et al.*, 2016), might lead to misrepresentation of the hydrodynamic conditions that generated them.

It is suggested that it is more accurate to associate bedforms with bulk Froude number calculations for the less stratified lower layer of the flow in which all bedform development took place in both the present experiments and in the experiments carried out by Fedele *et al.* (2016). Results from the present experiments that calculate  $Fr_d$  for the lower layer of the current (Figure 3.13b, red markers) plot both dunes and ripples within the subcritical region of the phase diagram.

Figure 3.13b shows that subcritical dunes and downstream migrating antidunes are also discontinuous in Froude number, allowing some refinement of the phase space associated with subcritical bedforms. Figure 3.13b also allows further refinement of the long wavelength antidunes phase space. Long wavelength antidunes were the stable bedform at the start of Experiment 2, results (based on the  $Fr_d$  calculation of the lower layer) suggest that the long wavelength antidune phase space should reflect their potential development in larger grain-sizes than depicted by Fedele *et al.* (2016).



**Figure 3.13.** Bedforms developed during the present experiments are plotted onto bedform phase diagrams for open-channel and density driven flows. **(A)** van den Berg and Van Gelder's (2009) dimensionless phase diagram. **(B)** A modified version of Fedele's et al. (2016) new bedform phase diagram for density currents: Particle parameters ( $D_*$ ) were calculated and re-plotted against  $Fr_d$ . The red markers signify bedforms and associated  $Fr_d$  numbers calculated for the lower layer of the current. Grey markers signify the same bedforms and associated  $Fr_d$  numbers calculated for the entire current.

### 3.7 Conclusions

This chapter reports on a series of experiments investigating the controls on bedform development and maintenance under both steady and waning saline density currents.

This work shows that:

1. Bedforms developed within a lower denser layer of density currents, whose dynamics dictated the bedform type.
2. Distinctions can be made between subcritical bedforms (ripples and dunes) and supercritical bedforms (downstream migrating antidunes and long wavelength antidunes), via an effective bedform classification method based on the phase relationship of bedforms with the upper surface of the lower layer of the current.
3. It is critical to adopt an appropriate Froude number calculation method for stratified flow in order to establish a reliable quantitative link between the flow regime and the type of bedform development.

4. It is evident that the reduced gravity experienced by the saline density currents enabled supercritical conditions to be achieved at slower flow rates than is the case for open channel flow.
5. Pre-existing bed states may exert a first-order influence on subsequent bedform development regardless of the nominal flow regime. It is proposed that this effect, which is not captured by current phase diagram designs, is recognised as a new control on bedform development.

## **Chapter 4. Bedform development and morphodynamics of beds of varying bimodal grain-size distributions**

### **4.1 Introduction**

The motivation of this research is to study the effects of different non-uniform sediment mixtures made up of differently distributed sand-sized grains on bedform development. As is detailed in the Literature Review, the previous work done into non-uniform and non-cohesive sediment recognises how non-uniform sediment alters the mobility of the bed. This research includes the development of sediment transport models based on gravel and sand sediment mixtures that account for the 'hiding factor' (Einstein, 1950; Egiazaroff, 1965; Ashida and Michiue, 1973; Wilberg and Smith, 1987; Wilcock, 1993; McCarron *et al.*, 2019). Work by Wilcock and McArdeil (1993), Lanzoni and Tubino (1999), Blom *et al.* (2003), Blom (2008), Kleinhans *et al.* (2014), Vendetti *et al.* (2017), amongst others, focusses on the stabilisation of the bed by coarse armour layers upon the bed, or bedform development in gravel and sand mixtures. By comparison, less is known about the impact of fine sediment in non-uniform sediment mixtures. Research by van Ledden *et al.* (2004), Bartzke *et al.* (2013) and Staudt *et al.* (2017) investigates how fine sediment increases bed stability. The reduced mobility of a bed must impact bedform development. It is, therefore, the purpose of the present research to further investigate exactly how the fine fraction of non-uniform sediment mixtures of wide and narrow grain-size distributions impact bedform development, dimensions and kinematics.

Chapter 5 describes cross-stratified beds made of non-uniform sands found in the Peira Cava turbidite basin in South East France. These cross-stratified beds are characterised by a range of grain-size distributions, some are made up of unimodally distributed grain-sizes, and others (some of the most identifiable examples of cross-stratification in Peira Cava) are formed from distinctly wide grain-size distributions. To test the impact of different grain-size distributions on bedform development under density currents requires long lasting density current flow durations that cannot be achieved in the laboratory. However, it was established in Chapter 3, that bedform development was confined to the bottom denser layer of the density current and that bedform generation and dynamics are controlled by the flow conditions within this bottom layer. Conditions within this layer can be approximated by shear flows created in a recirculating flume

for open channel flow. Therefore, a series of experiments were carried out upon two sediment beds of unimodally distributed grain-sizes for fine and coarse sediment, and two non-uniform beds of bimodally distributed sediment for a narrow grain-size distribution and a wide grain-size distribution. For each experiment, flow rate, slope and experimental run time were kept constant. The experimental results are extrapolated to help determine the sedimentary processes responsible for influencing bedform development and the associated cross-stratified beds in Peira Cava.

This chapter is organised as follows. Firstly, the experimental set up, parameters and methodologies are described, including the data processing techniques applied the flow velocity and bedform dimensional datasets. The experimental results that follow, contain a summary of each experiment and the types of bedforms that were formed throughout each run. The Discussion section analyses whether the different experimental beds achieved equilibrium with the flow and assess the predictive capabilities of an existing bedform phase diagram that characterises the bed using the median grain-size. Finally, a discussion is presented on the extent different grain-size distributions impact sediment mobility and therefore bedform development throughout each experiment.

## **4.2 Methodology**

### ***4.2.1 Experimental set up***

Four experiments were conducted in the Armfield recirculating flume in the Sorby laboratory at the University of Leeds. Figure 4.1 shows the experimental set up. The flume is 8.5 m long, 0.3 m wide and 0.3 m deep. A pipe rack was situated at the upstream end of the flume to dissipate the momentum inherited from the pipe flow and to distribute the flow evenly across the width of the flume and remove turbulence generated during flow along the return pipe. Four different mobile substrates made up of different grain-size distributions were laid within the flume. The sediment was supplied by Guyson Ltd., and the material used is known as ‘Guyblast’ or ‘US type 2 plastic media’. It comprises plastic particles with a specific gravity of 1.50. The grains are described as ‘jagged/angular’ in shape on the company website. For Experiments 3 and 4, two types of the plastic media were mixed to create sediment mixtures of different grain-size distributions. Experiment 3 used  $D_{50} = 500 \mu\text{m}$  and  $D_{50} = 937 \mu\text{m}$  sized sediment. Experiment 4 used  $D_{50} = 937 \mu\text{m}$  and  $D_{50} = 743 \mu\text{m}$  sized sediment (Figure 4.2). The finer sediment made up 40 – 45 % and the coarser sediment made up 55 – 60 % of each mixture. The different size fractions of particles were mixed using a cement mixer to ensure the even distribution of all sediment grain-

sizes throughout the sediment mixture. The prepared sediment mixtures were then laid across the flume to height of 10cm above the flume floor, with the upper surface levelled before the start of each run. The flume was filled with water to a depth of 15 cm above the bed; this was done slowly to not disturb the evenly laid substrate. Each experiment ran for 48 hours to ensure equilibrium conditions between the bed and the flow were reached.

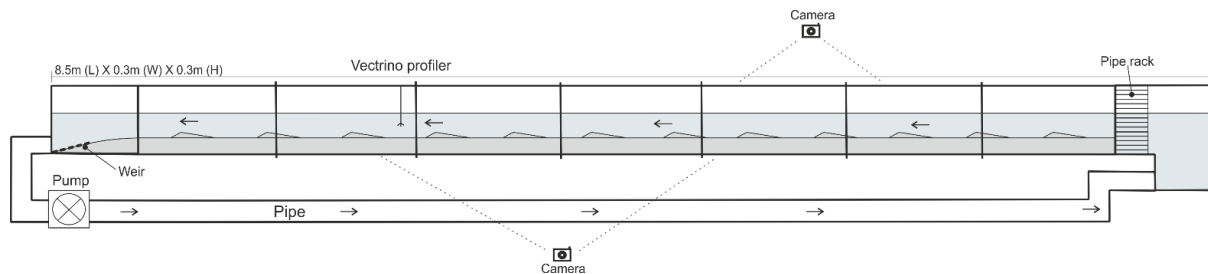


**Figure 4.1.** Experimental set up.

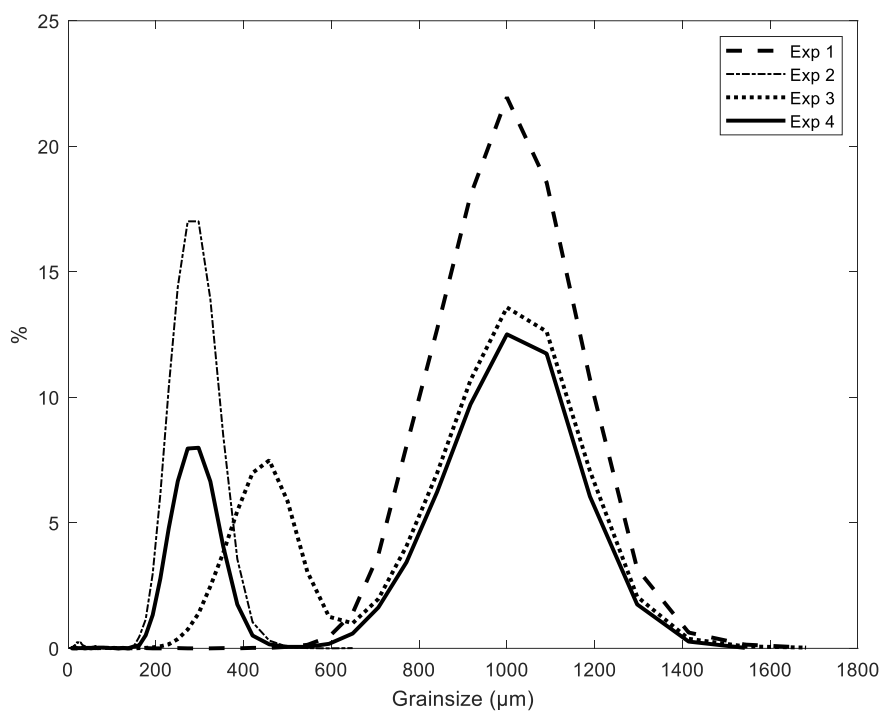


**Figure 4.2.** Grain-size distribution at the start of each experiment. Measurement of particle size distribution was carried out using a Malvern 2000e particle sizer.

A Nortek Velocimeter vectrino profiler was used to record downstream, cross-stream and vertical velocity components of the flow. The vectrino probe was orientated so that the principal measurement axes were aligned with the downstream (x), cross-stream (y), and vertical (z) directions of the flume then fixed in place so the three-dimensional components of the flow (x, y, z) were recorded consistently. The vectrino was positioned 5.6 m from the upstream end of the

flume so that it did not interfere with bedform development in the middle of the flume but was far enough away from the downstream end to minimise the influence of backwater effects. To collect bedform dimensional data, a camera with wide angle lens was set up with a view through the glass walls of the flume spanning 4 m. The camera had a view of the middle section of the flume where any backwater effects from the flume's inlet and outlet would have the least impact on bedform development. The cameras took photos every 60 seconds to record bedform dimensions, evolution and migration rates. Note: for Experiment 1, a camera malfunction prevented collection of data between 17-22 hours during the experiment; due to lab scheduling constraints it was not possible to re-run this experiment.

At the end of each experiment the flume was left to drain at a slow rate overnight so as not to disturb the bed. In the morning cores of the damp bed were taken from seven different points along the flume, which included multiple bedform troughs, crests and stoss sides. Cores were taken using individual 1-inch (25.4 mm) diameter and 15 cm long syringe tubes with the nozzle heads cut off. With the syringe plunger fully extended, the syringe was pressed down into the bed vertically until the syringe reached the base of the flume. Slowly, the syringe was extracted from the bed leaving the core of the bed within the syringe. While the core samples were still damp enough to maintain the bed structure, each core was cut into thin slices (0.5 – 1 cm thick; samples were taken more densely within the top 5 cm of the bed) and placed into individual sample pots. This was done by slowly pushing the syringe plunger forwards 0.5 – 1 cm at a time so that the core was pushed out of the syringe a little at a time. With the core maintaining its internal structure, it could be accurately sliced off using a scalpel into the sample pot. The final 2 – 3 mm of sediment left in the core (i.e. the very top of the bed) were discarded to exclude any fine grains that had settled out from the water onto the bed while it drained. The sediment samples taken from different levels of the bed were dried in an oven. Once dry, the grain-size distribution of each sample was analysed using a Malvern 2000e Particle Sizer.

### **4.3 Experimental parameters and data processing**

Four experiments were carried out in which the flow rate, slope and experimental run times were kept constant. Only the grain-size distribution of the substrate was varied between experiments. Table 4.1 summarizes the experimental parameters for each run. The methodologies for calculating flow and sediment parameters, including the Froude number and shear velocities, are described below. Calculations used in determining the critical parameters for sediment motion described below include, the dimensionless grain-size and Shields parameter models for both

unimodal and bimodal sediment mixtures. Tables 4.2 – 4.4 within the results section, detail the results for sediment parameters.

### 4.3.1 Froude number

The Froude number ( $Fr$ ) (Equation 4.1) is used to determine whether a current's regime is subcritical or supercritical.  $Fr$  is calculated by measuring the celerity of a surface wave in relation to the velocity of the current. Subcritical flows have a Froude number,  $Fr < 1$ , whereas supercritical flow have  $Fr > 1$  and critical flows have a  $Fr = 1$  (Baines, 1998). Under subcritical conditions, surface waves can move both upstream and downstream as surface wave celerity is slower than the flow rate. In supercritical flow, surface waves can only move downstream as surface wave celerity is faster than the flow rate. Commonly, the Froude number is used to predict the type of bedforms that are likely to develop in association with a particular flow regime, therefore subcritical flow conditions were set for each experiment to ensure the formation of subcritical bedforms such as ripples and dunes.

$$Fr = \frac{U}{\sqrt{gH}}, \quad (\text{Eq. 4.1})$$

where  $U$  is the depth-average velocity,  $g$  is acceleration due to gravity and  $H$  is the flow depth.

**Table 4.1.** *Experimental Parameters. The experiments were run either with a unimodal sediment size distribution in the substrate (Experiments 1 and 2), or with a bimodal distribution, formed by mixing different end-member sediment types (Experiments 3 and 4).*

<b>Experiment run time (hours)</b>	48			
<b>Slope (degrees)</b>	0.13			
<b>Flow depth (m)</b>	0.15			
<b>Depth averaged flow velocity (U) (m/s)</b>	0.27			
<b>Current criticality (Fr)</b>	0.22			
<b>Experiment</b>	1	2	3	4
<b>Time averaged shear velocity <math>u^*</math> (<math>ms^{-1}</math>)</b>	0.07	0.055	0.06	0.04
<b>Time averaged drag coefficient (Cd)</b>	0.095	0.031	0.042	0.029
<b><math>D_{50}</math> grain-size population 1 (<math>\mu m</math>)</b>	937	265	500	265
<b><math>D_{50}</math> grain-size population 2 (<math>\mu m</math>)</b>	-	-	937	937
<b>Median grain-size for populations 1&amp;2 (<math>\mu m</math>)</b>	937	265	809	743
<b>Grain-size distribution ratio <math>D_{50}</math> Coarse / <math>D_{50}</math> Fine</b>	-	-	1.87	3.15
<b>Dry weight (%) population 1</b>	100	100	42	45
<b>Dry weight (%) population 2</b>	-	-	58	55

### 4.3.2 Shear velocity

The shear velocity,  $u^*$  is a formulation of the shear stress in units of velocity. It may be estimated from the gradient of the velocity profile (Petrie and Diplas, 2015). Here, the velocity data were first filtered (data >2 standard deviations from a moving mean were not analysed) to remove any noise and outliers. It was assumed the flow in the region close to the bed (within 2 cm from the bed) followed a standard logarithmic profile above the near-bed viscous sublayer and below the outer layer (Petrie and Diplas, 2015), where velocity at a height  $z$  above the bed:

$$u = \frac{u^*}{K} \log\left(\frac{z}{z_0}\right), \quad (\text{Eq. 4.2})$$

where  $u$  is the velocity of the current,  $K$  is the von Kármán constant (taken as 0.41),  $z$  is the height above the bed and  $z_0$  is the height above the bed where flow velocity is zero. The measured velocity data included the log-law region and in the highest part of the velocity profile the lower part of the outer layer, which deviates from the logarithmic law of the wall. A set of values for the shear velocity was computed by progressively removing velocity data furthest away from bed and for each iteration calculating the line of best fit and coefficient of determination,  $r^2$ , to the log profile (Equation 4.2). The final estimation for shear velocity was taken as the value corresponding to the line of best fit with the highest value of the coefficient of determination to the log-law (Figure 4.3).

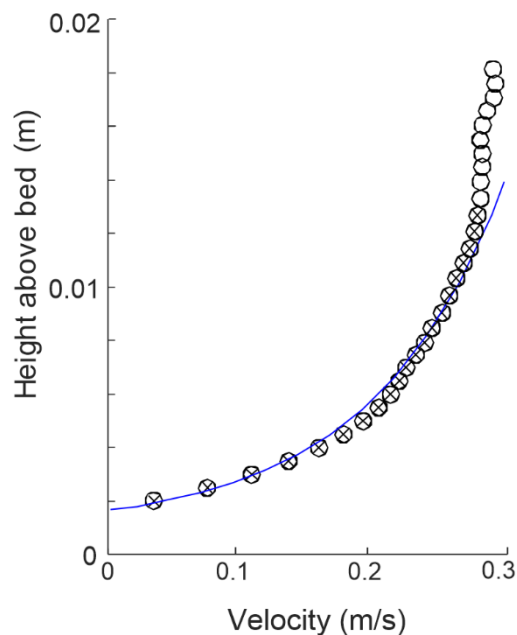


**Figure 4.3.** The blue curve follows the standard logarithmic profile away from the bed based on the logarithmic law of the wall. The curve of circles is a measured velocity profile. The data

excluded from shear velocity calculations are identified by the open circle datapoints. The final estimation for shear velocity was taken as the value corresponding to the line of best fit with the highest value of the coefficient of determination to the log-law.

Shear velocity calculations were taken approximately every 2 hours throughout each experiment to average over the influence of bedforms on the local flow field, 2 - 3 shear velocity measurements were calculated at a time to estimate the average shear velocity values for the whole run (Table 4.1).

### 4.3.3 Drag coefficient

The drag coefficient ( $Cd$ ) associated with bedform development throughout each run, was estimated (Equation 4.3) and time averaged for the duration of each experiment (Table 4.1).

$$Cd u^2 = u^{*2}. \quad (\text{Eq. 4.3})$$

### 4.3.4 Calculation of sediment parameters

Based on the data analysis methods of Staudt *et al.* (2017), the following calculations were used to determine the sediment parameters using different approaches for sediment that is unimodal and for non-uniform sediment mixtures. A flow's competence is its ability to mobilize sediment of a specific size. This is commonly quantified by the Shields parameter.

Soulsby (1997) and Soulsby and Whitehouse (1997), derived an algebraic expression that relates the critical Shields number ( $\theta_{cr}$ ) to the dimensionless grain-size ( $D_*$ ) in order to calculate the threshold of sediment motion (Equations 4.4 & 4.5).

$$\theta_{cr} = \frac{0.24}{D_*} + 0.055 (1 - e^{-0.020 D_*}) \text{ for } D_* > 5, \quad (\text{Eq. 4.4})$$

$$\theta_{cr} = \frac{0.3}{1+1.2 D_*} + 0.055 (1 - e^{-0.020 D_*}) \text{ for } D_* \leq 5, \quad (\text{Eq. 4.5})$$

where

$$D_* = \left[ \frac{g(\rho_s/\rho-1)}{v^2} \right]^{\frac{1}{3}} d_{50} \quad (\text{Eq. 4.6})$$

$v^2$  is the kinematic viscosity of water ( $0.89 \times 10^{-6} \text{ m}^2 \text{ s}^{-1}$ ),  $\rho$  is the density of the fluid ( $\text{kg m}^{-3}$ ) and  $d_{50}$  (m) is the median grain-size of sediment. Equations 4.4 and 4.5 are used for sediment characterised by different  $D_*$  values, as Equation 4.5 overestimates the threshold of motion for very fine sediment (Yang *et al.*, 2019). Equations 4.5 – 4.6 were used to calculate critical shear stress for sediment motion for each substrate in Experiments 1 – 4 based on the median grain-

size for each substrate (Table 4.1) and for the individual grain-size fractions used in the mixed substrates of Experiments 3 and 4 (Table 4.2).

The dimensional shear stresses calculated from velocity data collected throughout each run (shown in Table 4.1) exceed the critical shear stress needed for sediment motion (estimated using the Soulsby and Whitehouse (1997) algebraic expression) for both unimodal and mixed sediment.

### 4.3.5 Analysis of bedform dimensions

Photos were taken throughout each experiment to capture bedform dimensions and how they evolved. Bedform dimensions were measured using digital photos extracted at successive 10-minute intervals. Each bedform that could be seen in its entirety in the camera's field of view in the middle four metres of the flume was measured. In each experiment, superimposed bedforms rarely developed and when they did form, they were very small wavelets. As such, they were excluded from the analysis of bedform dimensions.

The images were edited to remove the barrel lens distortion (using Adobe Photoshop software) that could affect. In order to characterise bedforms, Image J software was used to obtain horizontal (x) and vertical (y) coordinates from five positions corresponding to the: i) upstream trough, ii) crest and iii) downstream trough, iv) midpoint of the stoss slope and v) midpoint of the lee slope (Figure 4.4) (cf. de Cala *et al.*, 2020, also in Chapter 3). Bedform wavelength ( $L$ ) was calculated as the distance between upstream and downstream troughs (Equation 4.7). Bedform height ( $h$ ) was recorded as the height difference between the downstream trough and the corresponding crest (Equation 4.8). Bedform steepness was approximated by calculating the bedform's aspect ratio ( $AR$ ) (Equation 4.9).

$$L = x_5 - x_1, \quad (\text{Eq. 4.7})$$

$$h = y_3 - y_1, \quad (\text{Eq. 4.8})$$

$$AR = h/L. \quad (\text{Eq. 4.9})$$



**Figure 4.4.** de Cala *et al.* (2020): Schematic diagram of asymmetric bedforms of different dimensions, indicating the points where each x, y coordinate was taken.

### 4.3.6 Bedform migration rate

Using the photos taken throughout each experiment bedform migration rates were computed by evaluating how long a bedform took to migrate 0.5 m downstream. This approach

was adopted as bedform morphology changed as they migrated, as did the migration rate. Had the distance been longer, bedform morphology was more likely to change entirely so that the new bedform bore no relation to the original bedform from which measurements were taken. As such, the time it took bedforms to migrate 0.5 m meant that bedform morphology remained relatively constant and therefore represented a good “average” of that particular bedform’s migration rate. At 15 minutes time intervals bedform dimensions were measured for those bedforms whose entire length was visible and downstream trough was not within 0.5 m of the downstream edge of the camera’s field of view. Each bedform was then tracked as it migrated along the bed, until it had migrated 0.5 m downstream, where its dimensions were measured again as well as the time it had taken to migrate 0.5 m. The migration rate was calculated using the distance migrated and the time it took to migrate 0.5 m ( $distance(m)/time(secs)$ ).

#### 4.3.7 Analysis of core sediment samples

The dry sediment samples were used to calculate the grain-size distribution of the sediment at each level of the bed. With multiple cores taken from bedform troughs, crests and stoss sides from the individual cores were often different lengths, as trough samples are associated with smaller bed thicknesses compared to the crest or stoss sides. To ensure the results were representative of the grain-size distribution of the entire bed thickness the results were averaged across all the samples taken at equivalent bed levels.

## 4.4 Results

### 4.4.1 Shields Parameter and sediment mobility

Tables 4.2 – 4.3 show the results calculated for the critical parameters for sediment mobility. Table 4.2 details the results for each experiment characterised by the median grain-size of the bed. The dimensional average bed shear velocity calculated for each experiment ( $u^*$ ) exceed the critical shear velocities ( $u^* cr$ ) required to initiate sediment motion (estimated from the Soulsby and Whitehouse (1997) algebraic expression of  $cr$  ).

**Table 4.2.** Critical parameters for median grain-size for all grains.

<i>Exp</i>	<b>Fine fraction</b>	<b>Coarse fraction</b>	<b>d50 Dm (um)</b>	<b><math>u^* cr</math></b>	<b><math>u^*(ms^{-1})</math></b>	<b>Grain Re*</b>	<b><math>D_*</math></b>
1	-	-	937	0.012	0.7	73.7	17.2
2	-	-	265	0.007	0.55	16.3	4.8
3	42%	58%	809	0.011	0.06	54.5	14.8
4	45%	55%	743	0.010	0.04	33.4	13.6

For the experiment using bimodal sediment mixtures (Experiments 3 and 4), Table 4.3 shows the results calculated using the median grain-size of the individual grain-size fractions (i.e. those mixed to make the bulk sediment composition). '*i*' is used to denote the parameters relating to individual grain-size fractions. Table 4.3 shows that the dimensional average bed shear velocity ( $u^*$ ) calculated for each experiment also exceeds the critical shear velocity ( $u^*_{cr\ i}$ ) required to initiate sediment motion (estimated from Soulsby and Whitehouse (1997) algebraic expression of  $\theta_{cr}$ ).

**Table 4.3.** Critical parameters for bimodal sediment fractions (*Di*).

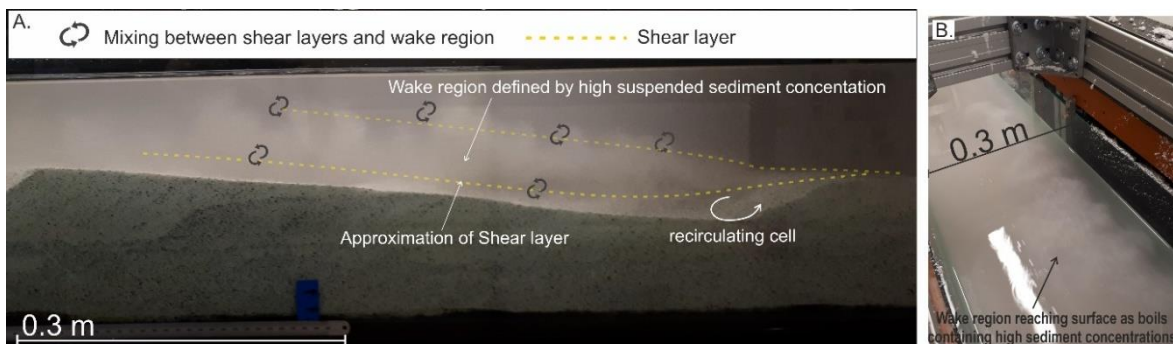
<i>Exp</i>	$d_{50\ D\ i}$ (um)	$u^*_{cr\ i}$	$u^*$ ( $ms^{-1}$ )	Grain $Re^*_{i}$	$D_*\ i$
3	500	0.01	0.06	33.7	9.2
3	937	0.012	0.06	63.2	17.2
4	265	0.007	0.04	12	5.5
4	937	0.012	0.04	42	17.2

#### 4.4.2 Observed bedform types

The bedforms developed throughout Experiments 1 – 4 are distinguished by the same criteria as defined in Chapter 3. Dunes and ripples are geometrically similar, so distinguishing between them is commonly based on two approaches: i) dunes and ripples may be distinguished by associated flow characteristics and bedform interaction with the flow (Bridge and Best, 1988; Bennet and Best, 1995, 1996); ii) alternatively, they may be defined according to their dimensions (Guy *et al.*, 1961; Raudkivi, 2006; Ashley, 1990; Colombini and Stocchino, 2011). It was apparent in the research carried out in Chapter 3, which is a combination of these methods works best to define bedforms that form under experimental conditions. This is because the comparatively shallow flow depths of the experimental flows (Chapter 3 and this chapter), compared to real world flows means that dune bedforms cannot usually grow to dimensions that greatly and obviously exceed those of ripple bedforms. However, shallow experimental flows do allow the potential to observe the interaction of the bedform with the flow's surface. As described in Chapter 3, dunes and ripples will interact with a current to cause flow separation at the crest. As dunes are larger, the flow separation at the crest is greater, as is the associated turbulent wake region and shear layer, which is generated from the crest and extends downstream (Venditti, 2013). This causes dunes to generate larger scale turbulence that arise from the shear layer as Kelvin Helmholtz instabilities (Baas, 1994; Bennett & Best, 1996; Schindler and Robert, 2005; Leeder, 2011; Venditti, 2013). These turbulent structures rise up through the flow as 'ejection

events', which if strong enough can interact with the flow's surface, a phenomena known as 'boils' (Yalin, 1992; Bennet and Best, 1995, 1996; Best, 1993, 2005; Fernandez *et al.*, 2006). Due to the smaller ripple separation zone and associated shear layer, they are restricted to the near- bed region (30 – 40 % of the water column) and therefore do not interact with the flow's surface (Baas, 1994; Bennett & Best, 1996; Schindler and Robert, 2005; Leeder, 2011; Venditti, 2013).

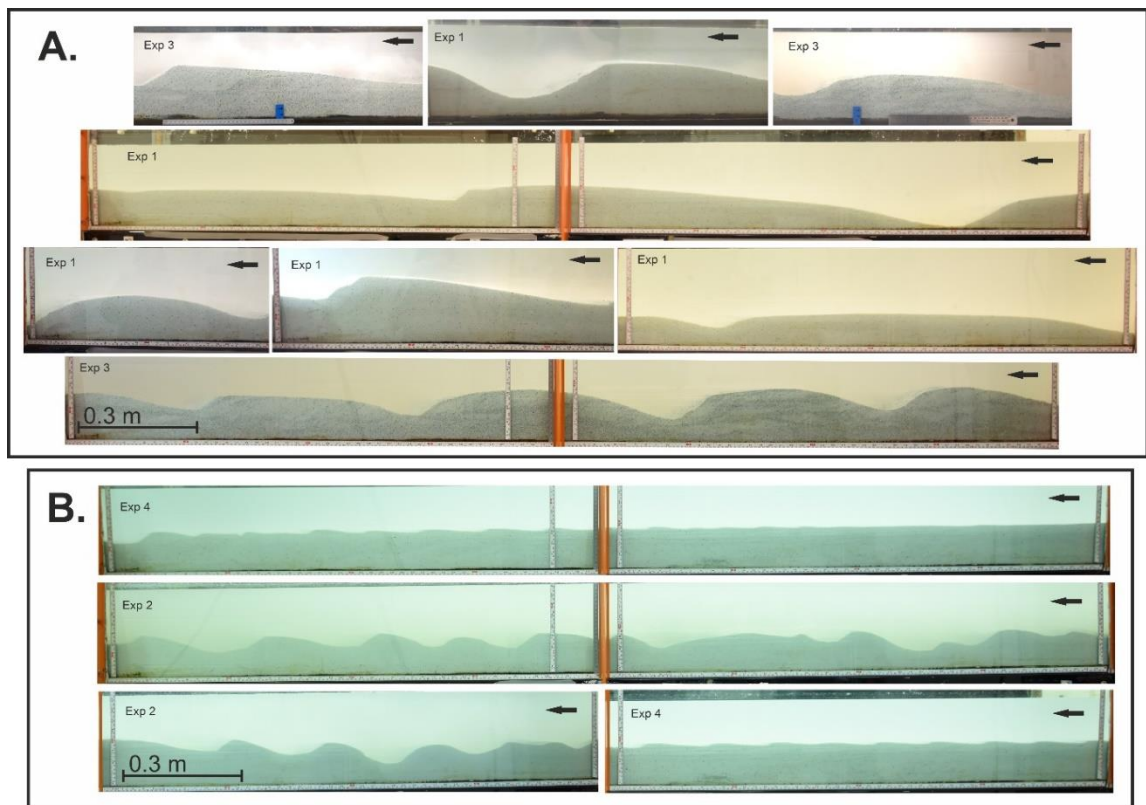
Dune bedforms developed throughout Experiments 1 and 3. They could be identified by observations of high concentrations of suspended sediment being eroded off a bedform and then incorporated into the wake region downstream of the dune. Figure 4.5a defines an approximation of the shear layers that extends from the dune crest and shows mixing between the shear layers and wake region, caused by turbulences arising from the shear layer. Figure 4.5b shows boil structures that reach the flow's surface due to strong ejection events generated from the shear layer. The dunes formed in the present experiments do not force the flow into an out-of-phase relationship with the current's surface. This is unlike the dunes formed by the density current experiments of Chapter 3, which due to the shallower flow depth of the current's lower denser layer, the dune created enough flow expansion to force the surface of the lower denser layer into an out-of-phase relationship.



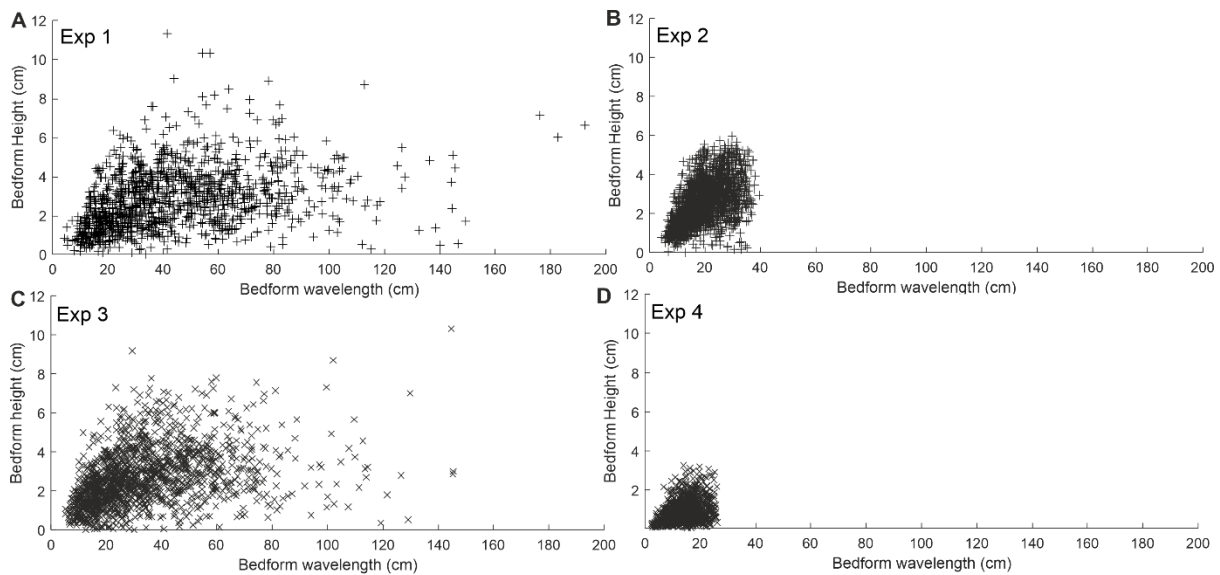
**Figure 4.5. (A)** Example of a dune interacting with the flow. This can be observed as there is high concentration of suspended sediment eroded off the bedform crest and stoss side, which is incorporated into the wake region that extends from the bedform crest. Shear layers are approximately defined in relation to the wake region. Mixing between the shear layer and wake region can be seen best towards the top of the wake region. **(B)** A view from above the flume looking down onto the flow's surface. An example of a 'boil' is visible due to high concentration of suspended sediment within the wake region. 'Boils' are the result of the wake region reaching the surface as strong turbulent 'ejection events' rise through the flow.

Figure 4.6 shows examples of dunes and ripples bedforms generated in Experiments 1 - 4. Although different types of dunes formed in Experiment 1, there is a clear distinction in the

dimensions of dunes compared to ripples. The measured bedform dimensions in Figure 4.7, further demonstrate the difference between ripples (mainly formed in Experiments 2 and 4) which rarely reach wavelengths of 40 cm (Figure 4.7b and d), and dunes (abundant in Experiments 1 and 3) which achieve maximum wavelengths of 150 cm and 190 cm (Figure 4.7a and c). Figure 4.7 does not specifically distinguish between dunes and ripples, but it does show that only Experiments 1 and 3 formed the largest bedforms with wavelengths greater than 40cm. As all experiments formed ripples, it is hard to determine an exact wavelength that constitutes a dune rather than a ripple. As previously outlined, the shallow flow depths of the experimental flows make it likely there is an overlap in ripple and dune geometry at this scale. It is approximated that the transition between dunes and ripples takes place between 25 – 40 cm.



**Figure 4.6.** Examples of **(A)** dune bedforms formed in Experiments 1 and 3, and **(B)** ripples formed in Experiments 2 and 4.



**Figure 4.7.** Bedform dimensions recorded throughout Experiments (A) 1, (B) 2, (C) 3 and (D) 4. Experiments 1 and 3 formed the largest bedforms with wavelengths greater than 50 cm.

A final method to distinguish between different types of bedforms (also used in Chapter 3) compares the shear velocities associated with dunes and ripples (as in Fedele *et al.* 2016; Koller *et al.*, 2017; 2019). The calculated shear velocity values associated with ripples in Experiment 1 - 4 ( $0.03 - 0.055 \text{ ms}^{-1}$ ) were smaller compared to the shear velocities measured for dunes ( $0.06 - 0.2 \text{ ms}^{-1}$ ). Larger dunes create stronger, deeper, zones of flow separation from the bedform crest, with upstream circulation reducing downstream flow depth. Decreased effective flow depth, implies faster downstream flow, given constant discharge fluid flow. Increased flow velocity implies greater shear velocities, turbulence and therefore greater levels of sediment transport.

#### 4.4.3 Bedform evolution

In this section an overview of bedform development throughout each experiment is presented, Experiments 1 - 4 are described in turn. Figure 4.8 shows bedform heights, wavelengths and aspect ratios (i.e. bedform steepness) recorded throughout each experiment.

##### 4.4.3.1 Experiment 1: Coarse-grained, unimodal grain-size distribution

During Experiment 1, Figure 4.8b shows that there were sustained periods lasting between 5 - 10 hours where bedforms with long wavelengths (approximately 80 - 130 cm) were prevalent on the bed. In between these periods of predominantly long wavelength bedforms, periods characterised by shorter wavelength bedforms (approximately 20 - 60 cm) prevailed on the bed for 10 - 15 hours. This process of cyclic bedform growth and reduction was observed throughout Experiment 1. Figure 4.9 describes these observations and details how bedform morphology change took place. Firstly, shorter wavelength dunes merged to form longer

wavelength dunes (Stages A – C, Figure 4.9). This was followed by the breakdown of long wavelength bedforms to form small ripples that, due to their smaller size could migrate downstream quickly (Stages D-E). The smaller, ripple bedforms combined to form tall, steep and medium wavelength dunes (Stages F-G) and the process would repeat itself.

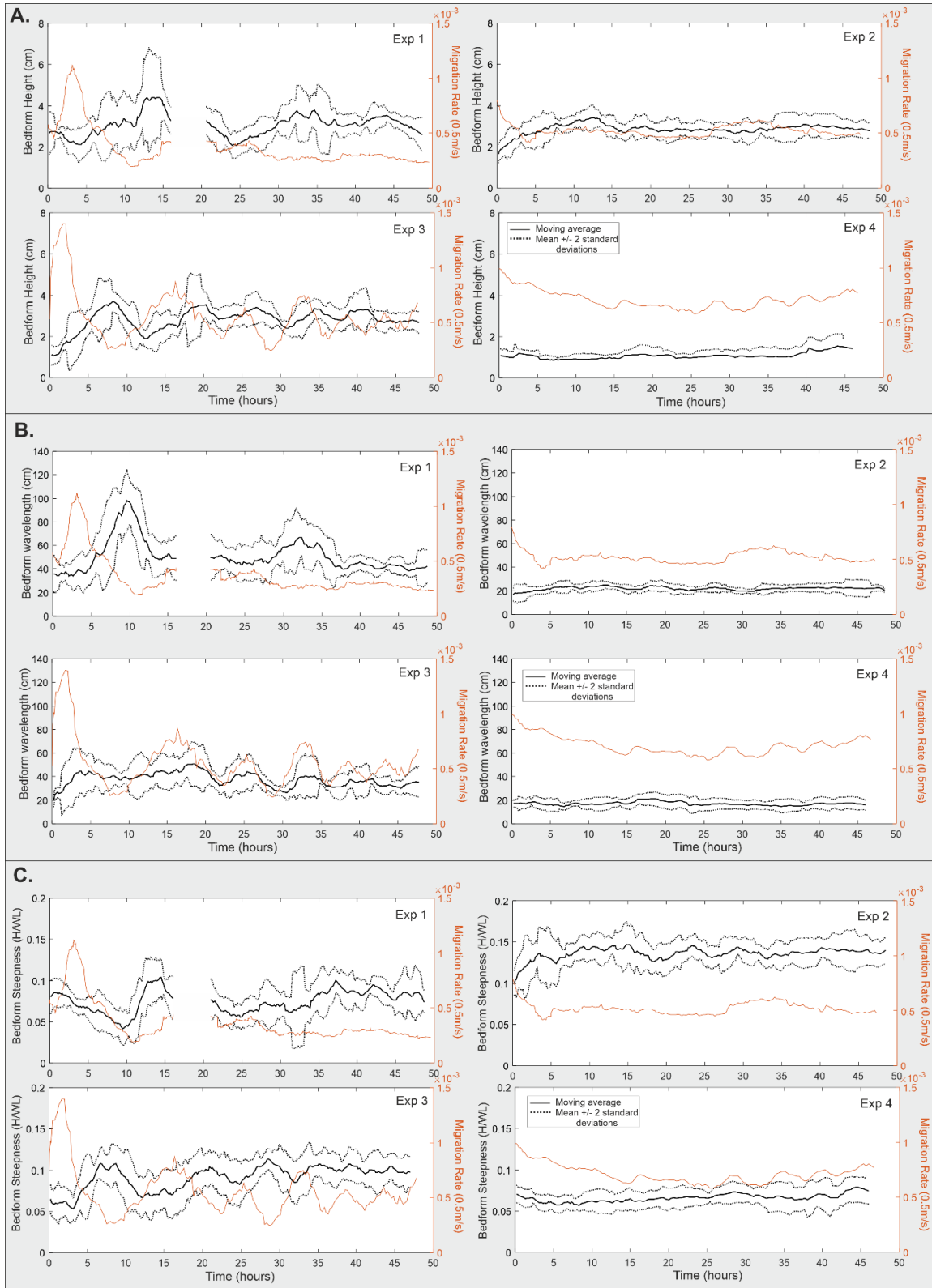


**Figure 4.8.** Moving average of (A) bedform height (B) wavelength and (C) steepness, including 2-standard deviations from the mean and the moving average of bedform migration rate (orange). The absence of data in Experiment 1 is due to a camera malfunction between 17 – 22 hours where no bedform dimensional data could be collected.

While the sequence in Figure 4.9 underpins the bedform development processes of Experiment 1, it did not always take place in such a simplistic manner. Observed deviations from this sequence further complicated bedform development in Experiment 1: Figure 4.8b (Experiment 1), shows periods of bedform wavelength growth (between 7 - 12 hours, 27 - 37 hours) that eventually reach a peak wavelength at 10 hours and 33 hours. These periods of gradual wavelength growth take place as the sequence previously described, deviates from the point of stage E (Figure 4.9). From stage E, ripples migrated away from longer wavelength forms and the height of the long wavelength form was reduced. In some instances, the ripples did not migrate far from the original upstream bedform, allowing them to re-combine and form a very long wavelength (100 – 200 cm) and shallow bedform (stages E – E.1). The bed then became characterised by only very long wavelength and low amplitude forms. Bedforms of this character, due to their long flat stoss sides and low amplitude, have very little impact on the downstream flow field or the downstream long wavelength bedform. As such, these bedforms could remain long and shallow until a stoss side bed perturbation initiated erosion of the stoss side and the following breakdown of the long wavelength low amplitude form. This breakdown took place quickly allowing the bed to become re-populated by short wavelength and steeper bedforms once again, thus arriving back at stage F in the sequence (Figure 4.9).

As previously noted, Experiment 1 experienced three (or possibly 4) periods characterised by shorter wavelength bedforms lasting for 5 – 10 hours. (The uncertainty surrounding the number of sustained periods of this character is due to the missing data in Experiment 1). These sustained periods of shorter wavelength bedforms started from stage G in the sequence (Figure 4.9). Stage G is characterised by bedforms with short wavelengths (relative to Experiment 1), and steep aspect ratios, i.e. large ripples and tall, asymmetric dunes. These shorter wavelength bedforms are associated with faster migration rates (Figure 4.8a) and higher levels of bedform interaction (McLean, 1990). It was frequently observed that faster migrating bedforms often caught up with and overtook the downstream bedform, leading to bedform superimposition or the combination of the two forms to create a new slightly larger bedform. Bedform splitting and scouring also took place, as did the spontaneous creation of bedforms and bedform diminishment in the wake of an upstream bedform. In the study of bedform kinematics, this type of complex interaction of bedforms has been previously documented (Gabel, 1993; 2003; McLean, 1990; Coleman and Melville, 1994; Leclair, 2002; Bridge, 2003; Venditti *et al.*, 2005). Bedform interaction in this manner did not lead to significant bedform dimensional growth or diminishment, instead for a sustained period of 5 – 10 hours, dimensions stayed relatively steady and relatively small.

Eventually, a series of larger dunes formed via the combination of smaller forms (stages G – A, Figure 4.9) and the sequence repeated.

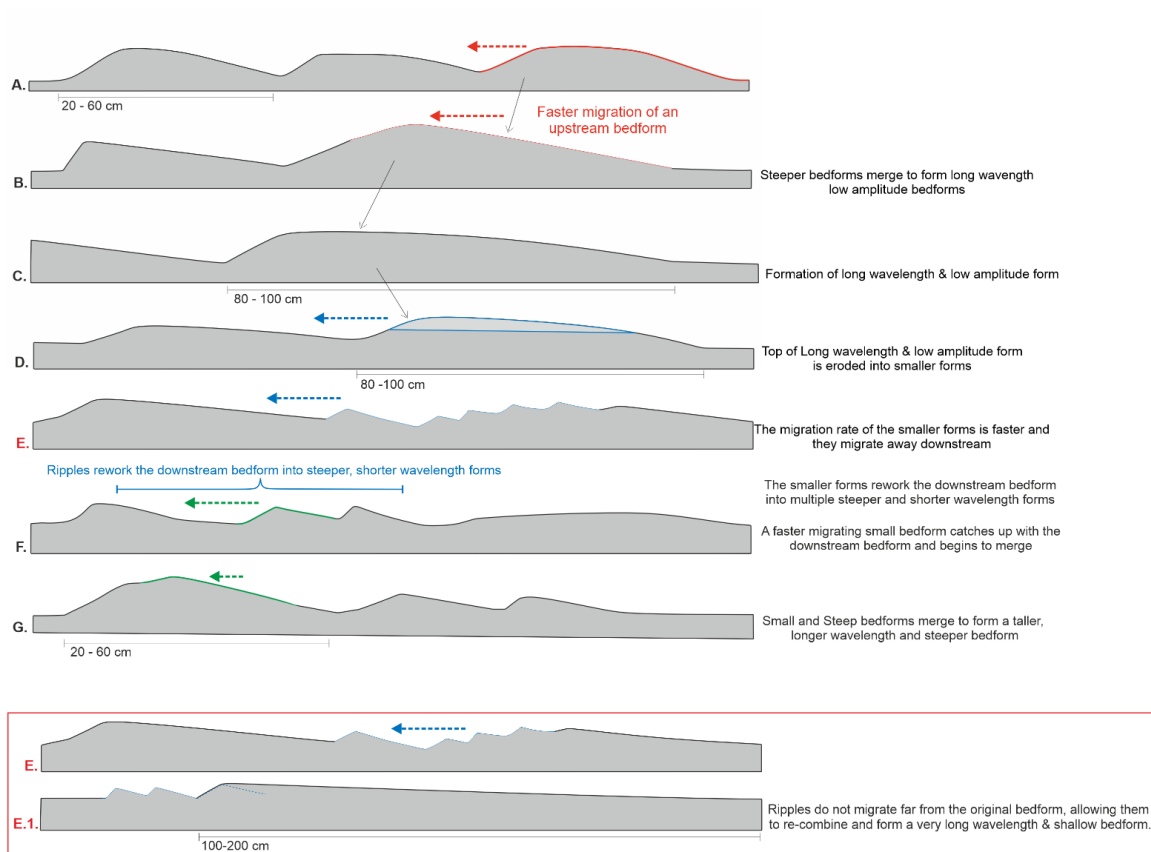


**Figure 4.9:** Stages of bedform change throughout Experiment 1.

#### 4.4.3.2 Experiment 2: Fine-grained, unimodal grain-size distribution

Experiment 2 was characterised by development of bedforms of small heights and short wavelength, which were maintained throughout the run (Figure 4.8). Ripples were the most prevalent bedform type. Compared to Experiment 1 there was far less variation in the dimensions of bedforms. This is apparent in the smaller spread of data shown in Figure 4.8 for bedform height, wavelength and steepness. These results were expected for a unimodal and fine grain-size substrate, as the fine grain-size would be unable to build larger bedforms (Allen, 1982; Raudkivi, 1997; Flemming, 2000; Bartholdy *et al.*, 2015).

#### 4.4.3.3 Experiment 3: Narrow bimodal grain-size distribution

Unlike Experiments 1 and 2, Experiment 3 had a bimodal grain-size distribution. Bedforms formed in Experiment 3 were steep, tall and medium wavelength dunes or large ripples, and bedform morphology was highly variable. A notable result from this experiment is the variability of the average bedform height and wavelength (and associated migration rate) measured throughout the run in Figure 4.8. This result is discussed further in the context of bedform equilibrium within the ‘Discussion’ section of this chapter.

The individual grain-size fractions in Experiment 3 played a key role in bedform development. Figure 4.10 shows how the coarse and fine grain fractions sorted into patches of finer and coarser sediment within the bed. This occurred due to bedform migration and associated sorting of grain-sizes associated with development of foreset cross-stratification with alternate coarser and finer grain-sizes, and the deposition of bottomsets made of predominantly fine sediment. The finer-grained bottomsets developed laterally and vertically complex networks of fine sediment laminations throughout the bed.

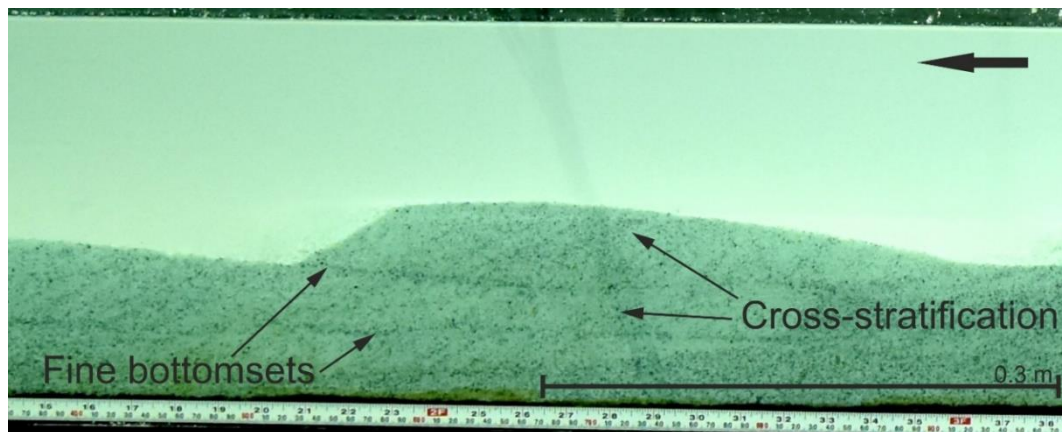


**Figure 4.10.** Experiment 3. Examples of fine bottomsets - one beneath a migrating bedform and the other deposited and buried deeper within the substrate as a fine lamination. The cross – stratified intervals are bound by the bottomsets top and bottom.

These fine laminations are interpreted to have significant impact on bedform morphology and behaviour throughout the run. On encountering previously deposited fine bottomsets, bedforms appeared unable to erode any further down into the bed beyond the height of the bottom set. This meant that bedforms were forced to migrate over the top of the fine sediment lamination, following the pathway dictated by the bottomset. As a result, the bedforms were starved of sediment and quickly diminished, unable to maintain their size. Examples of this taking place are detailed in Figures 4.11 & 4.13. The bedforms eventually became smaller than the upstream bedform so that they sat in the wake of the upstream form, which would often cause them to disappear entirely (Figure 4.11 e-h). The way in which bedform depositional processes developed networks of fine sediment laminae and created patches of irregularly sorted sediment throughout the bed is expanded upon within the discussion section.

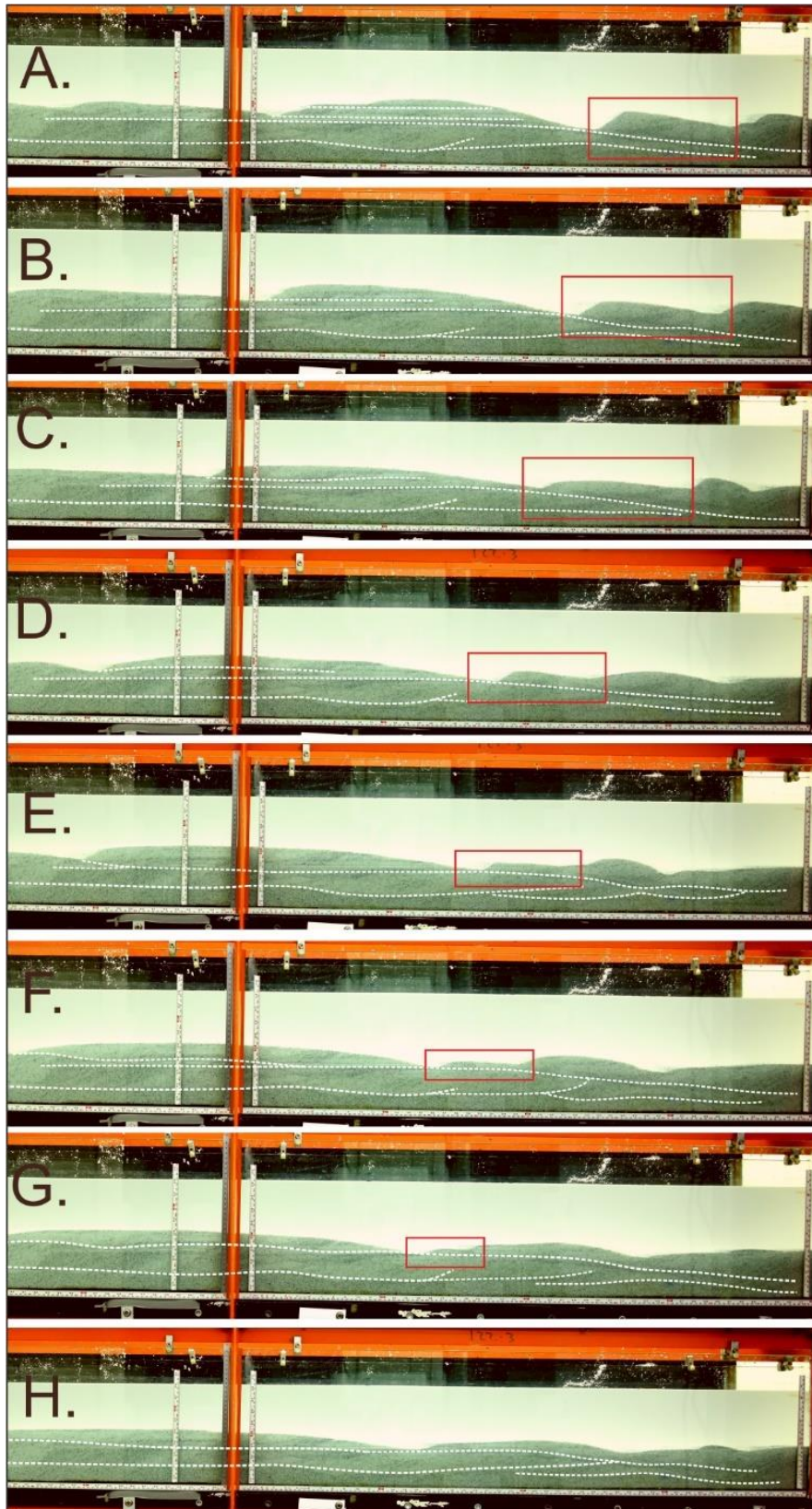


**Figure 4.11.** Experiment 3. (A-H) depict the process of bedform diminishment caused by its interaction with a previously preserved fine bottomset within the substrate. White lines depict the fine sediment laminations.

#### 4.4.3.4 Experiment 4: Wide bimodal grain-size distribution

The wide grain-size distribution of Experiment 4 had the most significant impact on bedform development. Bedform development was largely suppressed as only incipient and small ripples formed throughout the whole run. The bedforms also deposited fine bottomsets as they migrated, in the same manner as described in Experiment 3. The bottomsets formed intricate laterally extensive networks of fine sediment laminations (Figure 4.12) which, unlike Experiment 3, were confined to the uppermost 5 cm of the bed. The fine laminations acted an armour layer of fine sediment that created a barrier to the poorly sorted sediment beneath in which most of the coarser sediment resided (Figure 4.12a). In Experiment 4, the presence of larger ripples was always short-lived. On encountering a fine sediment lamination, the ripple was not able to erode any further down into the bed causing to become sediment starved and reduce in size in the same manner as previously described in Experiment 3 (Figure 4.13).

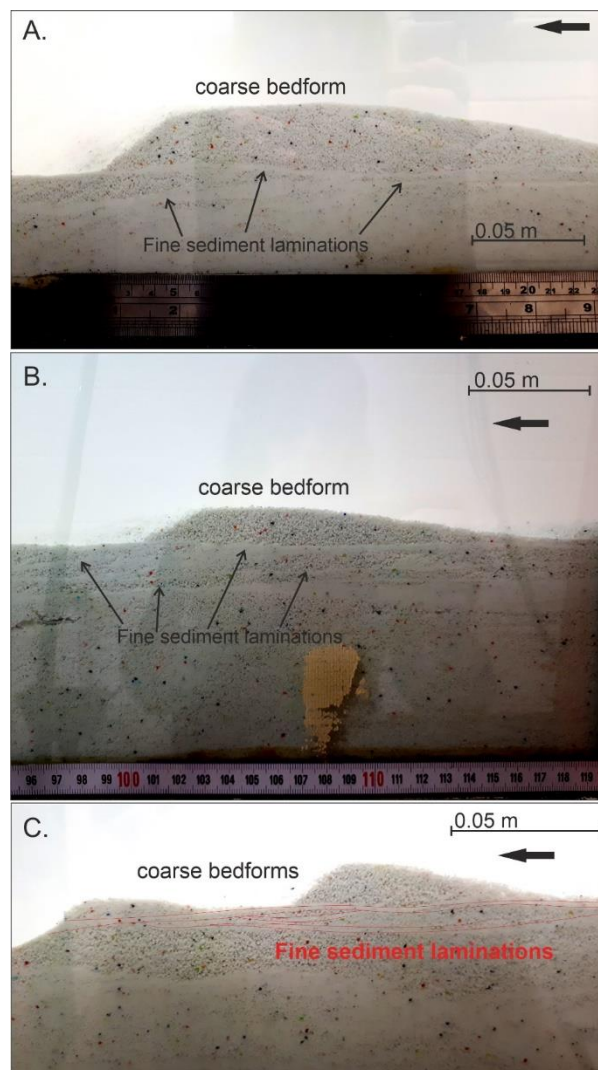


**Figure 4.12.** Examples of sediment starved ripples formed in Experiment 4. In the upper region of the bed there is a laterally extensive and intricate network of fine sediment laminations.

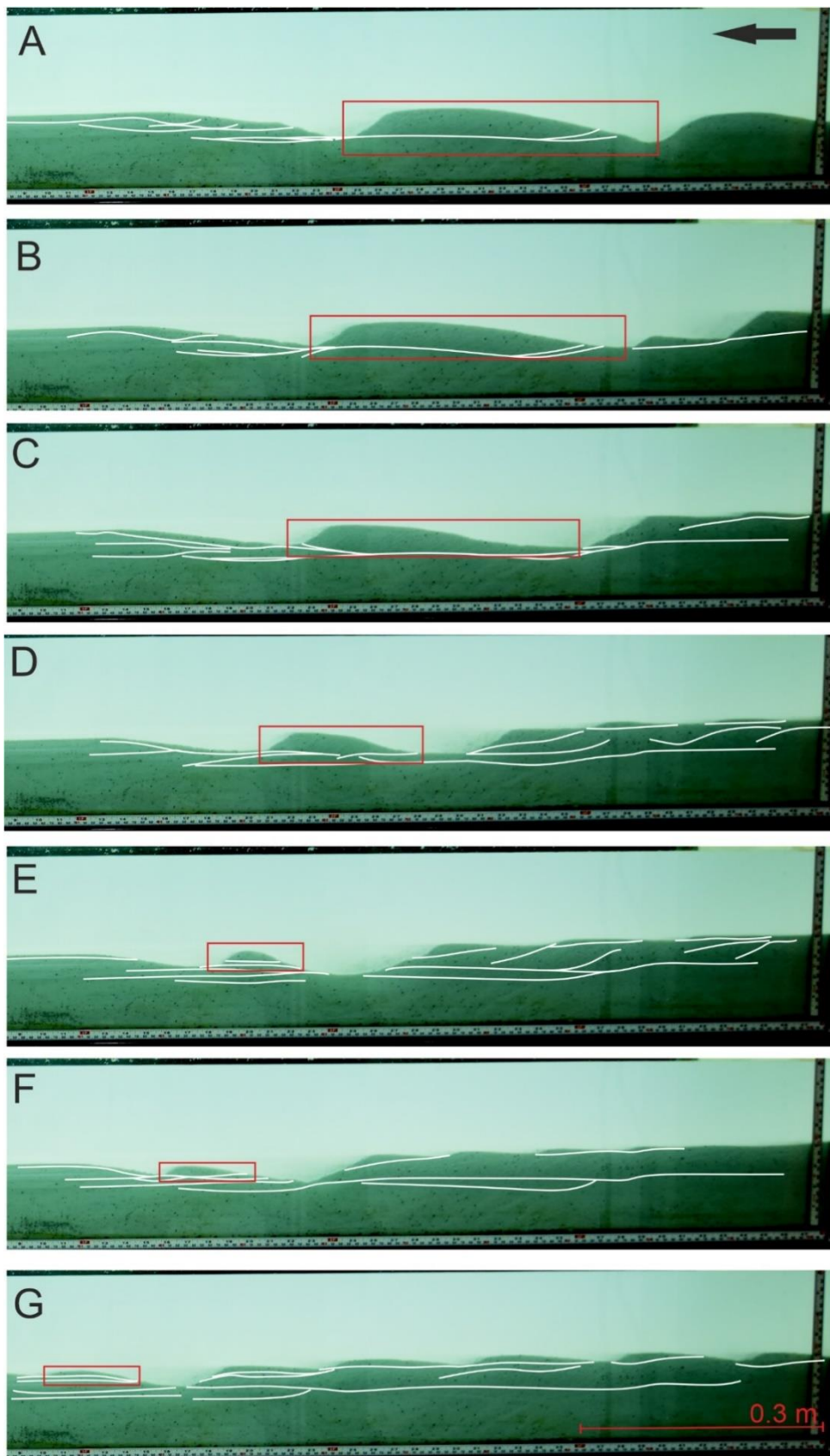


**Figure 4.13.** Experiment 4. (A-E) depict the process of bedform diminishment caused by its interaction with a previously preserved fine bottom set within the substrate. White lines depict the fine sediment laminations.

The discussion section contains further analysis into why the wide grain-size distribution in Experiment 4 may lead to suppressed bedform development and investigates what impact increased levels of grain fractionation in the substrate for bimodal sediment mixtures may have on sediment mobility and bedform development.

#### *4.4.3.5 Bedform Equilibrium*

Analysing bedform development, i.e. bedform dimensional change over the course of an experiment, is used to establish if equilibrium conditions between the bed and the flow were reached (Mohrig and Smith, 1996; Paarlberg et al., 2009; Baas 1994; 1999; Perillo *et al.* 2014).

This approach is used and discussed within the following discussion section. Further analysis was carried out to assess whether bedform equilibrium was achieved by calculating the percentage of bedforms that increased in size throughout each experiment. Figure 4.14 shows that in each experiment, the number of bedforms growing were overall equal to the number of bedforms reducing in size. The extent to which this type of analysis is successful in assessing whether equilibrium conditions are reached is also discussed further within the discussion section.

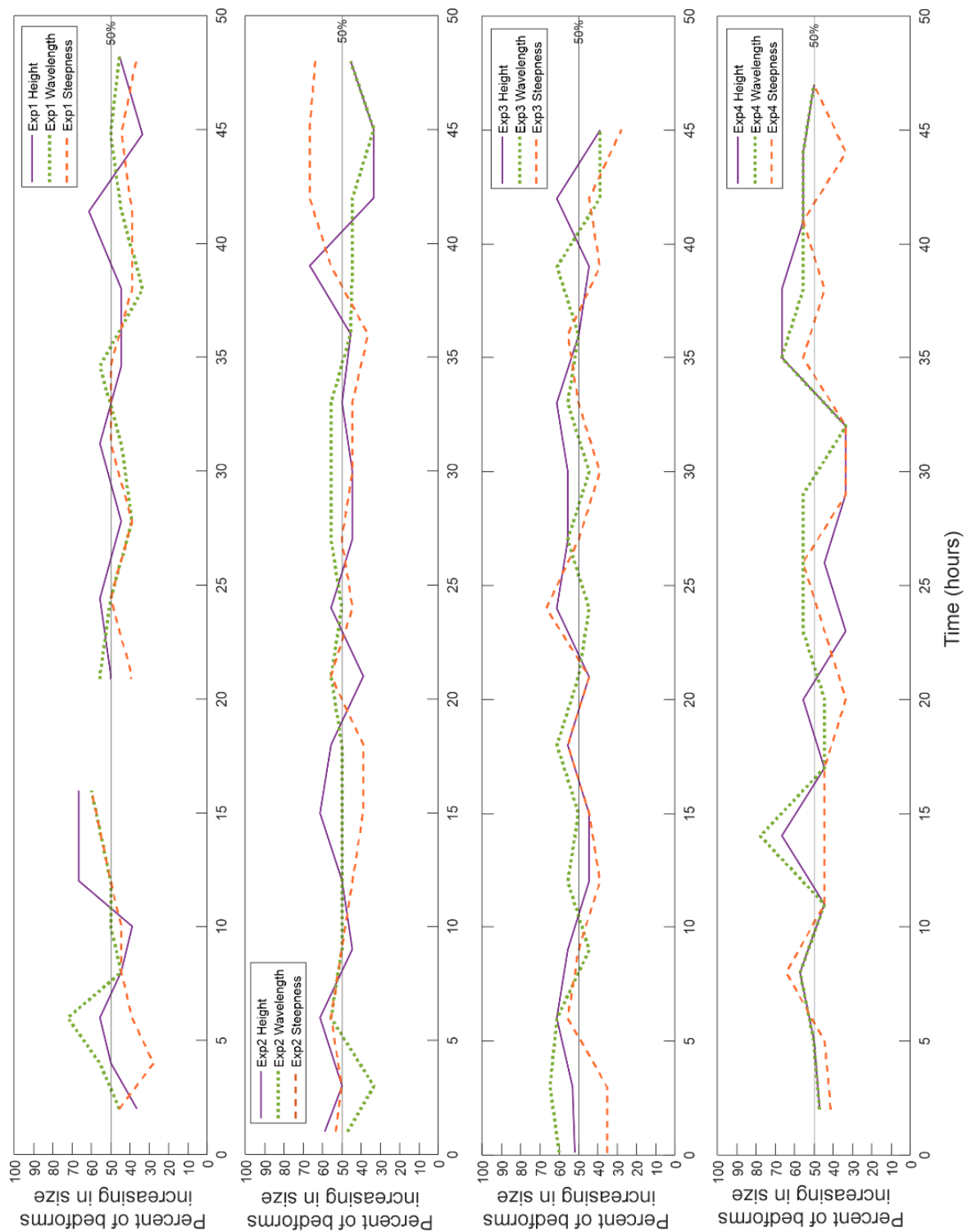


**Figure 4.14.** Percent of bedforms that increase in size.

#### 4.4.4 Bed grain-size variation

Figure 4.15 shows how the fine grain content (0 - 300  $\mu\text{m}$ ) varies with depth within the bed. These data are from the grain-size distributions measured from core samples taken from the bed at the end of each experiment. It is therefore worth noting that these results are only

representative of the final bed morphology. For Experiments 3 and 4, these results align with observations and photographs of the bed throughout each run, in which laminations made of fine sediment are seen situated towards the top of the bed (Figures 4.11, 4.12 & 4.13). In Experiment 4, over 1 - 8 cm bed depth, the percent of fine sediment content is relatively uniform, between 40 – 45 %, meaning that the coarse and fine fractions are well -mixed across these bed levels. Towards the top of the bed, the percentage of fine grain contents become more variable with some levels containing more fine sediment than coarse. It is worth noting that by averaging across the grain-size distributions measured for different bed levels, some of the original variability may be lost.

Figure 4.15 shows that Experiment 3 exhibited a more variable distribution of fine-grained sediment through the bed. This reflects the observations of the presence of fine-grained laminations at different levels through the entire bed (Figure 4.11). Figure 4.15 also shows that the upper 3 cm of the bed are characterised by a higher percentage of fine grain sediment compared to lower levels of the bed. Figure 4.15 also reveals new information about Experiments 1 and 2. Both experiments show a progressive reduction in the percentage of finer grain content higher up in the bed. In other words, by the end of the experiments, the bed had lost some of its fine-grained content from the top half of the bed due to winnowing.

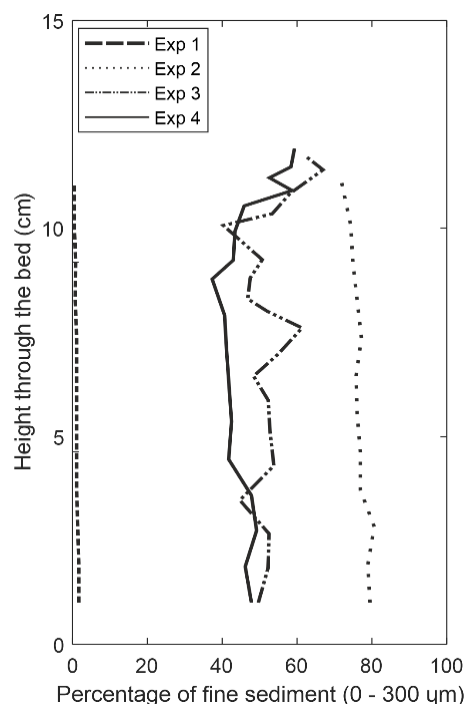


**Figure 4.15.** The percentage of fine sediment (0 – 300 μm) content found at different levels of the bed for Experiments 1 - 4. This data is extracted from the grain-size distributions calculated for bed core samples taken from different points across the flume, which were then averaged across equivalent bed levels.

## 4.5 Discussion

### 4.5.1 Bedform equilibrium

One measure of assessing whether bedforms have reached equilibrium is to establish when bedform dimensions do not vary as they migrate downstream (Mohrig and Smith, 1996; Paarlberg *et al.*, 2009). This approach is often applied in laboratory flumes, where flow conditions can be kept steady (Mohrig and Smith, 1996). For a bedform to maintain its morphology as it migrates, McLean (1990) argues that both the bedform's spatial structure and the sediment transport over the bedform must remain constant, noting that the sediment flux over a bedform is dependent on the flow, and the flow in turn, is dependent on the bedform morphology.

However, research by Sutherland & Hwang (1965); Baas (1994; 1999); Coleman *et al.* (2003); Perillo *et al.* (2014) describe bedform development in unidirectional steady flow as one in which bedforms experience asymptotic growth until they reach a fixed mean (equilibrium) size and then fluctuate about the equilibrium height and wavelength values. The experimental run time (~15 hours) in which Perillo *et al.* (2014) explains equilibrium conditions are reached, were shorter than the run times of the present experiments (48 hours), indicating that equilibrium conditions were likely reached during the 48 hours. Figure 4.8 shows how in the present experiments, bedform height and wavelength experience a period of growth at the start of the run as bedforms change from incipient forms into growing bedforms. In Experiment 1, the period of bedform growth takes place between 0 – 10 hours; in Experiment 2 this period is between 0 – 7 hours; in Experiment 3 it is between 0 - 4 hours for wavelength and 0 – 8 hours for height; Experiment 4 remains steady from the start of the run, without experiencing a period of growth.

A period of bedform stabilization follows: In Experiment 1, this takes place between 10 – 15 hours; in Experiment 2, between 7 – 15 hours; in Experiment 3, between 4 – 9 hours for wavelength and between 8 – 12 hours for height; finally, bedform dimensions in Experiment 4 remain steady. The remaining hours in Experiment 2 and 4 may be interpreted as being characterised by fully developed bedforms that fluctuate about the equilibrium bedstate. This breakdown of bedform development into stages that eventually reach a state of dynamic equilibrium, is in agreement with Baas (1994, 1999) and Perillo *et al.* (2014). In Experiments 1 and 3 however, there is large variability of average bedform growth and decrease throughout the run. To what extent can the bedforms in these runs be considered as in equilibrium?

Previously described is the cycle of bedform breakdown and growth that takes place throughout Experiment 1, which enabled sustained periods of larger bedform maintenance followed by sustained periods of smaller bedform maintenance, in a cyclic manner (Figure 4.9).

The repeated nature of this process suggests that the variability in average bedform dimensions over time may be indicative of a bed in dynamic equilibrium.

In Experiment 3, the moving average for bedform height and wavelength exhibits more frequent variability, compared to the sustained periods of growth and decrease in Experiment 1. Uncertainty remains as to whether this means the bedforms in Experiment 3 are not in equilibrium, or whether they are in fact in a highly dynamic equilibrium. Consideration is also given to whether the cause of this altered equilibrium state is the result of the bimodal sediment mixture set for Experiment 3. The following discussion details how grain sorting of the bimodally-distributed sediment caused bedforms in Experiment 3 to be highly morphologically variable, resulting in little maintenance of bedform dimensions.

Experiment 4 does achieve equilibrium, but the kind of equilibrium achieved in this run is entirely dictated by the grain-size distribution of the bed, which as is discussed in detail below, prevents sediment mobility and therefore bedform development. In this sense, equilibrium in Experiment 4 is one of constant bedform suppression.

Another type of analysis was carried out to further assess bedform equilibrium. Figure 4.14 shows the percentage of bedforms that increased in size throughout different experiments. It shows that in each experiment, the number of bedforms growing were overall equal to the number of bedforms reducing in size. Unlike Figure 4.8 and the work of Baas (1994; 1999) and Perillo *et al.* (2014), this method of assessing equilibrium does not represent the amount a bedform grows or reduces by. By omitting actual bedform size, this simplified way to characterise bedform dynamics over time might help to assess equilibrium in more dynamic systems, such as Experiments 1 and 3. Figure 4.14 suggests that each experiment did achieve equilibrium due to consistently experiencing a relatively equal number of bedforms that were growing and reducing in size at any one time.

#### ***4.5.2 Observed bedforms versus bedform stability fields***

This section analyses the predictive capabilities of the commonly used Van den Berg and Van Gelder's (2009) adaptation of Van Rijn's (1984) dimensionless phase diagram, to predict bedform development in sediments of varying grain-size distributions.

In all experiments, the threshold for sediment motion was met and on this basis sediment transport would be predicted to take place as mixed load transport leading to ripple or dune bedform development. To predict the specific types of bedforms that should form during each experiment, the results from the present experiments are plotted onto Van den Berg and Van

Gelder's (2009) adaptation of Van Rijn's (1984) dimensionless phase diagram (Figure 4.16). Van Rijn's (1984) phase diagram is widely used to gauge bedform regime boundaries and uses dimensionless variables to permit comparison between experimental data collected under different experimental parameters. This phase diagram plots the Particle Parameter ( $D_*$ ; Equation 4.6 (Bonnefille, 1963) against the mobility parameter ( $\theta'$ ; Equation 4.10 (Van Rijn, 1984)).

$$\theta' = \frac{\rho U^2}{(\rho_s - \rho)(C')^2 d_{50}}, \quad (\text{Eq. 4.10})$$

where

$$C' = \sqrt{1/Cd}, \quad (\text{Eq. 4.11})$$

where,  $\theta'$  is the grain mobility parameter and  $C'$  is the Chézy coefficient.

As is seen in Equation 4.10, the median grain-size is used to calculate the mobility parameter. Figure 4.16a plots the experimental phase space for each run based on the median grain-size for all the grains that made up the bed. Figure 4.16b plots the median grain-size for the individual grain-size populations in Experiments 3 and 4. Based on the median grain-size for all grains, Figure 4.16a predicts development of dunes – upper stage plane bed in Experiments 1, 3 and 4 and Experiment 2 plots near the boundary between ripples and dune-upper plane bed. The bedform phase diagram accurately predicts bedform development in Experiment 1, which mainly formed dunes. Dunes also formed throughout Experiment 3, but so did ripples, indicating the stability field of Experiment 3 was nearer the boundary between dune and ripple phase spaces. Experiment 2 formed ripples, the associated experimental conditions plot very near the boundary between dunes and ripples on the bedform phase diagram.

Ohata *et al.* (2017) and Southard and Boguchwal (1990) have suggested that the boundaries on phase diagrams are somewhat arbitrary as they do not usually account for transitions between bed states which would blur the boundary lines. As such, Van den Berg and Van Gelder's phase diagram is used as a guide to predict bedform development. Therefore, Figure 4.16a is considered to successfully predict ripple development in Experiment 2 (when the phase boundaries are not considered exact). The bedforms developed in Experiment 4 were not accurately predicted by the phase diagram, which plots dune development, rather than the small ripples that actually formed. This failure is likely the result of having to characterise the sediment in the bed by the medium grain-size of all the grains in the bed, which assumes the sediment is homogenous and unimodally distributed. Characterisation of the bed by a single median value is not an adequate representation of the wide grain-size distribution. Figure 4.16a plots the particle parameter for Experiments 3 and 4, based on the median grain-size, in very close proximity as the

median grain-size representation of these beds portrays them of similar grain-sizes. Therefore, the phase diagram inaccurately predicts the formation of similar types of bedforms due to its lack of consideration for the grain-size distribution of the bed, which greatly effects bedform development.

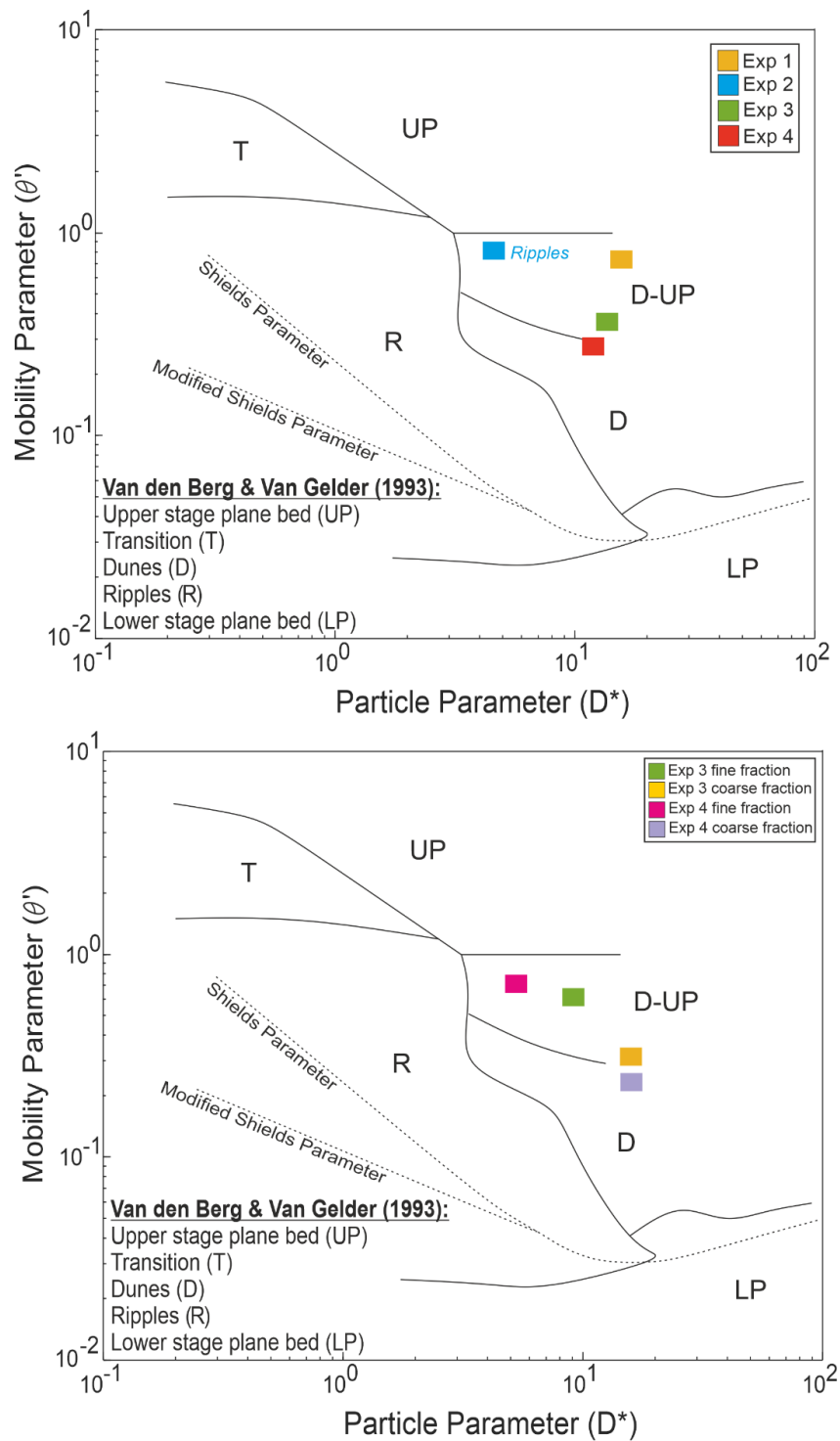


**Figure 4.16.** Bedforms developed during the present experiments are plotted onto Van den Berg and Van Gelder's (2009) dimensionless bedform phase diagram.

In summary, as expected, Van den Berg and Van Gelder's (2009) dimensionless bedform phase diagram overall, successfully predicts bedform development in unimodal sand-sized mixtures. It partially predicts bedform development in bimodally distributed sediment mixtures, but only for the narrow grain-size distribution of Experiment 3. For bimodal sediment mixtures with wide grain-size distributions in Experiment 4, Van den Berg and Van Gelder's phase diagram fails to predict bedform development.

### 4.5.3 Hiding factor

Within the 'Results' section it was established that the flow conditions met the threshold for sediment motion based on the median grain-size for the entire mixture and the median grain-size of the component sediment size fractions used to make bimodal mixtures. However, studies into sediment erosion thresholds of non-uniform sediment have shown that fine grains in a sediment mixture of coarse sediment require greater shear stresses/flow speeds to be entrained than would be predicted for a single grain-size bed (Einstein, 1950; Wilcock, 1993; McCarron *et al.*, 2019, amongst others referenced herein). Sediment transport models developed by Einstein (1950), Egiazaroff (1965), Ashida and Michiue (1973) and Wiberg and Smith (1987), incorporate 'the hiding factor'. The hiding factor accounts for the effect larger grains on the dynamics of smaller grains. Thus, the degree of exposure a grain has to the flow plays a significant role in determining its likelihood of erosion, if a grain is hidden or sheltered by a larger grain the efficiency of the flow to mobilize it is reduced (Einstein, 1950; Egiazaroff, 1965; Wilcock, 1988; Sutherland 1992; Wilcock and Crowe, 2003). In order to more accurately represent the thresholds of sediment motion in the bimodal substrates of Experiments 3 and 4, further calculations are carried out using models that considers the hiding factor. As in Staudt *et al.*, (2017), the model chosen to account for this factor in the present experiments is Ashida and Michiue's (1973) modification of Egiazaroff's (1965) model (Equations 4.12 and 4.13). This expression of the Shields parameter that considers the hiding factor is as follows:

$$\theta_{ih} = \frac{u^* cr_i}{g(\rho_s - \rho)D_i} \text{ for } D_i/D_m \geq 0.4, \quad (\text{Eq. 4.12})$$

$$\theta_{ih} = 0.0519 \frac{D_m}{D_i} \text{ for } D_i/D_m < 0.4, \quad (\text{Eq. 4.13})$$

where  $D_i$  is the median grain-size of the size fraction  $i$  and  $D_m$  is the mean grain-size of all the grains in the sediment mixture. Table 4.4 shows the critical shear velocities calculated for Experiments 3 and 4 using Ashida and Michiue's (1973) model. Table 4.4 shows that when the hiding factor is considered in the calculation for critical shear velocity, the dimensional shear

velocities for Experiments 3 and 4 ( $0.06 \text{ ms}^{-1}$ ,  $0.04 \text{ ms}^{-1}$  respectively) still exceed the threshold for sediment motion. Because the hiding factor is based on experiments using sands and gravel, it may not accurately express the hiding factor acting between fine and coarse sand-sized sediment. If the hiding factor does not explain the reduced mobility of the bed in Experiment 4, it suggests there may be other factors, which are discussed in detail below that might affect the stability of the bed.

**Table 4.4.** *Hiding factor: Critical parameters for bimodal sediment fractions ( $D_i$ ).*

<i>Exp</i>	<b>d50 <math>D_i</math>, (um)</b>	<b><math>D_i/D_m</math></b>	<b><math>\theta_{ih}</math></b>	<b><math>u^* cr_{ih}(\text{ms}^{-1})</math></b>
3	500	0.61	0.004	0.093
3	937	1.16	0.003	0.012
4	297	0.40	0.006	0.010
4	937	1.26	0.003	0.012

#### **4.5.4 Existing models that explain bed stability in non-uniform sediment**

Bedform suppression in Experiment 4 was extensive. Only very small coarse ripple forms developed on the bed. The reason the bedforms were so small was due to the inability of the flow to mobilize most of the sediment within the bed, i.e., the bedforms were starved of sediment and were therefore unable to grow. Here a discussion is presented as to how the bed in Experiment 4 became stabilized.

Just based on the knowledge that Experiment 4 was run with a sediment mixture of a wide grain-size distribution, three models can be used to explain increased bed stability in Experiment 4. The first model explains how non-cohesive silt particles surround the coarser grains in the sediment mixture (van Ledden *et al.*, 2004; Bartzke *et al.*, 2013). As a result, the intergranular contact between the coarser grains are reduced or eliminated, which increases the distance between individual coarse grains, and therefore increased the angle of repose. This causes an increase in the shear stress required to overcome the greater angle of repose and erode the bed (van Ledden *et al.*, 2004; Bartzke *et al.*, 2013).

A second aspect of how fine sediments may affect the properties of the bed to make it more stable relates to the amount of water that can enter the bed i.e. the hydraulic conductivity of the bed. Increased water content in a substrate causes sediment to become loosely packed resulting in a reduction in bed strength and stiffness, this is known as bed liquefaction (Campbell, 1978).

Bartzke *et al.* (2013) argue that increasing amounts of fine sediment within a bed reduces its hydraulic conductivity by infilling the pore space between the coarser grains and reducing the inflow of water into or through the bed. This means that the pore space created once a grain is mobilized is less likely to be infilled by flow fed from within the bed. However, in Experiments 3 and 4, the amount of fine sediment within the sediment mixtures was set to be approximately the same (40 – 45 % by weight). The observed differences in bed stability and bedform development between Experiments 3 and 4, suggest that it is not only the quantity of fines within a mixture that effects bed stability, but it is the relative size of the different grain fractions, i.e. the grain-size distribution, of the bimodal sediment mixture, that determines the extent of bed stabilization.

The proposal that a wider grain-size distribution could reduce hydraulic conductivity of the bed, is in agreement with the third model described by Staudt *et al.* (2017). Staudt *et al.* (2017) found that hydraulic conductivity was reduced by widening the distribution of fine and coarse sediment in a non-uniform sediment mixture. The effect of reduced hydraulic conductivity was to reduce the erodibility of the bed. Therefore, it is proposed that the wider grain-size distribution in Experiment 4 minimised the flow entering the bed as the fine sediments more effectively infilled the available space between the larger grains, and the resulting highly stabilized bed also prevented bedform development. It is also suggested that the narrower grain-size distribution of Experiment 3 less effectively stabilized the bed as there was more space between the particles. This enabled the flow to more easily enter and travel through the bed, which increased the bed's mobility and enabled bedform development to take place.

These three models define how a non-uniform mixed sediment bed can become stabilized due to the different impacts of the fine-grained fraction. However, they do not describe the formation nor the impact of fine sediment lamination networks/ anastomosing fine sediment networks, that developed in Experiments 3 and 4. It is speculated that the formation of these networks might have stabilized the bed further. A discussion into the stabilizing effects of fine sediment laminations is presented below, preceded by a description of the processes that led to their development.

#### ***4.5.5 Development of fine laminations - grain sorting in bimodal sediment mixtures***

The explanation as to how the different grain-size fractions became organized into laterally and vertically extensive networks of fine laminations, relates to depositional processes associated with the coarse and fine grain fractions as bedform migration took place. Sengupta (1979) also documents the formation of fine-grained sediment laminations within a mixed

sediment bed. This he attributes to sediment segregation by bedforms as they migrate. Here a more detailed description of the processes related to bedform sediment segregation is presented.

During Experiments 3 and 4, the finer grain fractions were transported as mixed load i.e. as both part of the bed load and in suspension. The coarser fractions were predominantly transported as bedload. As bedforms migrated, sediment was observed to deposit over the lee slope and into the trough of the bedform. Two mechanisms are inferred to be involved in this process. The first is grain fall. This refers to suspended sediment being caught in the counterflow which leads to fine grains in suspension settling out onto the bedform's lee slope and trough (Figure 4.17) (Kleinhans, 2004). This finer sediment forms the 'toeset' of the bedform, which is then buried as the bedform migrates over the top of it. It then becomes known as the 'bottomset' (Kleinhans, 2004). The second mechanism is grain flow – a gravity driven mass of grains (Lowe, 1976) where grains roll down the lee slope until the angle of repose is met (Figure 4.17). This deposit is made up of both the finer fraction and coarser fraction. As the bedforms migrated, coarse and fine sediment was deposited as cross-strata on top of the finer bottomset, leading to preservation of the bottomsets as fine laminations. Deposition and burial of bedform bottomsets in this manner meant that Experiment 3 was characterised by development of a vertically and laterally complex network of preserved fine laminations, which were continuously re-deposited in different patterns throughout the run as bedforms migrated. Bedform-related sediment sorting in Experiment 3 also led to the development of patches of predominantly coarser or finer sediment throughout the bed in association with cross-stratification. The lamination network formed in Experiment 4 was also laterally extensive, but the much smaller bedforms of Experiment 4 only deposited the fine bottomsets within the upper 5 cm of the bed (Figure 4.13).

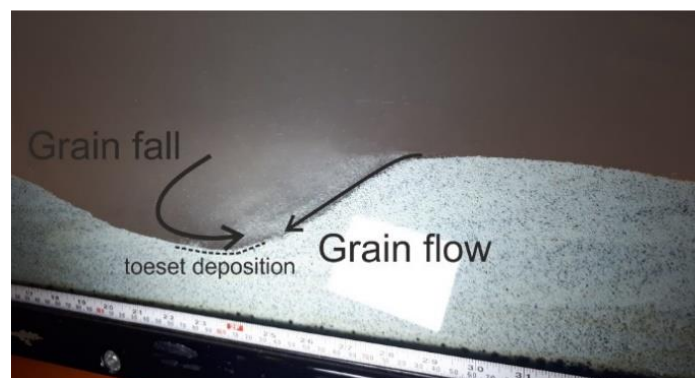


**Figure 4.17.** Experiment 3. Photograph depicting characteristic mechanisms of sediment deposition over the lee slope. Grain fall of fine sediment from suspension forms fine toeset deposits, grain flow forms cross-strata that deposit on top of the toesets and preserve them.

## **4.5.6 Fine sediment laminations and increased bed stability**

### **4.5.6.1 Reduced hydraulic conductivity**

It has been previously discussed how reduced hydraulic conductivity of a bed (i.e. the ability of the flow to enter the bed and flow through the bed) increases the stability of the bed (Staudt *et al.*, 2017; Bartzke *et al.*, 2013). Figure 4.18a depicts only a small amount of flow entering and moving through a bed made up of sediment with a wide grain-size distribution. Evidence for the bed becoming stabilized in Experiment 4 includes the development of sediment starved bedforms that were unable to erode the bed, and the preservation of primary structures within the bed (i.e. fine-grained laminations). This suggests liquefaction of the bed did not take place and that hydraulic conductivity of the bed was low.

It is suggested that the anastomosing network of fine-grained laminations helped to stabilize the bed by reducing the bed's hydraulic conductivity in a manner that has not yet been recognized. In Experiment 4, the fine lamination network was intricate, very dense and extended the length of the flume. These laminations are made up of fine angular sediment grains that can pack tightly together forming an embedded and interlocking structure (as described by Buxton *et al.*, 2014). Figure 4.18b depicts how a single very densely packed fine-grained lamination might act as an impermeable barrier to the flow entering the bed and to flow moving up through the bed. As such, the capacity of the fluid to pass through the local substrate from deeper within the bed and infill the void (an area of low-pressure) left behind once a grain is eroded from the substrate, is reduced (Figure 4.18b).

It is suggested that the laterally extensive network of fine laminations (Figure 4.13) stabilize the bed by reducing the bulk hydraulic conductivity throughout the top 5 cm of the bed. Figure 4.18c schematically presents how multiple laminations deposited at varying angles could obstruct the passage of water as it moves through the bed. Cells of non-uniform sediment in between the fine lamination network allow some movement of fluid, however due to the wide grain-size distribution of the non-uniform sediment, hydraulic conductivity is minimal due to the reduced pore space (Dorrell and Hogg, 2010; Bartzke *et al.*, 2013; Staudt *et al.*, 2017). Even if these cells of non-uniform sediment are exposed to the current, they are likely to resist erosion due to the increased stability of the bed caused by its reduced hydraulic conductivity (Bartzke *et al.*, 2013; Staudt *et al.*, 2017). As fine sediment laminations in Experiment 4 are confined to the upper region of the bed, they will prevent the flow effectively penetrating the bed beyond the top few centimeters.

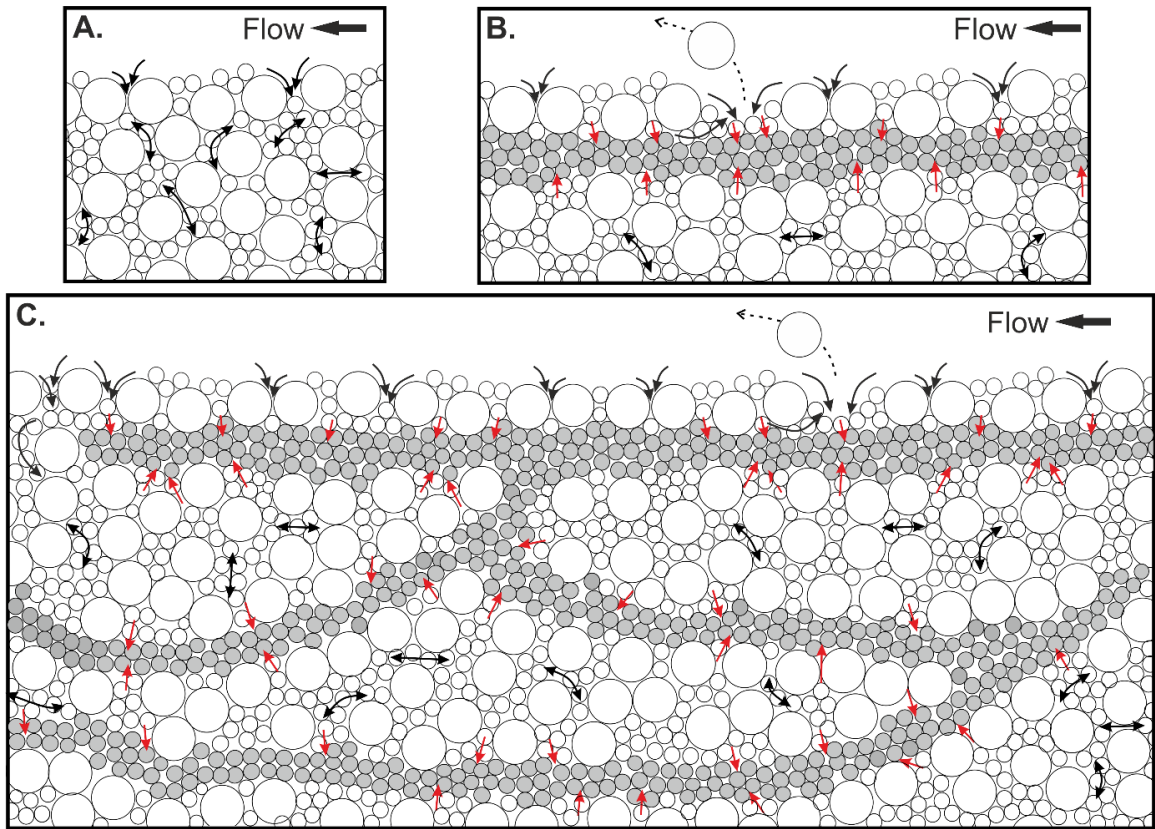


**Figure 4.18.** Schematic representations of the ability of water to enter and move through the bed in a wide grain-size distribution. **(A)** Some water is able enter and flow through the bed (signified by black arrows) when the fine and coarse grain-size fractions are poorly distributed. **(B)** Representative of the bed in Experiment 4, the grey-coloured grains represent the fine sediment lamination which formed within the top 5 cm of the bed in Experiment 4. The diagram shows how the flow's ability to pass through a single fine lamination is reduced (signified by red arrows) due to the impermeability of the fine lamination. As a result, much of the flow is prevented from penetrating to deeper levels of the bed. **(C)** Also representative of Experiment 4, this diagram depicts a wider section of the anastomosing fine-grained lamination network that further obstructs the flow's capacity to move through the bed as the fine-grained lamination network extends through poorly sorted parts of the bed in multiple directions and at different angles.

In summary, grain sorting by bedforms within widely distributed, bimodal, and non-uniform sediment creates greater disparity between the separation of grain-sizes compared to unimodally distributed sediment. The formation of a network of fine laminations which are suggested to have further reduced the bed's hydraulic conductivity, created a very stable bed that resisted erosion. This led to the development of sediment starved small ripple bedforms, that were also unable make more sediment available and increase in size as they could not mobilize the fine sediment making up the laminations and erode down into the bed.

#### 4.5.6.2 *Armouring of the bed by fine lamination networks*

An alternative depiction of how fine-grained lamination networks stabilized the bed in Experiments 3 and 4 is the way in which they collectively acted as an armour layer. Sengupta (1979), who also recognized the higher threshold of motion of these deposits, describes similar majority fine-grained laminations. Sengupta (1979) explains that the increased threshold of sediment motion associated with these deposits is due to their homogeneity (Fenton and Abbot, 1977). The tight packing and interlocking of the fine angular nature of the grains in Experiment 4 not only create impermeable blockages to water flow within the bed, but they are also hard to erode. Allen 1982; Kirchner *et al.* (1990) and Buxton *et al.* (2014) explain how the increased friction acting between so many fine, interlocking grains results in an increase in the critical shear stress required to mobilise the fine laminations.

Fine sediment laminations as thin as 1 millimeter were able to resist being eroded by the shearing of the current or by scouring of migrating bedforms. The collective impact of all the laminations forming an extensive network across the bed meant they essentially acted as an armour layer made of fine sediment. They formed a barrier to the poorly sorted and more mobile sediment beneath (Figure 4.12), thus ensuring bedforms were sediment starved, which prevented any bedform growth for the duration of Experiment 4.

The fine laminations in Experiment 3 however, were relatively coarse compared to those in Experiment 4. As a result, sediment packing was less dense and less embedded, therefore, the lamination could be more easily eroded by the shearing flow. It also meant that the fine-grained laminations were more permeable than the fine laminations in Experiment 4, so the hydraulic conductivity was likely to be comparatively greater in Experiment 3. Consequently, the bed in Experiment 3 was not as stabilized, nor did it experience the total suppression of bedform growth.

#### 4.5.6.3 *Winnowing of the fine-grained fraction*

The impact of the stabilised bed caused by reduced hydraulic conductivity and the armouring of the bed by fine laminations, is apparent within the data collected for grain-size change through the bed. Figure 4.15 shows that in Experiments 1 and 2, there is a small but progressive reduction in the percentage of fine grains towards the top of the bed. Winnowing is the progressive removal of fine sediments from a bed (Mitchener and Torfs, 1996; Topping *et al.*, 2000ab; 2007; Wilcock and Kenworthy, 2002; Baas *et al.*, 2013). Winnowing of fines from the bed into suspension within the flow, is interpreted to have caused the reduction in fine sediment from the bed in Experiments 1 and 2. The deepest depth from which fines were removed was approximately ~6 cm, this being also the approximate depth to which bedforms commonly

scoured into the bed. Bedform scouring would intermittently expose deeper bed levels to the flow allowing winnowing to take place at a reduced rate. The deepest bed depths appear to not have experienced the removal of fine sediment as the bed was very rarely exposed to the flow at this level.

Conversely, Experiments 3 and 4 did not show clear evidence of winnowing having taken place. In fact, Figure 4.15 shows that within the top 3 – 5 cm of the bed, there was frequently higher percentages of fine sediment content recorded due to the presence of increased concentration of fine sediment laminations higher up in the bed in Experiment 3, and laminations confined to the top 5 cm of the bed in Experiment 4. The apparent reduced amounts of winnowing in Experiments 3 and 4 suggests the prevention of the removal of fine sediment, which is interpreted to be due to the bed becoming stabilized via reduced bed hydraulic conductivity and armouring of the bed by anastomosing networks of fine-grained laminations.

#### ***4.5.7 Bedform Diminishment***

The impact of the fine laminations on individual bedforms is interpreted to have promoted their diminishment and often their eventual disappearance. As previously described within the results section (Figures 4.11 & 4.13) and via the schematic representation below (Figure 4.19), this took place as the bedform trough encountered a fine sediment lamination. Due to the reduced mobility of the densely packed and interlocked grains that make up the fine sediment laminations, in Experiments 3 and 4, bedforms were often unable to erode and scour through the lamination.

Unable to maintain the same rate of scour, the bedforms reduced in steepness and were forced to migrate on top of the fine lamination, which as schematically shown in Figure 4.19, altered the bedform's migratory path into an upward trending angle of climb that further reduced the angle of the lee slope. Wilcock and Southard (1989) and Klaassen (1990) describe how less steep bedforms are less effective at eroding through armoured layers (though this research is based on coarse-grained armour layers), due to the reduced turbulence being generated in the wake of the shallower bedform. Less steep bedforms also experience a reduction in their ability to transport sediment from the stoss to the crest of the bedform. As a result, individual bedforms reduced further in height and subsequently became even less able to erode the fine sediment laminations.

Often bedforms were observed to reduce in size so that they sat within the wake of the upstream bedform, the separation zone of the upstream bedform altered the local flow conditions around the downstream bedform by generating increased levels of turbulence, diminishing the bedform until it was extinguished, as described by Gabel (2003).

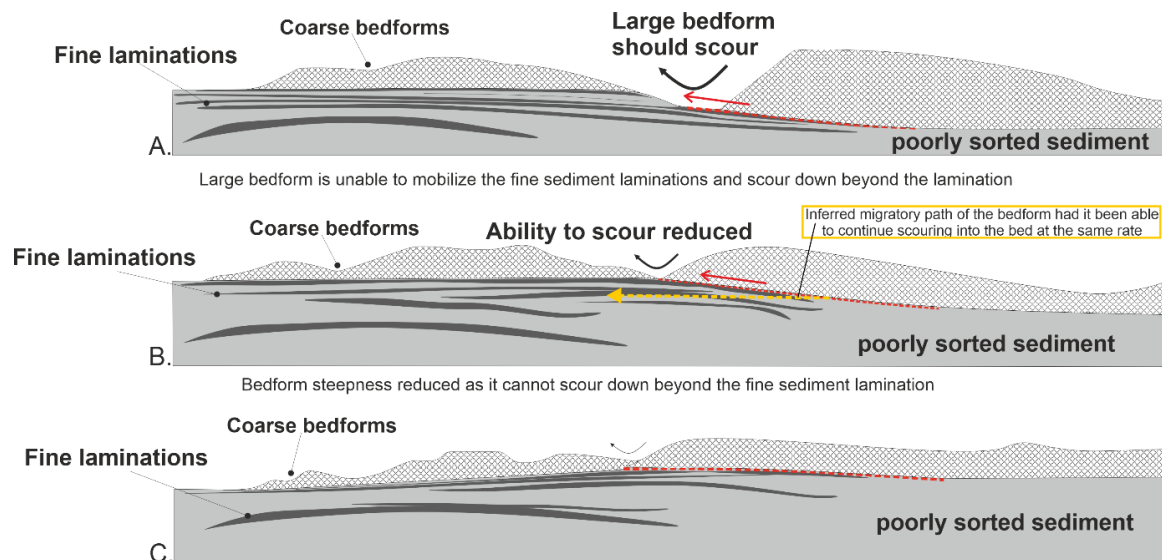


**Figure 4.19.** For clarity, a series of photographs were converted into a schematic diagram of a bedform interacting with a fine sediment lamination. The red dotted line highlights the steeper migratory path of the bedform as dictated by the immobile fine laminations. The yellow dashed line depicts the inferred migratory path of the bedform had it not encountered the fine sediment laminations and was able to continue scouring at the same rate and depth into the bed. **(A)** The bedform is unable to mobilize and erode the sediment making up the fine laminations. **(B – C)** The steepness of the bedform is reduced as its angle of climb steepens as it migrates over the fine lamination. Flow is from right to left.

#### 4.5.8 Bedform morphological variability

Bedforms in Experiment 3 were characterised by constantly altering individual bedform morphologies on relatively short time scales (5 – 10 minutes), and large variations in the types of morphologies that developed. Rapid and consistent bedform morphology change was not observed in any of the other experiments (Figure 4.8). Grain sorting of bimodal sediments by bedforms formed patches of finer and coarser sediment throughout the bed as well as fine-grained laminae. As bedforms migrated, they encountered differently sorted parts of the bed. Beds with variable vertical sorting profiles are known to alter bed roughness due to the preferential movement of finer grain fractions over coarser fractions (Lanzoni and Tubino 1999; Blom *et al.* 2003, Blom 2008). Size selective transport of sediment resulted in changes in bedform scouring capabilities as they migrated downstream and interacted with differently sorted parts of the bed.

The extent a bedform can erode into the bed partly determines its steepness and height (Reesink *et al.*, 2015), and therefore how it interacts with the flow. The scour depth varies

between different types of bedforms (Bridge, 1997; Bridge and Best, 1997; Alexander *et al.*, 2001; Bridge and Lunt, 2006). Experiment 3 consistently formed both ripples and dunes which, as explained previously, led to the interpretation that the bed state was transitional between the ripple and dune stability fields. It is proposed that the sorting of the bimodal sediment mixture into patches of sediment of different grain-sizes forced the development of smaller ripples by diminishing larger bedforms, by intermittently altering the ability of bedforms to scour into the bed. In a sediment mixture with a reduced grain-size distribution and the same median grain-size as Experiment 3, the disparity between the differently sorted parts of the bed would be less, having less impact on bedform scour and therefore bedform steepness, height and morphology. In summary, the combination of constant changes to a single bedform's scouring capabilities and therefore its steepness, height and the extent to which it protrudes into the flow and interacts with the flow, plus the continuous altering of local flow fields by other variable bedform morphologies, explains the highly variable bed state observed in Experiment 3.

## 4.6 Conclusions

This chapter reports on a series of experiments investigating how beds of non-uniform and bimodally distributed sediment mixtures impact bedform development and bedform dynamics.

This work has shown that:

1. Wide grain-size distributions can stabilize the bed by decreasing the bed's hydraulic conductivity. This agrees with previous work by Staudt *et al.*, (2017).
2. Grain sorting of bimodally-distributed sediment mixtures by bedforms, creates laterally extensive anastomosing networks of fine sediment laminations throughout the bed.
3. The laminations are formed of densely packed, interlocking fine-grained sediment that are less permeable than the poorly sorted parts of the bed that the laminations traverse. The fine laminations are interpreted to obstruct the passage of fluid through the upper 5 cm of the bed in Experiment 4, which further reduce the hydraulic conductivity of the bed, increasing its stability.
4. The fine laminations are likely to have a higher threshold of motion due to the increased friction acting between so many fine and interlocking grains. The laminations collectively act as an armour layer of fine sediment at the top of the bed, so that migrating bedforms were unable to mobilize the fine laminations and erode into the bed. As a result, they became sediment starved and were unable to increase in size.

5. Bimodal sediment mixtures of a narrower grain-size distribution did allow bedform development, however, bedform grain sorting of the bimodal sediment mixture, created an unevenly sorted bed that forced the development of smaller bedforms by diminishment of larger bedforms.
6. The ongoing inability of a bed to develop bedforms as a result of the bed becoming stabilized due to a wide grain-size distribution altered the manner in which equilibrium was achieved. It has been shown that equilibrium can be one of ongoing bedform suppression. However, the discussion as to whether a naturally variable system can be classed as in a highly dynamic state of equilibrium, remains unresolved.
7. Bedform phase diagrams that use the median grain-size of sediment in the bed, are poor predictors of bedform stability fields of beds with wide grain-size distributions.

## Chapter 5. Cross-stratified turbidite beds in the Grès de Peïra Cava, SE France

### 5.1 Introduction

The Upper Eocene and Lower Oligocene Grès d'Annot Formation, also known as the Annot Sandstones, crops out in south-eastern France in the Alps-Maritimes. The formation is a widespread turbidite succession that preserves a sand-rich, deep-marine depositional system that was deposited in the southern areas of the Alpine Foreland Basin (Joseph and Lomas, 2004). The Peïra Cava outlier, cropping out some 20 km north of Nice, is a particularly well-studied part of the Annot Sandstone Formation, and is considered an archetypal example of a sand-rich, ponded mini-basin (Pickering and Hilton, 1998; Amy, 2000). It was a key site in determining seminal facies models and quantification of system architectural patterns (Bouma, 1962; Mutti, 1992) that have been used as benchmarks for interpreting the deposits of subsurface systems worldwide.

This study investigates decimetre-scale cross-stratification in sandstone beds of the Peïra Cava Basin fill. Despite 50 years of research taking place studying this basin, the occurrence of often-superb examples of cross-stratification has received relatively little attention. While cross-stratification is rarely encountered in turbidite systems (Arnott, 2012), in certain sections of the Peïra Cava basin it is relatively common. The detailed facies analysis (Bouma, 1962) and the establishment of high resolution basin-wide stratigraphic correlations (Amy, 2000; see also Amy *et al.*, 2000; 2004; 2007) jointly provide a framework of the geological context of the wider system in which to study these beds characterised by decimetre-scale cross-stratification.

This chapter aims to answer the following questions:

- What are the different styles of cross-stratification in the Peïra Cava basin?
- Can specific bedform types be associated with the development of cross-stratification?
- How well do existing facies tract models describe the spatial occurrence of cross-stratified units?
- What does cross-stratification tell us about the flow conditions of the currents that deposited them?

## 5.2 Geological setting

### ***5.2.1 Plate tectonic framework of the southern Alpine Foreland Basin.***

Prior research into this well-known sand-rich turbidite system has provided detailed information regarding the geological setting and regional context of the Peïra Cava turbidites (Dercourt *et al.*, 1986; Ravenne *et al.*, 1987; Dewey *et al.*, 1989; Sinclair, 1997; Pickering and Hilton, 1998; Joseph and Lomas, 2004; Amy *et al.*, 2007). The Annot sandstone is part of the south-western margin of the western Alpine mountain belt and was deposited in the southern Alpine Foreland Basin (also known as the Palaeogene-Provençal Basin). The Alpine Foreland Basin is located to the west of an Alpine thrust belt and north of the Pyrenean–Provençal mountain belt (Joseph and Lomas, 2004), formed as a result of the collision between Africa and Eurasia. The late Eocene – early Oligocene saw thrusting, folding and faulting of the foreland basin, resulting in the development of complex inter-basin topography and the formation of mini-basins, such as Peïra Cava. Figure 5.1a is a chronostratigraphic diagram for the Palaeogene Provençal Basin. Of principal interest are the three lithostratigraphic units known collectively as the 'Nummulitic Trilogy', or the 'Priabonian Trilogy' (Boussac, 1912), which sit upon a Mesozoic 'basement' of Middle and Upper Jurassic black and mid-Cretaceous black shales and limestones (Joseph and Lomas, 2004). The oldest unit of the Nummulitic Trilogy is the transgressive Nummulitic limestone (also known as the Calcaires Nummulitique), which sits unconformably upon the Mesozoic basement (occasionally via an intervening fluvial or shallow marine interval); the succeeding Blue Marls (also known as the Marnes Bleues) are made up of hemipelagic marlstones and represent basin deepening (Ravenne *et al.*, 1987; Joseph and Lomas, 2004). The youngest unit of the interval is the Annot Sandstones, which principally comprise siliciclastic turbidites and debrites fed northwards from the Sardinia-Corsica Massif via deltaic feeder systems (Figure 5.1b) (Pickering and Hilton, 1998; du Fornel *et al.*, 2004). The gravity flows travelled parallel to the foreland basin's axis, albeit with significant secondary deflection, into tectonically confined sub-basins across SE France and NW Italy, depositing channelized and sheet-like turbidites. The turbidites onlap onto the underlying Blue Marls.

Pickering and Hilton (1998) distinguish two depositional systems entering the Southern Alpine Foreland Basin: the "West Basin-Floor System" and the "East Basin-Floor System" which includes the Peïra Cava mini-basin (Figure 5.1b). Their model describes infilling of sub-basins that were disconnected from one another by structural highs associated with thrusting within the Cretaceous substrate, except for narrow corridors through which sediment could be transported

(Apps, 1987). After the infilling of both the eastern and western basins, Pickering and Hilton (1998) propose that a period of spill occurred over the intra-basinal topographic highs that separated the sub-basins. Du Fornel *et al.* (2004) presented a regional correlation of the Annot Formation, across the southern part of the basin, providing a more detailed analysis of the diachronous onset of filling of the sub-basins; Figure 5.1c shows a geological map of the structural elements of the main Grès d'Annot sub-basins, including the Peira Cava system.

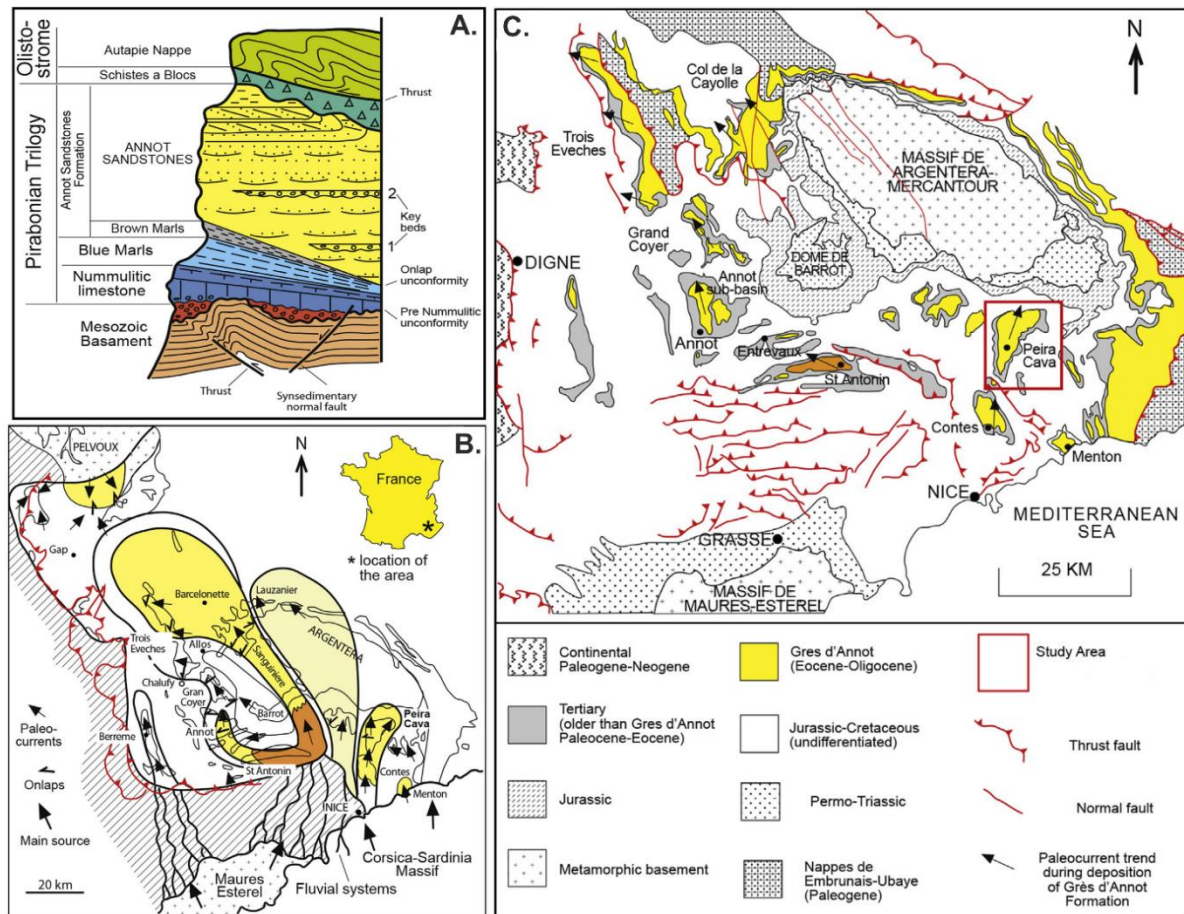


**Figure 5.1. (A)** Chronostratigraphic diagram for the Palaeogene Provençal Basin that shows three lithostratigraphic units collectively known as the 'Nummulitic Trilogy' or the Priabonian Trilogy' (Modified by Boussac, 1912, from Cunha *et al.* (2017)). **(B)** Paleogeography of the main Annot Sandstone sub-basins (from Joseph and Lomas, 2004, modified by Cunha *et al.* (2017)) **(C)** Geological map of the structural elements of the main Grès d'Annot sub-basins, including the Peira Cava system (from Du Fornel *et al.* (2004), modified by Cunha *et al.* (2017)).

### 5.2.2 Depositional setting - the Alpine Foreland Basin morphology and topography

Although the Southern Alpine Foreland Basin covers an area of over 5000 km<sup>2</sup>, early studies considered the basin's topographic character to be simple, without intra-basinal

topography (Kuenen *et al.*, 1957; Bouma, 1962). However, using onlap relationships and structural data, studies by Elliott *et al.* (1985), Ravenne *et al.* (1987), Hilton (1994), Pickering and Hilton (1998) and Apps (1987) reinterpreted the basin as having had a complex topography that was a key control on the locus of sand deposition. Sinclair (1994) and Kneller and McCaffrey (1998) described how confined turbidity currents within a basin might interact with basin topography: turbidity currents might experience local sedimentation on encountering the basin slope, current reflection and deflection, and flow ponding. Evidence for all these phenomena are found in the Annot Sandstone Formation. These include: distinctive onlap facies associated with the basin slope (Ravenne *et al.*, 1987; Amy, 2000; McCaffrey and Kneller 2001; Amy *et al.*, 2004; 2007; Cunha *et al.*, 2017); inconsistent palaeoflow patterns that follow the basin margin and complex palaeoflow patterns that are suggestive of reflection and deflection; and, finally, thick mud caps that are interpreted to indicate flow ponding – i.e., that the finest sediments carried by the turbidity currents were locally contained by topography (Amy, 2000; McCaffrey and Kneller 2001; Amy *et al.*, 2004; 2007; Aas *et al.*, 2010; 2014; Cunha *et al.*, 2017).

### **5.2.3 Correlation framework - Peïra Cava basin stratigraphy**

The Peïra Cava mini-basin fill outcrops in a NNE-SSW trending syncline with a steep western margin onlap (Ravenne *et al.*, 1987; McCaffrey and Kneller, 2001; Amy *et al.*, 2004, 2007). The outcrop is 12 km in length and 4 km wide, covering an area of ~130 km<sup>2</sup> (Pickering and Hilton, 1998) (Figure 5.2a). Various studies have described the thickness of the stratigraphic components of the 'Nummulitic Trilogy' in the Peïra Cava basin. Amy (2000), Amy *et al.* (2000; 2004) and Pickering and Hilton (1998) estimated the Peïra Cava sandstone to be approximately 1.2 km thick, the underlying Blue Marls formation 150 – 200 m thick and the Calcaires Nummulitique Formation 40 – 50 m thick. Figure 5.2b shows an east-west cross section of the Peïra Cava syncline showing the progressive onlap of the turbidite sandstones onto the Blue Marls towards the West.

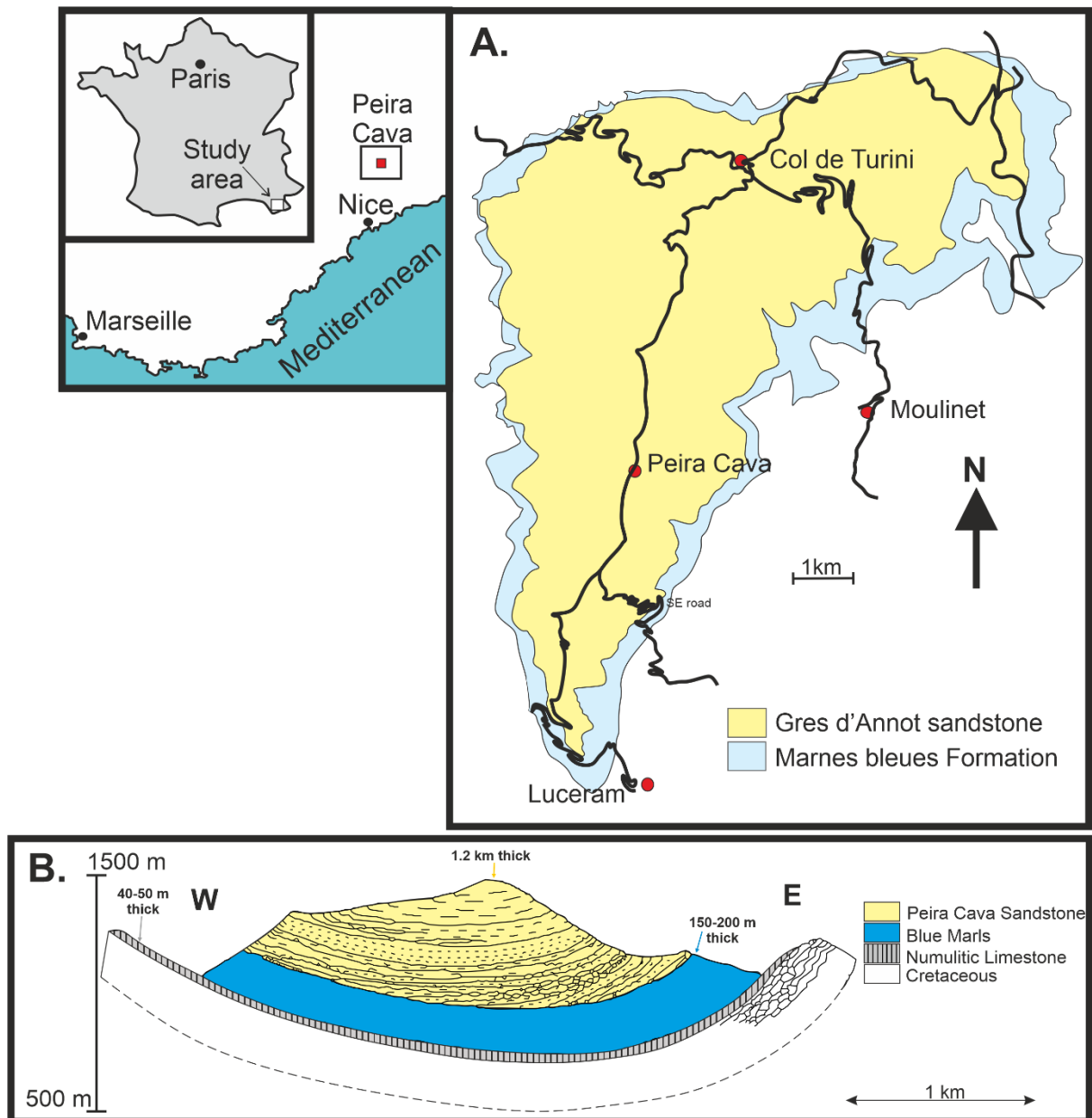


**Figure 5.2:** (A) Map of the Peira Cava basin. (B) geological map of the Grès de Peira Cava stratigraphic sequence via a schematic structural cross-section (modified from Ravenne *et al.*, 1987).

Bed-to-bed correlations were first established across the Peira Cava outlier, in a 420 m stratigraphic interval, exposed over a 10 km by 6 km area by Amy (2000) (also see Amy *et al.*, 2007) (Figure 5.3). Amy (2000) measured 8 sections along the eastern and western flanks of the basin and correlated between them by matching distinctive vertical sequences and by tracing marker beds (MU1-MU17 in Figure 5.3).

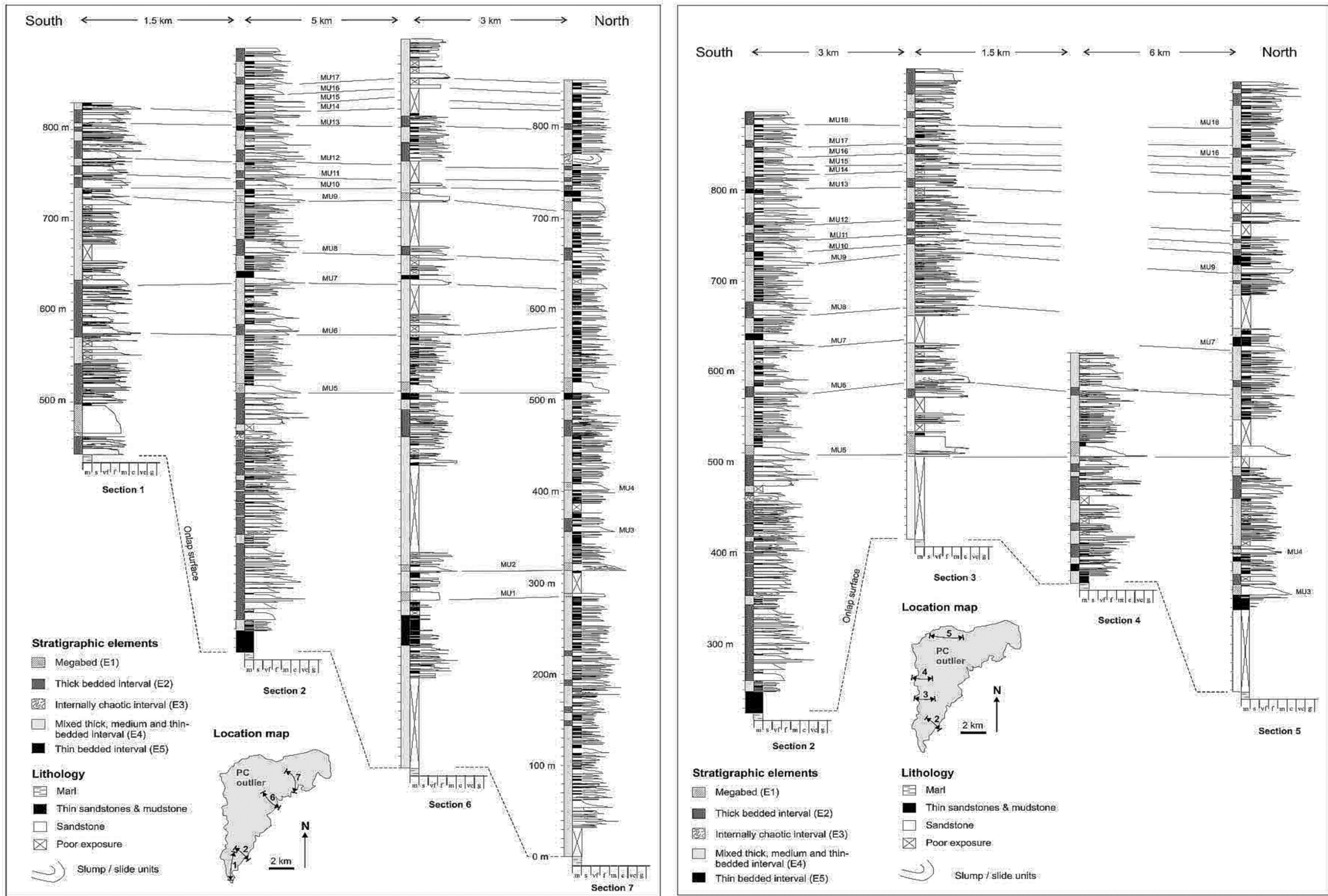


Figure 5.3. Bed to bed correlations established by Amy (2000) across the Peira Cava outlier, in a 420 m stratigraphic interval, exposed over a 10 by 6 km area (also see Amy et al., 2007).

#### **5.2.4 Basin architecture and depositional facies of Peira Cava**

The basin-fill comprises coarse-grained, sand-rich, scour-and-fill sandstone facies associated with the inbound slope in the proximal, southern part of the system; channel-to-lobe transition zones are not preserved. These base-of-slope facies step back with the inbound slope. Between 1 – 3 km from the inbound margin, the proximal facies change to tabular or sheet-like deposits of sandstone and mudstone couplets on the basin-floor (Amy, 2000; Amy *et al.*, 2007).

A wide range of facies and a wide range of grain-sizes (from gravels to mudstones) are observed in the Peira Cava outcrops (Bouma, 1962; Amy 2000; Cunha *et al.*, 2017). While many facies schemes have been developed to define turbidite deposits based on their sedimentological characteristics (e.g. Bouma, 1962; Lowe 1982) (Figures 5.4b and c), the facies scheme defined by Mutti (1992) has been the basis for recent studies carried out in the Peira Cava basin (Amy, 2000; 2007; Kneller and McCaffrey, 2003; Cunha *et al.*, 2017) and is also used in the present research. Mutti's (1992) facies scheme is described below and in Figure 5.4a which provides accompanying interpretations of the transport and depositional processes.

- The F1 facies describes a muddy matrix containing large floating clasts which may concentrate towards the top of the bed and shows no evidence of basal scour. The F1 facies is interpreted to be deposited by cohesive debris flows.
- The F2 facies describes a matrix of mud, sand and gravel, containing large floating clasts towards the base of the bed. Deep scours at the base of the bed are common. The F2 facies is interpreted to have been deposited by hyper-concentrated flows.
- The F3 facies consists of clast supported conglomerates that are associated with very coarse-grained sandstones (> 4 mm). The F3 facies is normally massive or inversely graded and is interpreted as being deposited by hyper-concentrated flows.
- The F4 facies is characterised by gravel and coarse-grained sandstone that contains thick parallel laminations interpreted as the deposits of traction carpets. The F4 facies is interpreted as the deposit of a high-density turbidity current that experienced rapid freezing. It is equated to the S2 division defined by Lowe (1982).
- The F5 facies also contains gravel and coarse-grained sandstones. It is relatively poorly sorted compared to F8 deposits and generally structureless. The F5 facies can normally be graded (either crudely or well-graded) or ungraded. The deposit is interpreted as the deposit of a high-density turbidity current that experienced sediment deposition due to rapid or gradual fallout of suspension. It is equated to the S1 division defined by Lowe (1982).

- The F6 facies comprises coarse-grained deposits containing cross-stratification and/or parallel lamination. They are well-sorted deposits and are commonly ungraded. They are interpreted to be the deposits of coarse-grained high-density turbidity currents, and the internal stratification is formed by traction with or without bedform development.
- The F7 facies contains fine-grained sandstones and is characterised by thin and coarse-grained parallel laminations that commonly fine upwards indicating waning flow conditions. Occasionally the F7 facies may also show inverse grading. It is interpreted as the deposit of a low-density turbidity current.
- The F8 facies contains structureless and medium to very-fine grained sandstones. It is generally structureless and often normally graded. The F8 facies is interpreted as the deposit of a low-density turbidity currents that experienced either en-masse or gradual fallout of sediment from suspension. It equates to the T<sub>a</sub> division of the Bouma sequence.
- The F9 facies is characterised by medium to very-fine grained sandstones containing parallel lamination and ripple cross-lamination. It is interpreted as the deposit of low-density turbidity currents via a combination of traction and sediment fallout from suspension. The F9 facies includes the T<sub>b</sub>, T<sub>c</sub> and T<sub>d</sub> divisions of the Bouma Sequence (Figure 5.4b).

Amy (2000), Amy *et al.* (2000) and Cunha *et al.* (2017) have all applied Mutti's (1992) facies scheme to the turbidites of the Peira Cava Basin. Amy (2000) provides detailed descriptions of the occurrence of different facies types (defined by Mutti, 1992) in the Peira Cava basin and adds two additional facies. Cunha *et al.* (2017) define different bed types associated with different sequences of facies (defined by Mutti, 1992). A brief overview of Amy (2000) and Cunha *et al.* (2017) and their description of the Peira Cava turbidites follows.

The F0 and F10 facies were added to Mutti's (1992) scheme by Amy (2000). The F0 facies consists of contorted or slumped beds, which are interpreted to have been deposited due to freezing of a slump due to friction at its base. The F10 facies contains massive mudstones and marls which cap the turbidite deposit. It is interpreted as the deposits of background hemipelagite sedimentation that deposits due to suspension fallout of sediment when there is no longer any current activity. Turbidite mudstone caps may be distinguished from hemipelagite units based on colour, with the latter often having a characteristic blue colour.

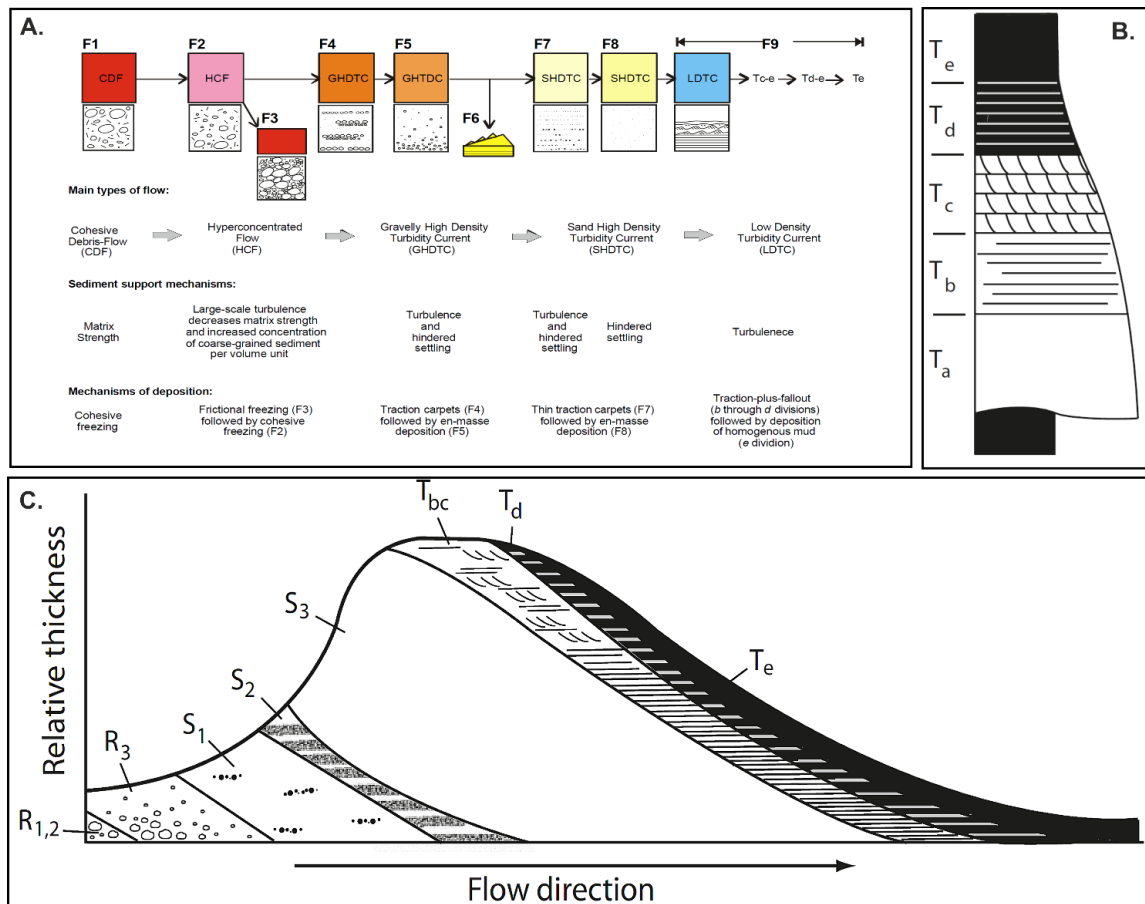


**Figure 5.4.** (A) Mutti's (1992) turbidite depositional sequence scheme (B) Idealized 'Bouma' sequence (Bouma, 1962) from Sumner et al. (2012). (C) Diagram showing an idealized turbidite depositional sequence after Lowe (1982), containing, tractional structures (R<sub>1</sub>); inversely graded gravel (R<sub>2</sub>); normally graded gravel (R<sub>3</sub>); coarse sand also with tractional structures (S<sub>1</sub>); coarse sand containing thin horizontal layers (S<sub>2</sub>); structureless coarse sand that may be graded (S<sub>3</sub>); sand containing tractional structures (T<sub>bc</sub>) interlaminated silt and mud (T<sub>d</sub>); and structureless mud (T<sub>e</sub>), from Sumner et al. (2012).

Cunha et al. (2017) grouped turbidite beds of the Peira Cava basin fill into different six bed types based on sequences of facies defined using Mutti's (1992) scheme (Figure. 5.5). Bed Types 1 and 2 are classified as 'massive sandstones deposited by dense flows'. They are characterised by thick and massive F3 facies which pass up into the F9 facies. Type 1 beds contain mudstone breccias in the basal part of the bed. The thick F5 interval is interpreted to have been deposited by dense basal parts of the flow, and the mudstone breccia intervals by rapidly decelerating flows. The F9 deposit is associated with the turbulent upper region of the bipartite current.

Type 3 and 4 beds are described as 'massive sandstones overlain by tractive structures indicating bypass'. Type 3 beds are characterised by massive F5 basal facies which are overlain by the F6 and F7 facies that are associated with bedform cross-stratification and parallel laminations

formed by traction. Bed Type 4 does not contain the F5 interval, only the F6 and F7 facies. Cunha *et al.* (2017) interpret Bed Type 4 as the lateral evolution of Bed Type 3. Both Bed Types 3 and 4 pass upwards into the F9 facies.

Bed Types 5 and 6 are defined as laminated fine-grained sandstones indicating ponding processes. Type 5 beds are characterised by massive medium-grained sandstone (F8 facies) which is followed by the finer sands of the F9 facies. Cunha *et al.* (2017) note that Bed Type 5 is equivalent to the Bouma T<sub>a</sub> – T<sub>e</sub> sequence. Bed Type 6 is characterised by a laminated F8 facies that does not contain the F9 fine sediment facies, instead the deposit passes upwards into mudstone.

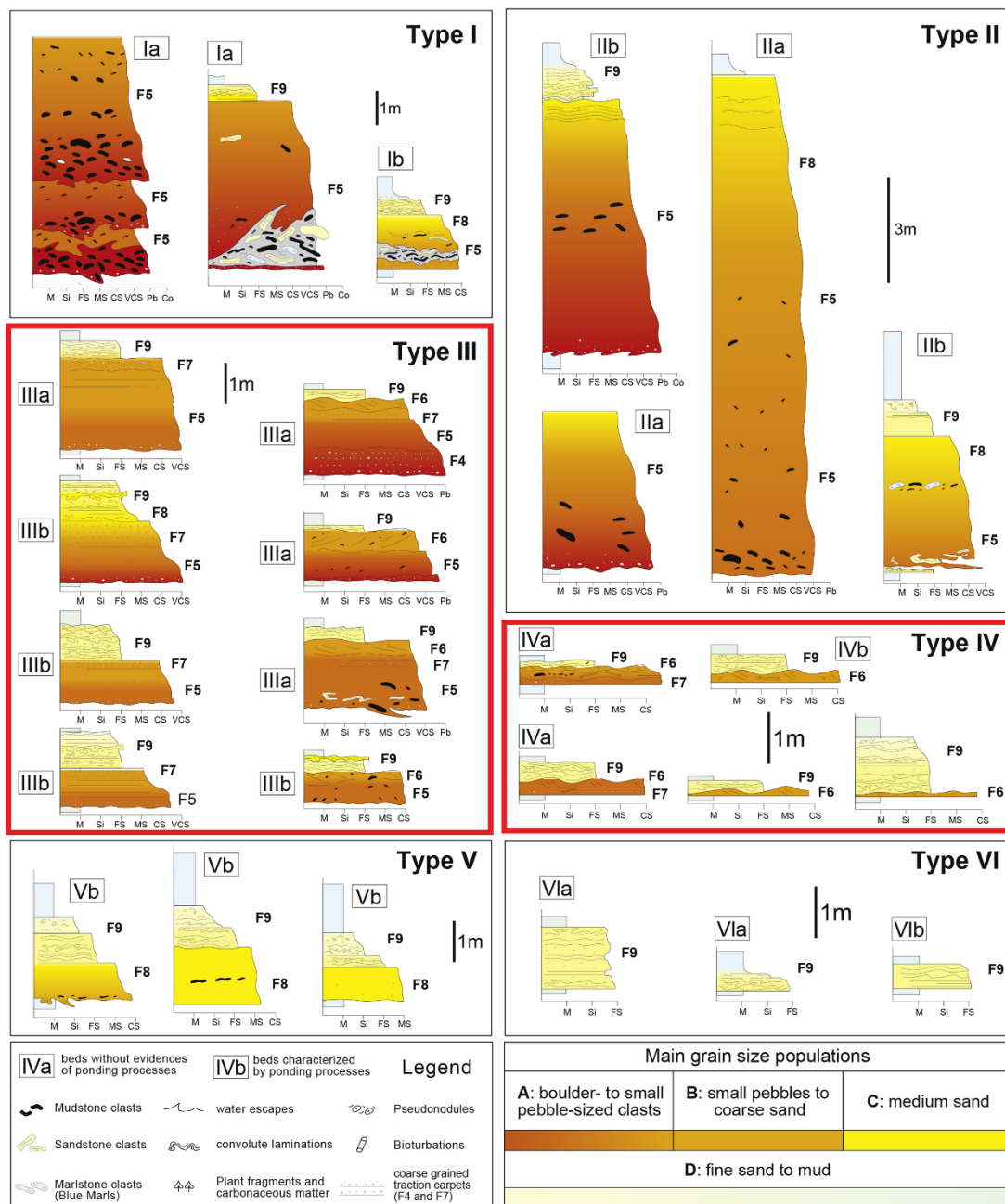


Figure 5.5. Cunha *et al.* (2017): six bed types identified in the Peira Cava outlier.

### ***5.2.5 Cross-stratified units of the Peira Cava basin: previous facies descriptions and models***

Previous research documented the occurrence of the decimetre-scale cross-stratification in the Peira Cava basin fill and provided descriptions of the cross-stratified units and models of the processes that lead to their development.

Mutti (1992) defined the occurrence of two types of cross-stratification in the Peira Cava basin fill: 1) cross-stratification that makes up the entire bed thickness and is bound by a distinct grain-size break into the fined-grained F9 facies comprising ripple and parallel laminations. This type of cross-stratification is interpreted to indicate significant sediment bypass due to the abrupt fining across the F6 to F9 divisions boundary (Mutti and Normark, 1987; Mutti, 1992). 2) F5 facies transitioning abruptly into the F6 facies across a grain-size break. The F6 facies is then overlain by the F9 rippled and laminated interval. This second type of cross-stratification is interpreted as evidence of flow transformation that causes a crudely sorted F5 facies to evolve into the comparatively well-sorted and cross-stratified interval, where the finer grains experience winnowing by a bypassing flow which then deposits its sediment downstream Mutti (1992). Mutti's (1992) facies tract model (Figure 5.6a) associates the F6 facies with thick sandy deposits downstream.

Kneller and McCaffrey (2003) proposed conceptual models for the longitudinal density structure of the currents and their evolution. Figure 5.6b shows two examples of downstream deposition by turbidity currents with distinct longitudinal variations in concentration (Kneller and McCaffrey, 2003). Figure 5.6a (i) depicts deposition due to flow velocity non-uniformity, i.e. spatial differences in flow velocity, and Figure 5.6b (ii) depicts deposition due to flow unsteadiness, i.e. changes in flow velocity over time. In both cases, the presence of cross-stratification and tractional structures is interpreted to be associated with significant bypass of sediment down-system, leading to thickening of correlative bypass intervals down-system. In Kneller and McCaffrey's (2003) facies tract model, three different styles of cross-stratification occurrence can be identified (cf. Lowe (1982)): 1) The cross-stratified F6 interval abruptly coarsens up from the F5 interval. This grain-size break is interpreted to signify the current's increased capacity to transport previously deposited coarser grains from further upstream in traction. 2) The bypassing flow may also rework the entire F5 facies to form a bed that is dominated by traction structures. 3) Cross-stratification may occur at the base of the F5 interval, where it is interpreted to have formed due to unsteady flow rates that led to a period of early bypass (Figure 5.6b).

As outlined above, Cunha *et al.* (2017) have grouped the turbidite beds of the Peira Cava basin fill into different bed types, based on the depositional sequence of different facies defined by Mutti (1992). Bed Types 3 and 4 contain the cross-stratified F6 intervals (highlighted by the red boxes in Figure 5.5) which are interpreted to be the deposits of “megaripple” bedforms. Cunha *et al.* (2017) explain that Bed Type 4 is the lateral (cross-current) evolution of Bed Type 3; it is interpreted as recording the lateral deceleration of the same flow that deposits the F5 facies. Unlike Mutti (1992) and Kneller and McCaffrey (2003), Cunha *et al.* (2017) use three logs (only) across a 10 km transect from the proximal to distal end of the basin to show that the cross-stratified beds apparently do not lead to significant bypass of sediment downstream.

Other models which describe the occurrence and development of cross-stratification in turbidites include those of Sumner *et al.* (2012), Tinterri and Tagliaferri (2015), Stevenson *et al.* (2015), Arnott and Al-Mufti (2017), and Tinterri *et al.* (2017). These are discussed further in the Discussion section of this chapter.

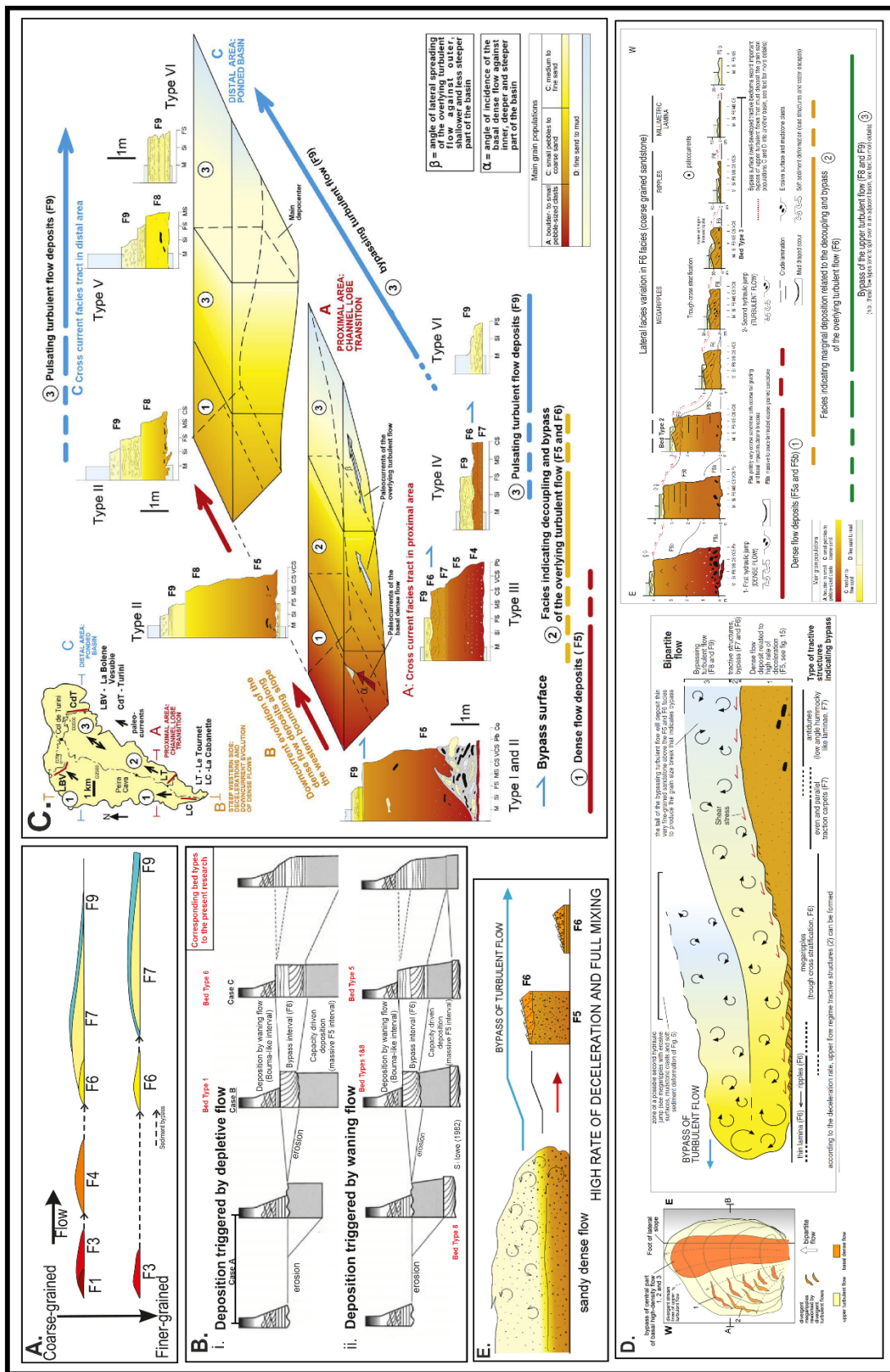


Figure 5.6. (A) Mutti (1992) facies tract model. (B) Kneller and McCaffrey (2003) Down-dip profiles of the proximal region of deposits. (C) paleogeographic scheme and facies tracts of the turbidite deposits of the Annot Sandstone in the Peira Cava sub-basin (from Cunha et al. (2017)). The letters

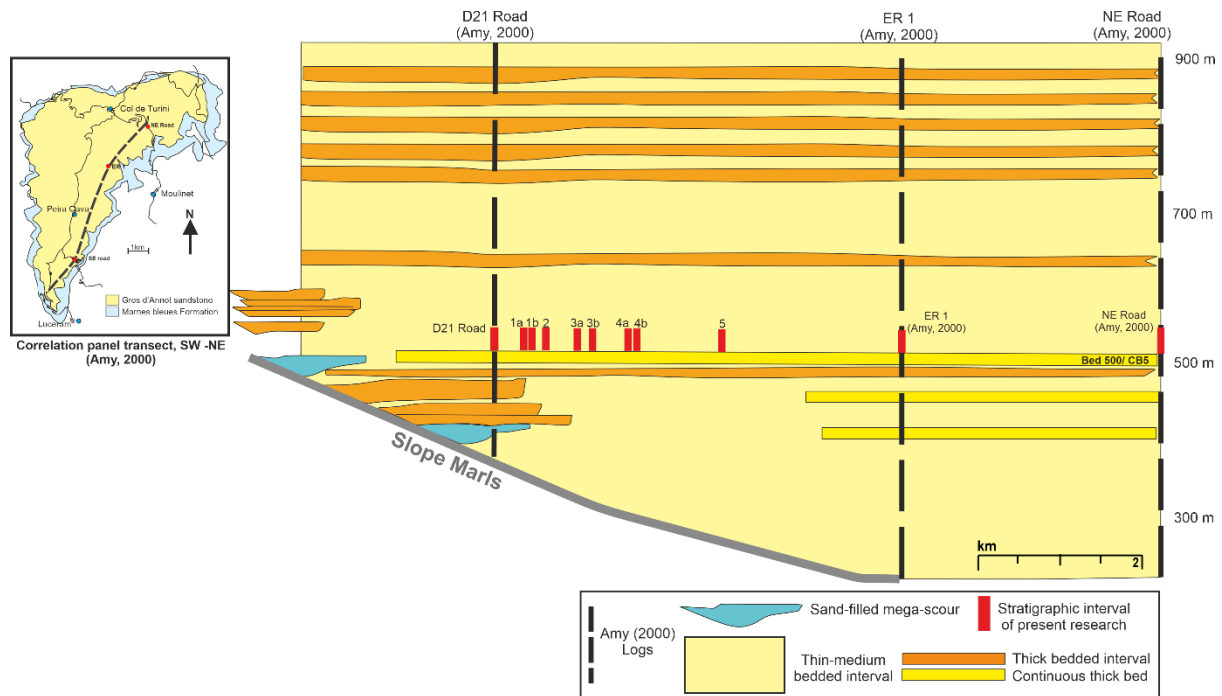
*A, B and C indicate the facies tracts in the proximal area, along the steep western margin and in distal area respectively. (D) from Tinterri et al. (2017): Far left – location of bedforms within the Priabonian-Rupelian, Ranzano Sandstone, formed by a deflected flow towards the NW. Middle - Depiction of the progressive formation of tractive structures related to the shear stress produced by the bypassing upper turbulent flows. Far right – Asymmetrical cross current facies tract and related processes of turbidite deposits containing cross-stratified beds. Paleocurrents are directed towards the page. (E) Downstream evolution of cross-stratified beds in the Marnoso-Arenacea Formation, Italy, Tinterri and Tagliaferri (2015).*

## **5.3 Collection of field data**

### ***5.3.1 Field site locations and stratigraphic setting***

As previously noted, Amy (2000) (see also Amy *et al.*, 2000; 2004; 2007) previously established bed-to-bed correlations at 8 localities throughout the Peira Cava basin fill (Figure 5.3); the key marker beds established enable new correlative sections to be easily identified and logged. For the present research, eight new sections in the Peira Cava outlier were studied. They were selected for the relative abundance of cross-stratified beds and for the confidence that they could be correlated due to the close presence of a key marker bed ('CB5' of Amy (2000), here called bed 500). Six of the eight new sections were measured and drawn in the field at a scale of 1:10 and they comprise the 36 m of stratigraphy directly above marker bed 500. Figure 5.7 represents the correlative framework established by Amy (2000) along a SW – NE transect through the basin. The intervals studied in the present research are included in Figure 5.7 to illustrate their stratigraphic setting in relation to the wider system.

The occurrence of ~0.5 m thick mud caps in the proximal – medial parts of the system, and the occurrence of ~ 1 m thick mud caps in the proximal end of the system suggests that ponding of flow has taken place during the deposition of the stratigraphic interval studied in the present research. Further, the marker bed (Bed 500) which immediately precedes this stratigraphic interval, has a distinct mud cap (~5 m thick) that can be correlated throughout the system, and is clear evidence of ponding having taken place in association with this stratigraphic interval (Amy, 2000).



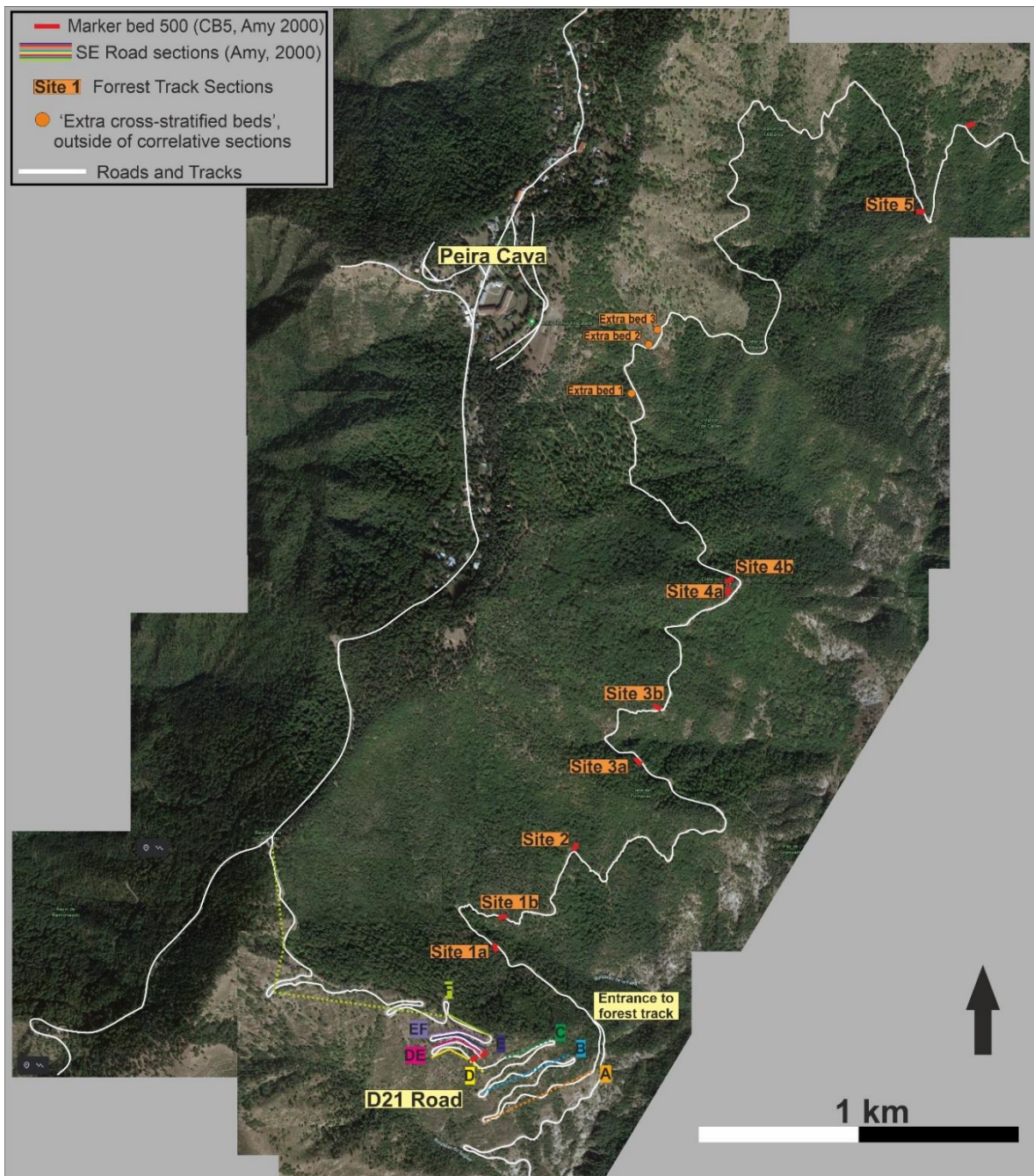
**Figure 5.7.** Diagram shows the stratigraphic interval and locations of correlative sections 1 – 5 within the stratigraphic context of Amy’s (2000) correlation of the wider system along a SW – NE transect. Figure modified from Amy (2000).

Table 5.1 lists each site, its coordinates, the thickness of the section and an approximation of its location within the system along a proximal to distal transect. Bed 500 was used to determine the start of the section in the field. Beds were named in relation to bed 500, such that each thick bed was sequentially numbered from 500 (Key marker bed) to 511. The thinner beds in between the thick beds were numbered in association with the preceding thick bed, for example, 501.1, 501.2 etc. Table 5.1 also describes parts of some sections on the D21 Road (previously logged by Amy (2000)), that lie outside of the correlative interval studied for the present research. These intervals were found to contain excellent examples of cross-stratified beds that were logged and sketched, but not correlated. These particular beds are named based on the section they are in (following nomenclature by Amy, 2000), and numbered based on how many cross-stratified beds there are in the section (e.g. ‘Bed F1, 2, 3 etc.’).

Figure 5.8 shows each log locality along the forest track and identifies the location of bed 500. Figure 5.8 also shows sections A – F along the D21 Road. The correlative intervals are defined by a solid line, the dotted lines lie outside of the correlative interval, but contain cross-stratified beds which are documented in the present research. Sections D – F are correlative with the section 1a – 5 along the forest track. The ‘Extra beds 1 – 3’ on the forest track also lie outside of the correlative interval and contain cross-stratified beds; they have not been previously logged.

**Table 5.1.** A summary of each site name, its location denoted by coordinates, the thickness of the stratigraphic interval studied and an approximation of each site's position within the basin.

Site Names	Site coordinates (Lat, Long)	Thickness of section (m)	Basin Setting
<b><i>D21 Road (Amy, 2000)</i></b>			
<i>9a (Amy, 2000)</i>	43.910477,7.364751	120 m (outside correlative interval)	Proximal
<i>9b (Amy, 2000)</i>	43.909457,7.3636830	122 m (outside correlative interval)	Proximal
<i>9c (Amy, 2000)</i>	43.909959,7.3628461	69m (outside correlative interval)	Proximal
<i>9d (Amy, 2000)</i>	43.909202,7.3603034	0-35 m (outside correlative interval). 35-84 m (within correlative interval).	Proximal
<i>9de</i>	43.909550,7.3601854	~45 m correlated in field & not measured	Proximal
<i>9e (Amy, 2000)</i>	43.909584,7.3602766	50 m (within correlative interval). 40 m outside correlative interval).	Proximal
<i>9ef</i>	43.909886, 73606092	~50 m correlated in field & not measured	Proximal
<i>9f (Amy, 2000)</i>	43.910778,7.3590481	10 m exposed (within correlative interval). 250 m (outside correlative interval).	Proximal
<b><i>Forest Track</i></b>			
<i>1a</i>	43.912688,7.3606038	36	Proximal
<i>1b</i>	43.913381,7.3609659	36	Proximal
<i>2</i>	43.915277,7.3638117	~36m correlated in field & not measured	Proximal
<i>3a</i>	43.918020,7.3661399	36	Proximal
<i>3b</i>	43.918020,7.3661399	36	Proximal
<i>4a</i>	43.922935,7.3698556	10	Proximal - medial
<i>4b</i>	43.922935,7.3697448	14	Proximal - medial
<i>5</i>	43.933264,7.3842430	35	Medial
<i>East Ridge (Amy,2000)</i>	43.952994,7.3842430	38	Medial - distal
<i>NE Road (Amy, 2000)</i>	43.976613,7.4091053	44	Distal



**Figure 5.8.** Map of all site locations

### 5.3.2 Sedimentary logging

As sites along the forest track were logged (logs 1a – 5), data on grain-size, sorting, sedimentary structures, bed thickness and bed contacts were collected. Grain-size classifications are listed in Table 5.2, based on the Wentworth scale. Logging of the sections was carried out using a Jacob’s Staff fitted with a rotatable laser pointer, compass and spirit level to allow accurate measurements of stratigraphic thicknesses (Patacci, 2016). Logging through individual beds could be accurately carried out using a ruler. Once logged, bed-to-bed correlations were established between the sections. Correlative beds were distinguished by comparing the logged stratigraphy

and using the similarities in the sequences and internal character of beds. Thicker sandstone beds were useful for correlating between relatively proximal and distal parts of the system, as they are more laterally continuous. Across shorter distances (20 – 40 m), beds could be correlated by their similar internal sedimentary character. Bed-to-bed correlations were also carried out over yet shorter distances on the D21 road which cuts into the hillside and exposes repeated intervals of the correlative sections (Sections D – F). Over 10 – 45 metres, correlative beds could also be determined using the modified Jacob’s Staff: thus, whilst standing on the edge of the road, the correctly-angled Jacobs Staff was used to point the laser across onto another exposed section and accurately correlate between individual beds.

**Table 5.2.** Classification scheme of sediment grain-size (represented by the median grain-size, applied to the Peira Cava turbidites, based on the Wentworth scale

<i>Sediment divisions</i>	<b>Median grain-size (µm)</b>
<i>Clay</i>	< 0.15
<i>Silt</i>	0.15 – 1.5
<i>Very fine lower sand (VFL)</i>	63
<i>Very fine upper sand (VFU)</i>	125
<i>Fine lower sand (FL)</i>	190
<i>Fine upper sand (FU)</i>	250
<i>Medium lower sand (ML)</i>	375
<i>Medium upper sand (MU)</i>	500
<i>Coarse lower sand (CL)</i>	750
<i>Coarse upper sand (CU)</i>	1000
<i>Very coarse lower sand (VCL)</i>	1500
<i>Very coarse upper sand (VCU)</i>	2000
<i>Gravel (G)</i>	≥ 4000

Additional highly detailed logs (drawn in the field at 1:10 scale) and field sketches were drawn of correlative beds containing cross-stratification contained within the 36 m stratigraphic section, and for cross-stratified beds found outside this stratigraphic interval. The grain-sizes that made up the cross-stratification were also recorded. Due to grain sorting processes by the bedform, a finer and a coarser fraction could be distinguished. The approximate grain-size of the finer and coarser fractions was measured for each cross-stratified bed. Both Bouma’s (1962) sequence and Mutti’s (1992) facies scheme was used to characterise the beds containing cross-stratification.

In all cases, the Jacob's Staff was used to assess whether the lenticular cross-stratified beds were positive relief structures and/or were infilling a concave upward scour surface that might have been shallow and/or wide enough to not be obvious through observation of the outcrop alone. The Jacob's Staff was also used to check whether the surface of the cross-stratified bed was characterised by positive relief in instances where there was uncertainty – for example, when the bed top was too high up for clear observation.

### ***5.3.3 Bedform geometric analysis***

Set heights of cross-stratified intervals were measured, as were bedform wavelengths where successive bedform profiles were preserved. However, some error was involved in measuring bedform wavelengths since bedform lee faces were often oriented at an angle to the outcrop. This meant that the angle the bedform is observed from may not have been perpendicular to its direction of migration, thus increasing the measured wavelength. The orientation of the bedform could be estimated based on palaeoflow reconstructions of bedform cross-stratification planes exposed in three-dimensions (see below). Because the dip of cross-stratification planes was rarely parallel to the outcrop face, this confirms that the bedform wavelength measurements are likely to underestimate the true bedform wavelength. For comparison, ripples heights and wavelengths that are preserved toward the top of beds containing cross-stratification were also recorded. An estimation of bedform three-dimensionality was achieved by comparing the spread of the palaeoflow data associated with the cross-stratification with other palaeoflow indicators such as ripples and sole marks.

### ***5.3.4 Palaeocurrent measurements***

Palaeocurrent measurements were collected from both ripples and thicker intervals of cross-stratification; 317 paleocurrent measurements were taken from ripples and sole marks which were corrected for structural tilt by rotation about the strike of bedding, then compared with previous paleoflow calculations taken by Amy (2000) and Cunha *et al.* (2017). Palaeoflow analysis was also carried out for 30 cross-stratified beds where the plane of the cross-stratification was exposed in three-dimensions. For example, exposures of individual foresets of cross-stratification or, on several beds, the rock had broken in multiple directions exposing the cross-stratification at different angles. Figure 5.9 shows examples of cross-stratification planes exposed in three dimensions.



**Figure 5.9.** *Examples of cross-stratification planes exposed in 3-dimensions.*

## 5.4 Results

### 5.4.1 Stratigraphic correlations

Figure 5.10 shows the logged sections 1 – 5 (collected during this study), and the correlative logged sections of the D21 Road, the East Ridge and the NE Road (which were previously logged by Amy (2000) and incorporated into this study). The bed numbers in orange indicate cross-stratified beds, or beds that thin and thicken at the top of the bed, which are indicative of bedforms. The correlations associated with these beds (also coloured orange) show how individual cross-stratified beds may be tracked from proximal regions to distal regions. The sections are easy to correlate through the most proximal reaches of the system (D21 Road to Site 3b), due to the good exposure of the sections allowing the identification of the internal sedimentary character of the beds; the presence of cross-stratification and positive relief bed tops were notable bed features. Through the medial-distal reaches of the system the quality of the exposure is slightly reduced as in some locations the internal bed structures are more weathered.

However, where correlation could not be made with confidence based on the bed character alone, the distinctive hemipelagic intervals were useful markers that were easily correlated throughout the system. The correlation in Figure 5.10 shows that there is a moderate overall thickening of the stratigraphic interval down-system. However, the detailed correlations of cross-stratified beds in detail (Figure 5.11) show that bed thickness essentially remains constant at all sites, except for Bed 512 which thins down-system.

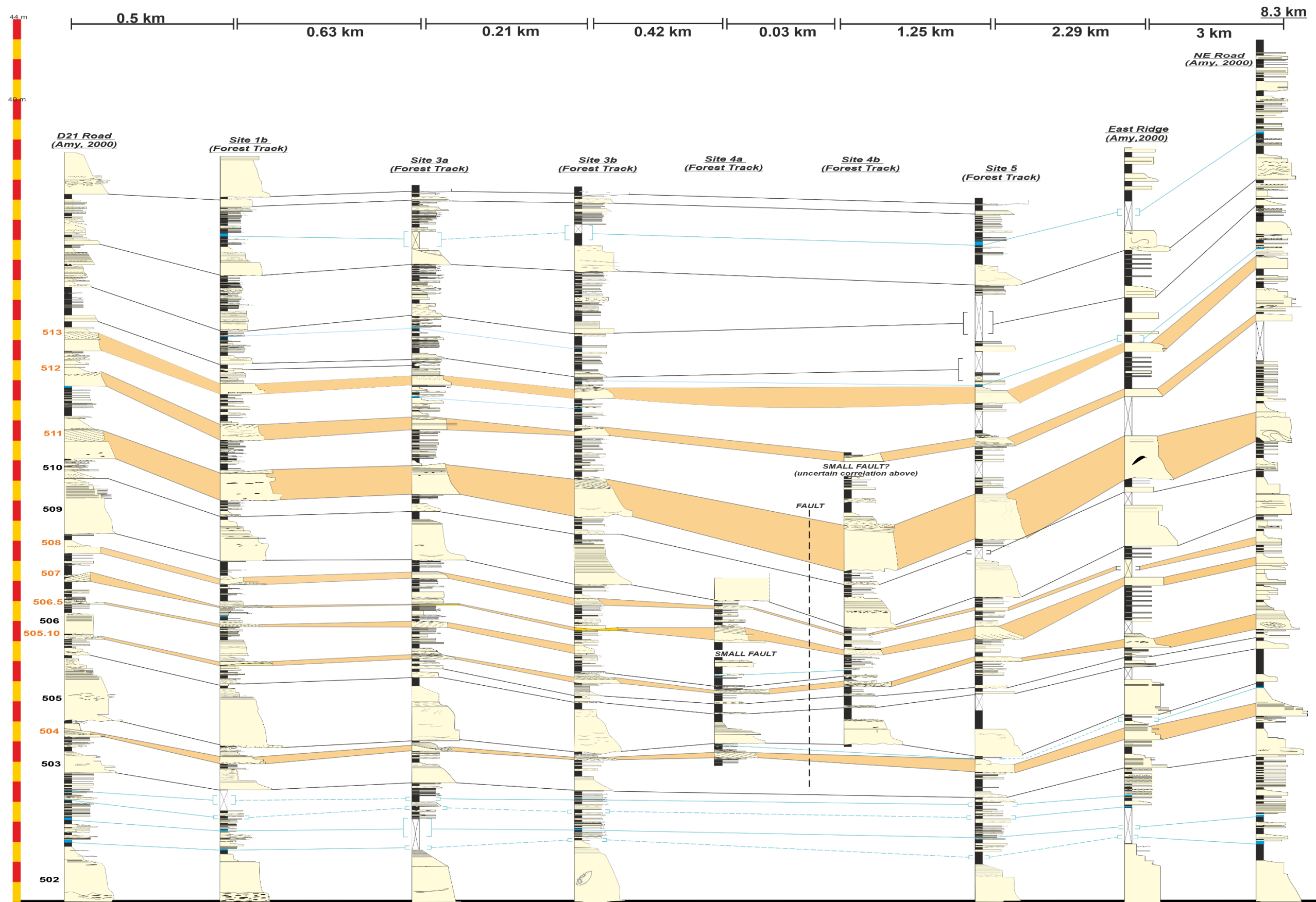


Figure 5.10. Bed-to-bed correlations over 8 km through the Peira Cava Basin. Correlations highlighted in orange correlate cross-stratified beds. Blue correlations indicate the presence of hemiplegic sediment that was often coloured yellow, white or blue.

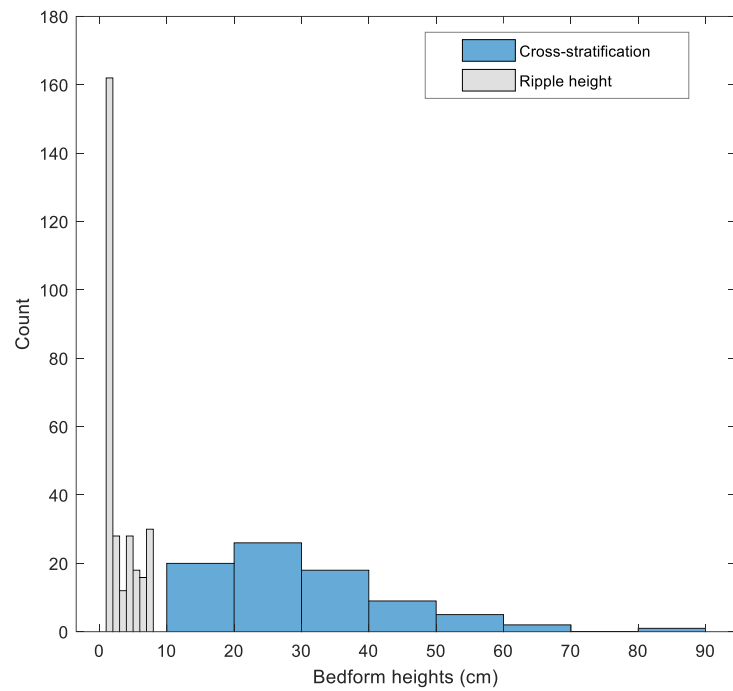


Figure 5.11. Correlations of cross-stratified beds

#### ***5.4.2 Comparison of the different bedforms found in the Peira Cava basin fill***

As outlined previously, the F9 facies of Mutti's (1992) facies scheme includes the  $T_b$ ,  $T_c$  and  $T_d$  divisions of the Bouma Sequence. The  $T_c$  division of the Bouma sequence includes cross-laminated rippled fine-grained sands (Figure 5.4b). The  $T_c$  facies is found throughout the Peira Cava system (Mutti, 1992; Amy 2000); however, the ripples of the  $T_c$ /F9 facies are not the only style of ripple bedform occurrence in Peira Cava. While examining the cross-stratified intervals, coarser-grained ripples were found to have formed superimposed upon individual foresets of the larger-scale cross-stratification and on top of the preserved larger bedforms. These superimposed ripples are made from the same grain-sizes that form the larger cross-stratification. Examples of this style of ripple development includes: Beds B1 and B2 (Figure 5.14), Bed C4 (Figure 5.22) and Bed D511 (Figure 5.14). Ripple development in coarse-grained sands in association with larger-scale cross-stratification of the same grain-size does not comply with either the F6 or F9/  $T_c$  facies. As a result, the present research defines a new facies of interbedded ripple cross-lamination and decimetre-scale cross-stratification made of the same coarse-grained sediment.

An aim of this research is to define the type of bedform associated with the decimetre-scale cross-stratification found in the Peira Cava basin fill. In order to do so, dimensional data was collected from ripple cross-stratifications to make distinctions between bedform types based on their dimensions. As stated previously, ripples of the F9/ $T_c$  facies are found throughout the Peira Cava basin fill, and ripples were also occasionally found as part of the newly defined interbedded ripple cross-lamination and decimetre-scale cross-stratification facies. Comparing the bedforms of the Peira Cava basin fill, there is a clear difference between the size of the ripple bedforms of the F6/  $T_c$  facies and the ripples formed in association with cross-stratification, and the bedforms that formed the larger-scale cross-stratification, as seen in Beds B1 and D511 (Figure 5.14), Bed B2 (Figure 5.21) and Bed C4 (Figure 5.22). Measured bedform heights and wavelengths of ripples and cross-stratified intervals also show a distinction between their dimensions (Figures 5.12 and 5.13).



**Figure 5.12.** *Ripple and cross-stratification height.*

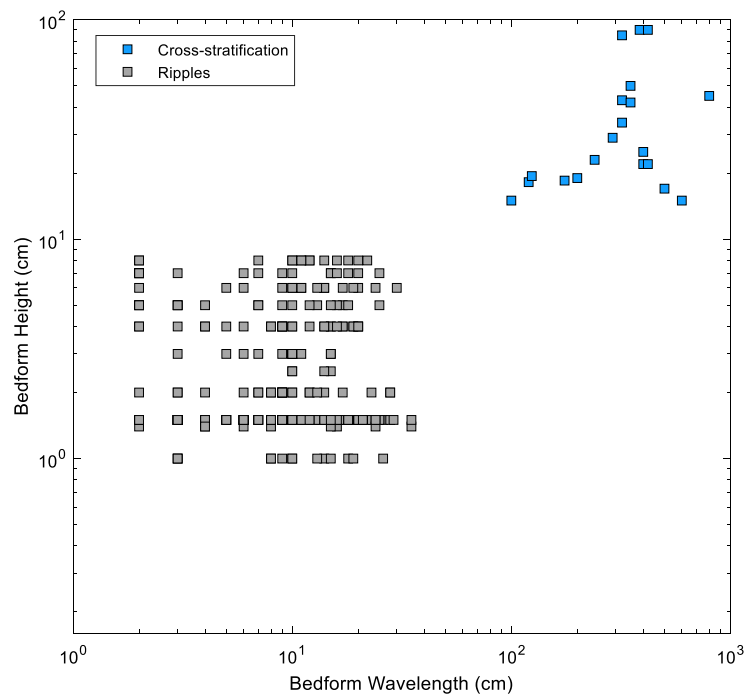


**Figure 5.13.** *Heights vs wavelengths of both Ripples and cross-stratified intervals.*

Ripple dimensional measurements are based only on fully preserved ripple forms so as not to underestimate the true ripple dimensions. Obtaining true height measurements that characterise the bedforms associated with the decimetre-scale cross-stratification was often impossible as the cross-stratified sets were commonly truncated at the top. Therefore, height

measurements of cross-stratified sets are likely to be an underestimate. Where the bedform profile shape is preserved, approximate measures of wavelength were recorded, but, as previously noted, the plane of cross-stratification planes were rarely oriented perpendicular to the outcrop face. This means that bedform wavelength measurements associated with the decimetre-scale cross-stratification are also likely to be underestimates. With this in mind, it is likely that the dimensional distinctions between ripples and the bedforms which developed the larger cross-stratified beds in Figures 5.12 and 5.13 are actually greater than is plotted. Further discussion to determine the type of bedform that might have deposited the decimetre-scale cross-stratification is presented in the Discussion section of this chapter.

### ***5.4.3 Types of Cross-stratified beds and facies associations***

Detailed logs, field sketches and photos of cross-stratified beds were collated into a catalogue of multiple examples of cross-stratification found in the Peira Cava basin fill (Figures 5.14 – 5.26). Ten newly recognised cross-stratified bed types are categorised (Figure 5.27). Descriptions and examples of each type of bed are given below. Analysis of the depositional processes associated with the different bed types is presented in the Discussion section of this chapter.

**Bed Type 1 (Figure 5.14):** Cross-stratification is restricted to the very coarse top of a relatively thick bed (100 – 200 cm thick). There is an abrupt grain-size change from the fining-up interval below (F5 facies) into the coarser cross-stratified interval above (F6 facies). The foresets alternate between coarser and finer sediments, but the most abundant grain-size that characterises the cross-stratified interval is the coarser fraction. The top of the bed may thin and thicken to produce positive relief geometries (Figure 5.14). The topography at the top of the cross-stratified interval is often infilled by fine-grained ripples and laminations, or has a very thin mud interval (0.5 – 2 cm thick) directly above the cross-stratified bed.

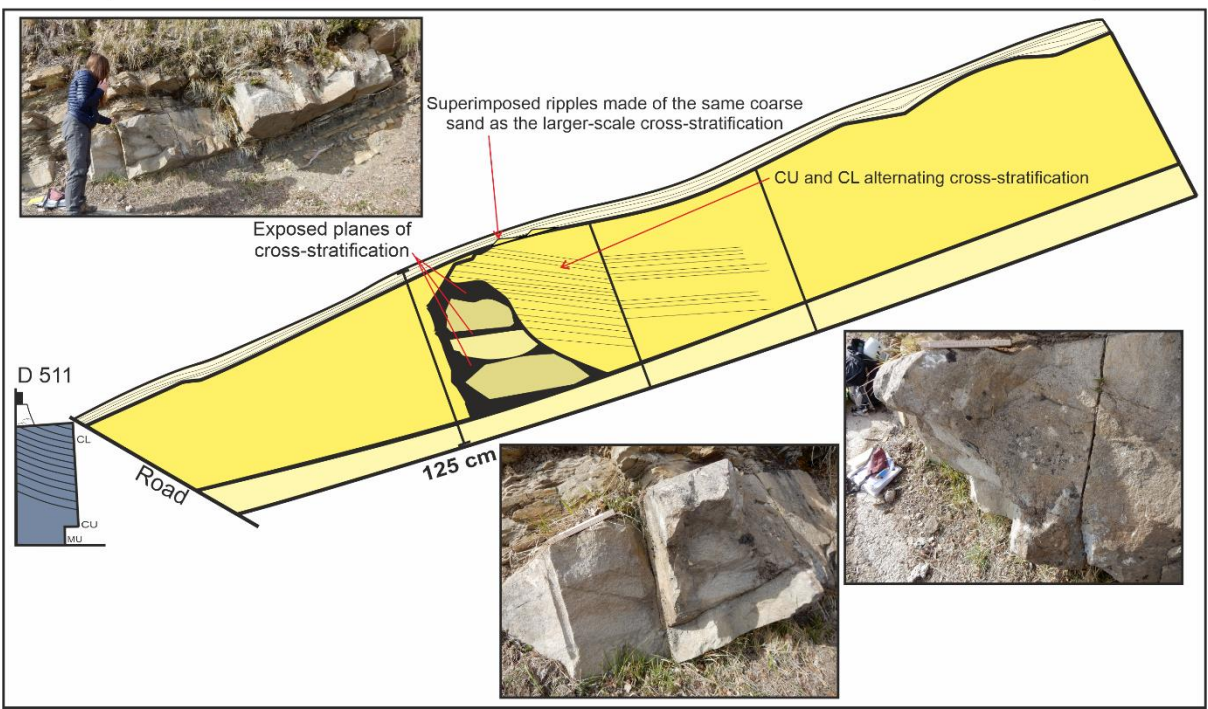
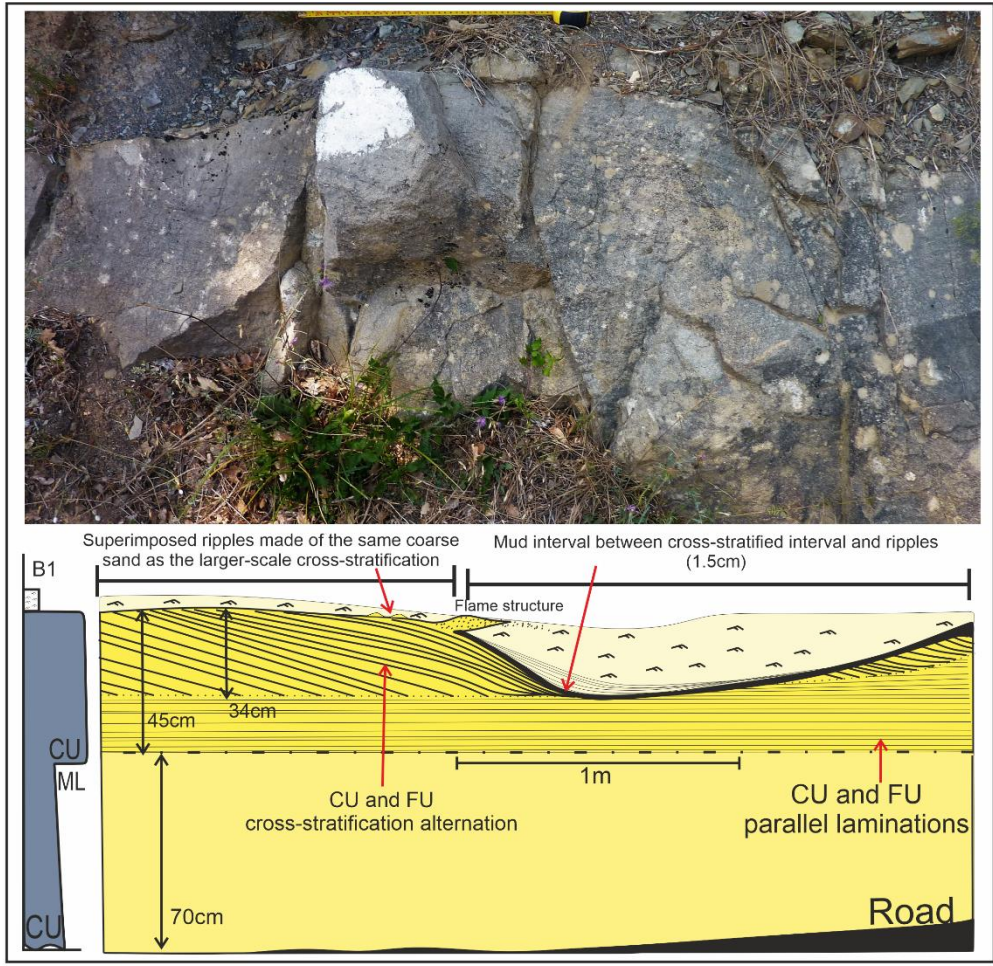
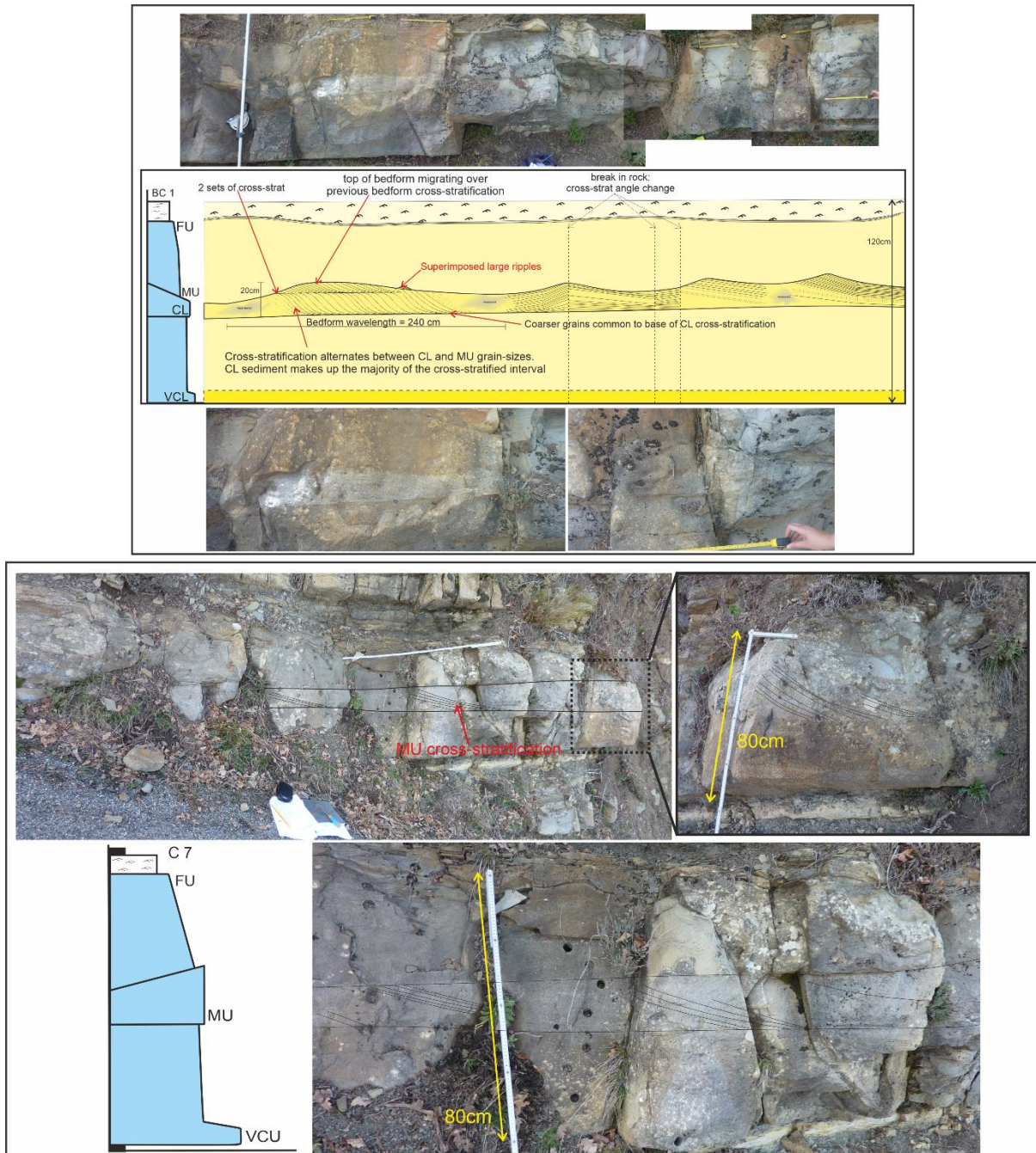


Figure 5.14. Bed Type 1.

**Bed Type 2 (Figure 5.15):** A cross-stratified interval sits in the middle of a thick (80 – 120 cm) amalgamated bed (Figure 5.15). The bottom interval that fines up is F5 facies, which abruptly coarsens into the cross-stratified interval (F6) as in Bed Type 1. However, the sequence of Bed Type 2 shows another F8 interval that was deposited directly on top of the cross-stratified interval, preserving the shape of the bedform profile.



**Figure 5.15.** Bed Type 2.

**Bed Type 3 (Figures 5.16 & 5.17):** Cross-stratification occupies the whole bed, which is relatively thin (10 – 55 cm). There is only one set of cross-stratification. The bed top is wavy while the base is flat, causing the bed to thin and thicken with a regular wavelength (Figure 5.16). Grain-size of the foresets often shows a wide distribution alternating between very fine and coarse sediments; the coarser fraction is the most common grain-size in the bed. The cross-stratified bed topography is often infilled by a fine-grained ripple interval or has a very thin mud interval directly above the cross-stratified bed.

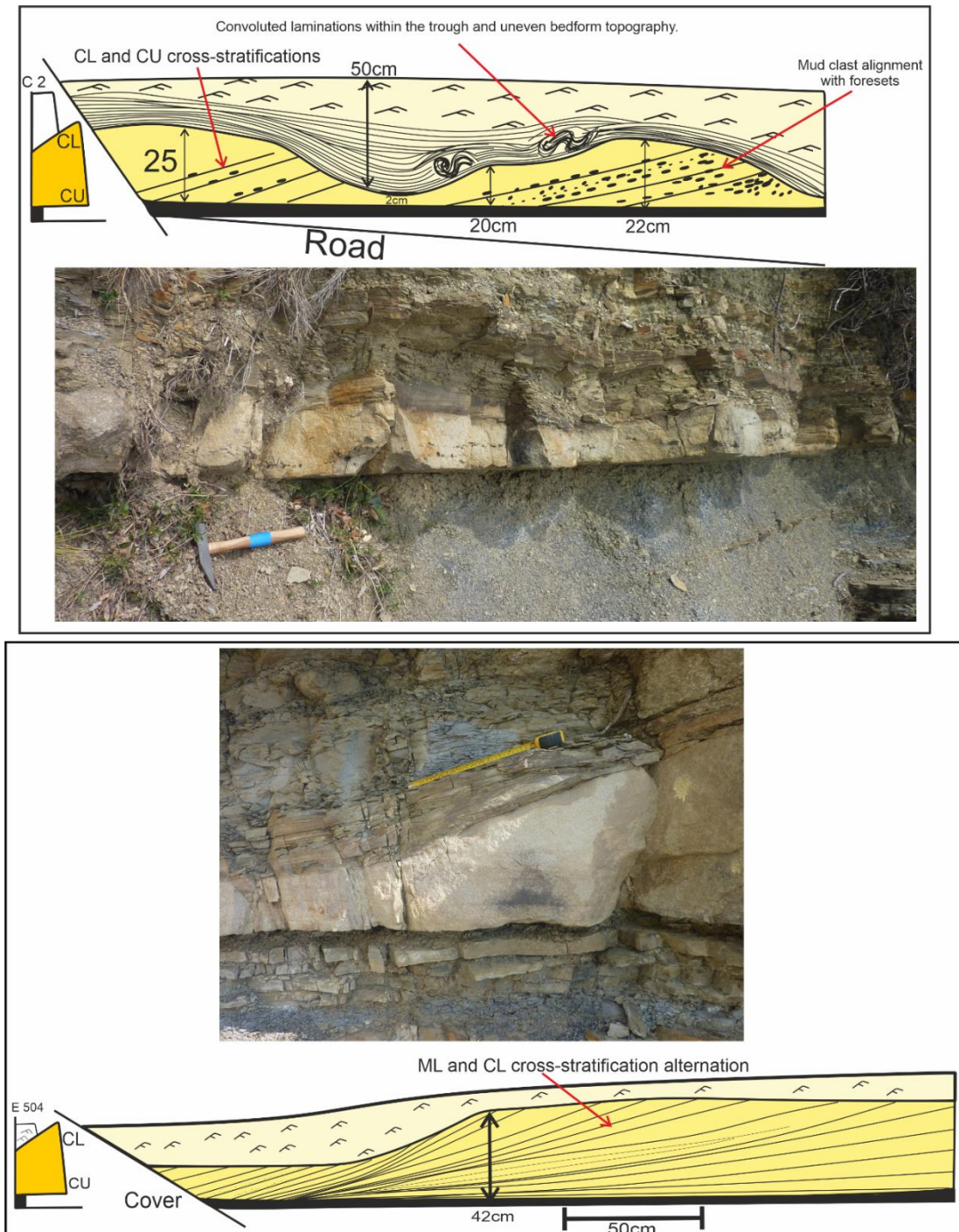


**Figure 5.16.** Bed Type 3.

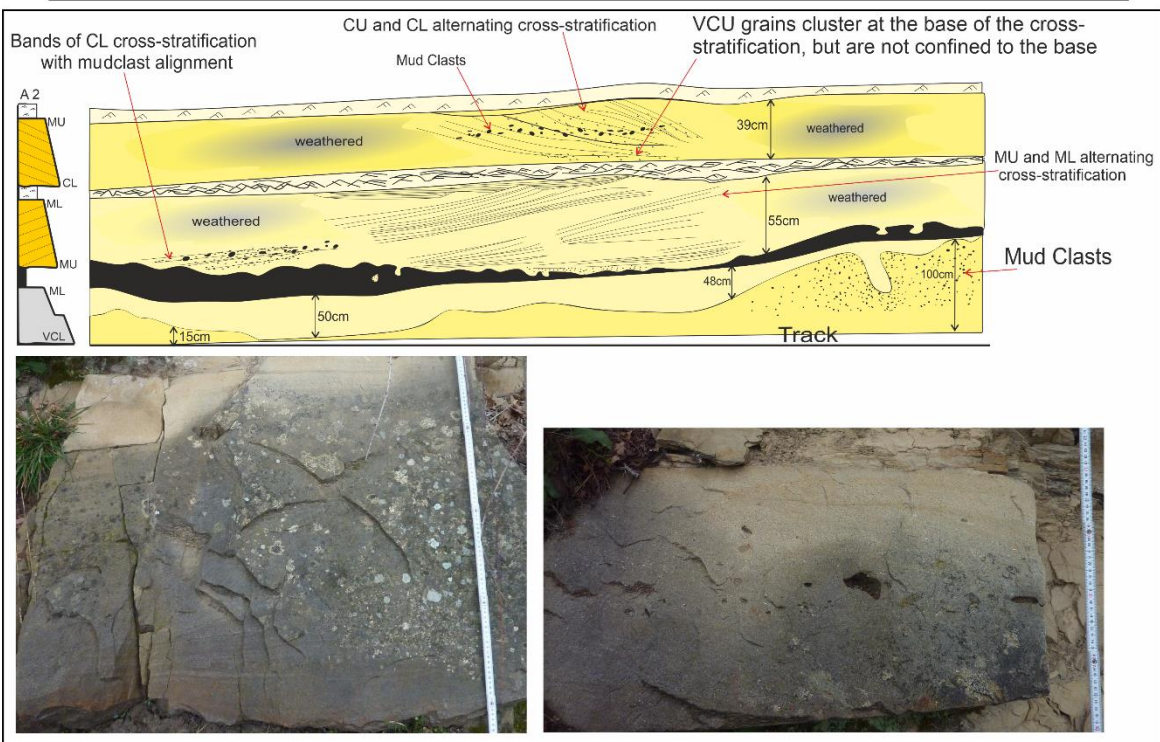
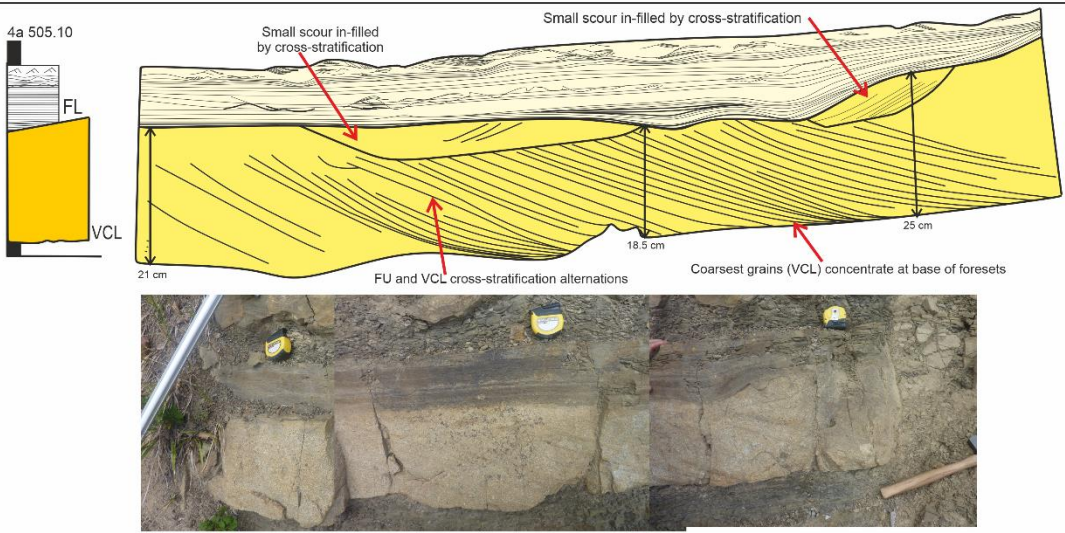
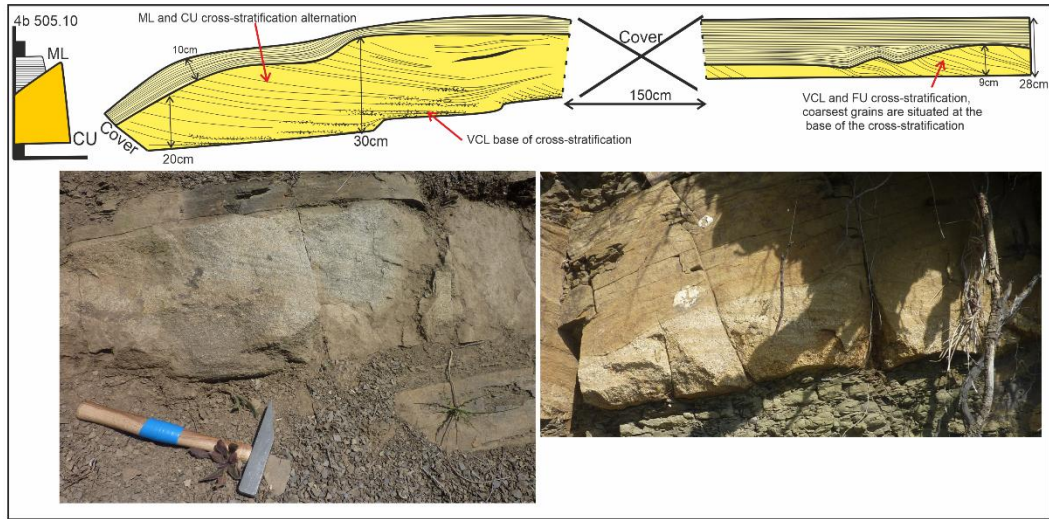
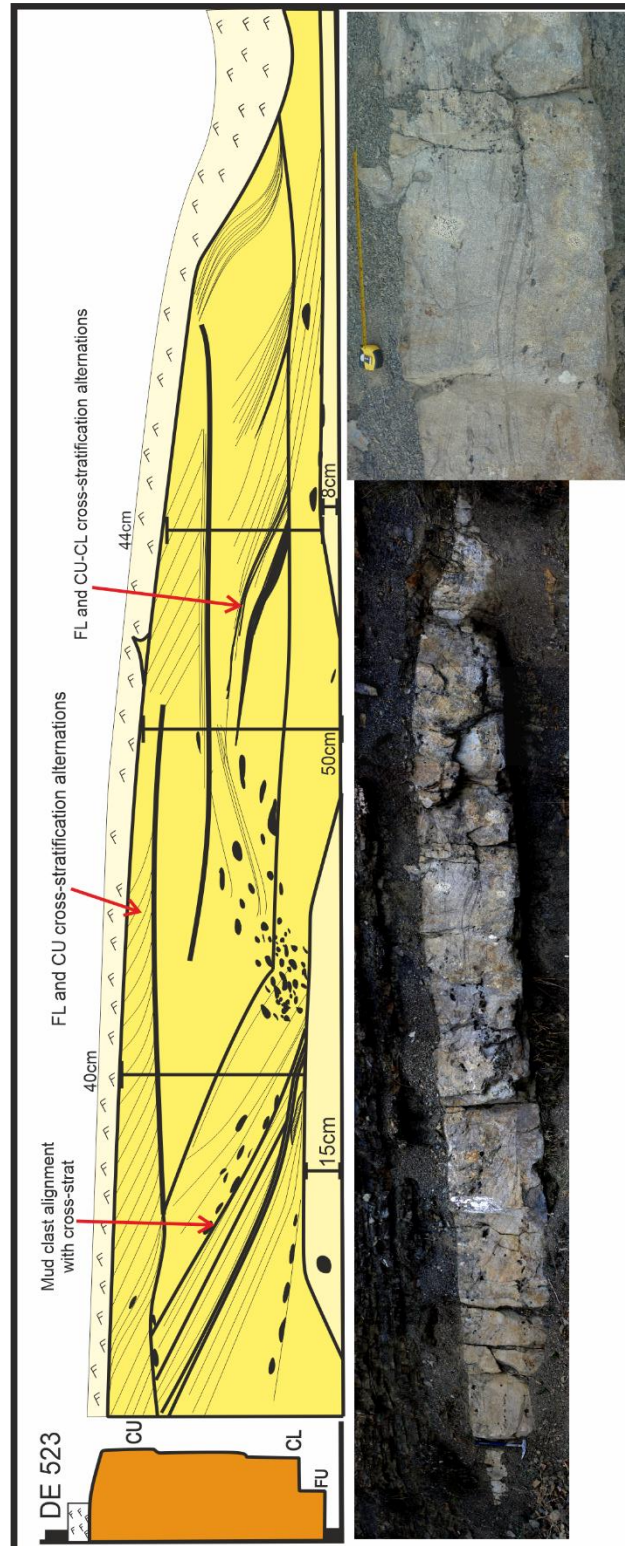


Figure 5.17. Bed Type 3.

**Bed Type 4 (Figure 5.18):** Bed type 4 is similar to Bed Type 3 as these beds are relatively thin (20 – 50 cm). Unlike Bed Type 3, Type 4 contains multiple sets of cross-stratification (Figure 5.18). The foresets are often made up of widely distributed grain-sizes, alternating between very-fine and coarse sediments; the coarser fraction is the most common grain-size in the bed. Very few examples of this bed type were found.



**Figure 5.18.** Bed Type 4.

**Bed Type 5 (Figure 5.19):** Cross-stratification occupies the top of the bed where the grain-size is finest. However, unlike Bed Types 1 and 3, there is no distinct grain-size break before the cross-stratified interval. The top of the bed sometimes thins and thickens (Figure 5.19). The cross-stratified interval is sometimes followed by a thin mud interval.

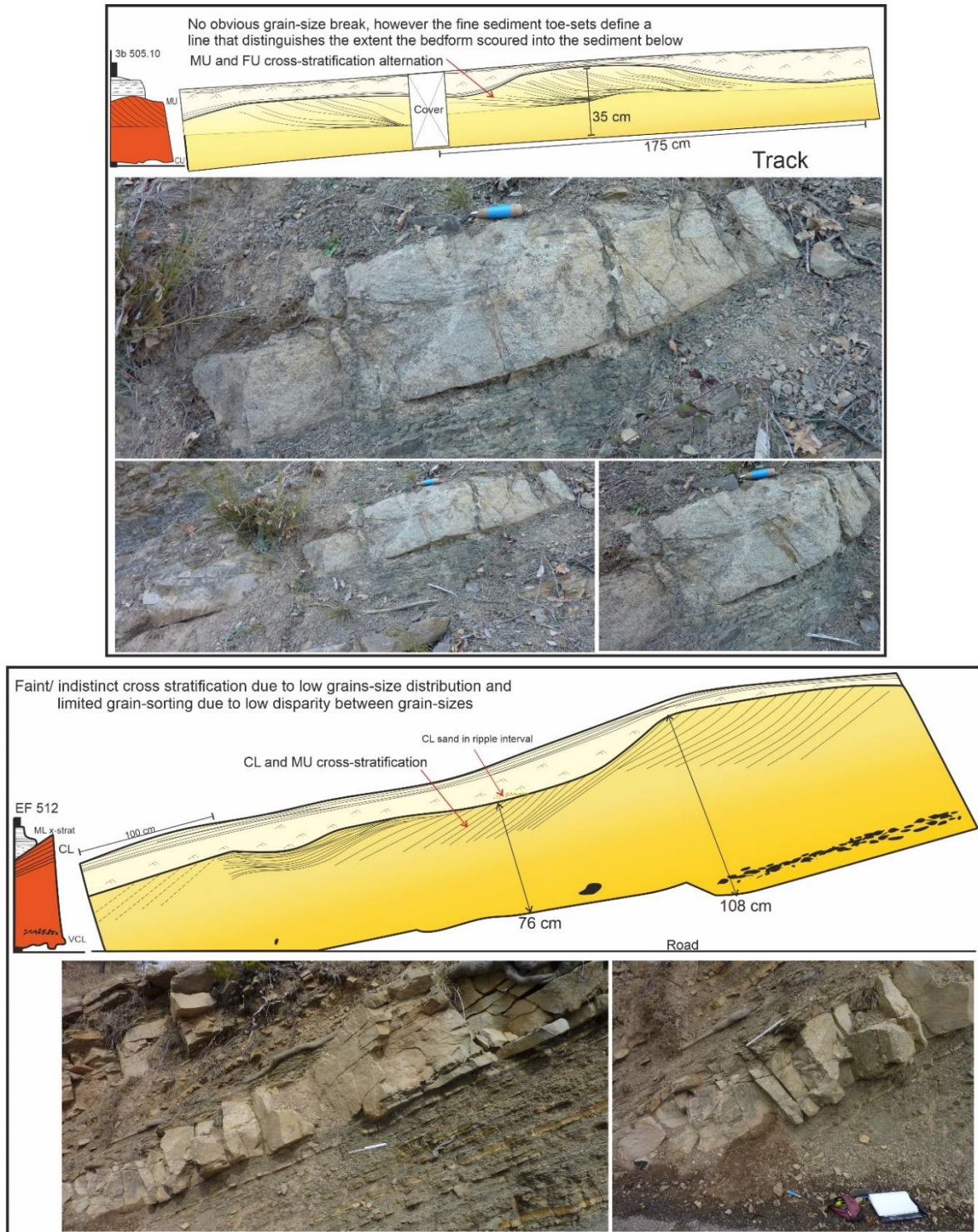


**Figure 5.19. Bed Type 5.**

**Bed Type 6 (Figure 5.20):** Cross-stratification is located towards the top of a bed of medium thickness (70 – 90 cm). Unlike Bed Type 5, Bed Type 6 does not fine up, but is ungraded. Cross-stratification has a narrow grain-size distribution where foresets alternate between a coarser grain-size fraction and a lesser amount of a slightly finer grain-size fraction. Occasionally the top of the bed may thin and thicken (Figure 5.20).

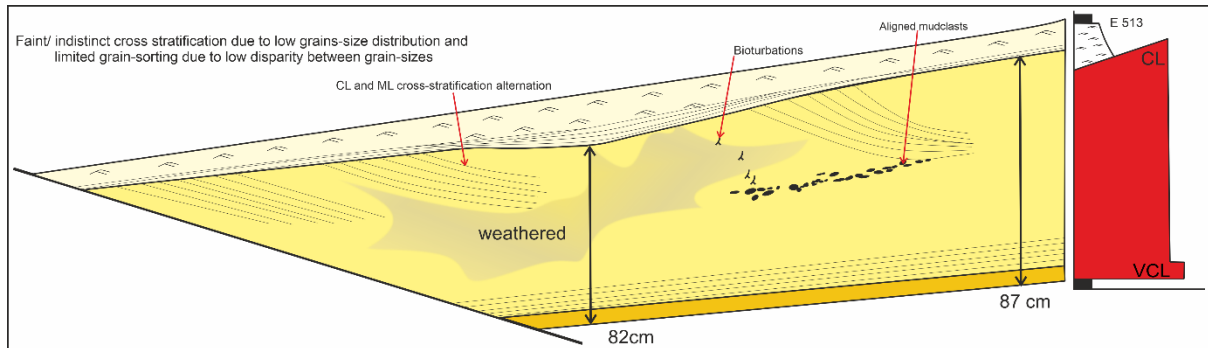


**Figure 5.20.** Bed Type 6.

**Bed Type 7 (Figures 5.21 & 5.22):** Cross-stratification is confined to the finer interval at the top of a bed of medium thickness (60 – 160 cm). There is an abrupt grain-size break between the coarser basal part of the bed and the finer cross-stratified interval (Figures 5.21 and 5.22). Cross-stratification foresets alternate between finer and coarser sediments. The top of the bed sometimes thins and thickens (Figures 5.21 and 5.22).

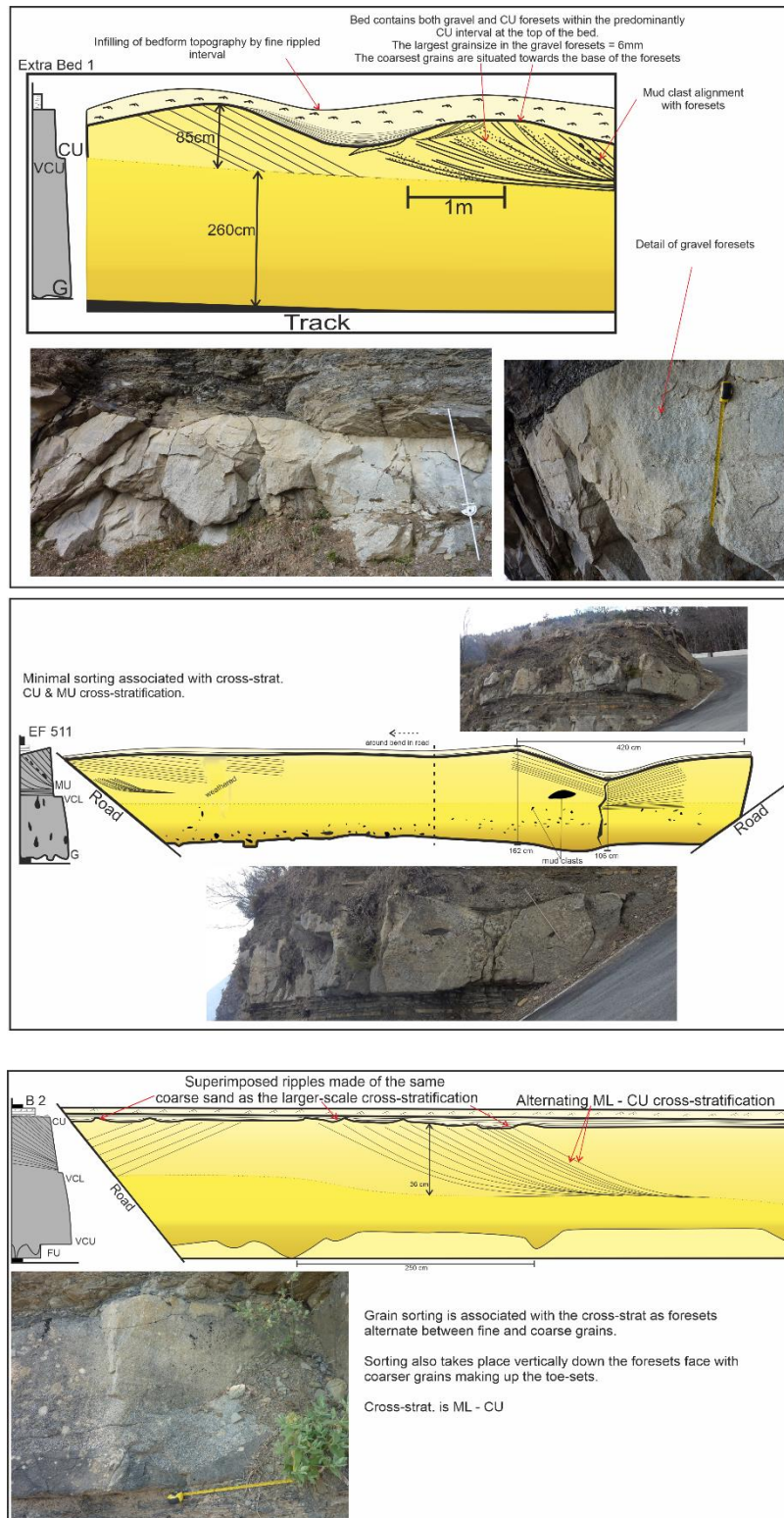


**Figure 5.21. Bed Type 7.**

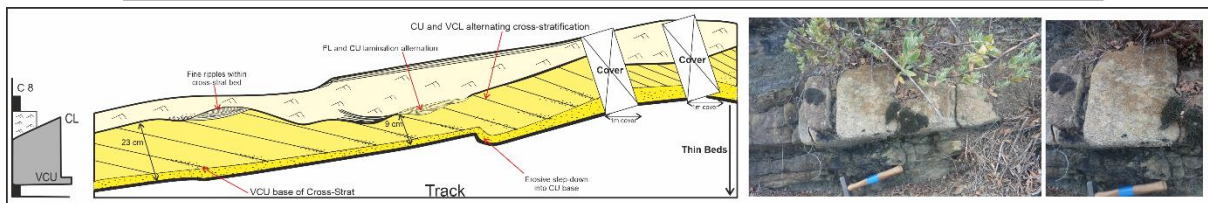
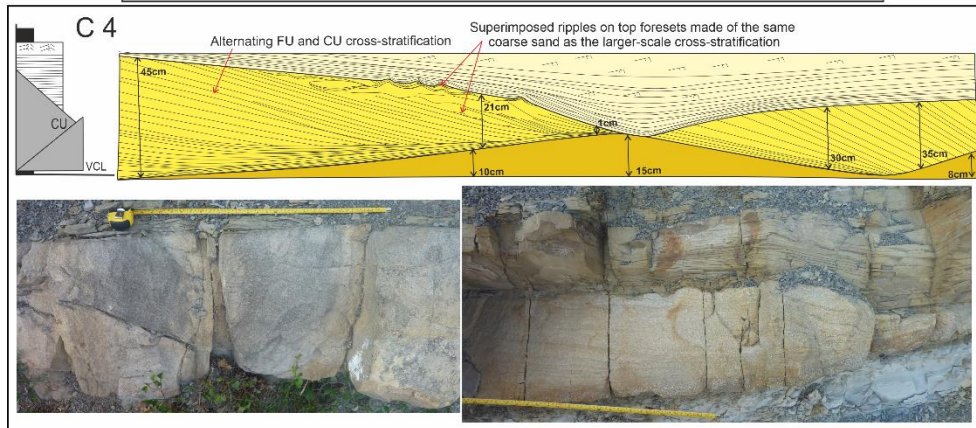
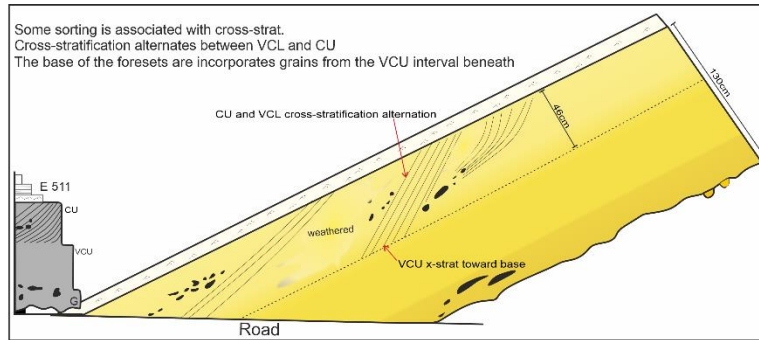


Figure 5.22. Bed Type 7.

**Bed Type 8 (Figure 5.23):** Cross-stratification occurs in the coarser base of the bed. Often, there is a very coarse sand-to-gravel interval at the very base of the bed which is also incorporated into the toesets of the cross-stratification (Figure 5.23).

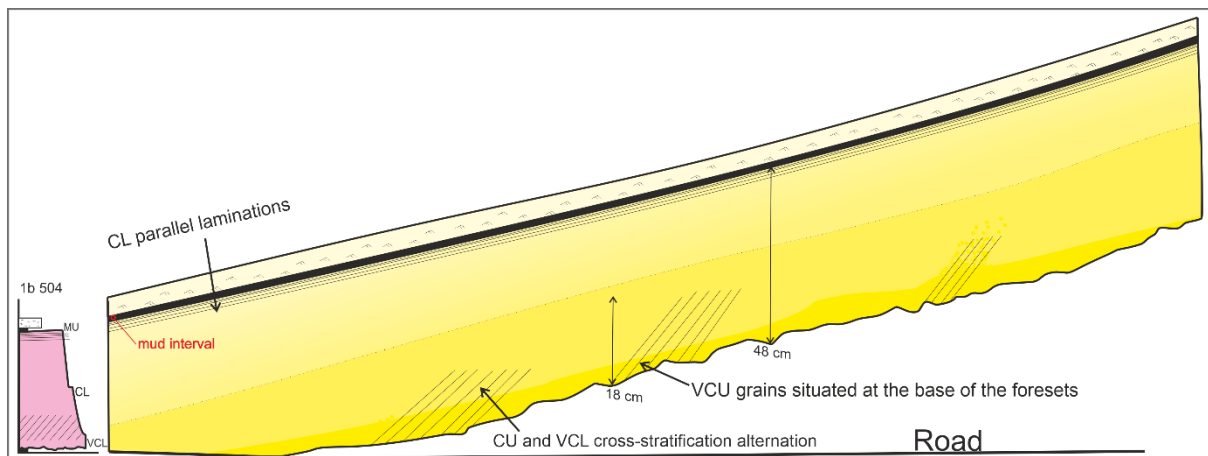
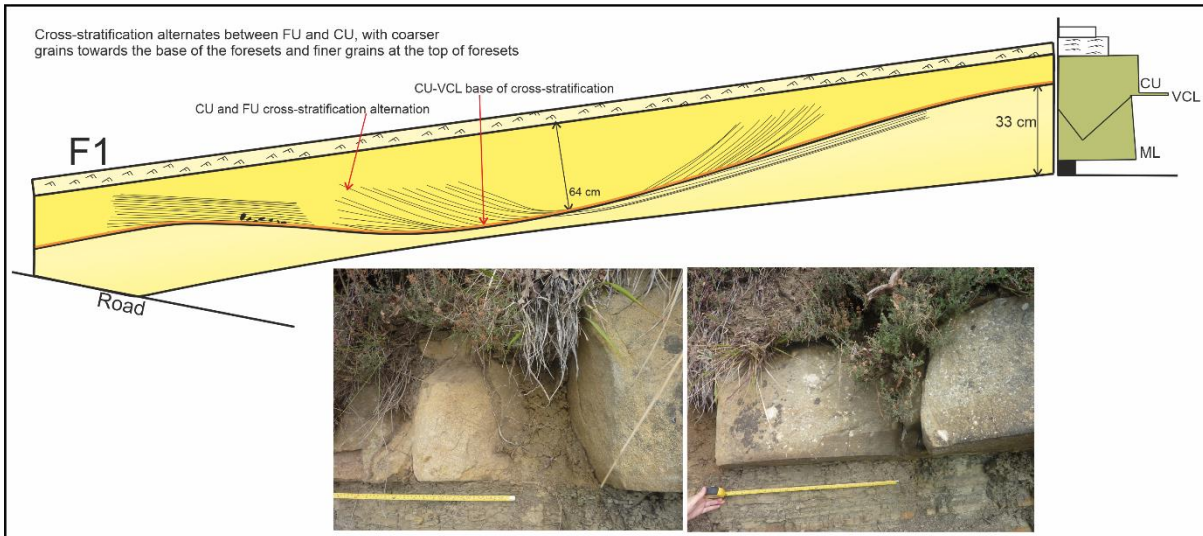


Figure 5.23. Bed Type 8.

**Bed Type 9 (Figures 5.24 & 5.25):** Cross-stratification has formed in association with a scour, which it infills. The cross-stratification is observed to occur within a depression, infilling it so the bed top is flat. The infilling cross-stratification can be either finer or coarser than the scoured interval beneath (Figures 5.24 and 5.25).



**Figure 5.24.** Bed Type 9.

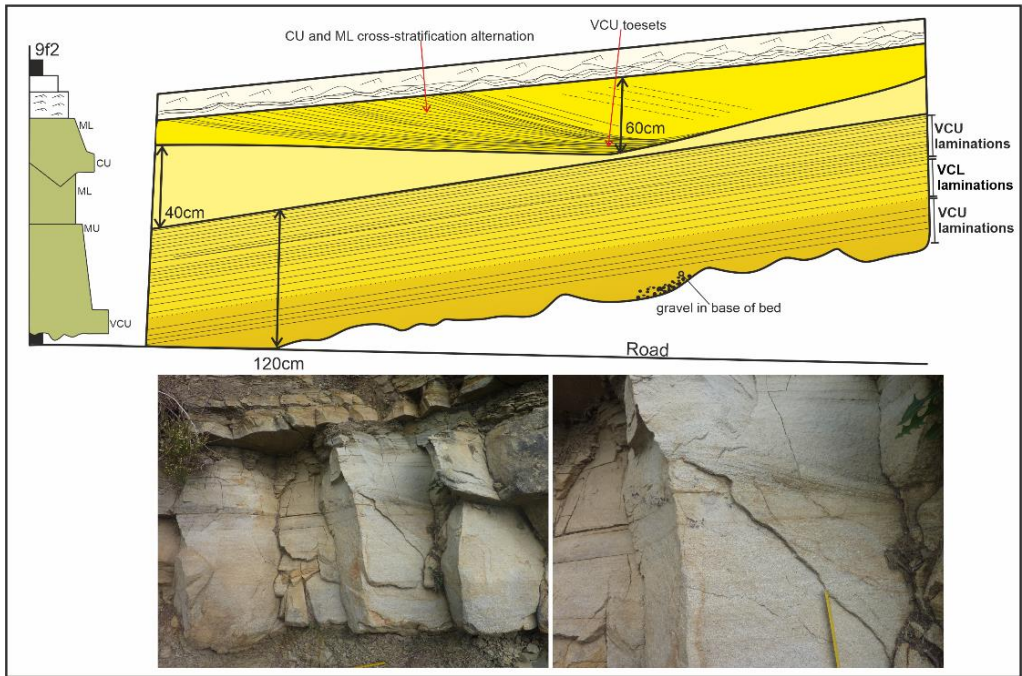
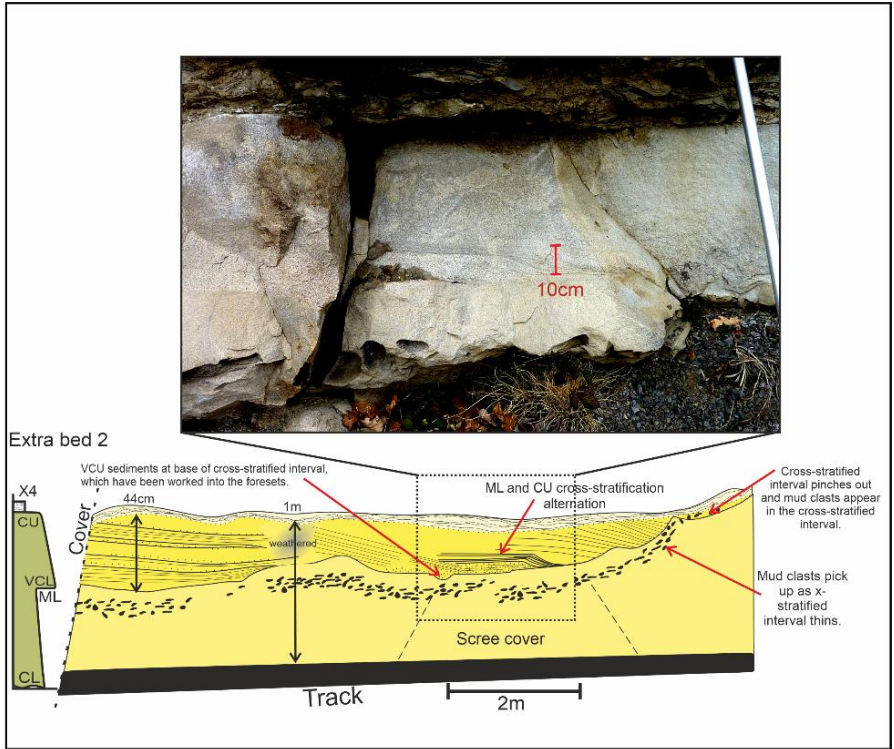
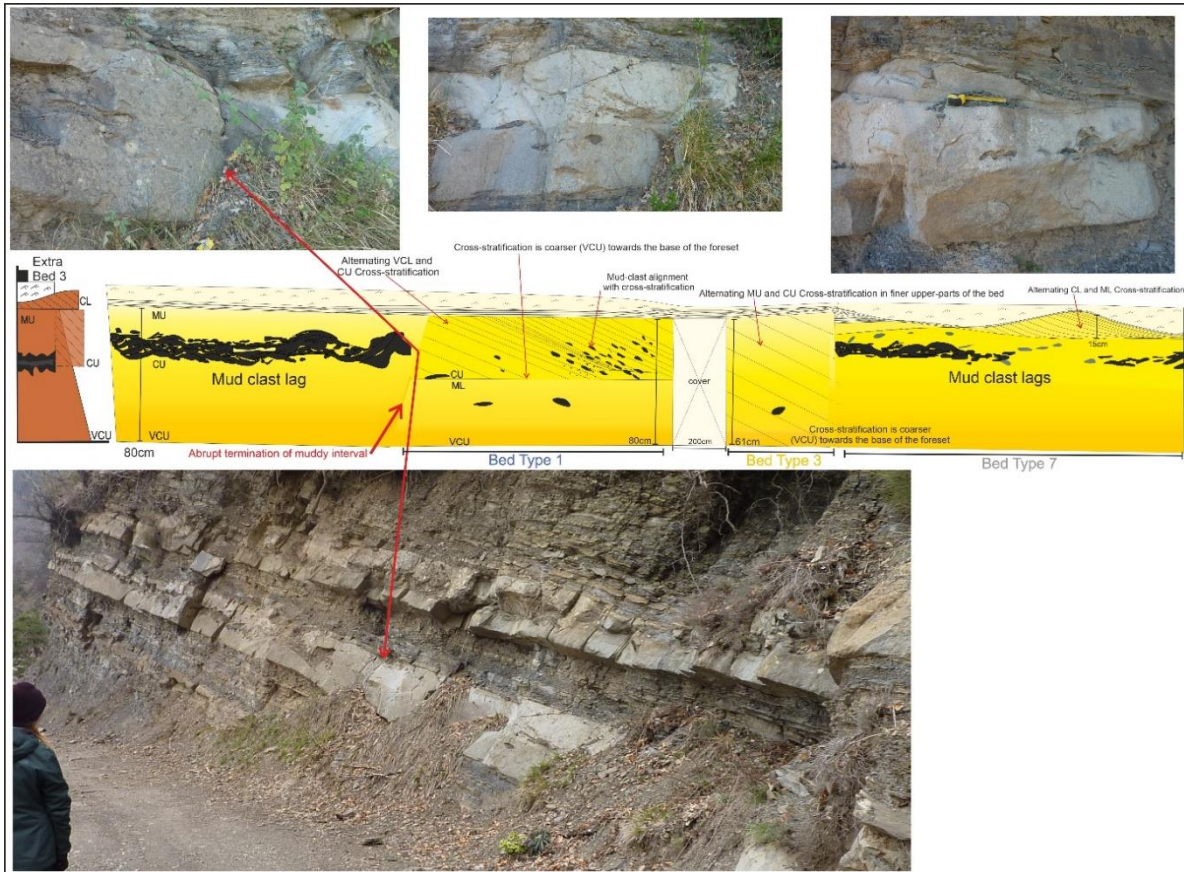
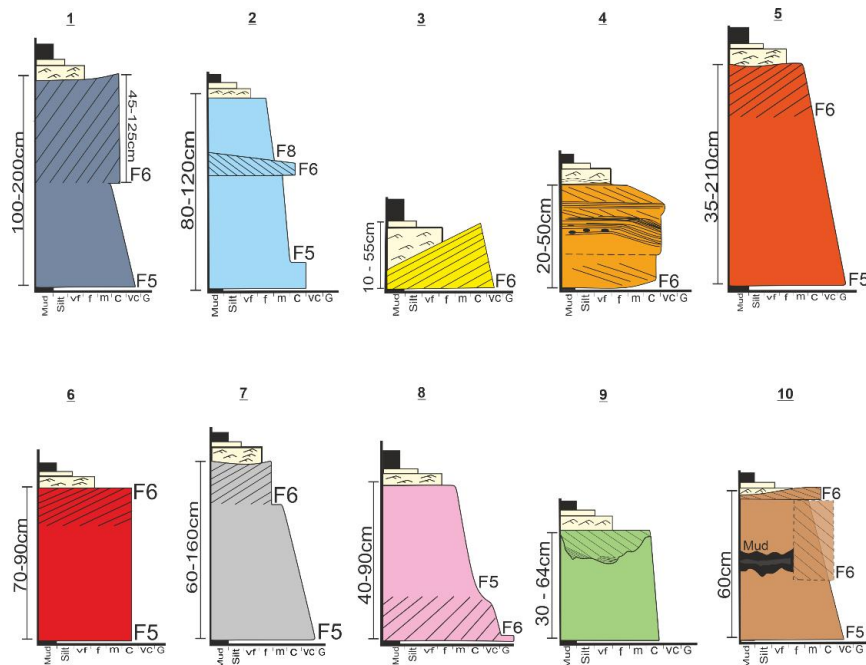


Figure 5.25. Bed Type 9.

**Bed Type 10 (Figure 5.26):** This bed type exhibits complex lateral variability. Normally graded sandstones pass laterally to “floating” mud-clast dominated intervals; different grain-sizes can also be laterally juxtaposed (for example, Figure 5.26 shows the lateral bed change from CU to ML). Figure 5.26 also shows the presence of cross-stratification in some parts of the bed and not others. Three different bed types associated with cross-stratification are shown in Figure 5.26. The same bed along a 10 m transect displays the characters of Bed Types 1, 3 and 7.



**Figure 5.26. Bed Type 10.**



**Figure 5.27. Bed Types 1-10.**

#### **5.4.4 Downstream evolution of cross-stratified beds**

Figures 5.10 and 5.28 show that cross-stratified beds were found up to 2.5 km NNE (downstream) of the D21 road but no further – i.e., cross-stratification is confined to the more proximal and medial parts of the outcropping system. Figure 5.28 shows detailed logs of correlative beds that were found to contain cross-stratification or have a bed top that thins and thickens, indicating the presence of positive relief structures; this figure repeats Figure 5.11, but here the beds are coloured to denote the bed type. Along the D21 Road, sections are repeated due to the hairpin nature of the road, allowing examination of correlative cross-stratified beds that are exposed over lengths of 10 – 200 m (sites D – F). Figure 5.28 shows that the style of cross-stratification occurrence is variable over short horizontal distances (over 20 – 50 m along the section on Road D21), changing between different bed types. Below is a description of each bed at different sites throughout the system.

**Bed 504** can be correlated into the distal reaches of the system. It is Bed Type 3 along the D21 Road, but changes to Bed Type 8 at Site 1b. This altered bed type and facies is not maintained, as at Sites 3a – 4a, Bed 504 reverts to Bed Type 3. At the medial – distal sites, Bed 504 does not contain any cross-stratification.

**Bed 505.10** regularly outcrops across the system and can be correlated to the most distal Site (the NE Road). The bed remains as Bed Type 3 throughout the proximal sites. A slight increase in bed thickness at Site 3 coincides with a change to Bed Type 5. The bed reverts to Bed Type 3 at Site 4, but cross-stratification was not found beyond Site 4b.

**Bed 506.5** only intermittently outcrops at the proximal locations. From 3 locations spread over approximately 1 km, the Bed Type remains as 3 and has pinched out by Site 4a.

**Bed 507** outcrops mainly along the forest track and can be correlated through to the distal setting of the NE Road. Bed 507 presents as Bed Type 3 throughout the proximal locations. As the bed reaches the proximal – medial reaches of the system, it changes to Bed Type 5. It then reverts to Bed Type 3. The last occurrence of cross-stratification in Bed 507 is in the medial setting at Site 5, where it presents as Bed Type 8.

**Bed 511** also outcrops frequently across the system, providing a good record of bed evolution. Cross-stratification is seen throughout the proximal regions along the D21 Road and onto the forest track; the bed is of Type 7 here. The style of cross-stratification changes to Bed Type 5 at Site 3a which is maintained until the medial setting at Site 4b. Cross-stratification is not present in the medial – distal sites at the East Ridge or the NE Road.

**Bed 512** outcrops at all but one location, providing a good record of the bed evolution throughout the exposed system. Bed 512 shows variability in bed type over very short distances (~20 m). The style of cross-stratification transitions from Bed Type 7 to Bed Type 5, which is then maintained throughout the proximal setting. At site 5 (a medial location), Bed 512 changes to Bed Type 8.

**Bed 513** outcrops frequently through the proximal region of the D21 Road and the forest track. It also outcrops at the medial reaches of the system at Site 5 and at the East ridge. Along the D21 Road, the bed type remains constant (Bed Type 6). At Sites 3a and 3b, the bed type changes to Bed Type 5. The medial locations (Site 5 and the East Ridge) do not show any occurrence of cross-stratification.

**Bed 523** only outcrops at the more proximal locations along the D21 Road and towards the start of the forest track sites. At Site DE, the bed type is 4, containing multiple sets of cross-stratification. Bed 523 then becomes characterised by only single sets of cross-stratification as Bed Type 3. Due to its poor exposure in the medial to distal regions of the system, the bed evolution beyond Site 3b is unknown. The lack of cross-stratification at Site 3b might indicate that no decimetre-scale bedform development took place more distally.

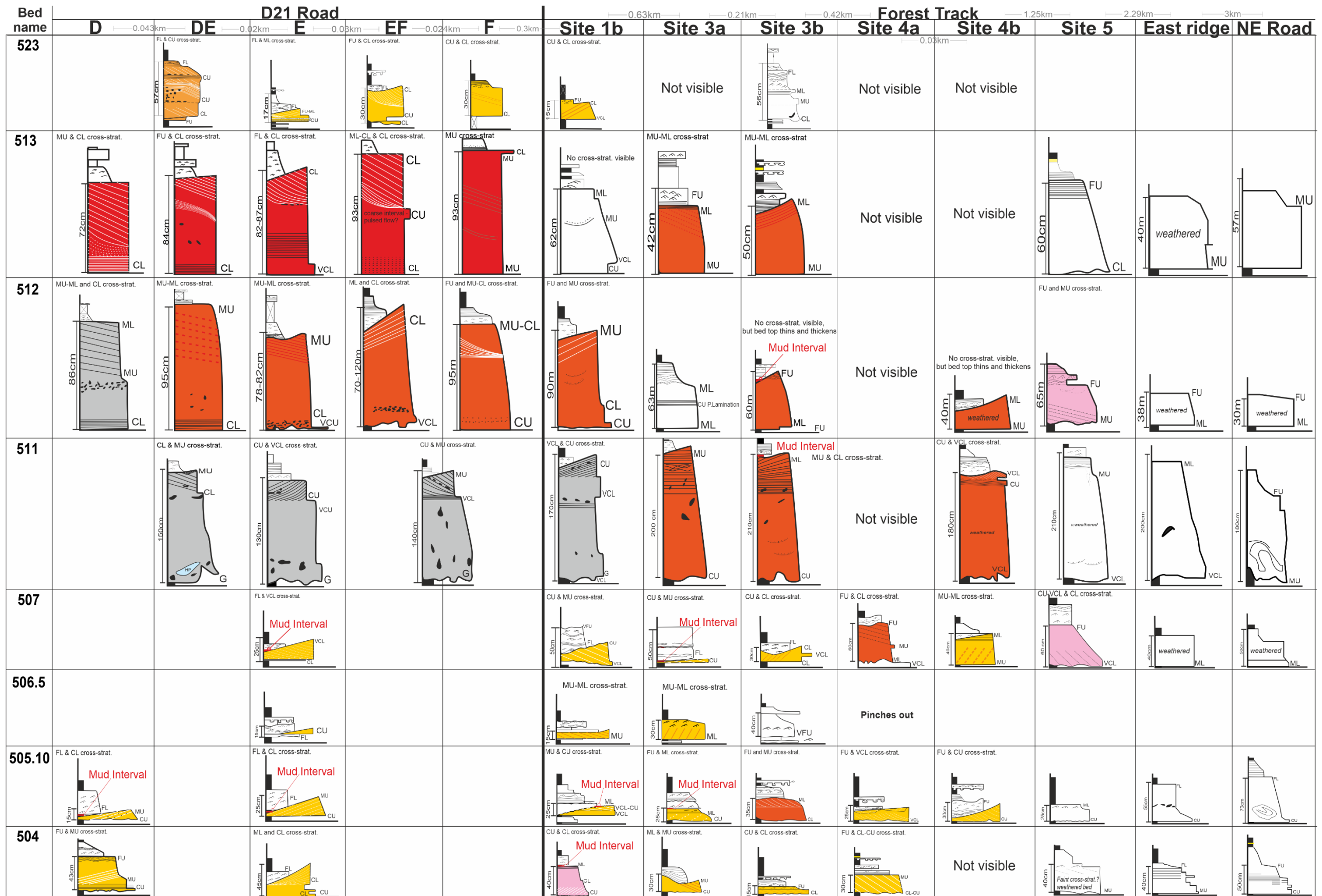


Figure 5.28. Detailed logs of correlative beds that were found to contain either cross-stratification or have a bed top that thins and thickens. The bed colours relate to the bed type.

### 5.4.5 Cross-stratification geometry

The geometries of the cross-stratification are described for the examples of the cross-stratified beds in Figures 5.14 – 5.23. The names of each bed referred to in Table 5.3 are included within the figures.

*Table 5.3. Summary of cross-stratification geometry*

<b><i>Bed name and related figure</i></b>	<b>Cross-stratification geometry</b>	<b>Depositional mechanism over the crest</b>	<b>Bedform dimensionality</b>	<b>Description of grain-size distribution</b>
<i>B1</i> (Figure 5.14)	Partially sigmoidal with tangential contacts at base of the foresets	Avalanching and rolling down the lee slope and fallout from suspension	3-dimensional	Bimodal & wide grain-size distribution CU-FU
<i>Bed D 511</i> (Figure 5.14)	Bedform is oriented as if migrating into a cliff. Cross-stratification appears planar, however the foresets may be slightly concave as the foreset terminations are interpreted into the cliff	Mainly avalanching, plus some fallout from suspension	Slightly 3-dimensional	Bimodal & low grain-size distribution CU-CL
<i>Bed BC 1</i> (Figure 5.15)	2 sets of cross-stratification The series of bedforms contain sigmoidal or concave cross-stratification	Avalanching plus fallout from suspension	Highly 3-dimensional	Bimodal & wide grain-size distribution CL-MU
<i>Bed C7</i> (Figure 5.15)	Planar - concave	Mainly avalanching, plus some fallout from suspension	Slightly 3-dimensional	Unimodal distribution MU
<i>Bed C2</i> (Figure 5.16)	Planar – slightly concave	Mainly avalanching, plus some fallout from suspension	2-dimensional	Bimodal & Low grain-size distribution CL-CU
<i>Bed E 504</i> (Figure 5.16)	Concave with tangential contact at base of foresets	Avalanching plus fallout from suspension	3-dimensional	Bimodal & wide grain-size distribution CL-ML

<i>Bed 4b</i> 505.10 (Figure 5.17)	Concave – sigmoidal cross-stratification. 2 sets of cross-stratification where cross-stratification truncates against and overlaps onto the lower set.	Avalanching plus fallout from suspension	Highly 3-dimensional	Bimodal & very wide grain-size distribution FL-VCL
<i>Bed 4a</i> 505.10 (Figure 5.17)	Concave cross-stratification with tangential contacts at base of foreset.	Avalanching plus fallout from suspension	3-dimensional	Bimodal & very wide grain-size distribution FU-VCL
<i>Bed DE 523</i> (Figure 5.18)	Multiple sets of cross-stratification with varying geometries: Sigmoidal and concave	Avalanching plus fallout from suspension	Highly 3-dimensional	Bimodal & very wide grain-size distribution FL-CU
<i>Bed 3b</i> 505.10 (Figure 5.19)	Concave and sigmoidal cross-stratification. Bedform likely to have an indistinct crest	Avalanching plus fallout from suspension	Highly 3-dimensional	Bimodal & wide grain-size distribution FU-MU
<i>Bed EF 512</i> (Figure 5.19)	Slightly concave	Mainly avalanching plus some fallout from suspension	Slightly 3-dimensional	Unimodal distribution MU-CL
<i>Bed E13</i> (Figure 5.20)	Planar - concave	Mainly avalanching plus some fallout from suspension	Slightly 3-dimensional	Unimodal distribution CL-ML
<i>Extra Bed 1</i> (Figure 5.21)	2 bedforms preserved side by side. One with planar cross-stratification, the other with concave cross-stratification.	Avalanching  Avalanching plus fallout from suspension	2-dimensional  3-dimensional	Bimodal & very wide grain-size distribution CU-Gravel
<i>Bed EF 511</i> (Figure 5.21)	Planar cross-stratification. Bedforms also have a clear crestal brink point preserved.	Avalanching	2-dimensional	Unimodal distribution CU-MU

<i>Bed B2</i> (Figure 5.21)	Concave cross-stratification with tangential contacts at the base of the foresets	Avalanching plus fallout from suspension	3-dimensional	Bimodal & wide grain-size distribution CU-ML
<i>Bed E 511</i> (Figure 5.22)	Planar – concave cross-stratification	Mainly avalanching plus some fallout from suspension	2 to slightly 3 - dimensional	Bimodal & medium grain-size distribution CL-VCL
<i>Bed C4</i> (Figure 5.22)	Concave cross-stratification with tangential contacts at the base of the foresets	Avalanching plus fallout from suspension	3-dimensional	Bimodal & wide grain-size distribution FU-CU
<i>Bed C8</i> (Figure 5.22)	Planar cross-stratification	Avalanching	2-dimensional	Bimodal & low grain-size distribution CU-VCL
<i>Bed 1b 504</i> (Figure 5.23)	Planar cross-stratification	Avalanching	2-dimensional	Bimodal & low grain-size distribution CU-VCL

#### 5.4.6 Mud intervals

A number of beds detailed in Figures 5.10 and 5.28 (504, 505.10, 507, 511 and 512) develop a very thin (0.5 – 2 cm) mud interval directly above the cross-stratified bed. Figure 5.23 contains an example of the mud interval of bed 1b 504. Bed B1 (Figure 5.14) lies outside the correlative interval of Figures 5.10 and 5.28 but is another example of a cross-stratified bed that contains a thin mud interval (1.5 cm thick) on top of the cross-stratified interval. The presence of a mud interval deposited directly on top of a coarse cross-stratified bed is a significant finding that has not been mentioned in previous research. This is likely due to the mud intervals being very thin, and rare; most of the cross-stratified beds in the system are directly followed by a sandy fine-grained rippled or parallel lamination interval.

#### 5.4.7 Paleoflow

Figure 5.29 shows that the paleoflow measurements taken from cross-stratified beds are predominantly oriented to the NNE. This is in alignment with the mean paleocurrent direction recorded by Amy (2000) and Cunha *et al.* (2017) who showed that flow was to the NNE based on ripples and erosional sole structures (grooves and flute marks) orientations (Figure 5.29). Amy

(2000) also mentioned that the few cross-stratified beds from which paleoflow directions were taken were also oriented towards NNE but did not include these measurements within the results. Cunha *et al.* (2017) do include paleoflow measurements taken from cross-stratified beds in Peira Cava (Figure 5.29) which indicate the same overall paleoflow direction as the present research. The measurements for the present research depict a wider spread of data than is recorded by Cunha *et al.* (2017) with a significant component of the paleoflow directed towards the NNW.

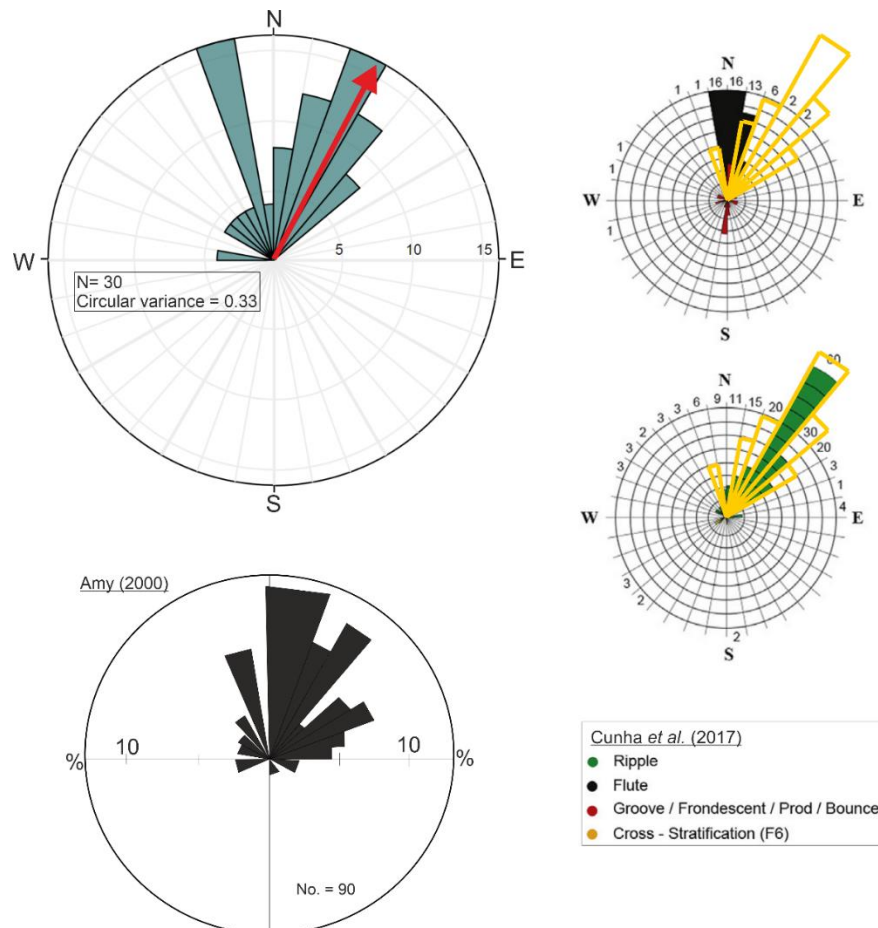


**Figure 5.29.** Palaeoflow measured for the present research (top left), Amy (2000) and Cunha *et al.* (2017).

#### 5.4.8 Cross-stratification grain-size

Previous research describes cross-stratified beds as being generally coarse-grained (Mutti and Normark, 1987; 1991; Postma, 1990; Mutti, 1992; Mutti *et al.*, 1999; Amy, 2000; Kneller and McCaffrey 2003; Cunha *et al.*, 2017; Tinterri *et al.*, 2017). However, Sumner *et al.* (2012) describe the cross-stratified beds of the Marnoso Arenacea Formation, Italy, as made of fine-medium sized sand. The cross-stratified beds of the Peira Cava basin are also found to be predominantly formed from coarse-grained sand. However, detailed logs of cross-stratified beds, photos and field sketches reveal that simply describing these beds as coarse-grained does not properly

characterise their grain-size character. Cross-stratified intervals included a range of grain-sizes from fine lower (FL) to very coarse lower (VCL) sand, which corresponds to a range in diameter of approximately 190 – 1500  $\mu\text{m}$  (Table 5.2). Some beds are characterised by a narrower grain-size distribution (e.g. Bed EF 512, Figure 5.19; Bed D15, Figure 5.14; Bed E 513, Figure 5.20; Bed EF 511, Figure 5.21). In these beds the cross-stratification was less distinctive due to the reduced range of grain-sizes forming successive laminae on the lee slope of bedforms. Beds which are made of a wider mix of grain-sizes exhibit some degree of bimodality in the sands that make up the cross-stratified intervals. Examples of cross-stratified beds that are characterised by bimodal grain-size distributions include Bed 523, which contains FL and CU cross-stratification (Figure 5.18); Bed B1, which contains CU and FU cross-stratification (Figure 14); Bed C4, which contains FU and CU cross-stratification (Figure 5.22); Bed 4b 505.10, which contains VCL and FU cross-stratification (Figure 5.17); and Extra Bed 1, which contains gravel (with a maximum clast size of 6 mm) and coarse upper sand (Figure 5.21). These differences may reflect differing capacities of flows to segregate different grain-size classes or may relate to variations in the grain-sizes in traction (see Chapter 6 – Discussion).

## 5.5 Discussion

### ***5.5.1 Defining the type of bedform associated with cross-stratification in Peira Cava***

The present research aims to more accurately define the type of bedform associated with cross-stratification in Peira Cava than has been achieved to date. A key approach is to make distinctions with reference to other types of bedforms, for example ripples, dunes and supercritical bedforms. Recognition of the bedform type will enable improved inferences of a depositing current's flow dynamics. This distinction is best made in the frame of reference of the palaeoflow direction of the flows depositing the studied cross-strata.

#### *5.5.1.1 Palaeoflow*

The collected bedform palaeoflow data are derived based on the restored direction of dip of foresets that are exposed in three-dimensions. Although these indicate NNE dispersal (Figure 5.29), it is possible that the measurements may be influenced by the sinuosity of the crest – i.e., the degree of bedform three-dimensionality. *A priori*, it might be expected that this effect would simply broaden the measured palaeoflow range (and thus, by assuming a single flow direction, an estimation of bedform three-dimensionality could be made based on the spread of palaeoflow data). However, other palaeoflow indicators such as sole marks and ripples show that

the dispersal direction may vary between flows. Because sole marks provide a linear representation of the palaeoflow that is not influenced by variable foreset plane geometry, a comparison of the spread of bedform-derived and sole structure-derived palaeoflow may therefore give an indirect indication of the sinuosity of bedform crests (and thus bedform three-dimensionality). Figure 5.29 details the palaeoflow data measured by Amy (2000), Cunha *et al.* (2017), and for the present research. The slightly greater spread in palaeoflow measurements for cross-stratification compared to sole marks suggests that the bedforms are likely slightly-to-moderately three-dimensional and, therefore, are likely to give an accurate indication of the actual palaeoflow direction. The common dispersal direction indicated by cross-stratification foresets and sole marks further supports this inference. While ripples may also be three-dimensional, the spread of palaeoflow data they show may be increased by flow reflection in confined settings (e.g., Kneller *et al.*, 1991; McCaffrey and Kneller, 2001).

#### 5.5.1.2 Megaripple terminology

Different authors have assigned different names to the bedforms associated with decimetre-scale cross-stratification found in Peira Cava. For example, Amy (2000; 2007) and Kneller and McCaffrey (2003) refer to them as dune bedforms, while Cunha *et al.* (2017) refer to them as megaripples. The usefulness of the term ‘megaripple’ associated with turbidites is discussed in the Literature review (Chapter 2). For reference, the term ‘megaripple’ is undefined in relation to other types of bedforms and therefore there is uncertainty in associating past current conditions and sedimentary processes to the formation of beds identified as megaripples. Regardless of the uncertainty surrounding terminology, the consensus of Amy (2000; 2007), Kneller and McCaffrey (2003) and Cunha *et al.* (2017) is that the cross-stratification in Peira Cava was formed by dunes/megaripples and developed under subcritical flow conditions after rapid flow deceleration had taken place at the channel lobe transition zone. Here, this interpretation will be evaluated, together with up- and down-stream migrating antidunes models, without recourse to megaripple terminology.

#### 5.5.1.3 Ripples

The results of the bedform dimensional analysis show there is distinction between the heights of ripple bedforms preserved in the basin fill and those of the decimetre-scale cross-stratification (Figures 5.12 and 5.13). It is reasonable to conclude that these bedforms are distinguishable as a result of the differences in their formative processes (Ashley, 1990), which may suggest a division between ripples and decimetre-scale cross-stratification. In addition, different types of ripples are found in the Peira Cava basin fill. The widely documented ripples of the F9/T<sub>c</sub> facies may be distinguished from the ripples of a newly defined facies that contains both

ripples and decimetre-scale cross-stratification within the same interval. However, the dimensions of both types of ripples are included in the ripple bedform class in Figures 5.12 and 5.13.

The ripples of the new type are made from a mixture of coarse sand (the most abundant grain-size in the cross-stratified interval), as well as a finer fraction of sediment (fine-medium sand), which is thought to be made more readily available due to grain-size sorting of sediment as it is deposited down the lee slope of the larger bedform. The occurrence of ripples associated with the new facies includes ripples that are superimposed upon both foresets and stoss slopes of the host bedforms (Bed 'C4', Figure 5.22). Those superimposed on the foresets are known as 'backflow ripples' and are interpreted to be created by the lee-side eddy in the trough of the host bedform (Herbert *et al.* 2015). Backflow ripple migration onto the foreset is associated with greater flow velocities within the trough, which is in turn linked to a more intense flow separation zone associated with the host bedform. The second style of superimposed ripple occurrence, upon the stoss slope of preserved host bedform profiles, is shown in Bed 'B2', Figure 5.21, and in Bed 'C4', Figure 5.22. There are two mechanisms that might explain the development of such stoss superimposed ripples. The first is that the larger bedforms are remnant from pre-existing flow conditions and the ripples formed under new flow conditions (Allen, 1978); in a waning turbidity current, ripples may have formed in an intermediary bedform phase space where the bypassing, non-depositional part of the flow is too slow to form decimetre-scale bedforms, but fast enough to rework the surface of the relict bedforms into ripples that are coarser than the ripples of the F9/  $T_c$  facies. Alternatively, superimposed ripple development may take place within the internal boundary layer of the larger host bedform, allowing ripple development even if the prevailing current conditions are too fast to support ripple formation (Rubin and McCulloch, 1980; Rubin, 2012). Crucially, these potential causes for superimposed ripple development, either on the stoss or foreset of a larger scale bedform, tells us that the ripples formed under different flow conditions compared to their host bedforms. Thus, it can be confirmed that the decimetre-scale cross-stratification may be distinguished from all the ripple types that formed in the Peira Cava basin, based on the differences in the flow processes that likely led to their formation and based on their dimensional differences.

#### 5.5.1.4 Decimetre-scale cross-stratification.

There is still uncertainty as to why the cross-stratified beds of the Peira Cava basin are confined to the proximal regions of the basin (Hilton, 1994; Amy *et al.*, 2000; 2007; McCaffrey and Kneller, 2001; Lee *et al.*, 2004; Cunha, 2017), despite the down-dip grain-size being coarse enough to support dune bedform development. Other authors have considered the presence of cross-stratification in the proximal regions of other basins, attributing their formation to supercritical

(Tinterri, and Tagliaferri, 2015; Tinterri *et al.*, 2017; Postma *et al.*, 2021), or near critical flow conditions that extend beyond the channel lobe transition zone (Hamilton *et al.*, 2017). Therefore, it is important to assess whether the cross-stratification in Peira Cava could be the result of the development of supercritical bedforms.

The types of supercritical bedforms that might develop cross-stratification include upstream migrating antidunes (which are in-phase with intraflow/flow surface waves and migrate upstream; the surface waves may break periodically – see also the Chapter 2 Literature Review) and downstream migrating antidunes (which are in-phase waves that migrate downstream – Chapter 2 describes the processes associated with antidune migration direction). It is concluded here that the cross-stratification of Peira Cava is generally too steep to be classified as the foresets of upstream migrating antidunes. Figure 5.30 contains examples of sedimentary structures in antidunes, which are characterised by shallow foresets that are oriented upstream, with backsets that sit within sub-horizontal to gently-inclined set boundaries, and have low-angle tangential terminations to the lower set boundary (Cartigny *et al.*, 2014). In the rock record, upstream migrating and stationary antidune deposits have also been described as waved structures with sinusoidal stratification (Lang and Winsemann 2013; Slootman *et al.*, 2016), and as hummocky cross-stratification (Yagishita 1994; Mulder *et al.*, 2009). The cross-stratification found in Peira Cava is oriented towards the NNE, indicating that the direction of bedform migration was downstream (Figure 5.29). Having determined that the decimetre-scale cross-stratification are not formed by ripples, that the foreset geometry is too steep to be upstream migrating antidune foresets, and that bedform migration was directed downstream, it may be concluded that the decimetre-scale cross-stratification of Peira Cava was produced either during the development of dunes or of downstream migrating antidunes.

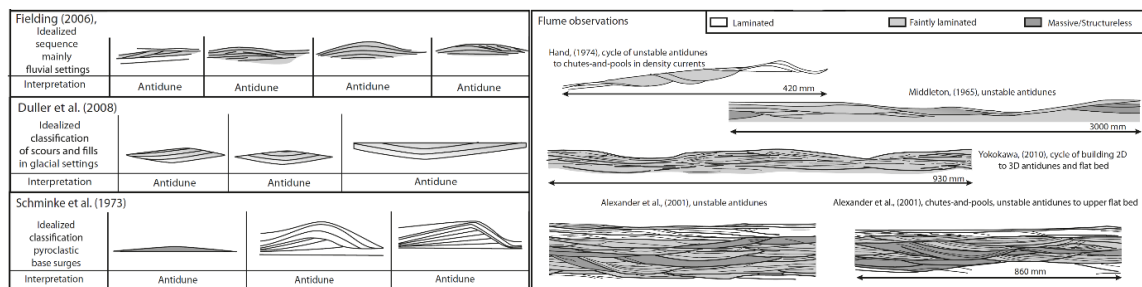


**Figure 5.30.** From Cartigny *et al.* (2014). Examples of antidune sedimentary deposits.

The palaeoflow directed downstream and high-angle foresets of the cross-stratified beds of Peira Cava is suggestive of formation by dune bedforms. However, such sedimentary structures may also characterise the deposits of downstream migrating antidune bedforms, which are defined by Kennedy (1963) as in-phase waves that migrate downstream under supercritical flow

conditions when the Froude number is close to unity. Figure 5.31a represents the cross-stratification of both dunes and downstream migrating antidunes as defined by Cartigny *et al.* (2011). However, Cartigny *et al.* (2011) make no reference as to what this depiction of downstream migrating antidune is based on, but still present a difference between dunes and downstream migrating antidune stratification, where downstream migrating antidunes have a symmetrical planform shape and form lower-angled cross-stratification. Arguably, this is too simplistic a representation of these sedimentary structures. For example, Figures 5.31b – d show examples of downstream migrating antidunes produced during physical modelling (including the downstream migrating antidunes formed in Chapter 2, Figure 5.31d). Figures 5.31b – d show the variability in the profile morphologies that may be achieved by downstream migrating antidunes. Some are symmetrical and some have asymmetric profiles (Carling and Shvidchenko, 2002; Núñez-González and Martín-Vide, 2011), and some have rounded crests while others have more defined crestal regions. Therefore, it is possible that the sedimentary structures formed by downstream migrating antidunes can display both low- and steep-angle foresets. Further, dune bedforms are known to be morphologically variable, forming both low-angle symmetrical profiles and asymmetric, steep profiles (Kostaschuk and Villard, 1996; Best and Kostaschuk, 2002; Best, 2005; Cisneros *et al.*, 2020). Therefore, what may be readily interpreted as dune deposits, could be downstream migrating antidunes.

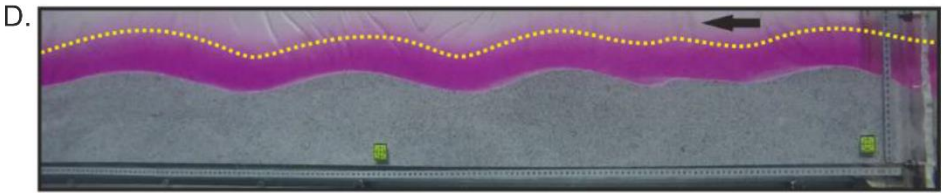
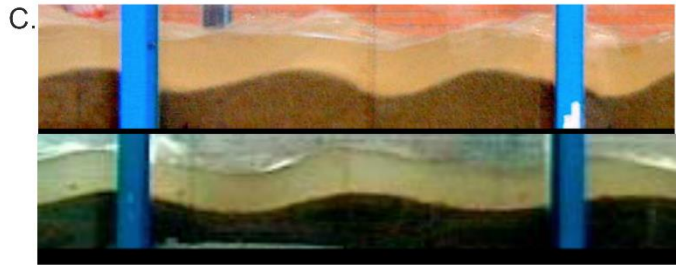
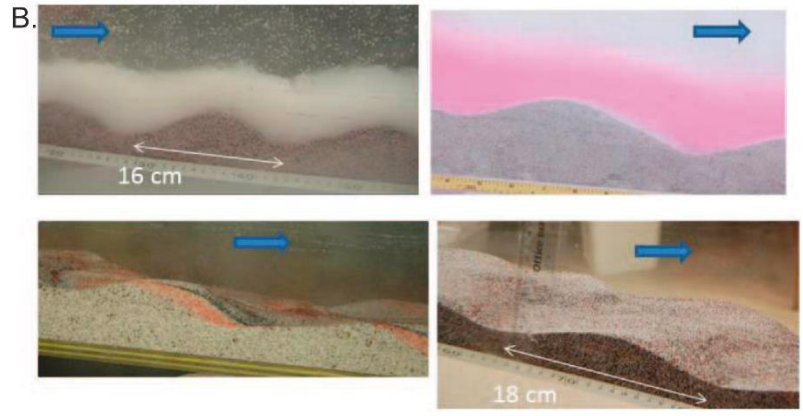
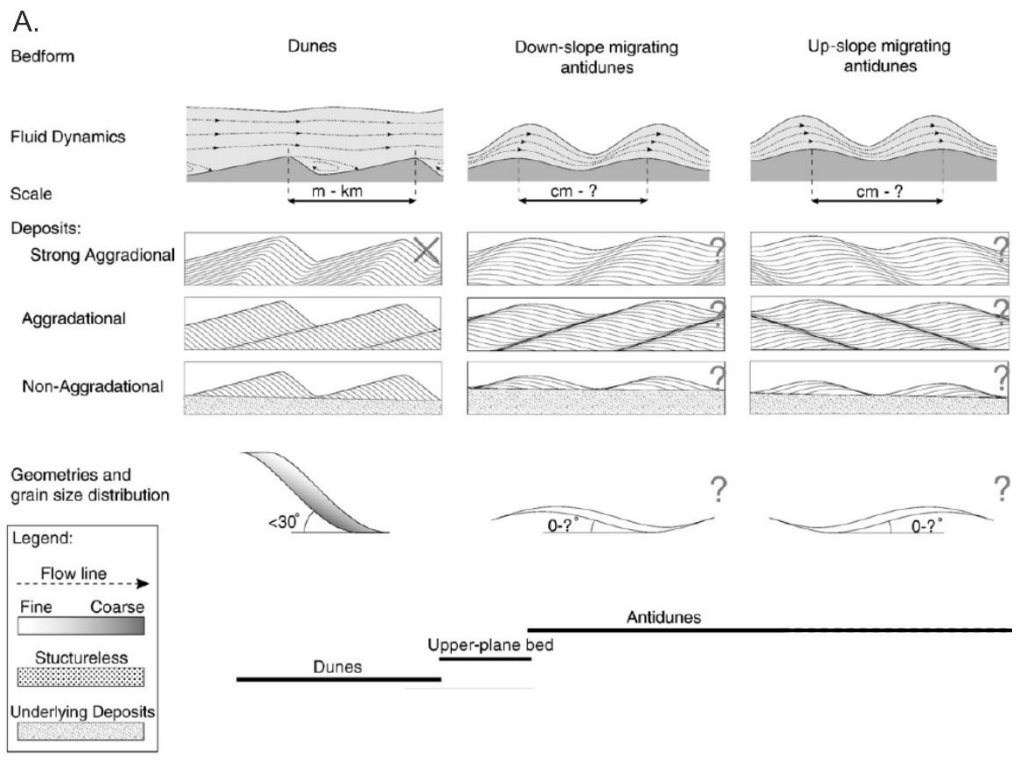


**Figure 5.31.** Examples of downstream migrating antidunes. **(A)** Cartigny et al. (2011) **(B)** Fedele et al. (2016) **(C)** Núñez-González and Martín-Vide (2011) **(D)** de Cala et al. (2020), also in Chapter 3.

Downstream migrating antidunes form when the Froude number is close to unity (Kennedy, 1961; Núñez-González and Martín-Vide, 2010). This means that they may be associated with unstable flow conditions that are transitioning between subcritical and supercritical flow regimes. Kennedy (1961), describes an unstable bedform regime and a complex spatial sequence where dunes and downstream migrating antidunes form upon the same bed. Alternatively, individual bedforms may alternate between the two bedform states as the flow alters from being in-phase with the bedform (signifying supercritical flow in association with downstream migrating antidunes), and out-of-phase (signifying subcritical flow in association with dunes). To this end, it is possible that the most proximal occurrence of cross-stratification may be associated with flow criticality near unity where downstream migrating antidunes form, further downstream cross-stratification may be formed under an unstable or transitioning flow regime between sub and supercritical flow. In this case, dunes and downstream migrating antidunes may form simultaneously (Kennedy, 1961). However, in conjunction with Amy (2000), Amy *et al.* (2000; 2007), Kneller and McCaffrey (2003) and Cunha *et al.* (2017), it is concluded here on contextual grounds that the occurrence of cross-stratification in the Peira Cava basin is not likely to be associated with supercritical flow, despite it being confined to proximal settings. This is based on the lack of any evidence for sedimentary deposits relating to upstream migrating antidunes that one would expect to form further upstream (Amy, 2000) where Froude numbers would likely have been higher.

### ***5.5.2 Depositional mechanisms and current conditions relating to cross-stratified beds***

In this section, interpretations of the depositional mechanisms associated with the different styles of cross-stratified bed deposited in the Peira Cava basin are detailed. Accordingly, Figure 5.32 groups the previously defined bed types according to the processes that are interpreted to have led to their formation. These interpretations are based on the model developed by Kneller and McCaffrey (2003) who describe the longitudinal velocity and density structure of turbidity currents in terms of their capacity to transport a certain amount of sediment and competency to transport sediment of a certain size. Kneller and McCaffrey (2003) describe that competency-driven deposition occurs when the shear velocity of the current falls below the threshold to keep the coarsest fraction in the flow in suspension; capacity-driven deposition occurs when there is insufficient turbulent kinetic energy to maintain the entire suspended mass of sediment within the current.

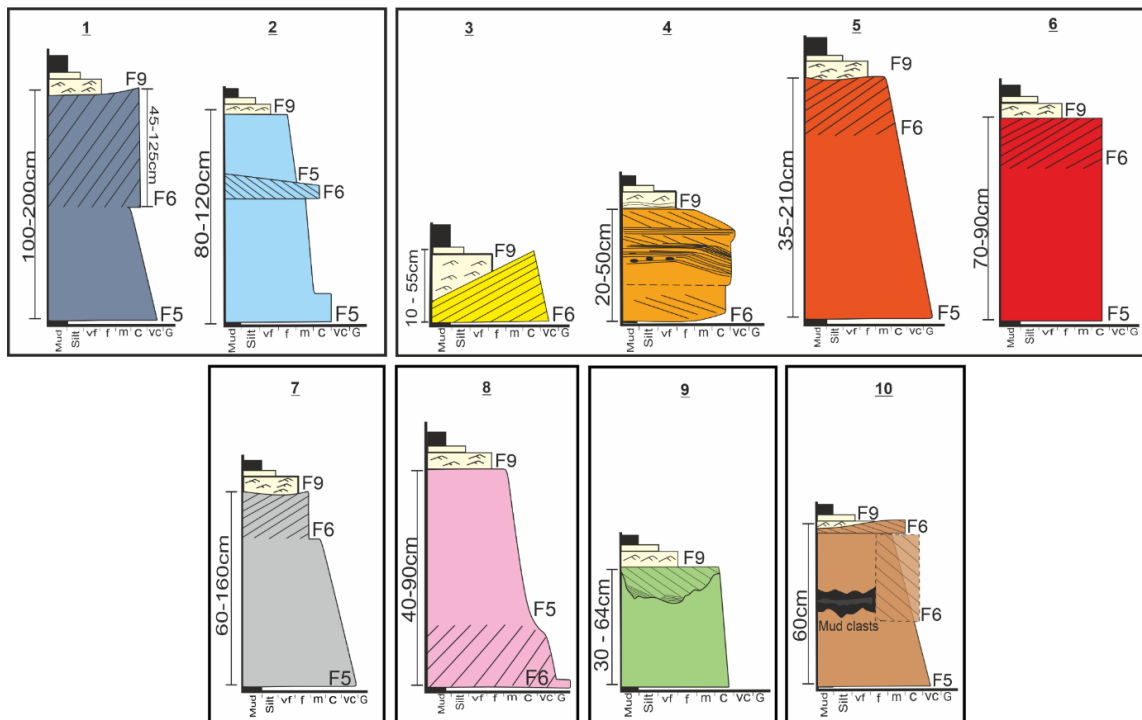


**Figure 5.32.** Bed types are grouped by the processes that are interpreted to be involved in their formation.

Both Bed Types 1 and 2 include a coarse-grained basal interval that fines up (F5 facies). The F5 facies is indicative of the deposit of a dense, sandy turbidity current. An abrupt grain-size increase occurs at the top of the basal F5 facies into coarse-grained cross-stratified sands. The introduction of the coarser sand is interpreted to be due to the remobilisation of coarser sediment that was previously deposited further upstream (as inferred by Kneller and McCaffrey, 2003). This is indicative of the current's increased competency to transport coarser grains as bedload in the form of migrating bedforms.

Bed Types 3 – 6 are interpreted to have formed due to the reworking of the F5 facies by the bypassing portion of the current carrying fine-grained sediment. The currents associated with Bed Types 3 and 4 are interpreted to be smaller and less dense, due to the relatively small deposit thickness (an interpretation of significant bypass can be ruled out based on the downstream correlations – see below). The less dense flows are interpreted to initially deposit a thin F5 coarse sediment facies which is then entirely reworked into dune bedforms. This the same interpretation as Kneller and McCaffrey (2003). The presence of multiple sets of cross-stratification in Bed Type 4 indicates it is associated with higher aggradation rates compared to Bed Type 3 which initiates bedform climbing during migration. It may also represent multiple depositional events where each set is generated upon the previous one (i.e., amalgamated F6 deposits).

The thicker beds that characterise Bed Types 5 and 6 are the deposits of high-density currents. They have coarser bottom intervals (F5 facies) which fine up in Bed Type 5 and remain constant in grain-size in Bed Type 6. Unlike Bed Types 1, 2 and 7, there is no grain-size break between the F5 and F6 cross-stratified interval. Bed Type 5 fines up through the cross-stratified interval indicating the progressive fallout of sediment from suspension from waning flow while dune development was also taking place. This allowed the fining up trend to continue through the cross-stratified interval. The ungraded Bed Type 6 is deposited due to ongoing sedimentation during steady flow that also took place during the formation of the cross-stratified interval, resulting in a continuation of the grain-size associated with the F5 facies into the cross-stratified interval. In both cases, the top of the F5 intervals are interpreted to have been reworked into dunes by a bypassing portion of the turbidity current carrying finer-grained sediment. Due to the greater bed thickness of Bed Types 5 and 6, compared to 3 and 4, the bypassing current did not rework the F5 deposit to the same extent.

Bed Type 7 contains a coarser F5 bottom interval that is normally graded, indicating that deposition took place due to the progressive aggradation of sediment as the current's capacity reduced (Kneller and McCaffrey, 2003). The following cross-stratified interval is defined by a grain-size break into finer cross-stratified sands. The grain-size break from coarse to fine sand is interpreted here to indicate a transition from capacity-driven deposition, associated with the F5 interval, to competency-driven deposition (*sensu* Kneller & McCaffrey, 2003) associated with the cross-stratified interval. A similar depositional pattern was observed by Sumner *et al.* (2008) under experimental conditions. They describe how a change in the settling regime can lead to distinct grain-size breaks. The absence of the intermediate grain-sizes, missing across the break, is associated with a period of no deposition from the turbidity current as it temporarily meets the capacity to transport and bypass the intermediate grain-size range. Before the change in depositional regime from capacity- to competency-controlled, aggradation rates were high. After the change in depositional regime, the depositional rates are thought to be lower. This may explain why only a single set of tractional bedforms develops which, due to low levels of sediment fallout from suspension, do not aggrade and do not result in climbing cross-stratification.

The cross-stratified interval in Bed Type 8 is confined to the bottom of the bed where the sediment is coarsest. This style of cross-stratification occurrence is also identified by Kneller and McCaffrey (2003). The basal part of the deposit is interpreted to have been deposited as a massive F5 interval formed by rapid sediment fallout as the current's capacity was exceeded. The formation of tractional bedforms took place due to a slight change in the current's competency to transport and rework the coarse grains that initially made up the F5 deposit. The increase in

current competency also prevented deposition of the intermediate grain-sizes missing across the grain-size break between the cross-stratified and following F5 facies. Increased competency is thought to only be temporary, as the cross-stratified interval is followed by a normally graded F5 facies. This indicates capacity-driven deposition (Kneller and McCaffrey, 2003) that was rapid enough to preserve the cross-stratification in the base of the bed. Cross-stratification situated at the base of the bed may therefore be indicative of a fluctuating current velocity.

The cross-stratified Bed Type 9, such as those illustrated in Figures 5.24 and 5.25, are interpreted to be examples of scour-infilling; the cross-stratification sits within a depression that is interpreted not to have been carved by the scouring action of the trough as the bedform migrated. This is based on the fact that the cross-stratification does not incorporate the grain of the underlying interval, which we would expect it to, had it eroded down into it. Further, the bed top of the cross-stratified intervals do not form positive relief; instead they are flat, indicating they have infilled a depression. The development of cross-stratification in association with scour-fills is interpreted to be unrelated to tractional bedform development. The cross-stratification is formed by near bed flow conditions altering from bypassing sediment in suspension to bedload transport from which parallel laminations are deposited (Arnott and Al-Mufti, 2017). Prograding parallel laminations down-lap into a scour that is tens of metres wide (Figure 5.33d). Arnott and Al-Mufti (2017) suggest a scour of a similar size could be due to the seabed becoming scoured by an up flow-migrating zone of flow expansion – i.e. a hydraulic jump – which causes the scour to progressively deepen (Figures 5.33a – c). However, Arnott and Al-Mufti (2017) note that scours formed mainly from deposits related to low-energy flows, and therefore favour an interpretation that scour development is more likely associated with a combination of bed-directed turbulent flow structures due to flow separation associated with an obstacle such as a large clast on the bed. The downward directed flow upon the bed lead to sediment erosion and excavation of a bed depression. The cross-stratified infilled scours found in the Peira Cava basin are also unlikely to be formed by supercritical flow conditions as there is no evidence of supercritical sedimentary structures above or below the scoured interval of the bed.

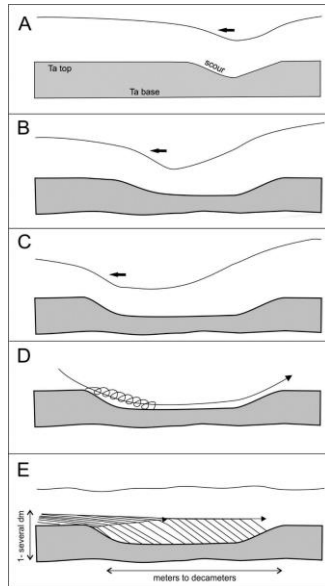


**Figure 5.33.** Arnott and Al-Mufti (2017), cross-stratification development as a result of scour infill and not tractional bedform migration.

Bed Type 10 is a laterally complex bed containing multiple and juxtaposing bed types in a short distance (20 m). Bed Type 10 also contains large quantities of mud clasts that are interpreted to be lag deposit. Notably, the sole example of Bed Type 10 lies outside of the stratigraphic interval studied (Figure 5.26). It contains a distinct change in bed character as the bed transitions from a part of the bed containing mud-clasts, to cross-stratified parts of the bed that change laterally from Bed Type 1 to Bed Type 3 and to Bed Type 7 over 20 m. Both the grain-size and the pattern of sediment deposition up through the bed changes laterally, as if the bed was deposited simultaneously by two or more components of flow with distinct, yet presumably linked, rheologies. This laterally complex bed in part resembles hybrid event beds in that there is a level of the bed containing a high concentration of mud clasts that are bounded by clean sands (Fonnesu *et al.*, 2017). It remains difficult to envisage the conditions that lead to the development of flows with such significant inferred rheological variability.

### **5.5.3 How well do existing facies tract models describe the spatial occurrence of cross-stratified units in the Peira Cava basin?**

Before commencing a discussion on how well the existing facies tract and cross-stratified bed evolutions models can be applied to the Peira Cava basin, some clarification is required on the use of term 'bypass' as applied in these models. There is potential for confusion when using the term 'bypass' in relation to cross-stratified beds, as the term has often been used to signify a current that bypasses the bulk of its suspended sediment downstream forming thick, sandy beds (for example, see Mutti (1992), Stevenson *et al.* (2015) and Kneller and McCaffrey (2003)). The

term has also been used to describe currents that have a low rate of deposition at the point in the system where their deposits are studied, for example, Amy *et al.* (2000; 2007) and Cunha *et al.* (2017) who report no evidence of bed thickening into sandy packages down-system in the Peira Cava basin. Cunha *et al.* (2017), Amy (2000) and Amy *et al.* (2000; 2007) reference the F6 facies of Mutti (1992) in relation to cross-stratified beds and associate their formation with sediment bypass, which may be misinterpreted as signifying the presence of thicker correlative sandy beds downdip. To avoid confusion, the term 'significant bypass' is used here to describe flows that deposit thick sandy beds downstream. When discussing an individual bed's vertical depositional sequence then the criteria proposed by Crisóstomo-Figueroa *et al.* (in press) has been adopted: the terms 'deposition' and 'bypass' will be applied to specific grain-sizes that are present in the bed or are absent (for example, coarse sand deposition and fine sand bypass). Below are summaries of the facies tract models and bed evolution descriptions of Mutti (1992), Kneller and McCaffrey (2003), Stevenson *et al.* (2015) and Cunha *et al.*, (2017).

#### 5.5.3.1 Model description summaries

The models and facies descriptions of cross-stratification in the Peira Cava basin fill (Mutti, 1992; Kneller and McCaffrey, 2003; Cunha *et al.*, 2017) were summarised in section 5.2.5. Here, these models are considered in their facies tract context. The facies tract models proposed by Mutti (1992) (Figure 5.8a) and Kneller and McCaffrey (2003) (Figure 5.8b) are not based on correlations within the basin, but instead are interpretations based on the authors' understanding of the longitudinal velocity and density structure of turbidity currents. The facies tract models of Cunha *et al.* (2017) are based on system-wide correlations between just four logs spaced ~2 – 8 km apart (Figure 5.8c). The spacing between the logs means that there is insufficient density of data to fully assess the spatial variation associated with cross-stratified beds.

Tinterri *et al.* (2017) describe the asymmetrical, cross-current evolution of the F6 facies in the Ranzano Sandstones in the northern Apennines (Italy) which are based on four logged intervals spaced over 1.8 km. They describe cross-stratified bed evolution in similar terms to Cunha *et al.* (2017) as being related to divergent flows (Figure 5.6c), defining different bed types associated with different depositional sequences of cross-stratified beds. Bed Type 2 in Tinterri *et al.* (2017) (corresponding to Bed Type 3 in Cunha *et al.* (2017)), describes a massive sandstone F5 interval that is overlain by tractive structures. Bed Type 3 (corresponding to Bed Type 4 in Cunha *et al.* (2017)), contains coarse-grained tractive megaripple structures. Both Bed Types 2 and 3 are interpreted as part of the same flow that deposited the coarse F5 facies, which was reworked by the bypassing low density and fine-grained upper part of the bipartite current into traction structures (Figures 5.5 and 5.6d). Unfortunately, Tinterri *et al.* (2017) do not describe the distal

character of cross-stratified beds, so it is unknown whether they are associated with significant levels of bypass down-system. Tinterri and Tagliaferri (2015) describe the downstream evolution of cross-stratified beds in the Marnoso-Arenacea Formation, Italy, in the same way as Tinterri *et al.* (2017) and Cunha *et al.* (2017), but relate their evolution to downstream changes in the bed, rather than lateral changes (Figure 5.6e).

Stevenson *et al.* (2015) describe cross-stratification from a range of sources including cores from offshore New Jersey (IODP Expedition 313) (Miller *et al.*, 2013), the Moroccan Turbidite System, which includes the Agadir Canyon and basin, and the Magallanes Basin of southern Chile (Hubbard *et al.*, 2014; Macauley and Hubbard, 2013). In all locations cross-stratification is interpreted to indicate significant sediment bypass as they can be correlated to thicker sandy turbidite packages down-system.

#### 5.5.3.2 Proximal – distal correlations of cross-stratified beds in the Peira Cava basin

The present research is based on bed-to-bed correlations of cross-stratified beds over 8 km from a higher density of logs compared to previous research on this topic in the Peira Cava outlier (Cunha *et al.*, 2017; Kneller and McCaffrey, 2003). In contrast to Mutti (1992), Stevenson *et al.* (2015) and Kneller and McCaffrey (2003), this work shows that cross-stratified beds are not associated with significant bed thickening or the development of amalgamated sand packages downstream (Figures 5.10, 5.28, and summary Figure 5.34). Therefore, the presence of cross-stratification does not indicate significant bypass of sediment downstream in the Peira Cava basin. This result supports the conclusion of Amy *et al.* (2000; 2007) and Cunha *et al.* (2017). Confirmation that cross-stratified beds in the Peira Cava basin are not indicative of significant bypass is important as it alters what inferences might be made of the wider system architecture on finding decimetre-scale cross-stratification in either core or in outcrop. Specifically, it indicates that cross-stratification need not always predict the existence of correlative large-scale sandy packages downdip.

Out of the models described above, Kneller and McCaffrey (2003) and Tinterri and Tagliaferri (2015) describe the downstream evolution of beds containing cross-stratified intervals, whereas Cunha *et al.* (2017) and Tinterri *et al.* (2017) describe both the cross- and downstream lateral changes in such bed types. Tinterri and Tagliaferri (2015), Cunha *et al.* (2017) and Tinterri *et al.* (2017) explain that cross-stratification first forms on top of the massive and coarse F5 facies then, as the current slows, the cross-stratified bed thins into smaller cross-stratified beds that are devoid of the massive basal F5 interval beneath (Figures 5.5, 5.6c and 5.6d). While the end-member bed type descriptions do correspond to two of the Bed Types defined by the present

research (Bed Types 3 and 5), it is shown here that correlated cross-stratified beds of the Peira Cava basin do not evolve downstream in this manner (no study was made of the lateral evolution of these beds). Figure 5.28 shows how bed types associated with cross-stratification changes down-system, as described above, where it was noted that there is very little evidence of bed thickness change from proximal to distal settings; and also that there is greater variability in cross-stratified bed types than has previously been documented. Thus, only Bed 512 shows thinning in a manner that corresponds to the bed evolution models of Tinterri and Tagliaferri (2015), Cunha *et al.* (2017) and Tinterri *et al.* (2017). It may be that the thinner cross-stratified beds (504 – 507) are preceded by larger beds that contain the F5 interval and cross-stratified interval above, that lie outside the correlations of the present research. However, the most distal expressions of thicker beds (511 and 513), show no evidence of thinning towards the thinner Bed Type 3 (as defined by the present research) (Figure 5.28). Figure 5.34 schematically represents the downstream evolution of different cross-stratified beds in comparison to Kneller and McCaffery (2003) and Cunha *et al.* (2017) models, showing that both thick and thinner beds containing cross-stratification tend to remain relatively constant in size downstream, or in one case slightly thin downstream. In all examples, the cross-stratification is only found in the proximal part of the system.

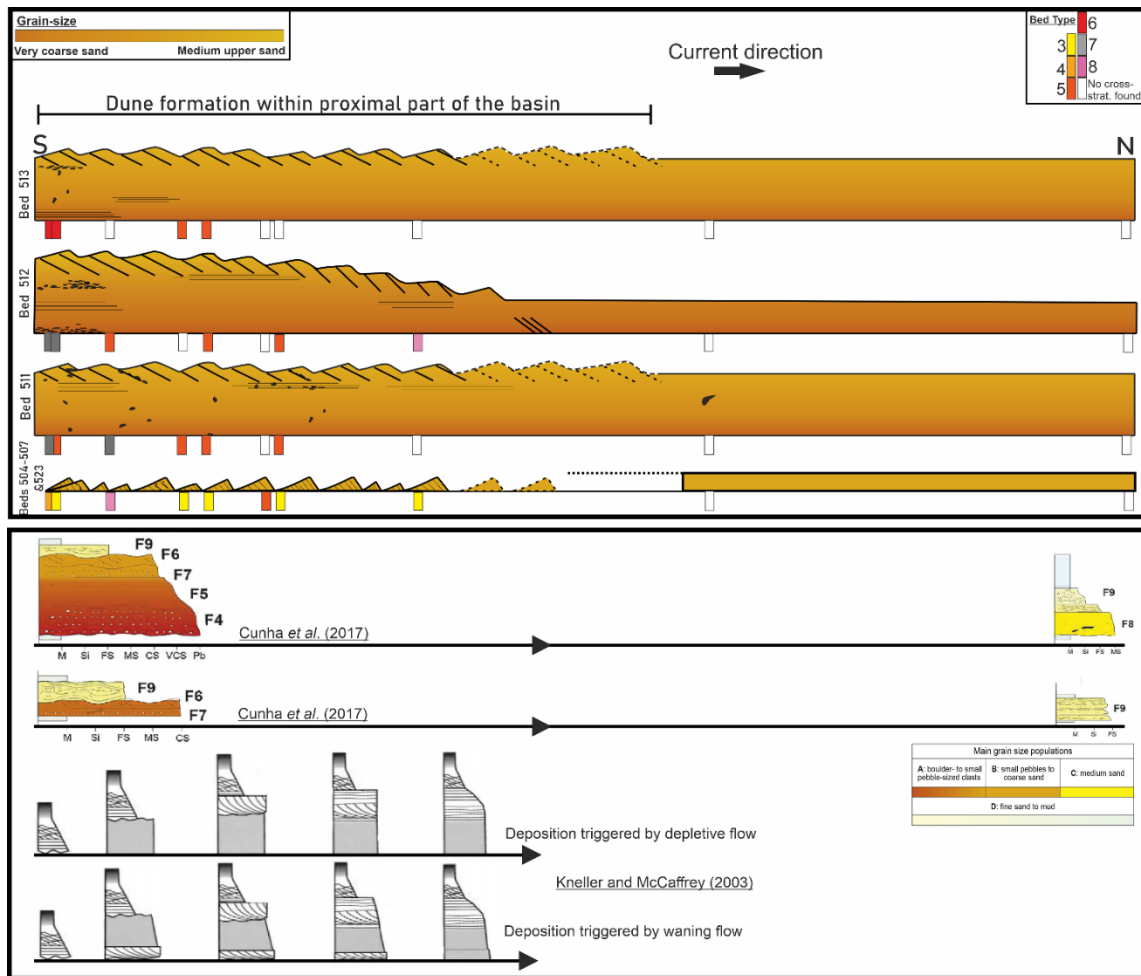


**Figure 5.34.** Schematic diagram of the downstream evolution of cross-stratified beds in the Peira Cava basin, based on the present research compared to the downstream evolution models proposed by Kneller and McCaffrey (2003) and Cunha et al. (2017).

Kneller and McCaffrey's (2003) model depicting the downstream evolution of cross-stratified beds (Figure 5.6b) is the most alike to the evolution of thick cross-stratified beds as documented by the present research in that the beds are shown to maintain their thickness and show variation in the vertical sequence of the cross-stratified beds through the system. Kneller and McCaffrey (2003) show: sharp grain-size breaks into the coarser cross-stratified interval (Bed Type 1 of the present research); fining up through the cross-stratified interval (Bed Type 5); constant grains-size from the basal massive facies into the cross-stratified interval (Bed Type 6); and the occurrence of cross-stratification in the base of the bed (Bed Type 8). However, they do not recognise Bed Types 2 – 4, 7, 9 or 10 in their discussion of competence- and capacity-driven deposition in the formation of cross-stratified beds.

## **5.5.4 Depositional sequences**

### *5.5.4.1 Single or multiple events*

Throughout this research thus far the sequence of a cross-stratified interval, followed by fine rippled/laminated sands, followed by silts and then mud, has been interpreted as having been deposited by a single flow event. This sequence incorporates the F6 and F9 facies of Mutti (1992) and Tb, Tc and Td divisions of the Bouma Sequence (Bouma, 1962) (Figure 5.4b). Previous research carried out in the Peira Cava basin by Bouma (1962), Mutti (1992), Amy (2000) and Cunha et al. (2017) has also defined this sequence as indicative of a single event. However, another interpretation may be that at least two separate events may form this sequence and that the sharp grain-size break between the generally coarse cross-stratified interval and the fine – very fine laminated and / or rippled interval could be an amalgamation surface.

Two key pieces of evidence are presented that support this interpretation. The first is that the correlation panel in Figure 5.10 shows an overall thickening of strata downdip (albeit that individual beds, e.g. Beds 505, 506.5, 509, 512, 513 and 523 – see Figure 5.35 - are found to thin). An explanation for this is that in the upstream reaches of the system, separate flow events became amalgamated but were deposited as a greater number of distinctly separate beds separated by mud intervals in the distal reaches of the system. The presence of thin mud intervals found deposited in between the coarse-grained cross-stratified interval and the fine-very fine rippled – laminated interval, is evidence that in these cases two separate flow events are associated with the deposition of these two beds. Figure 5.35 schematically represents the depositional evolution associated with proximally amalgamated cross-stratified beds creating the F6 and F9 facies depositional sequence, however, downstream the flows deposit as distinctly separate flow events.

A further test of the amalgamation theory would be to count the number of beds between correlation surfaces, which should resolve more beds downstream in the amalgamation case (subject to outcrop and minimum-thickness-to-be-logged constraints).

It is likely that this stratigraphic interval contains examples of beds that have formed under both of the depositional mechanisms invoked, i.e. some beds contain a grain-size break within an individual event bed and others contain grain-size breaks that represent amalgamation surfaces. In principle, the counting method described above would enable the relative importance of each to be determined.

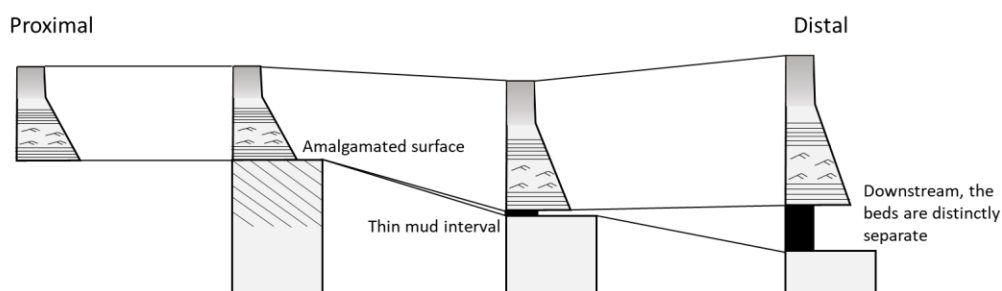


**Figure 5.35.** Schematic representation of the depositional evolution of proximally amalgamated cross-stratified beds, which downstream deposit as distinctly separate flow events separated by a mud interval.

#### 5.5.4.2 Coarse sand cross-stratified intervals overlain by thin muds

A number of beds contain thin (0.5 – 2 cm thick) mud intervals situated directly above coarse-grained cross-stratified intervals (e.g., beds 504 (Figure 5.23) , 505.10, 507, 511 and 512), which is then followed by a fine-grained depositional sequence that conforms to the facies characteristics of the  $T_c - T_e$  of the Bouma sequence. Figure 5.36 represents this full sequence. The presence of mud in between coarse cross-stratified sand and the overlying fine-grained  $T_c - T_e$  Bouma interval has not been previously documented and is therefore not included in the models and facies associations of previously published research. This section evaluates whether this depositional sequence is indicative of separate flow events that have become amalgamated or represents single flow events.

In a classic turbidite sequence, the mud interval caps the whole deposit (Bouma, 1962) (Figure 5.4b). Bouma (1962) includes mud in the Bouma sequence as the  $T_e$  facies, which is formed as the finest sediments carried by a turbidity current, settle out of suspension. If the thin mud intervals following coarse cross-stratified sand in Peira Cava are interpreted as the  $T_e$  facies, then the mud interval represents the top of the deposit formed by a flow event. In this interpretation, the following fine-grained interval ( $T_c - T_e$  of the Bouma sequence) that sits above the mud (Figure 5.36) must be a separate flow event that partially or totally eroded the preceding mud interval, causing mud to be present in some locations and absent in others (as in Figure 5.28, beds 504, 505.10, 506.5 507 and 512). Where the mud has been removed entirely, the two deposits will be amalgamated.

Regardless of whether the deposits represent single or combined flow events, an explanation is required as to how mud comes to be deposited directly on top of the coarse-grained cross-stratified interval. This sharp grain-size break could be explained by the formation of a fluid mud layer, as described by Stevenson *et al.* (2014). A fluid mud layer can form due to the

flocculation of mud and clay particles which enables mud to settle out of suspension faster than the silts and fine sands, and increases the levels of mud at the base of the flow. In this model, the high concentration of mud suppresses flow turbulence and reaches a yield strength to become a fluid mud layer which can then support the missing finer fraction from the deposit and transport it downstream. As the flow decelerates, the mud flow layer deposits en masse due to flow freezing, directly on top of the coarse sand deposit (Stevenson *et al.*, 2014). The intermediate sediment sizes missing from across the grain-size break are found in correlative bed sections downstream (Beds 507, 505.10 and 504, Figure 5.11), indicating the sediment was transported further downstream. Therefore, it is possible that the same phenomenon took place during the deposition of coarse-grained cross-stratified intervals followed by mud in the Peira Cava basin. However, the mud deposits found in Peira Cava were only 1.5 – 3 cm thick, compared to the thinnest mud deposits documented by Stevenson *et al.*, (2014), which were 10 – 20 cm thick. The small thicknesses of these mud intervals in Peira Cava might suggest that a mud flow large enough to transport and bypass the relatively coarse-grained sediment missing from the Peira Cava deposits, compared to the relatively fine-grained sediment missing from the beds described by Stevenson *et al.* (2014), did not exist. However, it is possible that the overlying mud deposit was eroded by the subsequent flow, leaving only a thin mud interval preserved in outcrop.

A number of explanations could account for the formation of the combined sequence, as shown in Figure 5.36, from a single flow. For example, the mud interval may be indicative of a single, pulsed flow event, as described by Ho *et al.* (2018). The current may have experienced a long enough duration between pulsed events to allow the flow velocity to reduce enough to enable a thin layer of mud to settle out of suspension. Potentially, flocculation of mud particles may have caused increased rates of mud deposition (Whitehouse *et al.*, 2000), conceivably reducing the time needed between pulsed flows to deposit such a thin mud interval. In this scenario the second pulse would be characterised as depositing the fine-grained sand, silt and mud that form the Bouma  $T_c - T_d$  sequence on top of the preceding mud interval. The second pulse of the current may have also partially or totally eroded the mud at different locations through the basin, creating the appearance of an amalgamated deposit.

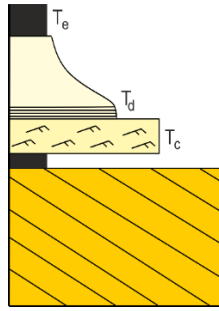


**Figure 5.36.** Schematic representation of a cross-stratified bed that is followed by a mud interval, followed by  $T_c - T_e$  of the Bouma sequence.

Another way in which a single flow event may deposit mud onto a coarse-grained interval is via the redirection of a current through the basin. Figure 5.37 schematically represents an idealised turbidity current that deposits its coarsest sediment first (orange) in one part of the basin, the current becomes slightly redirected and deposits finer sand (yellow) into a slightly different part of the basin. Houghton (1994), Mutti and Tinterri (2004) and Tinterri *et al.*, (2017) have all described how a turbidity current may experience flow stripping as divergence of the current's dense and less dense layers takes place when the flow is deflected off of the basin's bounding slopes. This may result in some areas that do not experience fine sand deposition (identified in Figure 5.37 by horizontal lines). The tail of the current containing the finest material can then deposit directly onto the coarsest sediment, developing a depositional sequence that includes a fining up distinct grain-size break that is not caused by the bypassing of fine sediment. The area of the basin where coarse-grained sediment may be followed directly by mud is also identified in Figure 5.37 as the area covered by horizontal lines. This model does not explain why in some locations in the Peira Cava basin, correlative beds do not contain mud intervals at every location. However, as previously suggested, the absence of mud may be attributed to the subsequent turbidity current eroding the underlying unconsolidated mud from the substrate.

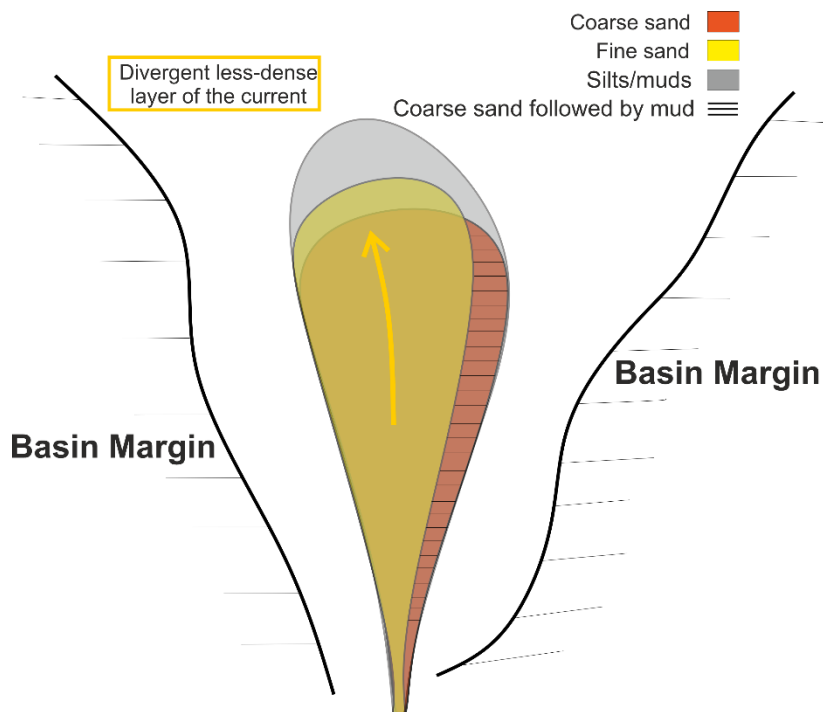


**Figure 5.37.** Idealized turbidite deposits. The coarsest sediment is deposited first (orange), then finer sand (yellow) deposits into a slightly different part of the basin, the horizontal lines depict an area that does not experience fine sand deposition. In this location, coarse sand may be followed directly by fine silts and muds which are deposited last (grey).

#### 5.5.4.3 Interpretations of temporal and spatial variation in current capacity and competency

Based on the depositional and flow processes that have been associated with each bed type (outlined in section 5.5.2) and the model developed by Kneller and McCaffrey (2003) that describes the evolution of current capacity and competency, a narrative of the flow character over time may be proposed. For each bed of the correlated section, every change in the bed type is shown in Figure 5.28 and is discussed below.

Bed 504 on the D21 Road and Beds 505.10, 506.5 and 507 throughout the D21 Road – Site 3a transect, all outcrop as Bed Type 3. They are interpreted to be the deposits of an entirely reworked F5 facies by the non-depositional portion of the current. Bed 504 at Site 1b changes into Bed Type 8, indicating that the flow’s capacity temporarily reduced resulting in deposition of finer grains than had been deposited upstream and development of a graded bed containing a wider grain-size distribution. However, the reduction in flow capacity did not initiate rapid deposition of all the sediment en-masse. The cross-stratified basal interval suggests that the current was temporarily able to regain enough velocity, i.e. a waxing current, to the point where its competency was sufficient to transport the coarsest grains as part of the bedload, for a duration long enough to allow bedforms to develop, before the succeeding deposition of the rest of the F5 facies. Where the bed changes back to Bed Type 3 at Localities 3a – 4a, the flow is interpreted to

have increased in competency so as to be able to transport finer sediment downstream and entirely rework the coarser sands of the F5 interval into traction structures.

The occurrence of Bed 505.10 at site 3b where the bed type changes to Type 5, is interpreted to represent a reduction in the current's competency, resulting in deposition of a thicker and graded F5 interval that the bypassing current was unable to entirely rework. The normally graded top of the bed, including the cross-stratified interval, suggests that sediment fallout from suspension took place simultaneously with bedform formation. The rate of fallout from suspension is interpreted to have been relatively low as the presence of tractional bedforms indicates turbulent flow structures must have existed in association with the bedforms (Gyr and Kinzelbach, 2004). Had deposition taken place too rapidly, turbulence would have been dampened, preventing bedform development (Baas and Best, 2008; Baas *et al.*, 2009; Baas *et al.*, 2011). The evidence suggests sediment fallout must also have also been low enough to prevent significant bedform aggradation. As the bed returns to being Bed Type 3 downstream, the current is interpreted to have undergone an increase in current competency, so that the medium-sized sands preserved at Site 3 were fully re-suspended in these locations.

The transition of Bed 507 from Bed Type 3 to Type 5 at Site 4a indicates progressive fallout of sediment from suspension and an overall reduction in the current's competency to carry the fine upper (FU) sediment ( $D_{50} = 250 \mu\text{m}$ ) that is deposited at the top of the bed. Deposition is interpreted to have taken place during the development of bedforms, meaning that the rate of sediment fallout from suspension was low enough to not dampen turbulence associated with bedform development, nor did it promote bedform aggradation and the formation of multiple sets of cross-strata (as described for Bed 505.10). The bed type changes between Site 4a, Site 4b and Site 5, might indicate longitudinal differences in current velocity. Firstly, the current is interpreted to have experienced an increase in current capacity transitioning from Bed Type 5 to 3. The transition from Bed Type 3 to 8 suggests a period of increased current capacity during which very coarse lower sand (VCL) grains ( $D_{50} = 1500 \mu\text{m}$ ), previously deposited upstream, became re-suspended and then re-deposited at Site 5 due to a reduction in flow capacity. The subsequent deposition of the rest of Bed Type 8 at Site 5 is associated with fluctuating flow velocities (as described for Bed 504).

Beds 511 and 512 initially outcrop as Bed Type 7. The grain-size break from coarse to fine sand indicates a transition from capacity-driven deposition associated with the basal F5 interval to competency-driven deposition associated with the cross-stratified interval (Kneller & McCaffrey, 2003). Beds 511 and 512 transition to Bed Type 5 at Sites 3a and DE, respectively. This

indicates that the current experienced a change in the flow's depositional regime back to competency-driven deposition and that the rate of sediment fallout was slow enough to allow simultaneously bedform formation and to not promote bedform aggradation. This transition in Bed 512 takes place over a very short distance (43 m), suggesting a spatial heterogeneity within the flow that allows the near simultaneous capacity- and competency-driven deposition across 43 metres. Differences in the current's depositional regime over such short distances may be caused by alterations to the flow field due to bedform-current interaction. This is a phenomenon observed in the experiments described in Chapter 3, where local flow conditions were altered from supercritical to subcritical as the flow became obstructed by a large relict bedform.

Bed 513 outcrops as Bed Type 6 along the D21 Road. Bed Type 6 is deposited due to the reduced capacity of the flow, resulting in the simultaneous deposition of a range of grain-sizes from the flow. The transition to Bed Type 5 signifies a change in the flow's depositional regime from capacity-driven deposition to competency-driven deposition. In both cases, the top of the F5 massive intervals were reworked by the bypassing current to form tractional bedforms.

Bed 523 is interpreted to have been deposited by a small and low-density flow that initially deposited an F5 interval that then became entirely reworked into traction structures by the bypassing current. In the most proximal setting, (Site DE), aggradation rates are interpreted to have been higher, producing multiple sets of cross-stratification. This bed is not observed in distal sections.

As noted above, the evolution of cross-stratified beds in the Peïra Cava basin fill do not fit the model described by Mutti *et al.* (2003), Tinterri and Tagliaferri (2015), Tinterri *et al.* (2017), and Cunha *et al.*, (2017) (Figure 5.34). By correlating individual cross-stratified beds through the Peïra Cava basin, the present research has shown the great variability in the occurrence of cross-stratification that can take place over short distances, within beds that do not significantly thicken or thin downstream.

## 5.6 Conclusions

This chapter reports on fieldwork carried out in the Peïra Cava turbidite system, SE France, to document beds containing distinct intervals of decimetre scale cross-stratification.

The principal conclusions are as follows:

1. By comparing the dimensional differences between the decimetre-scale cross-stratification and ripples preserved in association with the cross-stratification, a distinction can be made

between the ripples and the bedforms responsible for the development of the cross-stratification, which are interpreted to have developed via different formative processes.

2. The cross-stratification was not formed by supercritical flows as they do not match the geometry associated with upstream migrating antidunes, plus palaeoflow measurements indicate they migrated downstream. Downstream migrating antidunes were also probably not responsible for the formation of cross-stratification in the Peira Cava basin fill, as there is no evidence of the existence of supercritical structures associated with higher Froude numbers forming upstream of the cross-stratification.
3. In light of conclusions 1 and 2, it is further concluded that dune bedforms are responsible for the development of cross-stratification in the Peira Cava basin.
4. Ten bed types associated with the occurrence of cross-stratification can be recognised.
5. Down-flow bed correlations allow the formation of the different cross-stratified bed types to be associated with different depositional regimes relating to the spatiotemporal evolution of the competency and capacity of the depositing flow.
6. The simple term 'bypass' in relation to cross-stratified beds can be misleading. Previously the term has been used to describe the deposition of large sandy packages down-system. In other contexts, the term 'bypass' has been used to describe a turbidity current that is non-depositional at that location and point in time, regardless of the amount of sediment found downstream. Instead the term 'significant bypass' is preferred to describe the deposition of the majority of sediment downstream associated with downstream bed thickening.
7. Correlations of the cross-stratified beds of Peira Cava do not indicate 'significant bypass'; this is in contrast to the cross-stratification facies models of Mutti (1992) and Stevenson *et al.* (2015), and therefore cross-stratification may not be relied upon to indicate the presence of sandy packages downstream.
8. The Kneller and McCaffrey (2003) and Tinterri and Tagliaferri (2015) models do not accurately portray the downstream evolution of cross-stratified beds; however, they do accurately describe some of the bed types associated with cross-stratification.
9. The models of Cunha *et al.* (2017) and Tinterri *et al.* (2017) depict the downstream and lateral evolution of cross-stratified beds through the system and describe two representations of two bed types as defined by the present research. However, the spatial evolution of the beds often do not conform to the correlations documented by the present research.
10. Several mechanisms are proposed for the deposition of mud following coarse cross-stratified intervals: 1) the mud interval may be indicative of two separate flow events. 2) A fluid mud flow may have transported the intermediate grain-size missing across the grain-size break

downstream, allowing mud to be deposited directly on top of the cross-stratified interval. 3) The mud interval may be deposited by a single, pulsed flow event with a long enough period between pulse events to allow the deposition of mud. 4) Another way in which a single flow event may deposit mud onto a coarse-grained interval is via the redirection of a current through the basin.

## Chapter 6. Further discussion

The aim of this thesis was to investigate controls on the development of decimetre-scale cross-stratification within turbidites. The thesis objectives were to carry out three complementary components of work that involved experimental and field-based research to study bedform development and maintenance under steady and waning density currents, bedform development above sediment beds of uni- to bimodal grain-size distribution, and the characterisation of decimetre-scale cross-stratification preserved in outcrop. This chapter discusses the key themes of the thesis that link the three data chapters and identifies areas for future research.

This discussion extends those presented in the individual data chapters.

### 6.1 The impact of grain-size distribution on dune development in Peira Cava

Chapter 4 reports on a series of experiments investigating how beds of non-uniform and bimodally distributed sediment mixtures impact bedform development and bedform dynamics. A key conclusion was that bedform phase diagrams which characterise the substrate sediment using the median grain-size (for example: van Rijn, 1984), are poor predictors of the bedform stability fields of beds with wide grain-size distributions. This was concluded to be due to two reasons. Firstly, the wide grain-size distribution stabilised the bed by decreasing its hydraulic conductivity (cf. Staudt *et al.*, 2017). Secondly, grain sorting of widely distributed sediment by bedforms created laterally extensive anastomosing networks of fine sediment laminations throughout the bed.

As outlined in Chapter 5 (Table 5.3), cross-stratified intervals are often characterised by bimodally distributed sediment of both wide and narrow distributions. These results are based on field-based measurements of the peaks of the grain-size distribution in successive laminae made using a grain-size comparator card. Although only preliminary interpretations can be made, it is possible that the dunes associated with the bimodally distributed cross-stratification may have experienced similar effects to those documented in Chapter 4 during their development. In this section, the insights from the experimental research are applied to some of the cross-stratified beds found in the Peira Cava basin.

Table 5.3 describes the Peira Cava bedform geometries, and shows that the more 3-dimensional bedforms tend to have wider grain-size distributions. The experimental results of Chapter 4 also show how bedform variability and three-dimensionality are influenced by the different grain fractions in the bed which can become unevenly sorted into areas of finer and coarser sediment because of bedform grain sorting. As bedforms migrate they may encounter differently sorted parts of the substrate causing size-selective sediment transport, changes to their scouring capabilities and therefore changes to their morphology. Bed C4 (Figure 5.22) is an example of a Peira Cava bedform that appears to have been able to erode only intermittently into the coarser substrate beneath it. As is the case for the bedforms formed under experimental conditions in Chapter 4, alterations to the depth the bedform can scour into the substrate have led to changes in the bedform's morphology and steepness. This is apparent in the variability of the angle and geometry of the cross-stratification in Bed C4 (Figure 5.22).

Chapter 4 describes how grain sorting of the different grain fractions in a bimodally distributed bed leads to the formation of fine-grained bottomset laminations through the bed. Deposits of this kind were also found in Peira Cava. Figure 6.1 shows an example of the preservation of a fine-grained bottomset lamina that has formed a laterally extending fine-grained interval through the bed. It is interpreted to have been deposited via the fallout of fine sediment from suspension that became caught in the counterflow in the lee of the bedform (as previously described in Chapter 4).



**Figure 6.1.** An example a fine-grained bottomset lamination that has formed a laterally extending and fine-grained lamination through the bed.

Photos of some more complex deposits of widely distributed cross-stratified beds in Peira Cava, containing multiple sets of cross-stratification separated by fine-grained laminations are shown in Figures 6.2a-d and in Figure 6.3. Figure 6.2b shows a detail of the sorted coarse and fine

fractions. Figure 6.3 shows that between the field and the experimental deposits there is a likeness in the complexity and the spatial non-uniformity of the multiple sets of preserved cross-stratification and fine-grained bottomset laminations (defined by coloured lines). It is interpreted that the depositional character of these more complex cross-stratified and bimodally distributed beds containing multiple sets, may not have formed because of increased aggradation rates. Based on the experimental results of Chapter 4, multiple sets of cross-stratification may have developed due to the deposition of fine-grained bottomsets which deposit onto the bed via fallout from suspension just ahead of the bedform (creating the sigmoidal lee slope profile). These fine-grained deposits are reported to be less easily eroded, so as the body of the bedform migrates over the fine sediment deposited just ahead of it, the bedform cannot re-mobilise the sediment and therefore cannot scour deeper into the bed. The effect of this is that bedforms become superimposed or override existing bedforms (as described by Reesink and Bridge, 2009), rather than scouring into the bed and reworking any existing bedforms downstream. Thus, multiple sets of cross-stratification may be preserved.

The argument that multiple sets of cross-stratification arise from suppression of erosion due to deposition of fine-grained intervals also implies that there is material coming in from upstream to build the dunes (as it is not being eroded locally). This could be evidence that the outcrop area is not too far downstream from the upstream limit of dune formation, otherwise the upstream dunes would have built up and have starved the bedforms downstream.



**Figure 6.2.** Photos of complex deposits of widely distributed cross-stratified beds in Peira Cava that contain multiple sets of cross-stratification separated by fine-grained laminations.

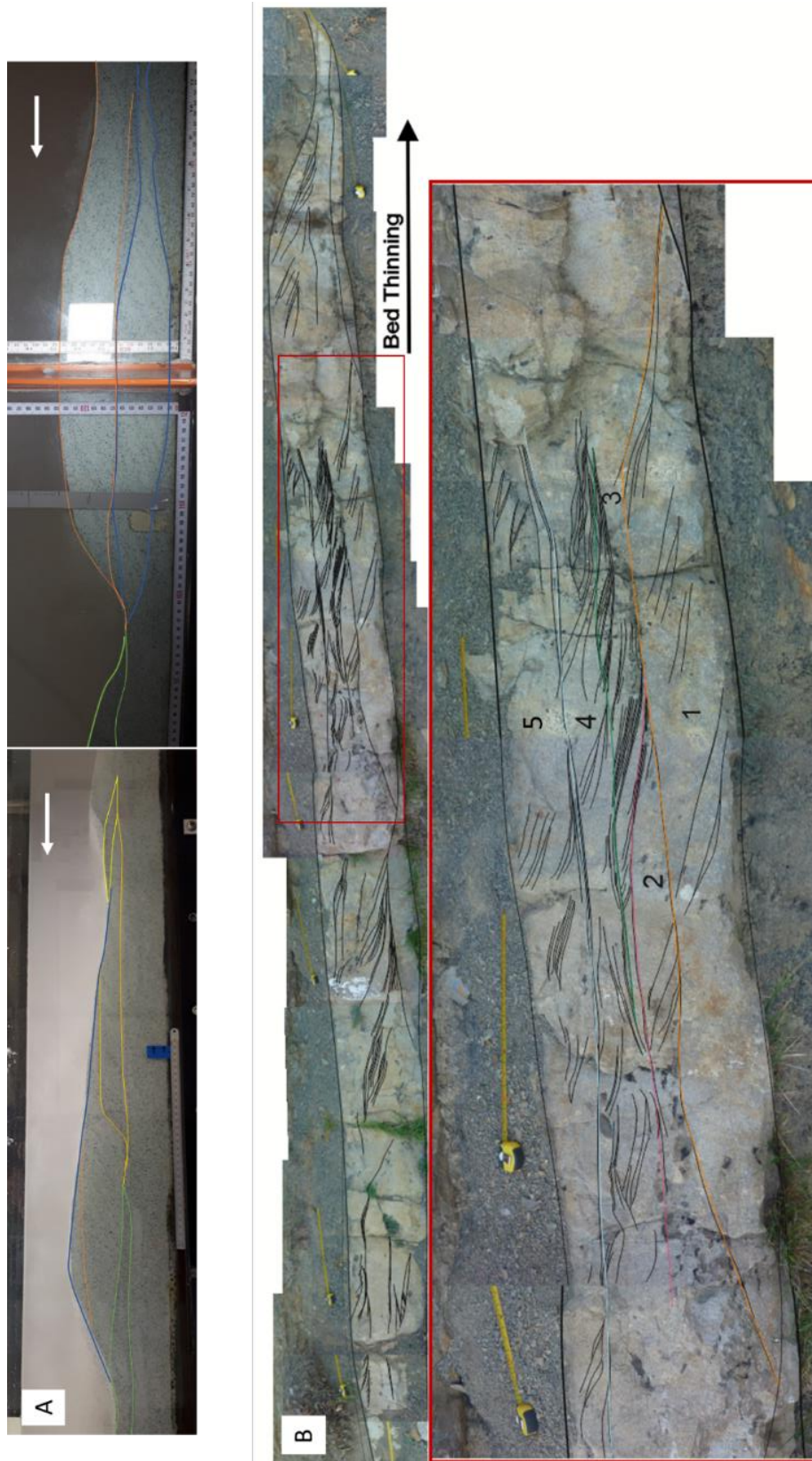


**Figure 6.3.** A comparison between the deposits of **(A)** experimental bedforms (c.f. Chapter 4) and **(B)** field-based cross-stratified beds found in the Peira Cava basin (Bed 523). Both have formed from bimodally distributed sediment.

Based on the finding that the decimetre-scale cross-stratification in Peira Cava likely represents the deposits of subcritical dunes, further interpretations can be made for the downstream evolution of bedforms throughout the system. Figure 6.4 presents a schematic 3-dimensional bedform phase diagram that represents a flow through time and space in the Peira Cava basin. Although there is no record of supercritical bedforms being preserved in outcrop, it is possible that in more proximal settings under faster flow rates and in coarser sediments, supercritical bedforms such as antidunes may have formed. In proximal – medial locations subcritical conditions likely prevailed and in coarse - medium sized sediments, dunes formed. In the distal reaches of the system, Figure 4.6 shows that no dunes formed, this is likely due to the finer sediments and waning flowrates.

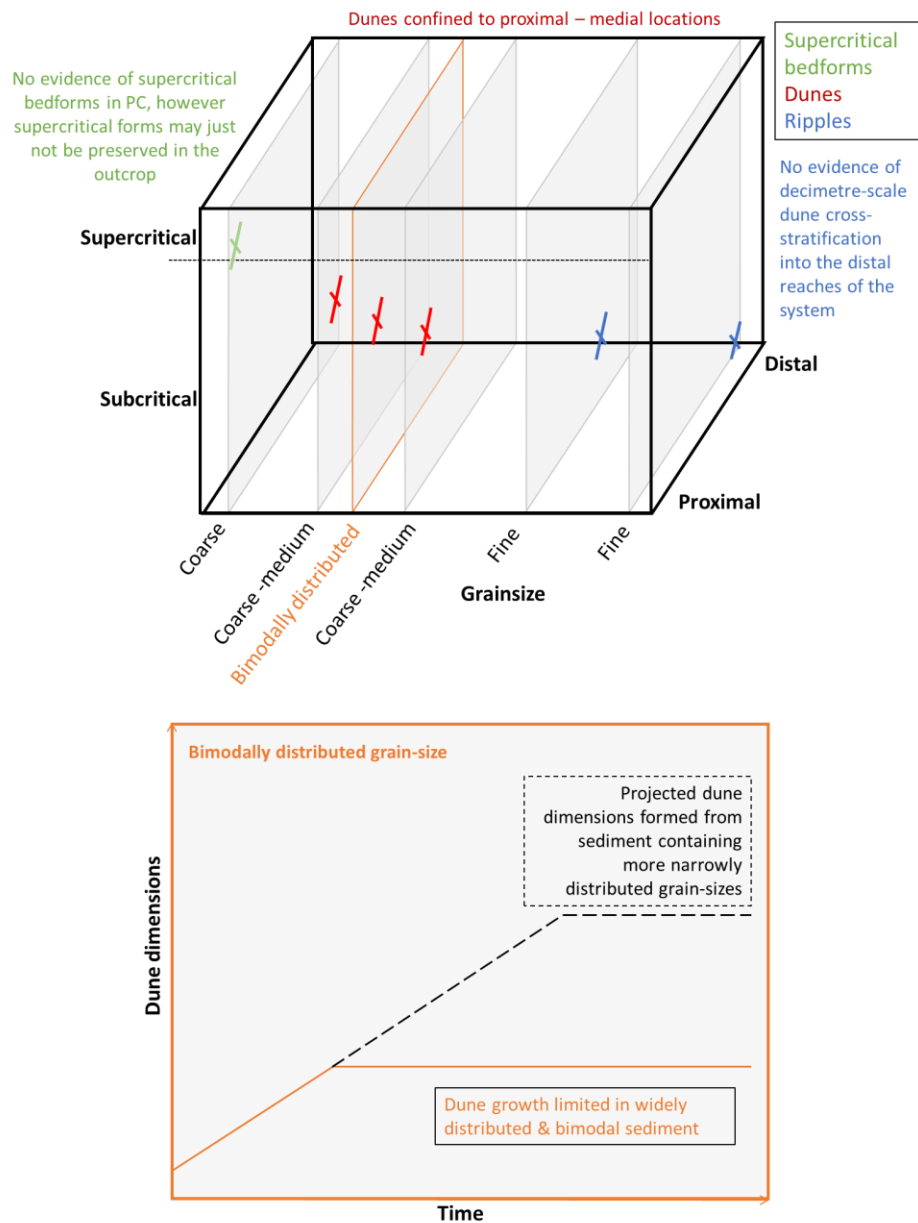


**Figure 6.4.** A schematic 3-dimensional bedform phase diagram that represents a flow through time and space in the Peira Cava basin.

## 6.2 Vertical flow structure and estimation of flow depth from bedform dimensions

Chapter 3 reports on a series of experiments investigating the controls on bedform development and maintenance under both steady and waning saline density currents. A key finding from these experiments was that bedforms developed within and scaled with a lower denser layer of the current, below the height of the velocity maximum, whose dynamics dictated the bedform type. The formation of two-layered flows characterised by a relatively thin and dense

basal layer overlain by a thicker dilute flow has been predicted in theoretical studies (Middleton, 1967; Mulder and Alexander, 2001; Luchi et al., 2018) and observed in experimental work (Postma et al., 1988; Garcia and Parker, 1993; Amy et al., 2005; Sumner et al., 2008; Fedele et al., 2016; Cartigny and Postma, 2017; de Cala et al., 2020 – Chapter 3 of this thesis). Two layered flows have also been directly measured from real-world turbidity and density currents by Xu et al. (2004), Clare et al. (2015), Hughes Clarke (2016), Dorrell et al. (2019), Paull et al. (2018), Wang et al. (2020) and Simmons et al. (2020).

Based on studies of open channel flow, the measured set heights of cross-stratification found in the geological record may be used to estimate the height of the flow in which it formed (Yalin, 1964; van Rijn, 1984; Julien and Klaassen, 1995; Bradley and Venditti, 2017). Bradley and Venditti (2017) describe a scaling relationship between the height of a dune and the flow depth, based on bedforms that are in equilibrium with steady flow conditions:

$$h = 6.96H^{0.95}, \quad (\text{Eq. 6.1})$$

where  $h$  is the flow depth and  $H$  is the dune height. To estimate the flow depth, only the fully preserved dune heights were used so as not to underestimate the flow depth. The Peira Cava dunes range in thickness from 0.15 – 0.90 m. Table 6.1 displays results that estimate the depth of the flow in which the dunes formed based on the scaling relationship defined in Equation 6.1; the estimated flow depths range from 1.15 m to 6.30 m. It is suggested that these estimates are not representative of the entire current thickness. Instead, based on the results of Chapter 3, it might be possible that the dune height and flow depth scaling relationship resolves the thickness of a lower denser layer within the current; it is further suggested that dune development took place within this lower layer (cf. Chapter 3).

The inference that a turbidite may have been deposited by a two layered flow is significant, not least because it is consistent with the idea that the current may have been driven by a dense basal layer (Paull *et al.*, 2018). However, if the concentration of sediment in the basal dense layer is too high, turbulence may be suppressed and prevent bedform development (Simons *et al.*, 1965; Nezu and Azuma 2004; Noguchi and Nezu 2009; Baas *et al.*, 2009; 2011; Arnott, 2012). The current conditions in the lower layer of the flow are of fundamental importance as they affect the rates of sediment erosion and deposition which in turn determine the current's velocity and run-out distance (Kneller and Buckee, 2000).

Defining the type of bedforms that are formed by the lower denser layers of stratified flows can help interpret the flow conditions more accurately within the dense lower layer. For

example, in Peira Cava, the presence of dune bedforms firstly indicates that the flow in the lower layer was subcritical and that the velocity within the lower layer was maintained for a long enough duration to form such bedforms. Secondly, the observation that most dune cross-stratification in Peira Cava is in the form of single sets indicates that aggradation and dune climbing did not take place, which is interpreted to reflect low rates of deposition from the flow during dune formation, which may further indicate that the dunes were sediment starved.

The total turbidity current thickness associated with the different dunes may be estimated by calculating the height of the lower layer compared to the height of the entire current. Earlier measurements of the thickness of lower denser layers in real-world and experimental density currents are used to indicate what proportion of the total current thickness is represented by the lower denser layer. Azpiroz-Zabala *et al.* (2017) report that the lower layer is 15% of the entire flow thickness. Dorrell *et al.* (2019) measure the lower denser layer to be 50% of the flow depth. Simmons *et al.* (2020) record the height of the velocity maximum as 15 – 50% up from the bed (depending on the current thickness). The height of the velocity maximum may also be used to indicate the height of the upper surface of the lower denser layer (Fedele *et al.*, 2016; Dorrell *et al.*, 2019; de Cala *et al.*, 2020 – Chapter 3 of this thesis). Finally, the bottom denser layer of the experimental density currents described in Chapter 3 were 20 – 50% of the entire current thickness. Based on these measurements from real-world and experimental density currents, it is reasonable to conclude that the bottom denser layer occupies between 15% and 50% of the entire current thickness. Having previously estimated the thickness of the lower layer of the flow associated with the Peira Cava dunes, a range in total current thickness may then also be calculated (Table 6.1).

**Table 6.1.** Estimations of the depth of the flow in which the Peira Cava dunes formed based on the scaling relationship defined in Eq. 6.1, and on the possible ranges of total current thickness associated with each dune height based on the lower layer of the flow equalling between 15 – 50 % of the entire flow thickness.

<b><i>Dune height (m)</i></b>	<b>Flow depth (m) based on Eq. 6.1</b>	<b>Current thickness (m) based on lower layer = 15 % of flow depth</b>	<b>Current thickness (m) based on lower layer = 50 % of flow depth</b>
0.34	2.27	15.11	4.53
0.23	1.72	11.49	3.45
0.19	1.44	9.58	2.87
0.182	1.38	9.20	2.76
0.194	1.47	9.77	2.93

0.22	1.65	11.01	3.30
0.25	1.86	12.43	3.73
0.45	3.26	21.73	6.52
0.17	1.29	8.62	2.59
0.22	1.65	11.01	3.30
0.29	2.15	14.32	4.29
0.5	3.60	24.02	7.21
0.15	1.15	7.65	2.30
0.43	3.12	20.81	6.24
0.185	1.40	9.34	2.80
0.15	1.15	7.65	2.30
0.42	3.05	20.35	6.11
0.9	6.30	41.98	12.59
0.85	5.96	39.76	11.93
0.9	6.30	41.98	12.59

### 6.3 Equilibrium in dune formation

These estimations of the height of the lower layer of the flow and the total current thickness stem from the assumption that the dune bedforms in Peira Cava were in equilibrium with steady flow conditions in the lower denser layer of the flow (Bradley and Venditti, 2017). However, whether dunes can reach a state of equilibrium when forming within an unsteady (generally waning) turbidity current warrants further discussion. A key result of the research presented in Chapter 3 is the maintenance of flow velocity in the bottom denser layer of the experimental density current even though the flow rate was set to wane throughout the experiment. The maintenance of current conditions enabled dune formative conditions to be sustained. Dorrell *et al.* (2019) also recorded the maintenance of density current concentration and momentum within the lower layer of real-world saline density currents. These findings suggest that it is possible for conditions to be maintained within the bottom layer of a current, even as the flow wanes. For dune equilibrium to be achieved, dune formative conditions need to be maintained for a long enough duration (Baas, 1994; 1999; Coleman *et al.*, 2003; Perillo *et al.*, 2014). Baas (1994; 1999) records the amount of time needed for ripples to reach equilibrium as

between 0.5 – 3 hours; the bedforms reported by Perillo *et al.* (2014) achieve equilibrium after 0.82 hours. The bedforms that formed during Experiments 1 – 3 (in Chapter 4) took 10, 7 and 8 hours, respectively, to achieve a state of dynamic equilibrium. Turbidity currents are widely reported to flow for periods that exceed these times, ranging from hours and days (Xu, 2010; Xu *et al.*, 2014; Hughes Clarke, 2016; Paull *et al.*, 2018) to weeks (Cooper *et al.*, 2013; 2016; Azpiroz-Zabala *et al.* 2017; Simmons *et al.* 2020). Therefore, it is entirely plausible that turbidity currents can flow for a duration long enough to form quasi-equilibrium dunes.

However, as noted in Chapter 3, as the upper layer continues to wane it may thin due to the interface between the two layers of the flow acting as an energy sink that absorbs momentum as internal gravity waves break at the interface (Dorrell *et al.*, 2019). The diminishment of the upper layer may also be due to considerations of mass balance, which dictates that if the basal layer is steady and of constant thickness, then the upper layer volume flux must decrease. As the upper layer of the current is diminished so too does the drag acting between the two layers of the flow, thus altering the flow conditions in the bottom layer so that the lower layer eventually must thin and/or slow as the upper layer progressively becomes extinguished. Whether equilibrium dunes can form within the lower layer of a current may therefore be affected by the rate of diminishment of the upper layer of the flow.

## 6.4 Areas for future research

The components of this thesis span physical modelling and field-based research and have provided new insight into bedform development under turbidity currents and the parameters which may affect their formation. The work prompts several suggestions for follow-on research topics:

1. The study of density currents under experimental conditions is currently limited by the fact that it is hard and expensive to achieve longer run times than have been achieved in the present research. Longer duration runs would enable further study of the lower denser layer of the current, including how it maintains its velocity under waning flow rates and for how long the lower denser layer can maintain its flow conditions as the upper layer gradually wanes. Longer run times would also enable continued dune development beyond that achieved in the present research, allowing assessment of whether the observed dunes were in equilibrium, and if not, of the time it takes for dunes to achieve equilibrium.
2. Continued data collection under controlled experimental conditions is needed to further define the bedform phase spaces on bedform phase diagrams for density currents.

3. In order to better understand how different grain-size distributions impact bedform development, further tests are required to assess the effects of a greater variety of non-uniform sediment mixtures, characterised by different grain-size distributions. Data collection relating to the bed's stability could be achieved by measuring the bed's hydraulic conductivity to evaluate the amount of water inflow through the bed (cf. Staudt *et al.*, 2017).
4. Further experiments could be run to test the extent to which different flow velocities affect sediment transport from beds made of different grain-size distributions and how this impacts bedform development.
5. As noted above, further work is needed to properly constrain how the grain-size distribution of the cross-stratified correlative intervals changes throughout the Peira Cava system. This should involve more accurate grain-size analysis techniques than the use of a grain-size comparator card in the field. For example, sediment samples taken from multiple parts of the cross-stratified intervals can be used to create thin sections which will better represent the different grain-size populations that make up the bedform.
6. Future work should establish whether the newly defined bed type scheme based on the decimetre-scale cross-stratified beds of the Peira Cava basin is applicable to other systems that contain similar deposits, and whether the depositional regimes that have been associated with the different bed types are applicable to other systems. Further detailed analysis of cross-stratified beds within other systems will also help identify any other bed types associated with decimetre-scale cross-stratification that have not yet been documented. This will enable development of an understanding of the different depositional regimes involved in the formation of decimetre-scale cross-stratification, which also helps to interpret the evolution of the flow downstream should multiple correlative cross-stratified bed types be identified. This work should better place dune occurrence within their host facies tracts.
7. Related to point 6., further work is needed to characterise the distal occurrence of decimetre-scale cross-stratified beds. It is suggested site this research might be carried out in the Marnoso Arenacea Formation, Italy (cf. Sumner *et al.*, 2012).
8. The research presented in this thesis has focused on bedforms that form decimetre-scale cross stratification. A follow-on research topic could be to evaluate what boundary conditions are associated with the development of larger-scale sediment wave fields. Also, the research presented in this thesis describes how pre-existing bedforms has been shown to exert a first order influence on the effective flow regime. A follow-on research topic could be to assess whether the presence of large-scale sediment waves affects the tendency of flows to generate the dune bedforms that have been associated with decimetre-scale cross-stratification

## 7. Conclusions

The principal conclusions of this thesis are that:

1. Under experimental saline density currents, subcritical and supercritical bedforms developed within a lower denser layer of density currents, whose dynamics dictated the bedform type.
2. The reduced gravity experienced by the experimental saline density currents, enabled supercritical conditions to be achieved at slower flow rates than may be achieved in open channel flow conditions.
3. Pre-existing bed states were observed to exert a first-order influence on subsequent bedform development regardless of the nominal flow regime of the density current. This effect is not captured by open channel flow and density current bedform phase diagrams. Therefore, such diagrams may inaccurately predict bedform development if the speed and direction at which currents pass through different bedform phase spaces are not considered.
4. Further experimental studies found that wide grain-size distributions may stabilise the bed by reducing its hydraulic conductivity.
5. Grain sorting of bimodally-distributed sediment mixtures by bedforms created laterally extensive anastomosing networks of fine sediment laminations throughout the experimental bed. The fine laminations were interpreted to have obstructed the passage of fluid through the upper 5 cm of the bed which further reduced the hydraulic conductivity of the bed and increased the bed stability.
6. The fine laminations were found likely to have a higher threshold of motion and collectively acted as an armour layer made of fine sediment at the top of the bed. Migrating bedforms were unable to mobilise the fine laminations and erode into the bed and so became sediment starved. Further, it was shown that this ongoing suppression of bedform development can be considered as the equilibrium state of the bed.
7. Bimodal sediment mixtures of a narrower grain-size distribution did allow bedform development; however, grain sorting by bedforms created an unevenly sorted bed that forced the formation of smaller bedforms by diminishment of larger bedforms.

8. Bedform phase diagrams that use the median grain-size of sediment in the bed were found to be poor predictors of the bedform stability fields of beds made up of wide grain-size distributions.
9. Field-based research concluded that dune bedforms are responsible for the development of decimetre-scale cross-stratification in the Peira Cava basin.
10. Ten bed types associated with the occurrence of decimetre-scale cross-stratification were recognised and the down-flow bed correlations allowed the formation of the different cross-stratified bed types to be associated with different depositional regimes relating to the spatiotemporal evolution of the competency and capacity of the depositing flow.
11. In contrast to the cross-stratification facies models of Mutti (1992) and Stevenson *et al.* (2015), the cross-stratified beds of Peira Cava were found to not indicate 'significant bypass'. Therefore, cross-stratification may not be relied upon to indicate the presence of sandy packages downstream.
12. The Kneller and McCaffrey (2003) and Tinterri and Tagliaferri (2015) models were found to inaccurately portray the downstream evolution of cross-stratified beds in the Peira Cava basin; however, they do accurately describe some of the bed types associated with cross-stratification.
13. The models of Cunha *et al.* (2017) and Tinterri *et al.* (2017) depict the downstream and lateral evolution of cross-stratified beds through the system; however, the spatial evolution of the beds often have been shown to not conform to those confirmed by the correlations documented by the present research.
14. Multiple mechanisms were proposed for the deposition of mud following coarse cross-stratified intervals. These include: (1) the mud interval may be indicative of two separate flow events; (2) a fluid mud flow may have transported the intermediate grain-size missing across the grain-size break downstream, allowing mud to be deposited directly on top of the cross-stratified interval; (3) the mud interval may be deposited by a single, pulsed flow event with a long enough period between pulse events to allow the deposition of mud; (4) a single flow event may deposit mud onto a coarse-grained interval via the redirection of a current through the basin.
15. Estimations of the vertical flow structure and the current flow depth were made based on preserved bedform dimensions from the Peira Cava system. It was suggested that the dunes in Peira Cava may have formed within a lower denser layer of the current in which flow conditions were maintained.

16. Previous research describes cross-stratified beds as being generally coarse-grained. However, the present research has shown that they are in fact often formed from non-uniform, bimodally distributed sediment. Therefore, it is possible that the dunes associated with the bimodally distributed cross-stratification may have experienced similar effects to those documented in Chapter 4 during their development, such as grain sorting by bedforms creating an unevenly sorted bed that can force the formation of smaller bedforms by diminishment of larger bedforms. Further, recognition that dune cross-stratification is often bimodally distributed creates the potential for more accurate interpretations of the flow conditions and depositional regimes at the time of dune formation.

## References

- Aas, T. E., Basani, R., Howell, J. A. & Hansen, E. 2014. Semi-automated registration of close range hyperspectral scans using oriented digital camera imagery and a 3D model. *Geological Society, London, Special Publications*, 387, pp. 247-269.
- Aas, T. E., Howell, J. A., Janocko, M. & Midtkandal, I. 2010. Re-created early Oligocene seabed bathymetry and process-based simulations of the Peira Cava turbidite system. *Journal of the Geological Society*, 167, pp. 857-875.
- Alexander, J., Bridge, J. S., Cheel, R. J. & Leclair, S. F. 2001. Bedforms and associated sedimentary structures formed under supercritical water flows over aggrading sand beds. *Sedimentology*, 48 (1), pp. 133-152.
- Alexander, J., McLelland, S. J., Gray, T. E., Vincent, C. E., Leeder, M. R., & Ellett, S. 2008. Laboratory sustained turbidity currents form elongate ridges at channel mouths. *Sedimentology*, 55, pp. 845–868.
- Allen, J. R. L. 1962. Asymmetrical ripple marks and the origin of cross-stratification: *Nature*, 194, pp. 167–169.
- Allen, J. R. L. 1963. The classification of cross-stratified units with notes on their origin. *Sedimentology*, 2, pp. 93–114.
- Allen, J. R. L. 1968. *Current Ripples: Their Relation to Patterns of Water and Sediment Motion*. Amsterdam: North-Holland Publishing Company.
- Allen, J. R. L. 1970. The sequence of sedimentary structures in turbidites: with special reference to dunes. *Scottish Journal of Geology*, 6, pp. 146-161.
- Allen, J. R. L. 1973. Phase differences between bed configuration and flow in natural environments, and their geological relevance. *Sedimentology*, 20 (2), pp. 323–329.
- Allen, J. R. L. 1978. Polymodal dune assemblages: an interpretation in terms of dune creation-destruction in periodic flows. *Sedimentary Geology*, 20, pp. 17-28.
- Allen, J. R. L. 1984. *Sedimentary Structures: Their Character and Physical Basis*. Amsterdam: Elsevier.

- Almedeij, J. & Diplas, P. 2005. Bed load sediment transport in ephemeral and perennial gravel-bed streams. *EOS Transactions of the American Geophysical Union*, 86 (44), pp. 429-434.
- Almedeij, J., and Diplas, P. 2005. Bed load sediment transport in ephemeral and perennial gravel bed streams, *Eos, Transactions, American Geophysical Union*, 86 (44), pp. 429– 434.
- Amy, L. A. & McCaffrey, W. D. & Kneller, B. C. 2004. The influence of a lateral basin-slope on the depositional patterns of natural and experiment turbidity currents. *Geological Society, London, Special Publications*, 221, pp. 311-330.
- Amy, L. A. 2000. *Architectural analysis of a sand-rich confined turbidite basin; the Gres de Peïra Cava, south-east France*. PhD Thesis. University of Leeds.
- Amy, L. A., Peakall, J. & Talling, P. J. 2005. Density- and viscosity-stratified gravity currents: Insight from laboratory experiments and implications for submarine flow deposits. *Sedimentary Geology*, 179, pp. 5-29.
- Amy, L. A., Talling, P. J., Sumner, E. J. & Malgesini, G. 2016. Current-aligned dewatering sheets and ‘enhanced’ primary current lineation in turbidite sandstones of the Marnoso-Arenacea Formation. *Sedimentology*, 63 (5), pp. 1260-1279.
- Amy, L.A., Kneller, B.C. & McCaffrey, W.D. 2000. Evaluating the links between turbidite characteristics and gross system architecture: upscaling insights from the turbidite sheet-system of Peïra Cava, SE France. In: Weimer, P ed. *Deep-Water Reservoirs of the World*. [Online]: SEPM Society for Sedimentary Geology. Available at: <https://pubs.geoscienceworld.org/books/book/1968/Deep-Water-Reservoirs-of-the-World>.
- Amy, L.A., Kneller, B.C. & McCaffrey, W.D. 2007. Facies architecture of the Grès de Peïra Cava, SE France: landward stacking patterns in ponded turbiditic basins. *Journal of the Geological Society, London*, 164, pp. 143–162.
- Apps, G. M. 1987. *Evolution of the Gres d'Annot Basin, South West Alps*. Ph.D. thesis, University of Liverpool.
- Arnott, R. 2012. Turbidites, and the case of the missing dunes. *Journal of Sedimentary Research*, 82, pp. 379-384.
- Arnott, R.W.C. & Al-Mufti, O. 2017. Deep-marine pseudo dune cross-stratification—similar, but completely different. *Journal of Sedimentary Research*, 87, 312-323.

- Ashida, K. & Michiue, M. 1971. An investigation of river bed degradation downstream of a dam. *Proc. of 14th IAHR Congress. Wallingford, U.K.*, pp. 1-9.
- Ashida, K., & M. Michiue. 1973. Study on bed load transport rate in open channel flows. *International Symposium on River Mechanics, International Association for Hydraulic Research, Bangkok.*
- Ashley, G. M. 1990. Classification of large-scale subaqueous bedforms: a new look at an old problem. *Journal of Sedimentary Research*, 60, pp. 160-172.
- Austin, M. J., Masselink, G., O'Hare, T. J., & Russell, P. E. 2007. Relaxation time effects of wave ripples on tidal beaches, *Geophysical Research Letters*, 34 (16).
- Azpiroz-Zabala, M., Cartigny, M. J. B., Sumner, E. J., Clare, M. A., Talling, P. J., Parsons, D. R. & Cooper, C. 2017. A general model for the helical structure of geophysical flows in channel bends. *Geophysical Research Letters*, 44 (23), pp. 11932-11941.
- Azpiroz-Zabala, M., Cartigny, M. J. B., Talling, P. J., Parsons, D. R., Sumner, E. J., Clare, M. A., Simmons, S. M., Cooper, C. & Pope, E. L. 2017. Newly recognized turbidity current structure can explain prolonged flushing of submarine canyons. *Science Advances*, 3 (10), e1700200.
- Baas, J. H. & Best, J. L. 2008. The dynamics of turbulent, transitional and laminar clay-laden flows over a fixed current ripple. *Sedimentology*, 55, pp. 635-666.
- Baas, J. H. 1978. Ripple, ripple mark, ripple structure. In: Fairbridge, R. W. ed. *Sedimentology. Encyclopedia of Earth Science*. Berlin: Springer.
- Baas, J. H. 1993. Dimensional analysis of current ripples in recent and ancient depositional environments. *Utrecht University Repository*, 106.
- Baas, J. H. 1994. A flume study on the development and equilibrium morphology of current ripples in very fine sand. *Sedimentology*, 41 (2), pp. 185-209.
- Baas, J. H. 1999. An empirical model for the development and equilibrium morphology of current ripples in fine sand. *Sedimentology*, 46 (1), pp. 123-138.
- Baas, J. H., Best, J. L. & Peakall, J. 2011. Depositional processes, bedform development and hybrid bed formation in rapidly decelerated cohesive (mud-sand) sediment flows. *Sedimentology*, 58, pp. 1953-1987.

- Baas, J. H., Best, J. L. & Peakall, J. 2015. Predicting bedforms and primary current stratification in cohesive mixtures of mud and sand. *Journal of Geological Society*, 173, pp. 12-45.
- Baas, J. H., Best, J. L. 2008. The dynamics of turbulent, transitional and laminar clay-laden flow over a fixed current ripple, *Sedimentology*, 55 (3), pp. 635-666.
- Baas, J. H., Best, J. L., Peakall, J. & Wang, M. 2009. A phase diagram for turbulent, transitional, and laminar clay suspension flows. *Journal of Sedimentary Research*, 79, pp. 162-183.
- Baas, J. H., Davies, A. G. & Malarkey, J. 2013. Bedform development in mixed sand–mud: The contrasting role of cohesive forces in flow and bed, *Geomorphology*, 182, 15, pp. 19-32.
- Bagnold, R. A. 1946. Motion of waves in shallow water. Interaction between waves and sand bottoms (with comments from Taylor, G.). *Proceedings of the Royal Society of London. Series A, Mathematical and Physical Sciences*, 187 (1008), pp. 1-18.
- Bagnold, R. A. 1962. Auto-suspension of transported sediment; turbidity currents. *Proceedings of the Royal Society of London, Series A: Mathematical and Physical Sciences*, 265, pp. 315-319.
- Baines, P. 1998. *Topographic Effects in Stratified Flows*. Cambridge: Cambridge University Press.
- Bakke, K., Gjelberg, J. & Petersen, S. A. 2008. Compound seismic modelling of the Ainsa II turbidite system, Spain: application to deep-water channel systems offshore Angola. *Marine and Petroleum Geology*, 25 (10), pp. 1058-1073.
- Bartholdy, J., Ernsten, V. B., Flemming, B. W., Winter, C., Bartholomä, A. & Kroon, A. 2015. On the formation of current ripples. *Scientific Reports*, 5, 11390.
- Bartzke, G., Bryan, K.R., Pilditch, C. A., Huhn, K. 2013. On the Stabilizing Influence of Silt on Sand Beds. *Journal of Sedimentary Research*, 83 (8), pp. 691–703
- Bennett, S. & Best, J. 1995. Mean flow and turbulence structure over fixed, two dimensional ripples: implications for sediment transport and bedform stability. *Sedimentology*, 42, pp. 491–513.
- Bennett, S. J. & Best, J. L. 1996. Mean flow and turbulence structure over fixed ripples and the ripple-dune transition. In: Ashworth, P. J., Bennett, S. J., Best, J. L., McLelland, S. J. eds. *Coherent Flow Structures in Open Channels*. Chichester, UK: Wiley & Sons, pp. 281–304.

- Best, J. 1992. On the entrainment of sediment and initiation of bed defects: insights from recent developments within turbulent boundary layer research. *Sedimentology*, 39, pp. 797-811.
- Best, J. 1993. On the interactions between turbulent flow structure, sediment transport and bedform development: some considerations from recent experimental research. In: Clifford, N., French, J. & Hardisty, J. eds. *Turbulence: Perspectives on Flow and Sediment Transport*. Chichester, UK: Wiley, pp. 61–92.
- Best, J. 2005. The fluid dynamics of river dunes: A review and some future research directions. *Journal of Geophysical Research, Earth Surface*, 110 (F4).
- Best, J. L. & Kostaschuk, R. 2002. An experimental study of turbulent flow over a low-angle dune. *Journal of Geophysical Research: Oceans*, 107 (C9), 3135.
- Best, J. L. 1996. The fluid dynamics of small-scale alluvial bedforms. In: Carling, P. A. & Dawson, M. eds. *Advances in Fluvial Dynamics and Stratigraphy*. Chichester, UK: Wiley and Sons, pp. 67-125.
- Best, J. L. 2005. The fluid dynamics of river dunes: a review and some future research directions. *Journal of Geophysical Research: Earth Surfaces*, 110, F04S02.
- Best, J. L., Kostaschuk, R. A. & Villard, P. V. 2001. Quantitative visualization of flow fields associated with alluvial sand dunes: results from the laboratory and field using ultrasonic and acoustic Doppler anemometry. *Journal of Visualization*, 4, pp. 373-381.
- Blom, A. 2008. Different approaches to handling vertical and streamwise sorting in modelling river morphodynamics. *Water Resources Research*, 44, W03415.
- Blom, A., Ribberink, J. S. & de Vriend, H. J. 2003. Vertical sorting bed forms: Flume experiments with a natural and a trimodal sediment mixture. *Water Resources Research*, 39 (2), 1025.
- Bonnefille, R. 1963. Essais de synthese des lois du debut d'entrainement des sediments sous l'action d'un courant en regime continu. *Bull. du Centre de Rech. et d'ess. de Chatou*, 5, pp. 17–22.
- Bouma, A. H. 1962. *Sedimentology of Some Flysch Deposits*. Amsterdam: Elsevier.
- Bouma, A. H., Normark, W. R. & Barnes, N. E. 2012. *Submarine Fans and Related Turbidite Systems*. New York: Springer.
- Boussac, J. 1912. *Études stratigraphiques sur le nummulitique alpin*. Paris, Imprimerie nationale.

- Bradley, R. W. & Venditti, J. G. 2017. Reevaluating dune scaling relations. *Earth-Science Reviews*, 165, pp. 356-376.
- Bridge, J. S. & Best, J. L. 1988. Flow, sediment transport and bedform dynamics over the transition from dunes to upper-stage plane beds: implications for the formation of planar lamination. *Sedimentology*, 35, pp. 753–763.
- Bridge, J. S. & Best, J. L. 1997. Preservation of planar laminae due to migration of low-relief bed waves over aggrading upper-stage plane beds: comparison of experimental data with theory. *Sedimentology*, 44 (2), pp. 253-262.
- Bridge, J. S. & Lunt, I. A. 2006. Depositional models of braided rivers. Braided Rivers, Processes, Deposits, Ecology and Management. *International Association of Sedimentologists Special Publications*, 36, pp. 11-55.
- Bridge, J. S. 1997. Thickness of sets of cross strata and planar strata as a function of formative bed-wave geometry and migration, and aggradation rate. *Geology*, 25 (11), pp. 971-974.
- Bridge, J. S. 2003. *Rivers and Floodplains: Forms, Processes, and Sedimentary Record*, Blackwell, Malden, Mass.
- Brooks, H. L., Hodgson, D. M., Brunt, R. L., Peakall, J., Hofstra, M. & Flint, S. S. 2018. Deep-water channel-lobe transition zone dynamics: Processes and depositional architecture, an example from the Karoo Basin, South Africa. *Geological Society of America Bulletin*, 130 (9-10), pp. 1723-1746.
- Bruschi, R., Bughi S., Spinazzè M., Torselletti E. & Vitali L. 2006. Impact of debris flows and turbidity currents on seafloor structures. *Norwegian Journal of Geology*, 86, pp. 317-337.
- Buxton, T., Yager, E., Buffington, J., Hassan, M. & Fremier, A. 2014. Grain packing resistance to particle mobility (in revision). *Journal of Geophysical Research Atmospheres*. MISSING INFO
- Campbell, C. S. 1978. Liquefaction and fluidization. In: *Sedimentology. Encyclopedia of Earth Science*. Berlin: Springer.
- Carling, P. 1992. The nature of fluid boundary layer and the selection of parameters for benthic ecology. *Freshwater Biology*, 28, pp. 273-284.
- Carling, P. A. & Shvidchenko, A. B. 2002. A consideration of the dune:antidune transition in fine gravel. *Sedimentology*, 49, pp. 1269-1282.

- Carter, L., Carter, R. M., Nelson, C. S., Fulthorpe, C. S. & Neil, H. L. 1990. Evolution of Pliocene to recent abyssal sediment waves on Bounty Channel levees, New Zealand. *Marine Geology*, 95, pp. 97-109.
- Carter, L., Gavey, R., Talling, P. J. & Liu, J. T. 2014. Insights into submarine geohazards from breaks in subsea telecommunication cables. *Oceanography*, 27, pp. 58–67.
- Cartigny, M. J. & Postma, G. 2017. Turbidity current bedforms. In: Guillén, J., Acosta, J., Latino Chiocci, F. & Palanques, A. eds. *Atlas of Bedforms in the Western Mediterranean*. Springer International Publishing Switzerland 2017, pp. 29-33.
- Cartigny, M. J. B., Postma, G., van den Berg, J. H. & Mastbergen, D. R. 2011. A comparative study of sediment waves and cyclic steps based on geometries, internal structures and numerical modelling. *Marine Geology*, 280, pp. 40-56.
- Cartigny, M. J., Eggenhuisen, J. T., Hansen, E. W. M. & Postma, G. 2013. Concentration-dependent flow stratification in experimental high-density turbidity currents and their relevance to turbidite facies models. *Journal of Sedimentary Research*, 83, pp. 1046–1064.
- Cartigny, M. J., Ventra, D., Postma, G. & van Den Berg, J. H. 2014. Morphodynamics and sedimentary structures of bedforms under supercritical-flow conditions: New insights from flume experiments. *Sedimentology*, 61, pp. 712-748.
- Cheel, R. J. 2005. *Introduction to Clastic Sedimentology (Notes for a University level, second year, half-credit course in clastic sedimentology)*. Available at: <https://brocku.ca/sedimentology/SedNotes/Chap1.pdf>
- Cheel, R. J., 1990. Horizontal lamination and the sequence of bed phases and stratification under upper-flow-regime conditions. *Sedimentology*, 37, 517-529.
- Church, M. 2006. Bed material transport and the morphology of alluvial river channels. *Annual Review of Earth and Planetary Sciences*, 34 (1), pp. 325-354.
- Cisneros, J., Best, J. van Dijk, T. de Almeida, R. P., Amsler, M., Boldt, J., Freitas, B., Galeazzi, C., Huzinga, R., Ianniruberto, M., Ma, H., Nittrouer, J. A., Oberg, K., Orfeo, O., Parsons, D., Szupiany, R., Wang, P. & Zhang, Y. 2020. Dunes in the world's big rivers are characterized by low-angle lee-side slopes and a complex shape. *Nature Geoscience*, 13, pp. 156-162.
- Clare, M. A., Cartigny, M. J. B., North, L. J., Talling, P. J., Vardy, M. E., Hizzett, J. L., Sumner, E. J., Hughes-Clarke, J. E., Fugro, B. & Cooper, C. C. 2015. Quantification of near-bed dense

layers and implications for seafloor structures: new insights into the most hazardous aspects of turbidity currents. *Proceedings of the Offshore Technology Conference, 4-7 May, Houston, Texas, USA*. Available at: <https://www.onepetro.org/conference-paper/OTC-25705-MS>.

- Clare, M. A., Hughes Clarke, J. E., Talling, P. J., Cartigny, M. J. B. & Pratomo, D. G. 2016. Preconditioning and triggering of offshore slope failures and turbidity currents revealed by most detailed monitoring yet at a fjord-head delta. *Earth and Planetary Science Letters*, 450, pp. 208-220.
- Clare, M. A., Vardy, M. E., Cartigny, M. J. B., Talling, P. J., Himsforth, M. D., Dix, J. K., Harris, J. M., Whitehouse, R. J. S. & Belal, M. 2017. Direct monitoring of active geohazards: emerging geophysical tools for deep-water assessments. *Near Surface Geophysics*, 15, pp. 427-444.
- Coleman, J. M. 1969. Brahmaputra River: Channel processes and sedimentation. *Sedimentary Geology*, 3 (2-3), pp. 129–239.
- Coleman, S. E. & Melville, B. W. 1994. Bed-form development. *Journal of Hydraulic Engineering*, 120 (4), pp. 544-560.
- Coleman, S. E. & Nikora, V. I. 2011. Fluvial dunes: initiation, characterization, flow structure. *Earth Surface Process & Landforms*, 36, pp. 39–57.
- Coleman, S. E., Fedele, J. J. & Garcia, M. H. 2003. Closed conduit bed-form initiation and development. *Journal of Hydraulic Engineering*, 129, pp. 956-965.
- Coleman, S. E., Nikora, V. I., & Aberle, J. 2011. Interpretation of alluvial beds through bed-elevation distribution moments. *Water Resources Research*, 47, W11505.
- Colman, S.E., & Nikora, V.I. 2009. Bed and flow dynamics leading to sediment-wave initiation. *Water Resources Research*, 45, W04402.
- Colombini, M. & Stocchino, A. 2011. Ripple and dune formation in rivers. *Journal of Fluid Mechanics*, 673, pp. 121-131.
- Cooper, C., Andrieux, O., & Wood, J. 2013. Turbidity current measurements in the Congo Canyon. *Offshore Technology Conference, 6-9 May, Houston, Texas, USA*. Available at: <https://www.onepetro.org/conference-paper/OTC-23992-MS>.

- Cooper, C., Wood, J., Imran, J., Islam, A., Wright, P., Faria, R., Tati, A., Casey, Z. & Casey, R. T. 2016. Designing for turbidity currents in the Congo Canyon. *Offshore Technology Conference, 2-5 May, Houston, Texas, USA*. Available at: <https://www.onepetro.org/conference-paper/OTC-26919-MS>.
- Covault, J. A. 2011. Submarine Fans and Canyon-Channel Systems: A Review of Processes, Products, and Models. *Nature Education Knowledge*, 3 (4).
- Cunha, R.S., Tinterri, R., Muzzi Magalhaes, P. 2017. Annot Sandstone in the Peira Cava basin: An example of an asymmetric facies distribution in a confined turbidite system (SE France). *Marine and Petroleum Geology*, 87, pp. 60-79.
- Dade, W., & Friend, P. 1998. Grain-Size, Sediment-Transport Regime, and Channel Slope in Alluvial Rivers. *The Journal of Geology*, 106 (6), 661-676.
- Dalrymple, R., Knight, R. & Lambiase, J. 1978. Bedforms and their hydraulic stability relationships in a tidal environment, Bay of Fundy, Canada. *Nature*, 275, 100–104.
- de Cala, I., Ohata, K., Dorrell, R., Naruse, H., Patacci, M., Amy, L. A., Simmons, S., McLelland, S. J. & McCaffrey, W. D. 2020. Relating the flow processes and bedforms of steady-state and waning density currents. *Frontiers in Earth Science*, 8.
- Dercourt, J., Zonenshan, L. R., Ricou, L. E., Kazmin, V. G., Le Pichon, X., Knipper, A. L., Grandjaquet, C., Sbertshikov, I. M., Geysant, J., Lepvrier, C., Pechesky, D. H. Boulín, J., Sibuet, J. C., Savostin, O., Westphal, M., Bazhenov, M. L., Iauer, J. P. & Biju-Duval, B. 1986. Geological evolution of the Tethys belt from the Atlantic to the Pamirs since the Lias. *Tectonophysics*, 123, pp. 241-315.
- Dewey, J. D., Helman, M. L., Turco, E., Hutton, D. H. W. & Knott, S. D. 1989. Kinematics of the western Mediterranean. In: Coward, M. P., Dietrich, D. & Park, R. G. eds. *Alpine Tectonics. Geological Society, London, Special Publication, 45*. London: The Geological Society, pp. 265-283.
- Dorrell, R. M. & Hogg, A. J. 2010. Sedimentation of bidisperse suspensions. *International Journal of Multiphase Flow*, 36, 481-490.
- Dorrell, R. M., Darby, S. E., Peakall, J., Sumner, E. J., Parsons, D. R. & Wynn, R. B. 2014. The critical role of stratification in submarine channels: implications for channelization and long runout of flows. *Journal Geophysical Research*, 119, pp. 2620–2641.

- Dorrell, R. M., Peakall, J., Darby, S. E., Parsons, D. R., Johnson, J. Sumner, E. J., Wynn, R. B., Özsoy, E. & Tezcan, D. 2019. Self-sharpening induces jet-like structure in seafloor gravity currents. *Nature Communications*, 10 (1381).
- Dorrell, R. M., Peakall, J., Sumner, E. J., Parsons, D. R., Darby, S. E., Wynn, R. B., Özsoy, E. & Tezcan, D. 2016. Flow dynamics and mixing processes in hydraulic jump arrays: Implications for channel-lobe transition zones. *Marine Geology*, 381, pp. 181–193.
- Du Fornel, E., Joseph, P., Desaubliaux, G., Eschard, R., Guillocheau, F., Lerat, O., Muller, C., Ravenne, C. & Sztràkos, K. 2004. The southern Grès d'Annot outcrops (French Alps): an attempt at regional correlation. *Geological Society, London, Special Publications*, 221, pp. 137-160.
- Dumas, S., Arnott, R. W. & Southard, J. B. 2005. Experiments on oscillatory-flow and combined-flow bed forms: implications for interpreting parts of the shallow-marine sedimentary record. *Journal of Sedimentary Research*, 75 (3), pp. 501-513.
- Duran Vinent, O., Andreotti, B., Claudin, P. & Winter, C. 2019. A unified model of ripples and dunes in water and planetary environments. *Nature Geoscience*, 12, pp. 345-350.
- Egiazaroff, I. V. 1965. Calculation of non-uniform sediment concentrations. *Journal of Hydraulic Division*, 91 (4), pp. 225-247.
- Einstein, H. A. 1950. The bed-load function for sediment transportation in open channel flows. Technical Bulletin 1026. United States Department of Agriculture, Soil Conservation Service, Washington DC. Available at: <https://naldc.nal.usda.gov/download/CAT86201017/PDF>.
- Elliott, T., Apps, G., Davies, H., Evans, M., Ghibaudo, G., and Graham, R.H., 1985, Field excursion B: a structural and sedimentological traverse through the Tertiary foreland IV basin of the external Alps of south-east France, *International Symposium on Foreland Basins Guidebook, Excursion 3*, pp. 39-73.
- Engelund, F. & Fredsøe, J. 1982. Sediment ripples and dunes. *Annual Review of Fluid Mechanics*, 14, pp. 13–37.
- Fedele, J., Barnaal, Z., Tulenko, J. & Awalt, S. 2016. Bedforms created by gravity flows. *SEPM Special Publication*, 106, pp. 65-121.

- Fenton, J. D., & J. E. Abbott. 1977. Initial movement of grains on a stream bed: The effect of relative protrusion. *Proceedings of the Royal Society of London. A. Mathematical and Physical Sciences*, 352 (1671), pp. 523–537.
- Fernandez, R., Best, J., & López, F. 2006. Mean flow, turbulence structure, and bed form superimposition across the ripple-dune transition. *Water Resources Research*, 42 (5).
- Fildani, A., Normark, W. R., Kostic, S. & Parker, G. 2006. Channel formation by flow stripping: large-scale scour features along the Monterey Easy Channel and their relation to sediment waves. *Sedimentology*, 53, pp. 1265-1287.
- Flemming, B. W. 1988. Zur Klassifikation subaquatischer, strömungstransversaler Transportkörper. *Bochumer geologische und geotechnische Arbeiten*. 29, pp. 44-47.
- Flemming, B. W. 2000. The role of grain size, water depth and flow velocity as scaling factors controlling the size of subaqueous dunes. In: Trentesaux, A. & Garlan, T. eds. *Marine Sandwave Dynamics, International Workshop, March 23-24 2000, Lille*. Lille: University of Lille, pp. 55-60. Available at: <https://www.researchgate.net/publication/234841879>.
- Flood, R. & Shor, A. 1998. Mud waves in the Argentine basin and their relationship to regional bottom circulation patterns. *Deep-Sea Research*, 35, pp. 943-971.
- Fonnesu, M., Felletti, F., Houghton, P.D.W., Patacci, M. & McCaffrey, W.D. 2018. Hybrid event bed character and distribution linked to turbidite system sub-environments: The North Apennine Gottero Sandstone (north-west Italy). *Sedimentology*, 65: 151-190.
- Fourrière, A., Claudin, P. & Andreotti, B. 2010. Bedforms in a turbulent stream: formation of ripples by primary linear instability and of dunes by nonlinear pattern coarsening. *Journal of Fluid Mechanics*, 649, pp. 287–328.
- Gabel, S. L. 1993. Geometry and kinematics of dunes during steady and unsteady flows in the Calamus River, Nebraska, USA. *Sedimentology*, 40, pp. 237-269.
- Galy, V., France-Lanord, C., Beyssac, O., Faure, P., Kudrass, H. & Palhol, F. 2007. Efficient organic carbon burial in the Bengal fan sustained by the Himalayan erosional system. *Nature*, 450, pp. 407–410.
- Garcia, M. & Parker, G. 1993. Experiments on the entrainment of sediment into suspension by a dense bottom current. *Journal of Geophysical Research*, 98, pp. 4793-4807.

- Garcia, M. H. 1993. Hydraulic jumps in sediment-driven bottom currents. *Journal of Hydraulic Engineering*, 119, pp. 1094-1117.
- Grabowski, R., Droppo, I. & Wharton, G. 2011. Erodibility of cohesive sediment: The importance of sediment properties. *Earth-Science Reviews*, 105, pp. 101-120.
- Guy, H. P., Simons, D. B. & Richardson, E. V. 1961. Summary of alluvial channel data from flume experiments 1956–1961. *U.S. Geological Survey, Professional Paper, 462, 1*. Available at: <https://pubs.er.usgs.gov/publication/pp462I>.
- Gyr, A. & Kinzelbach, W. 2004. Bed forms in turbulent channel flow. *Applied Mechanics Review*, 57 (1), pp. 77-93.
- Hage, S., Cartigny, M. J. B., Clare, M. A., Sumner, E. J., Vendettuoli, D., Clarke, J. E. H., Hubbard, S. M., Talling, P. J., Gwyn Lintern, D., Stacey, C. D., Englert, R. G., Vardy, M. E., Hunt, J. E., Yokokawa, M., Parsons, D. R., Hizzett, J. L., Azpiroz-Zabala, M. & Vellinga, A. J. 2018. How to recognize crescentic bedforms formed by supercritical turbidity currents in the geologic record: Insights from active submarine channels. *Geology*, 46, pp. 563–566.
- Hamilton, P., Gaillot, G., Strom, K., Fedele, J. & Hoyal, D. 2017. Linking hydraulic properties in supercritical submarine distributary channels to depositional lobe geometry. *Journal of Sedimentary Research*, 87 (9), pp. 935-950.
- Hand, B. M. 1974. Supercritical flow in density currents. *Journal of Sedimentary Research*, 44 (3), pp. 637-648.
- Harms, J. C. & Fahnstock, R. K. 1965. Stratification, bed forms, and flow phenomena (with an example from the Rio Grande). In: Middleton, G. V. *Primary Sedimentary Structures and Their Hydrodynamic Interpretation*. S.E.P.M. Special Publication 12, pp. 84-115.
- Haughton, P. D. W. 1994. *Depositional and reservoir modelling of sheet turbidite sandstones in confined basins*. In: Weimer, P., Bouma, A. H. & Perkins, B. F. eds. GCSSEPM Foundation 15th Annual Research Conference, Submarine Fans and Turbidite Systems: Sequence Stratigraphy, Reservoir Architecture and Production Characteristics, Gulf of Mexico and International. pp. 135-136.
- Heezen, B.C. & Ewing, W.M. 1952. Turbidity currents and submarine slumps, and the 1929 Grand Banks (Newfoundland) earthquake. *American Journal of Science*, 250 (12) pp. 849-873.

- Herbert, C., Alexander, J. & Álvaro, M. 2015. Back-flow ripples in troughs downstream of unit bars: Formation, preservation and value for interpreting flow conditions. *Sedimentology*, 62 (7), pp. 1814-1836.
- Hilton, V. C. 1994. *Architecture of deep-marine confined sandstone bodies, Eocene-Oligocene Gres d'Annot Formation SE France*. Ph.D. thesis, University of Leicester.
- Hiscott, R. N. 1994a. Loss of capacity, not competence, as the fundamental process governing deposition from turbidity currents. *Journal of Sedimentary Research, Section A: Sedimentary Petrology and Processes*, 64, pp. 209-214.
- Hiscott, R. N. 1994b. Traction-carpet stratification in turbidites; fact or fiction? *Journal of Sedimentary Research, Section A: Sedimentary Petrology and Processes*, 64, pp. 204-208.
- Hjulstrom, F. 1939. *Transportation of detritus by moving water*. Trask, P. D. ed. In: Recent Marine Sediments. AAPG Special Publication, 10, pp. 5-31.
- Hodgson, D. M. & Wild. R., 2008. Facies and Architecture of the Lezonabar Member, Higuer-Getaria Formation, Errentzun Zabala, Spain. In: Nilsen, T. H., Shew, R. D., Steffens, G. S. & Studlick, J. R. eds. *Atlas of Deep-Water Outcrops, Volume 56*. American Association of Petroleum Geologists.
- Hodgson, D. M. 2009. Distribution and origin of hybrid beds in sand-rich submarine fans for the Tanqua depocenter, Karoo Basin, South Africa. *Marine & Petroleum Geology*, 26, 1940-1956.
- Hofstra, M., Peakall, J., Hodgson, D. M. & Stevenson, C. J. 2018. Architecture and morphodynamics of subcritical sediment waves in an ancient channel-lobe transition zone. *Sedimentology*, 65 (7), pp. 2339-2367.
- Howe, J. A. 1996. Turbidite and contourite sediment waves in the northern Rockall Trough, North Atlantic Ocean. *Sedimentology*, 43, pp. 219-234.
- Huang, H., Imran, J., Pirmez, C., Zhang, Q. & Chen, G. 2009. The critical densimetric Froude number of subaqueous gravity currents can be non-unity or non-existent. *Journal of Sedimentary Research*, 79, pp. 479-485.
- Hubbard, S. M., Covault, J. A., Fildani, A. Romans, B.W. 2014. Sediment transfer and deposition in slope channels: Deciphering the record of enigmatic deep-sea processes from outcrop. *GSA Bulletin*. 126 (5-6), pp. 857-871.

- Hubert, J. F. 1966a. Sedimentary history of Upper Ordovician geosynclinal rocks, Girvan, Scotland. *Journal of Sedimentary Petrology*, 36, pp. 677-699.
- Hubert, J. F. 1966b. Modification of the Model for Internal Structures in Graded Beds to include a Dune Division. *Nature*, 211, pp. 614–615.
- Hughes Clarke, J. E. 2016. First wide-angle view of channelized turbidity currents links migrating cyclic steps to flow characteristics. *Nature Communications*, 7, pp. 1-13.
- Huntley, D. & Coco, G. 2009. How do bedforms respond to changing conditions? A study using abstracted models. In Mizuguchi, M. & Sato, S. eds. *Proceedings of Coastal Dynamics 2009: Impacts of Human Activities on Dynamic Coastal Processes*. World Scientific Publishing, pp. 21-36.
- Huntley, D., Coco, G., Bryan, K. & Murray, A. 2008. Influence of ‘defects’ on sorted bedform dynamics. *Geophysical Research Letters*, 35 (2).
- Jackson, R. 1976. Sedimentological and Fluid-dynamic Implications of the Turbulent Bursting Phenomenon in Geophysical Flows. *Journal Fluid Mech*, 77 (3), 531-560.
- Jerolmack, D. J. & Mohrig, D. 2005. A unified model for subaqueous bed form dynamics. *Water Resources Research*, 41 (12).
- Joseph, P. & Lomas, S. A. 2004. Deep-water sedimentation in the Alpine Foreland Basin of SE France: New perspectives on the Grès d’Annot and related systems – an introduction. *Geological Society, London, Special Publications*, 221, pp. 1-16.
- Julien, P. Y. & Klaassen, G. J. 1995. Sand-dune geometry of large rivers during floods. *Journal of Hydraulic Engineering*, 121, pp. 657-663.
- Kane, I. A., McCaffrey, W. D., Peakall, J. & Kneller, B. C. 2010. Submarine channel levee shape and sediment waves from physical experiments. *Sedimentary Geology*, 223 (1-2), pp. 75-85.
- Keith, B. D. & Freidman, G. M. 1977. A slope-fan-basin-plain model, Taconic Sequence, New York and Vermont. *Journal of Sedimentary Research*, 47 (3), pp. 1220–1241.
- Kennedy, J. F. 1961. Stationary waves and antidunes in alluvial channels. Report number KH-R-2, WM Keck Laboratory of Hydraulics and Water Resources, California Institute of Technology, Pasadena

- Kennedy, J. F. 1963. The mechanics of dunes and antidunes in erodible-bed channels. *Journal of Fluid Mechanics*, 16 (4), pp. 521-544.
- Kennedy, J. F. 1969. The formation of sediment ripples, dunes and antidunes. *Annual Review Fluid Mechanics*, 1, pp. 147-168.
- Kirchner, J. W., Dietrich, W. E., Iseya, F. & Ikeda, H. 1990. The variability of critical shear stress, friction angle, and grain protrusion in water-worked sediments. *Sedimentology*, 37 (4), pp. 647-672.
- Kleinans, M. 2004. Sorting in grain flows at the lee side of dunes. *Earth-Science Reviews*, 65, pp. 75–102.
- Kneller, B. & Branney, M. 1995. Sustained high-density turbidity currents and the deposition of thick massive sands. *Sedimentology*, 42 (4), pp. 607-616.
- Kneller, B. & Buckee, C. 2000. The structure and fluid mechanics of turbidity currents: A review of some recent studies and their geological implications. *Sedimentology*, 47, pp. 62–94.
- Kneller, B. & McCaffrey, W. 2003. The interpretation of vertical sequences in turbidite beds: the influence of longitudinal flow structure. *Journal of Sedimentary Research*, 73, pp. 706–713.
- Kneller, B. 2013. Turbidites. In: Middleton G.V., Church M.J., Coniglio M., Hardie L.A. & Longstaffe F.J. eds. *Encyclopedia of Sediments and Sedimentary Rocks, Encyclopedia of Earth Sciences Series*. Dordrecht: Springer.
- Kneller, B. C, Edwards, D., McCaffrey, W., Moore. R. 1991. Oblique reflection of turbidity currents. *Geology*, 14, pp. 250-252.
- Kneller, B. C. & McCaffrey, W. D. 1998. *Topographic effects on turbidite systems: The Gres d'Annot, Alpes Maritimes and Hautes Provence, SE France*. Conference Field Excursion handbook: Sediment Transport and Deposition by Particulate Gravity Currents, Leeds.
- Kneller, B. C. 1995. Beyond the turbidite paradigm: Physical models for deposition of turbidites and their implications for reservoir prediction. *Geological Society, London, Special Publications*, 94, pp. 31-49.
- Kneller, B. C., Bennett, S. J. & McCaffrey, W. D. 1999. Velocity structure, turbulence and fluid stresses in experimental gravity currents. *Journal of Geophysical Research*, 104, pp. 5381-5391.

- Knighton, D. 1998. Fluvial forms and processes, a new perspective. *London: Routledge*.
- Koller, D., de Oliveira Borges, A. L., Puhl, E. & Manica, R. 2017. Prediction of the bedforms generated by density currents based on fluvial phase diagrams. *Brazilian Journal of Water Resources*, 22.
- Koller, D., Manica, R., de Oliveira Borges, A. L. & Fedele, J. 2019. Experimental bedforms by saline density currents. *Brazilian Journal of Geology*, 49 (2).
- Kostaschuk, R. & Villard, P. 1996. Flow and sediment transport over large subaqueous dunes: Fraser River, Canada. *Sedimentology*, 43 (5), pp. 849–863.
- Kostic, S. & Parker, G. 2006. The response of turbidity currents to a canyon-fan transition: Internal hydraulic jumps and depositional signatures. *Journal of Hydraulic Research*, 44, pp. 631-653.
- Kostic, S. 2011. Modeling of submarine cyclic steps: Controls on their formation, migration and architecture. *Geosphere*, 7, pp. 294-304.
- Kostic, S., 2014. Upper flow regime bedforms on levees and continental slopes: Turbidity current flow dynamics in response to fine-grained sediment waves. *Geosphere*, 10 (6), pp. 1094-1103.
- Kubo, Y. & Nakajima, T. 2002. Laboratory experiments and numerical simulation of sediment-wave formation by turbidity currents. *Marine Geology*, 192 (1-3), pp. 105-121.
- Kuenen P. H., A. Faure-Muret, Lanteaume M., P. 1957. Fallot Observations sur les flyschs des Alpes Maritimes françaises et italiennes. *Bulletin de la Société Géologique de France*, 6, 7, pp. 11-26.
- Kuenen, P. H. & Sengupta, S. 1970. Experimental marine suspension currents, competency and capacity. *Geologie en Mijnbouw*, 49, pp. 89-118.
- Lanzoni, S. & Tubino, M. 1999. Grain sorting and bar instability. *Journal of Fluid Mechanics*, 393, pp. 149-174.
- Leclair, S. F. 2002. Preservation of cross-strata due to the migration of subaqueous dunes: an experimental investigation. *Sedimentology*, 49, pp. 1157-1180.
- Lee, H.J., Syvitski, J.P.M., Parker, G., Orange, D. L., Locat, J., Hutton, E. W. H., & Imran, J. 2002. *Marine Geology*, 192 (1-3), pp. 79-104.

- Lee, S. E. Amy, L. A. & Talling, P. J. 2004. The character and origin of thick base-of-slope sandstone units of the Peira Cava outlier, SE France. *Geological Society, London, Special Publications*, 221, pp. 331-347.
- Leeder, M. 2012. *Sedimentology and sedimentary basins: from turbulence to tectonics*. 2<sup>nd</sup> ed. Chichester, UK: Wiley-Blackwell.
- Leeder, M.R. 1983. On the dynamics of sediment suspension by residual Reynolds stresses—confirmation of Bagnold's theory. *Sedimentology*, 30, pp. 485-491.
- Lichtman, I. D., Baas, J. H., Amoudry, L., Thorne, P. D., Malarkey, J., Hope, J. A., Peakall, J., Paterson, D. M., Bass, S. J. Cooke, Richard D., Manning, A. J., Davies, A. G., Parsons, D. R., Ye, L. 2018. Bedform migration in a mixed sand and cohesive clay intertidal environment and implications for bed material transport predictions. *Geomorphology*, 315, pp. 17-32.
- Lowe, D. R. 1976. Subaqueous liquefied and fluidized sediment flows and their deposits. *Sedimentology*, 23, pp. 285-308.
- Lowe, D. R. 1982. Sediment gravity flows; II, Depositional models with special reference to the deposits of high-density turbidity currents. *Journal of Sedimentary Research*, 52 (1), pp. 279–297.
- Lowe, D. R. 1988. Suspended-load fallout rate as an independent variable in the analysis of current structures. *Sedimentology*, 35, pp. 765-776.
- Lucchi, F. R. & Valmori, E. 1980. Basin-wide turbidites in a Miocene, over-supplied deep-sea plain: a geometrical analysis. *Sedimentology*, 27, pp. 241-270.
- Luchi, R., Balachandar, S., Seminara, G. & Parker, G. 2018. Turbidity currents with equilibrium basal driving layers: A mechanism for long runout. *Geophysical Research Letters*, 45, pp. 1518-1526.
- Macauley, R. V. & Hubbard, S. M. 2013. Slope channel sedimentary processes and stratigraphic stacking, Cretaceous Tres Pasos Formation slope system, Chilean Patagonia. *Marine and Petroleum Geology*, 41, pp. 146-162.
- Martin, R. & Jerolmack, D. 2013. Origin of hysteresis in bed form response to unsteady flows. *Water Resources Research*, 49, pp. 1314-1333.

- Masson, D. G., Harbitz, C. B., Wynn, R. B., Pedersen, G. & Løvholt, F. 2006. Submarine landslides: processes, triggers and hazard prediction. *Philosophical Transactions of the Royal Society A: Mathematical, Physical & Engineering Sciences*, 364 (1845), pp. 2009-2039.
- Matthes, G. H. 1947. Macroturbulence in natural stream flow. *Eos, Transactions American Geophysical Union*, 28 (2), pp. 255– 265.
- McCaffrey, W. D. & Kneller, B. C. 2001. Process controls on the development of stratigraphic trap potential on the margins of confined turbidite systems and aids to reservoir evaluation. *AAPG Bulletin*, 85 (6), pp. 971-988.
- McCarron, C. J.; Van Landeghem, K. J. J., Baas, J. H., Amoudry, L. O., Malarkey, J. 2019. The hiding-exposure effect revisited: A method to calculate the mobility of bimodal sediment mixtures. *Marine Geology*, 410, pp. 22-31.
- McCave, I. N. & Carter, L. 1997. Recent sedimentation beneath the Deep Western Boundary Current off northern New Zealand. *Deep Sea Research Part I: Oceanographic Research Papers*, 44 (7), pp. 1203-1237.
- McCave, I. N. 1986. Local and global aspects of the bottom nepheloid layers in the world ocean. *Netherland Journal of Deep-Sea Research*, 20 (2/3), pp. 167-181.
- McLean, S. R. 1990. The stability of ripples and dunes. *Earth Science Review*, 29, pp. 131–144.
- Meiburg, E. & Kneller, B. 2010. Turbidity currents and their deposits. *Annual Review of Fluid Mechanics*, 42, pp. 135-156.
- Middleton, G. V. 1993. Sediment deposition from turbidity currents. *Annual Review of Earth and Planetary Sciences*, 21, pp. 89-114.
- Middleton, G.V. 1967. Experiments on density and turbidity currents: III. Deposition of sediment. *Canadian Journal of Earth Sciences*, 4 (3), pp. 475-505.
- Miller, K. G., Mountain, G. S., Browning, J. V., Katz, M. E., Monteverde, D., Sugarman, P. J., Ando, H., Bassetti, M. A., Bjerrum, C. J., Hodgson, D., Hesselbo, S., Karakaya, S., Proust, J. N. & Rabineau, M. 2013. Testing sequence stratigraphic models by drilling Miocene forests on the New Jersey shallow shelf. *Geosphere*, 9, pp. 1236-1256.
- Milliman, J. D. & Meade, R. H. 1983. World-wide delivery of river sediment to the oceans. *The Journal of Geology*, 91, pp. 1-21.

- Mitchener, H. & Torfs, H. 1996. Erosion of mud/sand mixtures. *Coastal Engineering*, 29 (1-2), pp. 1-25.
- Mohrig, D. & Smith, J. D. 1996. Predicting the migration rates of subaqueous dune. *Water Resources Research*, 32 (10), pp. 3207 – 3217.
- Morris, S. A., Kenyon, N. H., Limonov, A. H. & Alexander, J. 1998. Downstream changes of large-scale bedforms in turbidites around the Valencia channel mouth, north-west Mediterranean: implications for paleoflow reconstruction. *Sedimentology*, 45 (2), pp. 365-377.
- Mulder, T. & Alexander, J. 2001. The physical character of subaqueous sedimentary density flow and their deposits. *Sedimentology*, 48, pp. 269-299.
- Mulder, T. & Cochonat, P. 1996. Classification of offshore mass movements. *Journal of Sedimentary Research*, 66, pp. 43-57.
- Mulder, T., Razin, P. & Faugeres, J. C. 2009. Hummocky cross-stratification-like structures in deep-sea turbidites: Upper Cretaceous Basque basins (Western Pyrenees, France). *Sedimentology*, 5, pp. 997-1015.
- Mulder, T., Syvitski, J. P. M., Migneon, S., Faugeres, J. C. & Savoye, B. 2003. Marine hyperpycnal flows: initiation, behaviour, and related deposits. A review. *Marine and Petroleum Geology*, 20, pp. 861-882.
- Mutti, E. & Normark, W. R. 1987. Comparing examples of modern and ancient turbidite systems: problems and concepts. In: Leggett, J. K. & Zuffa, G. G. eds. *Marine Clastic Sedimentology*. London: Graham and Trotman, pp. 1-38.
- Mutti, E. & Normark, W. R. 1991. An integrated approach to the study of turbidite systems. In: Weimer, P. & Link, H. eds. *Seismic Facies and Sedimentary Processes of Submarine Fans and Turbidite Systems*. Berlin: Springer-Verlag, pp. 75-106.
- Mutti, E. & Tinterri, R. 2004. Cross-stratified sandstones and multiple beds: Evidence of internal flow divergence in turbidity currents caused by submarine topography. AAPG Annual Meeting, April 18-21, 2004, Dallas, Abstract Book.
- Mutti, E. 1992. *Turbidite Sandstones*. Parma, IT: Istituto di Geologia, Università di Parma, AGIP.
- Mutti, E., Bernoulli, D., Luchi, F. R. & Tinterri, R. 2009. Turbidites and turbidity currents from alpine 'flysch' to the exploration of continental margins. *Sedimentology*, 56, pp. 267-318.

- Mutti, E., Tinterri, R., Benevelli, G., di Biase, D., Cavanna, G. 2003. Deltaic, mixed and turbidite sedimentation of ancient foreland basins. *Marine and Petroleum Geology*, 20 (6-8), pp. 733-755.
- Mutti, E., Tinterri, R., Remacha, E., Mavilla, N., Angella, S. and Fava, L. 1999. *An Introduction to the Analysis of Ancient Turbidite Basins from an Outcrop Perspective*. American Association of Petroleum Geologists, Tulsa.
- Muzzi Magalhaes, P., Tinterri, R., 2010. Stratigraphy and depositional setting of slurry and contained (reflected) beds in the Marnoso-arenacea Formation (LanghianeSerravallian) northern Apennines, Italy. *Sedimentology* 57, pp. 1685 -1720.
- Nakajima, T. & Satoh, M. 2001. The formation of large mudwaves by turbidity currents on the levees of the Toyama deep-sea channel, Japan Sea. *Sedimentology*, 48, pp. 435-463.
- Nakajima, T., Satoh, M. & Okamura, Y. 1998. Channel-levee complexes, terminal deep-sea fan and sediment wave fields associated with the Toyama deep-sea channel system in the Japan Sea. *Marine Geology*, 149, pp. 25-41.
- Nezu, I. & Azuma, R. 2004. Turbulence characteristics and interaction between particles and fluid in particle-laden open channel flows. *Journal of Hydraulic Engineering*, 130, pp. 988-1001.
- Nielsen, T., Shew, R. D., Steffens, G. S. & Studlick, J. R. J. 2007. *AAPG Studies in Geology Volume 56: Atlas of Deepwater Outcrops*. [No Place]: American Association of Petroleum Geologists.
- Noguchi, K. & Nezu, I. 2009. Particle-turbulence interaction and local particle concentration in sediment-laden open-channel flows. *Journal of Hydro-environment Research*, 3, pp. 54-68.
- Normark, W., Hess, G.R, Stow, D.A.V. & Bowen, A.J. 1980. Sediment waves on the Monterey fan levee: A preliminary physical interpretation. *Marine Geology*, 37 (1-2), pp. 1-18.
- Normark, W.R., Piper, D.J.W. 1991. Initiation processes and flow evolution of turbidity currents: implications for the depositional record. Osborne, H. eds. In: *From Shoreline to Abyss: Contributions in Marine Geology in Honor of Francis Parker Shepard*. SEPM Society for Sedimentary Geology, *Special Publications*, 46, pp. 207-230.
- Núñez-González F, Martín-Vide JP. 2010. Downstream-migrating antidunes in sand, gravel and sand-gravel mixtures. *Proceedings, River Flow 2010*, Braunschweig.

- Núñez-González, F., & Martín-Vide, J. P. 2011. Analysis of antidune migration direction. *Journal Geophysical Research*, 116 (F2).
- Ohata, K., Naruse, H. Yokokawa, M. & Viparelli, E. 2017. New bedform phase diagrams and discriminant functions for formative conditions of bedforms in open-channel flows. *Journal of Geophysical Research Earth Surface*, 122, pp. 2139-2158.
- Osborne, P. & Vincent, C. 1993. Dynamics of large and small scale bedforms on a macrotidal shoreface under shoaling and breaking waves. *Marine Geology*, 115 (3-4), pp. 207-226.
- Ouillon, R., Meiburg, E. & Sutherland, B. R. 2019. Turbidity currents propagating down a slope into a stratified saline ambient fluid. *Environmental Fluid Mechanics*, 19, pp. 1143-1166.
- Paarlberg, A. J., Dohmen-Janssen, C. M., Hulscher, S. J. M. H. & Termes, A. P. P. 2009. Modelling river dune development using a parameterization of flow separation. *Journal of Geophysical Research*, 114, F01014.
- Paarlberg, A., Dohmen-Janssen, C., Hulscher, S. J., Termes, P. & Schielen, R. 2010. Modelling the effect of time-dependent river dune evolution on bed roughness and stage. *Earth Surf. Processes Landforms*, 35 (15), pp. 1854–1866.
- Pantin, H. M. 1979. Interaction between velocity and effective density in turbidity flow; phase plane analysis, with criteria for autosuspension. *Marine Geology*, 31, pp. 59-99.
- Parker, G., Garcia, M., Fukushima, Y. & Yu, W. 1987. Experiments on turbidity currents over an erodible bed. *Journal of Hydraulic Research*, 25 (1), pp. 123-147.
- Parsons, D.F. & Garcia, M.H. 1998. Similarity of gravity current fronts. *Physics of Fluids*, 10 (12), pp. 3209 – 3213.
- Parsons, J.D., Friedrichs, C.T., Traykovski, P.A., Mohrig, D., Imran, J., Syvitski, J.P.M., Parker, G., Puig, P., Buttles, J.L. & García, M.H. 2007. The Mechanics of Marine Sediment Gravity Flows. In: Jarvis, I., Nittrouer, C.A., Austin J.A., Field, M.E., Kravitz, J.H., Syvitski, J.P.M & Wiberg, P.L. eds. *Continental Margin Sedimentation*. [Online]: International Association of Sedimentologists, 275-337. Available at: <https://onlinelibrary.wiley.com/doi/book/10.1002/9781444304398>.
- Paull, C. K., Talling, P. J., Maier, K. L., Parsons, D, Xu, J., Caress, D. W., Gwiazda, R., Lundsten, E. M., Anderson, K., Barry, J. P., Chaffey, M., O'Reilly, T., Rosenberger, K. J., Gales, J. A., Kieft, B., McGann, M., Simmons, S. M., McCann, M., Sumner, E. J., Clare, M. A. &

- Cartigny, M. J. 2018. Powerful turbidity currents driven by dense basal layers. *Nature Communications*, 9, 4114.
- Perillo, M. M., Best, J. L., Yokokawa, M., Sekiguchi, T., Takagawa, T. & Garcia, M. H. 2014. A unified model for bedform development and equilibrium under unidirectional, oscillatory and combined flows. *Sedimentology*, 61, pp. 2063-2085.
- Petrie, J. & Diplas, P. 2015. Evaluation of the Logarithmic Law of the Wall for River Flows. *River Research and Applications*, 2 (5), pp. 1082-1093.
- Pettingill, H. S. 2004. Global overview of deepwater exploration and production. In: Weimer, P., Pettingill, H. S. & Nilsen, T. H. eds. *Petroleum Systems of Deepwater Settings*. Society of Exploration Geophysicists and European Association of Geoscientists and Engineers, pp. 1-40.
- Pickering, K. T. & Hilton, V. C. 1998. *Turbidite systems of SE France*. London: Vallis Press.
- Pickering, K. T. & Hiscott, R. N. 1985. Contained (reflected) turbidity currents from the Middle Ordovician Cloridorme Formation, Quebec, Canada: an alternative to the antidune hypothesis. *Sedimentology*, 32, pp. 373-394.
- Piper, D. J. W. & Savoye, B. 1993. Processes of late quarternary turbidity current flow and deposition on the Var deep-sea fan, North-West Mediterranean Sea. *Sedimentology*, 40, pp. 557-582.
- Piper, D. J. W., Hiscott, R. N. & Normark, W. R. 1999. Out-crop-scale acoustic facies analysis and latest quaternary development of Hueneme and Dume submarine fans, off-shore California. *Sedimentology*, 46, pp. 47-78.
- Pohl, F. 2019. *Turbidity currents and their deposits in abrupt morphological transition zones*. Ph.D. thesis, University of Durham.
- Pohl, F., Eggenhuisen, J. T., Kane, I. A. & Clare, M. A. 2020. Transport and burial of microplastics in deep-marine sediments by turbidity currents. *Environmental Science & Technology*, 54 (7), pp. 4180-4189.
- Postma G, Cartigny M. 2014. Supercritical and subcritical turbidity currents and their deposits - a synthesis. *Geology*, 42, pp. 987-990.
- Postma, G. 1990. Depositional architecture and facies of river and fan deltas: a synthesis. *International Association of Sedimentologists Special Publications*, 10, pp. 13-27.

- Postma, G., Cartigny, M. & Kleverlaan, K. 2009. Structureless, coarse-tail graded Bouma Ta formed by internal hydraulic jump of the turbidity current? *Sedimentary Geology*, 219 (1-4), pp. 1-6.
- Postma, G., Lang, J., Hoyal, D.C., Fedele, J. J., Demko, T., Abreu, V. and Pederson, K. H. 2021. Reconstruction of bedform dynamics controlled by supercritical flow in the channel–lobe transition zone of a deep-water delta (Sant Llorenç del Munt, north-east Spain, Eocene). *Sedimentology*, [Online version of record before inclusion in an issue]. Available at: <https://onlinelibrary.wiley.com/doi/full/10.1111/sed.12735>.
- Postma, G., Nemec, W. & Kleinspehn, K. L. 1988. Large floating clasts in turbidites: a mechanism for their emplacement. *Sedimentary Geology*, 58, pp. 47-61.
- Raudkivi, A. & Witte H. H. 1990. Development of bed features. *Journal of Hydraulic Engineering ASCE*, 116, pp. 1063–1079.
- Raudkivi, A. J. & Ettema, R. 1982. Stability of armour layers in rivers. *Journal of Hydraulics Division*, 108 (9), pp. 1047-1057
- Raudkivi, A. J. 1976. *Loose Boundary Hydraulics*. 2<sup>nd</sup> ed. Oxford: Pergamon Press.
- Raudkivi, A. J. 1997. Ripples on stream bed. *Journal of Hydraulic Engineering*, 123, pp. 58-64.
- Raudkivi, A. J. 2006. Transition from Ripples to Dunes. *Journal of Hydraulic Engineering*, 132 (12).
- Ravenne, C., Vally, R., Riche, P. & Tremolieres, P. 1987. Sedimentation and tectonics in the upper Eocene-Oligocene marine Basin in the Southern Alps. *Oil & Gas Science and Technology – Rev. IFP*, 42 (5), pp. 529-553.
- Recking, A., Bacchi, V., Naaim, M. & Frey, P. 2009. Antidunes on steep slopes. *Journal of Geophysical Research*. 114 (F4).
- Reesink, A. J, Berg, J. H, Parsons, D., Amsler, M, Best, J., Hardy, R. J., Orfeo, O. & Szupiany, R. 2015. Extremes in dune preservation: Controls on the completeness of fluvial deposits. *Earth-Science Reviews*, 150, pp. 652-665.
- Ricci Lucchi, F. & Valmori, E. 1980. Basin-wide turbidites in a Miocene deep-sea plain: The Marnoso-Arenacea of the Northern Apennines. *Geology and Mining*, 57, pp. 559-576.
- Richards, K. 1980. The formation of ripples and dunes on an erodible bed. *Journal of Fluid Mechanics*, 99 (3), pp. 597-618.

- Rubin, D. M. & McCulloch, D. S. 1980. Single and superimposed bedforms: a synthesis of San Francisco Bay and flume observations. *Sedimentary Geology*, 26, pp. 207-231.
- Rubin, D. M. 2012. A unifying model for planform straightness of ripples and dunes in air and water. *Earth Science Reviews*, 113 (3-4), pp. 176-185.
- Schindler, R. J. & Robert, A. 2005. Flow and turbulence structure across the ripple-dune transition: an experiment under mobile bed conditions. *Sedimentology*, 52, pp. 627-649.
- Schindler, R. J. Parsons, D. R., Ye, L., Hope, J. A., Baas, J. H., Peakall, J., Manning, A. J., Aspden, R. J., Malarkey, J., Simmons, S., Paterson, D. M., Lichtman, I. D., Davies, A. G., Thorne, P. D., Bass, S. J. 2015. Sticky stuff: Redefining bedform prediction in modern and ancient environments. *Geology*, 43 (5), pp. 399–402.
- Sengupta, S. 1979. Grain-size distribution of suspended load in relation to bed materials and flow velocity. *Sedimentology*, 26, pp. 63-82.
- Sequeiros, O. E., Pittaluga, M. B., Frascati, A., Pirmez, C., Masson, D. G., Weaver, P., Crosby, A. R., Lazzaro, G., Botter, G. & Rimmer, J. G. 2019. How typhoons trigger turbidity currents in Submarine Canyons. *Scientific Reports*, 9, 9220.
- Sequeiros, O. E., Spinewine, B., Beaubouef, R., Sun, T., Garcia, M. & Parker, G. 2010. Bedload transport and bed resistance associated with density and turbidity currents. *Sedimentology*, 57 (6), pp. 1463-1490.
- Shao, D. L., Fan, G. Z., Wang, H. Q., Ma, H. X., Zuo, G. P, Ding, L. B., Cai, Z. & Li, W. Q. 2020. 3D anatomy and flow dynamics of net-depositional cyclic steps on the world's largest submarine fan: a joint 3D seismic and numerical approach. *Petroleum Science*, [Online]. Available at: <https://doi.org/10.1007/s12182-020-00512-3>.
- Shields, A. 1936. *Application of similarity principles and turbulence research to bed-load movement*. Pasadena, California: Soil Conservation Service, California Institute of Technology.
- Simmons, S. M., Azpiroz-Zabala, M., Cartigny, M. J. B., Clare, M. A., Cooper, C., Parsons, D. R., Pope, E. L., Sumner, E. J. & Talling, P. J. 2020. Novel acoustic method provides first detailed measurements of sediment concentration structure within submarine turbidity currents. *Journal of Geophysical Research: Oceans*, 125 (5), e2019JC015904.
- Simons, D. B., Richardson, E. V. & Nordin, C. D. 1965. Sedimentary structures generated by flow in alluvial channels. In: Middleton, G. V. ed. *Primary Sedimentary Structures and Their*

- Hydrodynamic Interpretation*. SEPM Society for Sedimentary Geology, Vol 12. Society of Economic Palaeontologists & Mineralogists, pp. 34-52.
- Sinclair, H. D. 1994. The influence of lateral basinal slopes on turbidite sedimentation in the Annot sandstones of SE France. *Journal of Sedimentary Research, Section A: Sedimentary Petrology and Processes*, 64, pp. 42–54.
- Sinclair, H. D. 1997. Tectonostratigraphic model for underfilled peripheral foreland basins: An Alpine perspective. *GSA Bulletin*, 109 (3), pp. 324-346.
- Slootman, A. and Cartigny, M. J. B. 2020. Cyclic steps: review and aggradation-based classification. *Earth Science Reviews*, 201, 102949.
- Slootman, A., Cartigny, M. J. B., Moscariello, A., Chiaradia, M., De Boer, P. L. 2016. Quantification of tsunami-induced flows on a Mediterranean carbonate ramp reveals catastrophic evolution. *Earth and Planetary Science Letters*, 444, pp. 192-204.
- Soulsby, R.L., & Whitehouse, R.J.S., 1997. Threshold of sediment motion in coastal environments. In: *Pacific Coasts and Ports '97: Proceedings of the 13th Australasian Coastal and Ocean Engineering Conference and the 6th Australasian Port and Harbour Conference*, 1, pp. 145–154.
- Soulsby, R.L., 1997. Dynamics of marine sands. London, UK. Thomas Telford, pp. 249.
- Southard, J. B. & Boguchwal, L. A. 1990. Bed configuration in steady unidirectional water flows; Part 2, Synthesis of flume data. *Journal of Sedimentary Research*, 60, pp. 658-679.
- Spinewine, B., Sequeiros, O. E., Garcia, M. H., Beaubouef, R. T., Sun, T., Savoye, B. & Parker, G. 2009. Experiments on wedge-shaped deep-sea sedimentary deposits in minibasins and/or on channel levees emplaced by turbidity currents. Part 2: Morphodynamic evolution of the wedge and of the associated bedforms. *Journal of Sedimentary Research*, 79, pp. 608-628.
- Staudt, F., Mullarney, J. C., Pilditch, C. A. & Huhn, K. 2017. The role of grain-size ratio in the mobility of mixed granular beds. *Geomorphology*, 278, pp. 314-328.
- Stevenson, C. J., Jackson, C. A-L, Hodgson, D. M., Hubbard, S. M. & Eggenhuisen. 2015. Deep-Water Sediment Bypass. *Journal of Sedimentary Research*, 85 (9), pp. 1058 - 1081.

- Stevenson, C.J., Talling, P.J., Masson, D.G., Sumner, E.J., Frenz, M. & Wynn, R.B. 2014. The spatial and temporal distribution of grain-size breaks in turbidites. *Sedimentology*, 61, 1120-1156.
- Sumner, E. J. & Paull, C. K. 2014. Swept away by a turbidity current in Mendocino submarine canyon, California. *Geophysical Research Letters*, 41 (21), pp. 7611-7618.
- Sumner, E. J., Amy, L. A. & Talling, P. J. 2008. Deposit structure and processes of sand deposition from decelerating sediment suspensions. *Journal of Sedimentary Research*, 78, pp. 529-547.
- Sumner, E. J., Talling, P. J., Amy, L. A., Wynn, R. B., Stevenson, C. & Frenz, M. 2012. Facies architecture of individual basin-plain turbidites: comparison to existing models and implications for flow processes. *Sedimentology*, 59 (6), pp. 1850-1887.
- Sun, T. & Parker, G. 2005. Transportational cyclic steps created by flow over an erodible bed. Part 2. Theory and numerical simulation. *Journal of Hydraulic Research*, 43 (5), pp. 502-514.
- Sutherland, A. J. and Hwang, L. S. 1965. A study of dune geometry and dune growth on a sand bed. *W.M. Keck Laboratory of Hydraulics and Water Resources, Division of Engineering and Applied Science*, Technical Memorandum, no. 65-5. Pasadena, CA.: California Institute of Technology.
- Sylvester, Z. & Lowe, D. R. 2004. Textural trends in turbidites and slurry beds from the Oligocene flysch of the East Carpathians, Romania. *Sedimentology*, 51, pp. 945-972.
- Symons, W. O., Sumner, E. J., Talling, P. J., Cartigny, M. J. B. & Clare, M. A. 2016. Large-scale sediment waves and scours on the modern seafloor and their implications for the prevalence of supercritical flows. *Marine Geology*, 371, pp. 130-148.
- Talling, P. J., Allin, J., Armitage, D. A., Arnott, R. W. C., Cartigny, M. J. B., Clare, M. A., Felletti, F., Covault, J. A., Girardclos, S., Hansen, E., Hill, P. R., Hiscott, R. N., Hogg, A. J., Clarke, J. H., Jobe, Z. R., Malgesini, G., Mozzato, A., Naruse, H., Parkinson, S., Peel, F. J., Piper, D. J. W., Pope, E., Postma, M., Rowley, P., Sguazzini, A., Stevenson, C. J., Sumner, E. J., Sylvester, Z., Watts, C. & Xu, J. 2015. Key future directions for research on turbidity currents and their deposits. *Journal of Sedimentary Research*, 85, pp. 153-169.

- Talling, P. J., Amy, L. A., Wynn, R. B., Blackbourn, G. & Gibson, O. 2007. Evolution of turbidity currents deduced from extensive thin turbidites: Marnoso Arenacea Formation (Miocene), Italian Apennines. *Journal of Sedimentary Research*, 77, pp. 172-196.
- Talling, P. J., Malgesini, G., Sumner, E. J., Amy, L. A., Felletti, F., Blackbourn, G., Nutt, C., Wilcox, C., Harding, I. C. & Akbari, S. 2012a. Planform geometry, stacking pattern, and extrabasinal origin of low strength and intermediate strength cohesive debris flow deposits in the Marnoso-arenacea Formation, Italy. *Geosphere*, 8 (6), pp. 1207-1230.
- Talling, P. J., Paull, C. K. & Piper, D. J. W. 2013. How are subaqueous sediment density flows triggered, what is their internal structure and how does it evolve? Direct observations from monitoring of active flows. *Earth Science Reviews*, 125, pp. 244-287.
- Talling, P. J., Sumner, E. J., Masson, D. G. & Malgesini, G. 2012b. Subaqueous sediment density flows: depositional processes and deposit types. *Sedimentology*, 59, pp. 1937-2003.
- Thorpe, S. 2010. Turbulent hydraulic jumps in a stratified shear flow. *Journal of Fluid Mechanics*, 654, pp. 305-350.
- Thorpe, S., & Li, L. 2014. Turbulent hydraulic jumps in a stratified shear flow. Part 2. *Journal of Fluid Mechanics*, 758, pp. 94-120.
- Tilston, M., Arnott, R. W. C., Rennie, C. D. & Long, B. 2015. The influence of grain-size on the velocity and sediment concentration profiles and depositional record of turbidity currents. *Geology*, 43, pp. 839–842.
- Tinterri, R., Laporta, M. & Ogata, K. 2017. Asymmetrical cross-current turbidite facies tract in a structurally-confined mini-basin (Priabonian-Rupelian, Ranzano Sandstone, northern Apennines, Italy). *Sedimentary Geology*, 352, pp. 63-87.
- Tinterri, R., Muzzi Magalhaes, P., 2011. Synsedimentary structural control on foredeep turbidites: an example from Miocene Marnoso-arenacea formation, northern Apennines, Italy. *Mar. Petroleum Geol.* 28, pp. 629 -657.
- Tinterri, R., Tagliaferri, A., 2015. The syntectonic evolution of foredeep turbidites related to basin segmentation: facies response to the increase in tectonic confinement (Marnoso-arenacea Formation, Miocene, Northern Apennines, Italy). *Marine and Petroleum Geology*. 67, pp. 81–110.

- Topping, D. J., Rubin, D. M. & Vierra Jr., L. E. 2000a. Colorado River sediment transport 1. Natural sediment supply limitation and the influence of Glen Canyon Dam. *Water Resources Research*, 36, pp. 515-542.
- Topping, D. J., Rubin, D. M., Melis, T. S. 2007. Coupled changes in sand grain size and sand transport driven by changes in the upstream supply of sand in the Colorado River: Relative importance of changes in bed-sand grain size and bed-sand area. *Sedimentary Geology*, 202 (3), pp. 538-561.
- Topping, D.J., Rubin, D.M., Nelson, J.M., Kinzel III, P.J. & Corson, I.C. 2000b. Colorado River sediment transport 2. Systematic bed-elevation and grain-size effects of sand supply limitation. *Water Resources Research*, 36, pp. 543–570.
- Traykovski, P, Geyer, W. R., Irish, J. D. & Lynch, J. F. 2000. The role of wave-induced density-driven fluid mud flows for cross-shelf transport on the Eel River continental shelf. *Continental Shelf Research*, 20 (16), pp. 2113-2140.
- van den Berg, J. H. & Van Gelder, A. 1993. A new bedform stability diagram, with emphasis on the transition of ripples to plane bed in flows over fine sand and silt. In: Marzo, M. & Puigdefrègas, C. eds. *Alluvial Sedimentation*. [Online]: Wiley-Blackwell. Available at: <https://www.wiley.com/en-us/Alluvial+Sedimentation-p-9781444303995>.
- van Den Berg, J. H. & Van Gelder, A. 2009. A New Bedform Stability Diagram, with Emphasis on the Transition of Ripples to Plane Bed in Flows over Fine Sand and Silt. In: Marzo, M. & Puigdefrègas, C. eds. *Alluvial Sedimentation*. [Online]: Wiley-Blackwell. Available at: <https://www.wiley.com/en-us/Alluvial+Sedimentation-p-9781444303995>.
- van Ledden, M., van Kesteren, W. G. M., Winterwerp, J.C. 2004. A conceptual framework for the erosion behaviour of sand–mud mixtures. *Continental Shelf Research*, 24, (1), p. 1-11.
- van Rijn, L. C. 1984. Sediment transport, Part III: Bedforms and alluvial roughness. *Journal of Hydraulic Engineering, ASCE*, 110, pp. 1733-1754.
- van Rijn, L. C. 1989. *Handbook of Sediment Transport by Currents and Waves*. 2<sup>nd</sup> ed. Delft, The Netherlands, Delft Hydraulics.
- van Rijn, L. C. 1990. Principles of fluid flow and surface waves in rivers, estuaries and coastal seas. Amsterdam, Aqua Publications.
- Venditti, J. G. 2013. Bedforms in Sand-Bedded Rivers. In: Shroder, F. ed. *Treatise on Geomorphology*. London: Academic Press, pp. 137-162.

- Venditti, J. G., Church, M. and Bennett, S. J. 2005. On the transition between 2D and 3D dunes. *Sedimentology*, 52, pp. 1343-1359.
- Venditti, J. G., Nelson, P. A., Bradley, R. W., Hought, D. & Gitto, A. B. 2017. Bedforms, structures, mobile patches and sediment supply in gravel-bedded rivers. In: Tstusumi, D. & Laronne, J. B. eds. *Gravel-Bed Rivers: Process and Disasters*. Chichester, UK: Wiley, pp. 439-466.
- Walker, R. G. 1965. The origin and significance of the internal sedimentary structures of turbidites. *Yorkshire Geological Society Proceedings*, 35, pp. 1-29.
- Waltham, D. 2004. Flow Transformations in Particulate Gravity Currents. *Journal of Sedimentary Research*, 74, pp. 12-134.
- Walton, E. K. 1967. The sequence of structures in turbidites. *Scottish Journal of Geology*, 3, pp. 306-317.
- Wang, Z., Xu, J., Talling, P. J., Cartigny, M. J. B., Simmons, S. M., Gwiazda, R., Paull, C. K., Maier, K. L. & Parsons, D. R. 2020. Direct evidence of a high-concentration basal layer in a submarine turbidity current. *Deep Sea Research Part I: Oceanographic Research Papers*, 161, 103300.
- Whitehouse, R.J.S., Soulsby, R., Roberts, W. & Mitchener, H. J. 2000. *Dynamics of Estuarine Muds*. Thomas Telford Publications, London.
- Wilberg, P. L. & Smith, J. D. 1987. Calculations of the critical shear stress for motion of uniform and heterogeneous sediments. *Water Resources Research*, 23 (8), pp. 1471-1480.
- Wilcock, P. R. & Kenworthy, S. T. 2002. A two-fraction model for the transport of sand/gravel mixtures. *Water Resources Research*, 38 (10), pp. 1194.
- Wilcock, P. R. 1993. Critical shear stress of natural sediments. *Journal of Hydraulic Engineering*, 119, pp. 491-505.
- Wilcock, P. R. and Crowe, J. C., 2003. A surface-based transport model for sand and gravel. *Journal of Hydraulic Engineering*, 129 (2), pp. 120-128.
- Wilcock, P. R., and B. W. McArdell. 1997. Partial transport of a sand-gravel sediment. *Water Resources Research*, 33, pp. 233-245.
- Wilcock, P. R., and Southard, J. B. 1989. Bed load transport of mixed size sediment: Fractional transport rates, bed forms, and the development of a coarse bed surface layer. *Water Resources Research*, 25 (7), pp. 1629- 1641.

- Williams, P. B., & P. H. Kemp. 1971. Initiation of ripples on flat sediment beds. *Journal of the Hydraulic Division, ASCE*, 97 (4), pp. 505 – 522.
- Wilson, P. A. & Roberts, H. H. 1995. Density cascading: off-shelf sediment transport, evidence and implications, Bahama Banks. *Journal of Sedimentary Research*, A65 (1), pp. 45-56.
- Winsemann, L. J. 2013. Lateral and vertical facies relationships of bedforms deposited by aggrading supercritical flows: from cyclic steps to humpback dunes. *Sedimentary Geology*, 296, pp. 36-54.
- Winterwerp, J. C., Bakker, W. T., Mastbergen, D. R. & van Rossum, H. 1992. Hyperconcentrated sand-water mixture flows over erodible bed. *Journal of Hydraulic Engineering*, 118, pp. 1508–1525.
- Wright, L. D., Friedrichs, C. T., Kim, S. C. & Scully, M. E. 2001. Effects of ambient currents and waves on gravity-driven sediment transport on continental shelves. *Marine Geology*, 175 (2001), pp. 25-45.
- Wynn, R. B. & Stow, D. A. V. 2002. Classification and characterisation of deep-water sediment waves. *Marine Geology*, 192 (1-3), pp. 7-22.
- Wynn, R. B., Masson, D. G. & Bett, B. J. 2002a. Hydrodynamic significance of variable ripple morphology across deep-water barchan dunes in the Faroe-Shetland Channel. *Marine Geology*, 192 (1-3), pp. 309-319.
- Wynn, R. B., Piper, D. J. W. & Gee, M. J. R. 2002b. Generation and migration of coarse-grained sediment waves in turbidity current channels and channel-lobe transition zones. *Marine Geology*, 192 (1-3), pp. 59-78.
- Wynn, R. B., Masson, D. G., Stow, D. A. V. & Weaver, P. P. E. 2000a. Turbidity current sediment waves in subsurface sequences. In: Bouma, A. H., Stelling, C. E. & Stone, C. G. eds. *Fine-Grained Turbidite Systems*. Boulder CO, USA: AAPG/SEPM, pp. 299-306.
- Wynn, R. B., Masson, D. G., Stow, D. A. V. & Weaver, P. P. E. 2000b. Turbidity current sediment waves on the submarine slopes of the western Canary Islands. *Marine Geology*, 163, pp. 185-198.
- Wynn, R. B., Weaver, P. P. E., Ercilla, G., Stow, D. A. V. & Masson, D. G. 2000c. Sedimentary processes in the Selvage sediment- wave field, NE Atlantic: new insights into the formation of sediment waves by turbidity currents. *Sedimentology*, 47, pp. 1181-1197.

- Wynn, R. B., Weaver, P. P. E., Ercilla, G., Stow, D. A. V. & Masson, D. G. 2000d. Sedimentary processes in the Selvage sediment-wave field, NE Atlantic: new insights into the formation of sediment waves by turbidity currents. *Sedimentology*, 47, pp. 1181-1197.
- Xu, J. P., Noble, M. A. & Rosenfeld, L. K. 2004. *In-situ* measurements of velocity structure within turbidity currents. *Geophysical Research Letters*, 31, L09311.
- Xu, J. P., Swatzenski, P. W., Noble, M. & Li, A. C. 2010. Event-driven sediment flux in Hueneme and Mugu submarine canyons, southern California. *Marine Geology*, 269, pp. 74-88.
- Xu, J. P., Wong, F. L., Kvitek, R., Smith, D. P. & Paull, C. K. 2008. Sandwave migration in Monterey submarine canyon, Central California. *Marine Geology*, 248 (3), pp. 193-212.
- Xu, J.P., Sequeiros, O. E. & Noble, M. A. 2014. Sediment concentrations, flow conditions, and downstream evolution of two turbidity currents, Monterey Canyon, USA. *Deep Sea Research Part I: Oceanographic Research Papers*, 89, pp. 11-34.
- Yagishita, K. 1994. Planar cross-bedding associated with rip currents of Upper Cretaceous formations, northeast Japan. *Sedimentary Geology*, 93, pp. 155-163.
- Yalin, M. S. 1964. Geometrical properties of sand waves. *Journal of the Hydraulics Division*, 90 (5), pp. 105-119.
- Yalin, M. S. 1977. *Mechanics of Sediment Transport*. New York: Elsevier.
- Yalin, M. S. 1992. *River Mechanics*. Oxford: Pergamon Press.
- Yang, Y., Gao, S., Wang, Y.P, Jia, J., Xiong, J., Zhou, L. 2019. Revisiting the problem of sediment motion threshold, *Continental Shelf Research*, 187, 103960.